

Innovative Technology of Thermoelectric Generator for Waste Heat Recovery in Automotive Application

Kuo Huang, MEng. BEng.

Thesis submitted to the University of Nottingham for the degree of

Doctor of Philosophy

August 2019

ABSTRACT

This research project aims to provide an in-depth understanding on waste heat recovery (WHR) technologies for vehicles, especially thermoelectric generator (TEG) system. Thermoelectric (TE) devices convert the temperature difference between both sides directly into electric potential difference, thus provide electrical power for external load. Because they have advantages of compact package, no mechanical moving parts and high reliability, TE devices are normally applied in WHR for various situation. Based on previous researches, the low in heat transfer efficiency and insufficient in space utilisation of automotive TEG system are the main reasons that prevent the TEG system from massive utilisation in WHR for automotive.

Therefore, in these presented works, a novel designed structure for automotive TEG system is promoted, regarding to these issues. The novel TEG system is design in concentric cylindrical structure, which perfectly accords with the shape of the exhaust pipe in vehicle, thus improve the space utilisation of TEG system. Moreover, an efficient heat-transfer device, heat pipe, is employed in this concentric cylindrical TEG system for enhancing heat transfer performance. A heat pipe combines the principles of both thermal conductivity and phase transition to effectively transfer heat between two interfaces, thus has an effective thermal conductivity could approach 100 kW/(m·K), in comparison with approximately 0.4 kW/(m·K) for copper. By introducing heat pipes into TEG system, the heat transfer between exhaust gas and heat exchanger could be significantly enhanced.

In this thesis, the thermal performance of concentric cylindrical TEG system is investigated both numerically and experimentally. The investigation on thermal performance separates in two direction: conductive heat transfer and convective heat transfer. Three-dimensional models for annular thermoelectric module (TEM) and single annular TE unit in concentric cylindrical TEG system is established, in order to simulate the conductive heat transfer of this system in COMSOL Multiphysics. The performance comparison between annular TEM and traditional square TEM is conducted with these three-dimensional models. A proof-concept test rig is built up for verifying the feasibility of heat pipe combined heat exchanger and exploring the influence of different arrangement. In addition, the simulation of a two-dimensional model for cross section of heat exchanger is performed in COMSOL Multiphysics as well, with the aim of inspecting the convective heat transfer within concentric cylindrical TEG system. Four optimized heat exchanger structures with fins or different heat pipe length are designed and compare in the simulation. By compared several structures, a general guidance for designing the heat exchanger for concentric cylindrical TEG system is summarised.

Besides the investigation on thermal performance, the system-level of concentric cylindrical TEG system, especially the fuel economy improvement, is studied in this thesis as well. Fuel economy improvement is an important indicator to measure the performance of automotive TEG systems. One-dimensional model of vehicle, engine and TEG system is established in GT-Suite and their performances are simulated consequently. The standardized driving cycle, Worldwide Harmonised Light Vehicles Test Procedure (WLTP), is utilised during the simulation to get a relatively accurate result for fuel economy improvement. In addition, the

experimental data obtained from engine test rig of cooperating car manufacture is set as reference data for the fuel consumption model.

Based on the calculation of fuel consumption model, a method to improve efficiency of automotive TEG system is introduced by utilising phase change material (PCM) as the thermal energy storage for the system. PCM system could deposit the extra thermal energy during vehicle acceleration and release those energy while vehicle deceleration. Pentaerythritol (PE) is selected as a potential PCM for automotive TEG system with its suitable thermal properties and investigated in this thesis. A test rig for inspecting the feasibility of integrating PCM with TE devices is built up and the experiment is conducted with single TEM with PE. Furthermore, in order to improve thermal conductivity of PE, three different containers with volume ratio at 50 %, 65 % and 80 % are tested experimentally.

PUBLICATIONS ARISING FROM THIS WORK

- **KUO HUANG**, BO LI, YUYING YAN, YONG LI, SSENNOGA TWAHA and JIE ZHU. A Comprehensive Study on a Novel Concentric Cylindrical Thermoelectric Power Generation System, Applied Thermal Engineering. 117 (2017), 501-510
- **KUO HUANG**, YUYING YAN, BO LI, YONG LI, KAI LI, JUN LI. A Novel Design for a Thermoelectric Generator for Waste Heat Recovery for Automotive Applications, Automotive Innovation, Volume 1 (2018), Issue 1, pp 54–61
- BO LI, **KUO HUANG**, YUYING YAN, YONG LI, SSENNOGA TWAHA and JIE ZHU. Heat Transfer Enhancement of a Modularised Thermoelectric Power Generator for Passenger Vehicles, Applied Energy. 205C (2017), 868-879
- BO LI, **KUO HUANG** and YUYING YAN, Thermoelectric Power Generation for Heat Recovery in Automotive Industries, Bringing Thermoelectricity into Reality, IntechOpen, 2018
- CONG QI, **KUO HUANG**, JIAAN LIU,GUOHUA WANG and YUYING YAN, Thermal Management and Heat Transfer Enhancement Using Porous Materials, Convective Heat Transfer in Porous Media, Taylor & Francis, 2019
- **KUO HUANG**, BO LI, YUYING YAN. Performance Comparison between Annular Thermoelectric Module and Square Thermoelectric Module. International Symposium of Heat Transfer and Heat Powered Cycle 2016, Nottingham, UK.
- **KUO HUANG**, YUYING YAN, BO LI. Working Performance Analysis of Concentric Cylindrical Thermoelectric Generator. 9th International Symposium on Heat Transfer, Beijing, China.
- **KUO HUANG**, BO LI, YUYING YAN, JUN LI. Thermal and electric analysis of a modularised thermoelectric power generator for passenger vehicles. 13th Vehicle Thermal Management System Conference and Exhibition, London, UK.

- **KUO HUANG**, YUYING YAN, BO LI. The Thermal and Electrical Performance of Concentric Cylindrical Thermoelectric Generator under Different Driving Cycles. 3rd International Symposium of Fluids and Thermal Engineering, Ningbo, China.
- **KUO HUANG**, YUYING YAN, BO LI. Comprehensive Performance Analysis of Concentric Cylindrical Thermoelectric Generator for Light-duty Vehicles. 16th International Heat Transfer Conference, Beijing, China.

ACKNOWLEDEGEMENTS

The past four-year PhD programme is a very important experience in my life. I gained not only the knowledge of being a qualified researcher but also the critical thinking for my further career and life.

First and foremost, I would like to express my most sincere gratitude to my supervisor, Prof. Yuying Yan for all the guidance, support and patience throughout my PhD study. Without his helpful advices and assistance, this thesis would never been able to finish.

I also appreciate my colleagues and all technical staff of the Built Environment Department. Thanks to Mr. James Hazzledine and Mr. Tony Gospel for their unselfish assistance in the laboratory. Special thank goes to Dr. Guohang Wang for his suggestions and assistance on my test rig during his visit in our group. My thanks are extended to Dr. Jiaju Hong, Dr. Rong Fu, Mr. Wei Gong, Miss Yiyi Chen, Mr. Zeyu Liu, Mr. Thomas Werner, Mr. Xin Wang, Mr. Edward Wright, Mr. Li Wang and Mr. Dahui Yu. Thanks for meeting them and we would share very beautiful memories for living and studying in Nottingham.

Thanks to China Scholarship Council for funding the living expenses during my study abroad.

Last but not least, I am extraordinarily grateful to my family: my parents for their encouragement, trust and expectation on me; my fiancée Miss Anqi Liang for her understanding and love. Thanks for your support and you all are the most precious person in my life.

NOMENCLATURE

Roman Letters

A	Effective heat transfer area (m2)
A_r	Effective heat transfer area of heat exchanger (m2)
be	Specific fuel consumption (g/kWh)
c_{cl}	Specific heat capacity of coolant (J/kg·K)
C_p	Constant pressure heat capacity (J/kg·K)
C_v	Constant volume heat capacity (J/kg·K)
C_{Pex}	Constant pressure specific heat capacity of exhaust gas (J/kg·K)
D	Hydraulic diameter of pipe (m)
E	Electromotive field
F	Force (N)
f	Darcy resistance coefficient; Melt fraction
g	Gravitational acceleration (m/s2)
h	Heat transfer coefficient (W/m2·K)
H_L	Low heat value of fuel (kJ/kg)
$H_{N,P}$	Height of TE legs (m)
I	Electric current (A)
J	Current density (A/m2)
k	Thermal conductivity (W/m·K)
k_e	Flow loss coefficient
L	Hydraulic length of pipe (m)
l	Characteristic linear dimension (m)
$L_{N,P}$	Length of the TE legs (m)

m	Weight (kg)
m_{cl}	Mass flow rate of coolant (kg/s)
m_{ex}	Mass flow rate of exhaust gas (kg/s)
m_f	Mass flow rate of fuel (kg/s)
n	Number of TE legs; engine speed (rpm)
N_c	Number of engine cylinders
P	Power output (W); Pressure (Pa)
P_{me}	Brake Mean Effective Pressure (BMEP) of the engine (bar)
Q	Peltier heat (J)
Q_{cool}	Energy taken away by the cooling system (J)
Q_{ex}	Energy carried away by the exhaust gas (J)
Q_f	Fuel combustion energy (J)
Q_{misc}	Residual energy loss in miscellaneous (J)
Q_s	Storage capacity of PCM (J)
R	Electrical resistance (Ω)
R	Uncertainty
S	Seebeck coefficient (V/K)
S_{air}	Spectral radiance of air (W/m2·K4)
S_b	Stefan–Boltzmann constant (W/m2·K4)
S_{TEM}	Cross section area of TEM (m2)
$T_{1,2,3,4}$	Temperature at the end of each process of Otto Cycle (℃)
$T_{ex,a}$	Temperature of exhaust gas and ambient (℃)
$T_{hj,cj}$	Temperature at hot and cold junction (℃)
$T_{in,out}$	Temperature at outlet and inlet (℃)
t_m	Melting temperature (℃)

t_w	Boundary temperature
V	Volume (m3)
V	Effective heat transfer volume (m3)
V_c	Engine capacity (L)
v_i	Independent variables
W_e	Effective mechanical power (W)
W_R	Overall uncertainty
ZT	Figure of merit

Greek Letters

γ	Specific heat ratio
δ_M	Momentum boundary layer thickness (m)
δ_{vi}	Uncertainties of independent variables
ε	Emissivity
η	Efficiency of Otto Cycle
η_m	Mechanical efficiency of ORC
η_{th}	Thermal efficiency of ORC
κ	Thomson coefficient ($J \cdot m^2/A \cdot K$)
λ	Kinematic viscosity (m^2/s); thermal conductivity ($W/m \cdot K$)
v	Velocity (m/s)
$\Pi_{A,B}$	Peltier coefficients of conductors A and B (V/A)
ρ	Electrical resistivity (Ω/m); density (kg/m^3)
σ	Electrical conductivity (S/m)
Φ_w	Heat carried away within the TEG system (J)

ω	Local exhaust gas velocity (m/s)

Abbreviations

Bi	Biot number (hl/λ), λ is the thermal conductivity of solid
BMEP	Brake Mean Effective Pressure
EHRS	Exhaust heat recovery system
FDM	fused deposition modelling
FTP-75	EPA Federal Test Procedure
HCCI	Homogeneous Charge Compression Ignition
HEV	hybrid electric vehicles
IEC	Internal combustion engine
LMTD	log mean temperature difference
MPPT	Maximum power point tracking
Mtoe	Million Tonnes of Oil Equivalent
NEDC	New European Driving Cycle
N-type	negative-type
Nu	Nusselt number (hl/λ), λ is the thermal conductivity of liquid
OEM	original equipment manufacturer
ORC	Organic Rankine Cycle
PCM	phase change material
PE	Pentaerythritol
Pr	Prandtl number (v/a)
P-type	positive-type
RC	Rankine Cycle

Re	Reynolds number (vl/λ)
SI	spark-ignition
TA	thermoacoustic
TAC	Thermoacoustic Converter
TC	Turbocharging
TE	Thermoelectric
TEG	Thermoelectric generator
TEM	Thermoelectric material
toe	tonne of oil equivalent
VCR	Variable Compression Ratio
VC-T	Variable Compression Turbocharged
VVT	Variable Valve Timing
WHR	Waste heat recovery
WLTP	Worldwide Harmonised Light Vehicle Test Procedure

Contents

ABSTRACT I

PUBLICATIONS ARISING FROM THIS WORK IV

ACKNOWLEDEGEMENTS VI

NOMENCLATURE VII

Roman Letters VII

Greek Letters IX

Abbreviations X

Contents XII

LIST OF TABLES XVIII

LIST OF FIGURES XIX

Chapter 1. Introduction 1

1.1 Background of Engine Energy Distribution 1

1.2 Background of Improving Thermal Efficiency for ICE 4

1.3 Outline of Research 10

Chapter 2. Literature Review for WHR Technologies of Vehicles and Automotive TEG system 13

2.1 Introduction 13

2.2 WHR Technologies for Light-Duty Passenger Vehicles 17

2.2.1 Thermoelectric Generator (TEG) 17

2.2.2 Organic Rankine Cycle (ORC) 20

2.2.3 Exhaust Heat Recovery System (EHRS) 24

2.2.4 Thermoacoustic Converter (TAC) 26

2.3 Introduction of Thermoelectric Effects 28
2.3.1 Fundamental Theory of Thermoelectric 30
2.3.2 Thermoelectric Materials 33
2.4 TEG for Automotive Waste Heat Recovery 38
2.4.1 Heat Exchanger for Automotive TEG system 38
2.4.2 Prototypes of Automotive TEG system 41
2.5 Challenges of TEG Systems for Light-Duty Passenger Vehicles ... 45
2.5.1 Pressure Drop Control 45
2.5.2 Variable Driving Condition 46
2.5.3 Energy Storage 48
2.5.4 System Matching and Integration 49
2.5.5 Efficiency, Cost & Life Cycle 51
2.6 Further Development of TEG Systems for Light-Duty Passenger Vehicles 52
2.6.1 Application on Different Vehicle Platform 52
2.6.2 3D Printing Technology in Automotive TEG System 53
2.7 Summary 55
Chapter 3. Model Description and Research Methodology 57
3.1 Model Description of Concentric Cylindrical TEG System 57
3.2 Heat Transfer Model of Concentric Cylindrical TEG System and Heat Exchanger 60

3.2.1 Conductive Heat Transfer in TEM and Heating or Cooling Plate ……..61

3.2.2 Convective Heat Transfer between Exhaust Pipe and Heat Pipes ……..65

3.3 Conjugate Heat Transfer and Lumped Parameter Analysis in Conjugate Heat Transfer 68

3.3.1 Conjugate Heat Transfer Process..... 68

3.3.2 Methods of Numerical Solution for Conjugate Heat Transfer 70

3.3.3 Lumped Parameter Analysis..... 71

3.3.4 Criteria for Lumped Parameter Analysis..... 74

3.4 Test Rig and Experiment Set Up..... 75

3.4.1 Experimental Test Rig for Investigation of Convective Heat Transfer 75

3.4.2 Experimental Test Rig for Transient Performance Improvement 77

Chapter 4. Numerical Investigation on Conductive Heat Transfer within Concentric Cylindrical TEG System 80

4.1 Introduction 80

4.2 Model Description and Governing Equation..... 82

4.2.1 3D Model of Annular TEM and Annular TE Unit 82

4.2.2 Materials Properties in Simulation 86

4.2.3 Boundary Conditions and Heat Transfer Equation..... 88

4.3 Results and Discussion..... 92

4.3.1 Simulation Model Verification 92
4.3.2 Performance Comparisons of Single TEM 96
4.3.3 Influence of Heat Transfer Area 99
4.3.4 Performance of Single Annular TE Unit 101
4.3.5 Performance Comparisons of Two Different Exhaust Configurations 105
4.3.6 Temperature Distribution 108
4.3.7 Heat Transfer Filling Factor 110
4.4 Summary 112
Chapter 5. Experimental and Numerical Investigation for Convective Heat Transfer Enhancement of Concentric Cylindrical TEG System 115
5.1 Introduction 115
5.2 Test Section and Numerical Model Description 118
5.2.1 Experimental Test Section 118
5.2.2 Numerical Model Description 122
5.2.3 Governing Equation in Conjugated Heat Transfer 124
5.3 Results and Discussion 130
5.3.1 Uncertainty Analysis 130
5.3.2 Experimental Results 131
5.3.3 Lumped Parameters Method 138
5.3.4 Simulation Results Presentation 139
5.3.5 Discussion on Simulation Results 147

5.3.6 Log Mean Temperature Difference Analysis 159

5.4 Summary 161

Chapter 6. Comprehensive Model of Fuel Economy Estimation for Vehicles with Concentric Cylindrical TEG System 164

6.1 Introduction 164

6.2 Engine, Vehicle and TEG Model Description 167

6.3 Model for Fuel Economy Estimation 169

6.3.1 Back Pressure Impact 170

6.3.2 System Weight Impact 171

6.3.3 Pumping Power Impact 172

6.3.4 DC-DC Converter Impact 173

6.3.5 Fuel Consumption Improvement 173

6.4 Result and Discussion 175

6.4.1 Engine Performance and Waste Heat 176

6.4.2 Power Generation of Concentric Cylindrical TEG System under Standardised Driving Cycle 178

6.4.3 Improvement of Fuel Economy under Standardised Driving Cycle 184

6.5 Summary 187

Chapter 7. Experimental Investigation for Transient Performance Improvement of TEG by Integrating Phase Change Material 190

7.1 Introduction 190

7.1.1 Background 190

7.1.2 Energy Storage System 192
7.1.3 PCM for Thermal Energy Storage 199
7.1.4 Heat Transfer Enhancement for PCM 206
7.2 Test Section 207
7.2.1 PCM Selection 207
7.2.2 Material Properties and Preparation 210
7.2.3 Experimental Test Section 212
7.3 Result and Discussion 214
7.3.1 Uncertainty Analysis 214
7.3.2 Performance of Single TEM with Different Match Load 215
7.3.3 Transient Performance Comparison by Integrating PCM 218
7.3.4 Temperature Distribution of Different Experimental Test Case 222
7.3.5 Voltage and Power Comparison of Different Samples 227
7.4 Summary 232
Chapter 8. Conclusions and Further Work 234
8.1 Conclusions of Current Work 234
8.2 Future Work 237
References 240
Appendix 1 264
Appendix 2 272

LIST OF TABLES

Table 1-1 Comparison between each thermal efficiency improving techniques 9

Table 2-1 Recently presented ORC systems in research works 23

Table 2-2 Comparison between four WHR technologies 28

Table 2-3 Prototypes of automotive TEG system 43

Table 4-1Geometric details of two TEMs 84

Table 4-2 Geometric details of major components in annular TE unit 85

Table 4-3 Materials properties of major components in annular TE unit 87

Table 4-4 Temperature-dependent polynomials of TE materials properties 88

Table 4-5 Heat transfer filling factor of different topological TEG system 111

Table 6-1 Detailed Specifications of Test Vehicle 169

Table 7-2 Comparison between different energy storage system 198

Table 7-3 Advantages and disadvantages of different type of PCM 205

Table 7-4 Properties of Bi_2te_3 TEM 210

Table 7-5 Properties of Pentaerythritol 211

LIST OF FIGURES

Figure 1-1 Pressure–Volume and Temperature-Entropy diagrams of Otto Cycle .. 2

Figure 1-2 Heat balance map for internal combustion engine (ICE) 4

Figure 1-3 Heat balance of the different type of engine under 50% load 5

Figure 1-4 Principle of automotive turbocharger 6

Figure 1-5 Basic mechanical of Infiniti VC-T engine 8

Figure 2-1 Sankey diagram of the global energy usage by sources and end sectors 14

Figure 2-2 Energy usage of transportation sector 15

Figure 2-3 Energy distribution within transportation sector 16

Figure 2-4 Energy distribution of ICE 17

Figure 2-5 Schematic diagram of Rankine Cycle and basic Organic Rankine Cycle 20

Figure 2-6 T–s diagram of a typical Rankine cycle 21

Figure 2-7 Schematic diagram and gas-liquid heat exchanger of EHRS 25

Figure 2-8 Scheme of the TAC and detailed view on core component 27

Figure 2-9 Schematic diagram of a single TEM and TE leg..... 29

Figure 2-10 Relationship between Seebeck coefficient, electrical conductivity and thermal conductivity 34

Figure 2-11 ZT value of different types of TE materials in recent research……. 36

Figure 2-12 Schematic diagram and photo for a printed cylindrical TEM 55

Figure 3-1 Schematic diagrams of the concentric cylindrical TEG system 59

Figure 3-2 Schematic diagram of the single unit in concentric cylindrical TEG system..... 60

Figure 3-3 Heat transfer within the concentric cylindrical TEG system 61
Figure 3-4 Conductive heat transfer within the concentric cylindrical TEG system 62
Figure 3-5 Cross section of the concentric cylindrical TEG system 65
Figure 3-6 Schematic diagram of convective heat transfer test rig 76
Figure 3-7 Photo of convective heat transfer test rig 77
Figure 3-8 Schematic diagram of transient performance improvement set up 78
Figure 3-9 Photo of the main test section in transient performance improvement set up 78
Figure 4-1Overall architecture of a thermoelectric power generation system in the form of heat energy flow 80
Figure 4-2 3D model of square TEM and annular TEM and single annular TE unit 84
Figure 4-3 Detailed mesh model for single annular TE unit 86
Figure 4-4 Schematic diagram and photo of the model-scale experimental test rig 93
Figure 4-5 Comparison of numerical model, Hi-Z model and experiment 94
Figure 4-6 Performances of each TEM under different hot-side condition 98
Figure 4-7 Average temperature & open circuit voltage of both TEMs under different inward heat flux 100
Figure 4-8 Temperature distribution simulation and P-I-V curve of external exhaust channel and internal exhaust channel configuration 102
Figure 4-9 Temperature distribution of (a) cooling blocks (b) heating block (c) cross section of TEM and (d) longitudinal section of annular TE unit 104

Figure 4-10 Power output contour of annular TE unit under different heat transfer coefficient for (a) external and (b) internal exhaust channel. 105
Figure 4-11 Performance curves of internal-exhaust-channel configuration 106
Figure 4-12 Performance curves of external-exhaust-channel configuration 107
Figure 4-13 Temperature distribution in radial direction of concentric cylindrical TEG system 109
Figure 5-1 Schematic of experimental selection in concentric cylindrical TEG system 118
Figure 5-2 Schematic for test section 119
Figure 5-3 Arrangement of thermocouples in test section 120
Figure 5-4 Schematic for flow arrangement in experiment test 121
Figure 5-5 Corresponding air flow rate with blower frequency 122
Figure 5-7 Verified simulation model & experimental test section 124
Figure 5-8 Results comparison between realizable k-ε model and experimental data 129
Figure 5-9 Temperature distribution with different air flow rate 133
Figure 5-10 Temperature distribution with different water flow rate 134
Figure 5-11 Average temperature distribution with different flow arrangement 136
Figure 5-12 Average temperature distribution with different heat pipe arrangement 137
Figure 5-13 Temperature distribution of heat exchanger without fins 141
Figure 5-14 Temperature difference contour of heat exchanger without fins 142
Figure 5-15 Pressure Drop contour of heat exchanger without fins 142
Figure 5-16 Reynold Number contour of heat exchanger without fins 143

Figure 5-17 Temperature distribution of heat exchanger with 30°fins 144
Figure 5-18 Temperature difference contour of heat exchanger with 30° fins ... 145
Figure 5-19 Pressure drop contour of heat exchanger with 30° fins 146
Figure 5-20 Reynold Number contour of heat exchanger with 30° fins 147
Figure 5-21 Temperature distribution of heat exchanger with 45° fins 148
Figure 5-22 Temperature difference contour of heat exchanger with 45° fins ... 149
Figure 5-23 Pressure drop contour of heat exchanger with 45° fins 150
Figure 5-24 Reynold Number contour of heat exchanger with 45° fins 150
Figure 5-25 Temperature distribution of heat exchanger with 60° fins 151
Figure 5-26 Temperature difference contour of heat exchanger with 60° fins ... 152
Figure 5-27 Pressure drop contour of heat exchanger with 60° fins 153
Figure 5-28 Reynold Number contour of heat exchanger with 60° fins 153
Figure 5-29 Temperature distribution of heat exchanger with different heat pipe length 154
Figure 5-30 Temperature difference contour of heat exchanger with different heat pipe length 155
Figure 5-31 Pressure drop contour of heat exchanger with different heat pipe length 156
Figure 5-32 Reynold Number contour of heat exchanger with different heat pipe length 157
Figure 5-33 Comparison of each heat exchanger with different engine speed ... 158
Figure 5-34 Comparison of each heat exchanger with different exhaust temperature 159
Figure 5-35 LMTD under different engine speed and exhaust temperature 161

Figure 6-1 GT-Suite models of the engine and vehicle & calculating procedure168

Figure 6-2 GT-Suite models of concentric cylindrical TEG system & location. 168

Figure 6-3 Engine experiment test rig for validating GT-Suite models..... 169

Figure 6-4 Schematic diagram for comprehensive fuel consumption model..... 174

Figure 6-5 Flow chart for calculating fuel economy improvement..... 175

Figure 6-6 Experimental results of contours for exhaust properties 177

Figure 6-7 Contours of exhaust gas energy and energy percentage..... 178

Figure 6-8 Contour of power generation of concentric cylindrical TEG system 179

Figure 6-9 Vehicle speed in WLTP class 3 driving cycle..... 181

Figure 6-10 Engine speed and torque & exhaust properties under WLTP class3 cycle..... 182

Figure 6-11 Temperature grad difference ient and power output under WLTP class3 cycle..... 183

Figure 6-12 Contour of specific fuel consumption of the test vehicle 185

Figure 6-13 Contour of the percentage improvement in fuel consumption by utilising concentric cylindrical TEG system 186

Figure6-14 Fuel economy improvement under different driving cycle 187

Figure 7- 1 General classification of PCMs 201

Figure 7-2 Temperature range of different PCMs..... 202

Figure 7-3 PE's chemical structure and molecule model of & heating and cooling curves..... 212

Figure 7-4 Photo of four different containers..... 213

Figure 7-5 Containers with PE before and after experiment..... 213

Figure 7-6 Arrangement of thermocouples in the main test section 214

Figure 7-7 I-V characteristics and P-I-V characteristics of a single TEM 216
Figure 7-8 Power output of a single TEM with different match load resistance 217
Figure 7-9 Comparison of temperature distribution of TEM with and without TEM 219
Figure 7-10 Comparison of open circuit voltage and temperature difference 220
Figure 7-11 Power output and temperature difference at 3.5 Ω match load resistance 221
Figure 7-12 Hot-side & cold-side temperature distribution of TEM with each sample 223
Figure 7-13 Comparison of hot-side temperature for each sample 225
Figure 7-14 Open circuit voltage and temperature difference of different sample 228
Figure 7-15 Comparison of open circuit voltage for each sample 229
Figure 7-16 Power output and temperature difference of each sample 230
Figure 7-17 Comparison of power output for each sample 231
Figure 0-1 Temperature and velocity field of heat exchanger with 30° fins 273
Figure 0-2 Temperature and velocity field of heat exchanger with 45° fins 274
Figure 0-3 Temperature and velocity field of heat exchanger with 60° fins 275
Figure 0-4 Temperature and velocity field of heat exchanger with different heat pipe length 276
Figure 0-5 Temperature and velocity field of heat exchanger without fin 277

Chapter 1. Introduction

1.1 Background of Engine Energy Distribution

In 1876, Nikolaus Otto patented the first four-stroke spark ignition internal combustion engine (ICE) based on the Otto Cycle. This engine could only achieve thermal efficiency of around 10 % through combustion of compressed air-fuel mixture. The Otto Cycle is an idealised thermodynamic cycle used to describe the functioning of a typical spark ignition engine [1] and it is the one most commonly employed in automobile engines [2]. There are four strokes in the Otto Cycle and Figure 1-1 shows the pressure–volume, and temperature-entropy diagrams of the Otto Cycle [3]:

1) Intake stroke—the air-fuel mixture enters the piston combustion chamber;
2) Compression stroke—the piston compresses the mixture;
3) Power stroke—the fuel mixture is ignited by flame and later electric spark;
4) Exhaust stroke—exhaust gas is released from the piston chamber.

In these four processes, process 1 and 3 are isentropic compression and isentropic expansion processes and processes 2 and 4 are isochoric heat addition and isochoric heat rejection processes, respectively. According to the ideal gas equation, the efficiency of engine combustion based on the Otto Cycle can be expressed by the following equation [4]:

$$\eta = 1 - \left(\frac{C_v(T_4 - T_1)}{C_v(T_3 - T_2)}\right) = 1 - \left(\frac{T_1}{T_2}\right)\left(\frac{T_4/T_1 - 1}{T_3/T_2 - 1}\right) \qquad \text{Eq. 1-1}$$

Since the Otto Cycle uses isentropic processes during the volume change phase and isochoric processes during the heat change phase, the equations of ideal gases

and the constant pressure/volume relations are tenable during the whole cycle. Therefore, the Eq. 1-1 can be transformed into:

$$\eta = 1 - \left(\frac{1}{(V_1/V_2)^{(\gamma-1)}}\right) \qquad \text{Eq. 1-2}$$

where $\gamma = C_P/C_V$ is called specific heat ratio. Eq. 1-2 demonstrates that the efficiency of engine combustion depends directly upon the compression ratio of the engine.

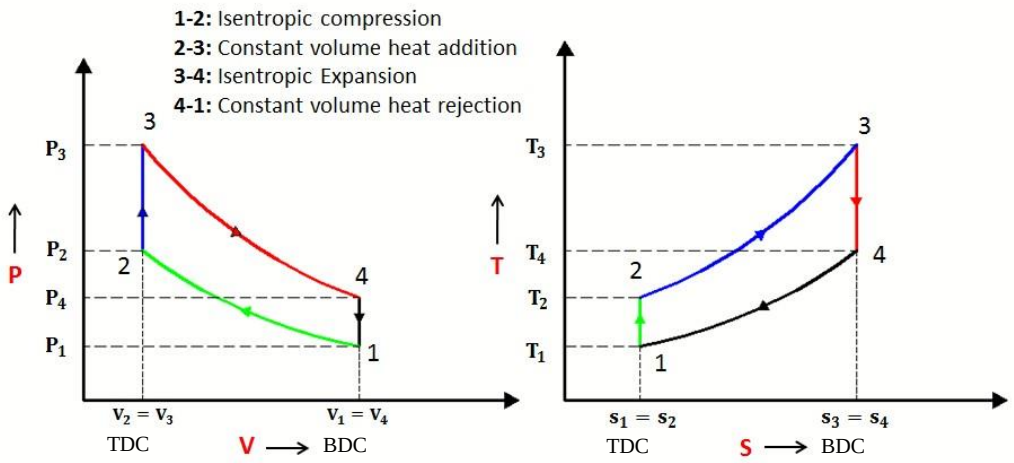


Figure 1-1 Pressure–Volume and Temperature-Entropy diagrams of Otto Cycle [3]

However, according to the second law of thermodynamics, not all the energy generated by combustion can be transformed into effective mechanical power for automobile steering. As a matter of fact, more than 60% of fuel combustion energy is consumed by different type of depletion [5].

Normally, the energy generated by the fossil fuel combustion is distributed in four paths: effective mechanical power, engine cooling, exhaust, and miscellaneous loss. The thermal balance figure, shown in Figure 1-2, expresses the equality between the energy generated by burning fuel in the cylinders of the engine and the

various energy flows out. According to the law of thermodynamics, the following energy balance equation gives the relationship among various kinds of energy [6-9]:

$$Q_f = W_e + Q_{cool} + Q_{ex} + Q_{misc} \quad \text{Eq.1-3}$$

The various kinds of energy in the equation are explained in the following equations:

Q_f is the energy generated by the fuel combustion, which can be given as:

$$Q_f = \dot{m}_f \cdot H_L \quad \text{Eq.1-4}$$

where $\dot{m}_f$ is the mass flow rate of fuel and H_L is the low heat value of fuel.

W_e is the effective mechanical power of the engine.

Q_{cool} is the energy taken away by the cooling system, including water and oil, which is given as:

$$Q_{cool} = \dot{m}_{cl} \cdot c_{cl} \cdot (T_{out} - T_{in}) \quad \text{Eq.1-5}$$

where $\dot{m}_{cl}$ is the mass flow rate of coolant; c_{cl} is the specific heat capacity of coolant; T_{out} and T_{in} are the coolant temperature at outlet and inlet, respectively

Q_{ex} is energy carried away by the exhaust gas, which can be given as:

$$Q_{ex} = \dot{m}_{ex} \cdot c_{P_{ex}} \cdot (T_{ex} - T_a) \quad \text{Eq.1-6}$$

where $\dot{m}_{ex}$ is the mass flow rate of exhaust gas; $c_{P_{ex}}$ is the specific heat capacity at constant pressure of exhaust gas; T_{ex} and T_a are the temperature of exhaust gas and ambient, respectively

Q_{misc} is the residual energy loss owing to miscellaneous factors such as friction, accessories and heat radiation.

Figure 1-3 is the heat balance diagrams of gasoline and diesel engines, under 50 % load. It shows that diesel engines usually have higher thermal efficiency than gasoline engines due to a higher compression ratio.

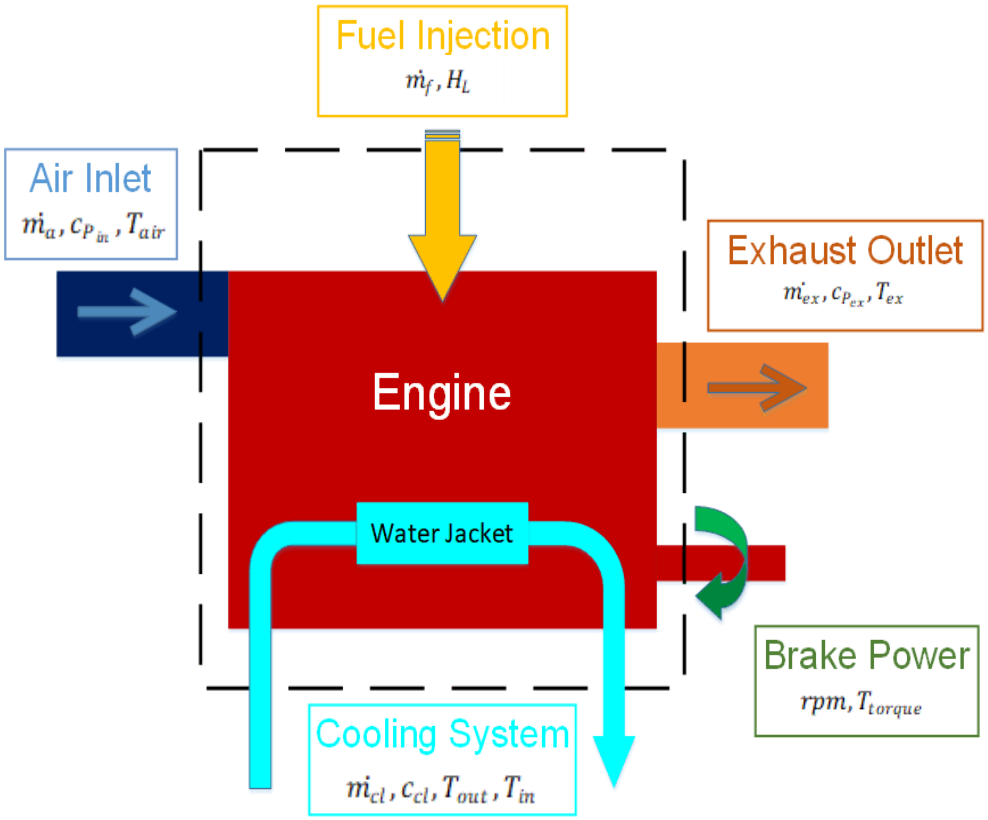


Figure 1-2 Heat balance map for internal combustion engine (ICE)

1.2 Background of Improving Thermal Efficiency for ICE

Research into improving the thermal efficiency of ICE has been undertaken since the invention of ICE. Nowadays, the highest thermal efficiency of ICE that can be achieved is 55% and is obtained using different thermal efficiency improving techniques [10]. Many techniques have been identified in the past few decades such

as turbocharging (TC) [11], variable valve timing (VVT) [12], homogeneous charge compression ignition (HCCI) [13], variable compression ratio (VCR) [14] and waste heat recovery (WHR) [15]. Researchers and engineers have invested enormous amounts of time and energy into studying these techniques in the past several years. Nowadays, most of these techniques have a widely commercial usage in current vehicles to improve fuel economy and exhaust emission. Undoubtedly, each has its own advantages and disadvantages during practical application.

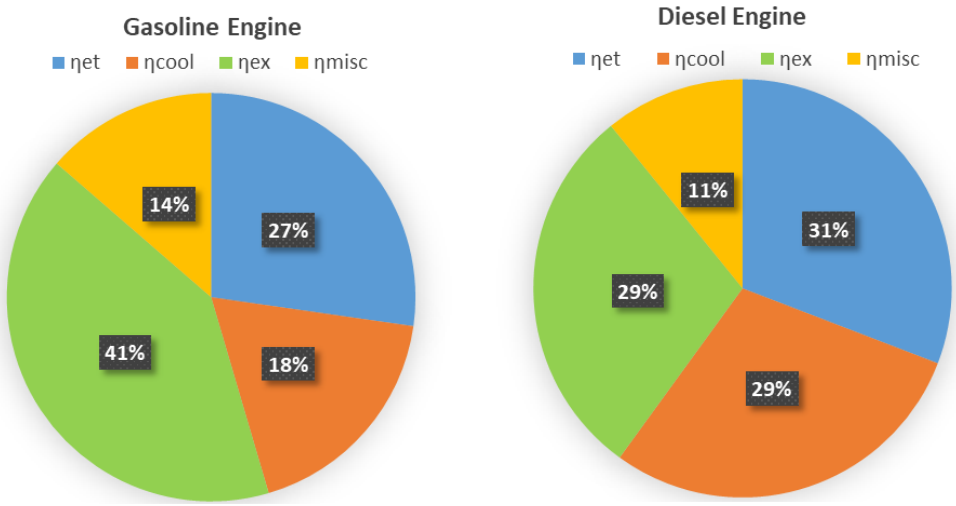


Figure 1-3 Heat balance of the different type of engine under 50% load [9]

Turbocharging (TC) is one of the most popular thermal efficiency improving techniques for ICE and has been studied the most and further developed than the others. Gottlieb Daimler firstly patented the prototype of turbocharger in 1885 and TC techniques saw significant development during 1970s when the automobile industry grew at a rapid rate [16]. Show in Figure 1-1, the difference between the exhaust and intake pressures and temperatures means that efficiency can be boosted by transferring the energy from the exhaust flow to the intake flow by forcing extra

compressed air into the combustion chamber. This technique results in a greater mass of air entering the cylinders on each intake stroke and improves the power density of the engine [17]. Figure 1-4 shows the principle diagram of a turbocharger used in automotive industries.

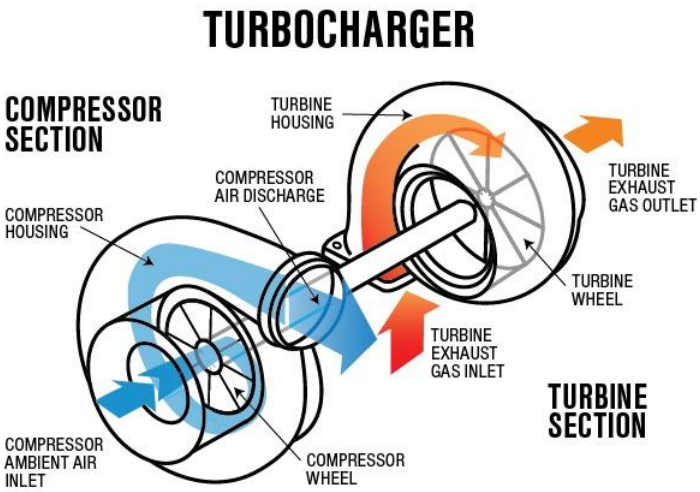


Figure 1-4 Principle of automotive turbocharger [18]

Compared with a naturally aspirated engine, the advantages of TC engines include lower fuel consumption, higher thermal efficiency and higher power-to-weight ratio owing to the exhaust energy contributing to the efficiency of the engine and lower volumetric displacement of TC engines. The disadvantages, however, are turbo lag, boost threshold and power surges [18, 19].

Variable Valve Timing (VVT) first became known in the 1920s and the aim of VVT is to improve volumetric efficiency, decrease emissions, and decrease pumping losses of the engine [20]. The VVT system allows intake and exhaust valves to open earlier or later in the four-stroke cycle. There are many ways of achieving VVT, ranging from mechanical devices to electro-hydraulic system and

cam-less system [21]. Even though different VVT system has various strengths, overall, there are two main advantages of VVT: continuous improvement of efficiency across whole engine speed range and general reduction of vehicle emission [22]. However, the uppermost drawback of VVT is that a complex system is required compared to the other techniques [23, 24].

Homogeneous Charge Compression Ignition (HCCI) is a novel form of internal combustion, which was introduced in the 1950s and experienced rapid development during the 1970s [25]. The main purpose of HCCI is to mix fuel and air outside of the cylinder and compress the mixture to the point of auto-ignition [26]. Differing from other forms of combustion, HCCI combines the characteristics of conventional gasoline and diesel engines and allows engines to have a lower-temperature combustion, resulting in nearly no NO_x emissions [27].

HCCI engines also have the advantages of a higher thermal efficiency than spark-ignition (SI) engines, almost no NO_x and soot emissions and low scavenging losses [28, 29]. However, the disadvantages are also obvious as follow: weak cold start capability, high pressure to engine piston, difficulty in controlling auto ignition and small power range [30-32].

The concept of Variable Compression Ratio (VCR) was presented firstly in the 1930s [33]. In 2019, the mass production of VCR engine is the Variable Compression Turbocharged (VC-T) engine in Infiniti QX50 [34]. Figure 1-5 shows the basic mechanical diagram of the Infiniti VC-T engine. VCR is a technique that can adjust the compression ratio of ICE while it is in operation to increase efficiency under various driving conditions. VCR engines achieve optimal compression ratios by allowing for variation of combustion chamber space. The mechanisms for VCR

include either two-step systems or continuously variable systems [35]. A VCR engine has the benefits of achieving higher power output without detonation in a broad range of engine speeds and torques, which can make the engine smaller and more efficient [36]. Conversely, in order to archive optimal compression ratios, an extremely complicated mechanical structure is essential for VCR engines, which increases the cost of the vehicles.

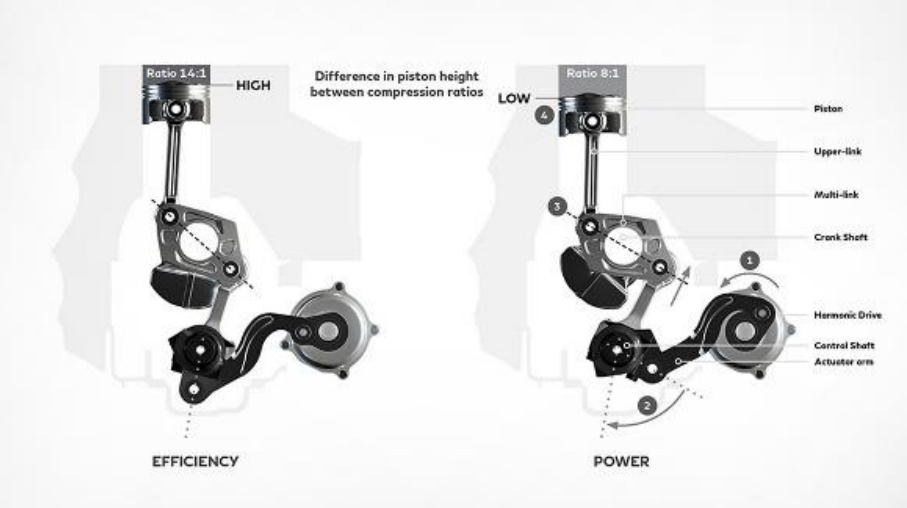


Figure 1-5 Basic mechanical of Infiniti VC-T engine [34]

Waste Heat Recovery (WHR) is a technique to recover the waste heat from engine exhaust gas and transform it into mechanical or electrical power that can be reused by the engine. As stated in the first section of this chapter, over one-third of combustion energy is expelled with exhaust gas. In order to improve the thermal efficiency of an engine, it is necessary to recover this part of energy into application. The first patent for a WHR facility used in ICE was presented in 1946 [37], where WHR system and muffler were combined to obtain higher thermal efficiency. Nowadays, there are several different techniques for WHR in the automotive and

the details of each technique will be introduced in Chapter Two. Generally speaking, the advantages for WHR are high reliability, regardless of driving cycle and utilising at all time. On the contrary, the WHR requires an insert component in the automobile exhaust system, which will increase the backpressure of engine. Furthermore, the relatively low energy conversion efficiency of WHR is a factor that prevents this technique from being used commercially [38-40].

A summary of the advantages and disadvantages for each technique is provided in Table 1-1.

Table 1-1 Comparison between each thermal efficiency improving techniques

Techniques	Advantages	Disadvantages
Turbocharging (TC)	• Significant increase in engine horsepower • Reduce engine size for better fuel economy	• Turbo lag • Boost threshold • Power surge
Variable Valve Timing (VVT)	• Improving efficiency across whole engine working range	• Complex VVT system is required
Homogeneous Charge Compression Ignition (HCCI)	• Low level of NOx and soot emissions • Reduce scavenging losses in the same time	• Cold start capability • High pressure to engine piston • Controlling auto ignition • Small working range
Variable Compression Ratio (VCR)	• Prevent detonation in a broad range • Downsize for the engine	• Extremely complicated mechanical structure • Increase vehicle cost
Waste Heat Recovery (WHR)	• High reliability • Regardless of driving cycle • Operating at all time	• Increase engine backpressure • Low energy conversion efficiency

1.3 Outline of Research

In this presented research, a novel design of a TEG system combined with heat pipes, called concentric cylindrical TEG system, is designed for WHR of automobile. The aims of this project are to enhance heat transfer within this novel TEG system and improve the total power generation under various driving conditions. These two aims will be accomplished through the optimisation of structure design, software simulation and experimental investigation. The objectives of this research include:

- Comprehensively understand the fundamental theory and mechanism of thermoelectric (TE) and the current status of TEG system.
- Understand fluid characteristics and heat transfer characteristics of internally finned tubes and heat exchangers in TEG systems.
- Numerically investigate the performance of the annular thermoelectric module (TEM) in concentric cylindrical TEG system and the annular TE unit of concentric cylindrical TEG system.
- Improve heat transfer of concentric cylindrical TEG system by optimising the structure of heat exchanger.
- Establish a conjugate model for calculating fuel economy of passenger vehicles by utilising concentric cylindrical TEG system.
- Experimentally investigate the improved transient performance of TEM by employing phase change material (PCM) for energy storage.

In order to improve space utilisation in engine exhaust system, the concentric cylindrical TEG system is designed in relation to the shape of exhaust pipe. With the help of annular TEM, the concentric cylindrical TEG system arranges more TEM than other existing TEG systems. Furthermore, by employing heat pipes, the heat transfer in the hot and cold sides of concentric cylindrical TEG system is improved. The main concept and design are described in Chapter Three, as well as the methodologies and experimental set-up of this project. A comprehensive literature review related to WHR and TEG technologies for automobile is performed in Chapter Two. In-depth understandings of the advantages and disadvantages of different WHR technologies as well as the potential and challenge of TEG system are assessed. Through literature review, it is discovered that TEG is the most suitable technique for light-duty passenger vehicle. Chapters Four and Five mainly present the simulation results of the concentric cylindrical TEG system. Simulations using COMSOL Multiphysics, for power generation of a single annular TE unit and heat transfer enhancement in concentric cylindrical TEG system are carried out. Because of the difficulty of manufacturing annular TEM, the experimental test is based on square TEM in Chapter Five. Moreover, the system-level performance of concentric cylindrical TEG system is discussed in Chapter Six, the results of fuel economy improvement under various standardised driving cycles are presented in this chapter. According to the results of Chapter Six, in order to improve the total efficiency of the TEG system under real-time driving, the potential of PCM integrated TEM system is experimentally investigated in Chapter Seven. PCM stabilises the hot side temperature of the TEM when the temperature

of heat source falls sharply. Finally yet importantly, the conclusions and recommendations for works are summarised in Chapter Eight.

Chapter 2. Literature Review for WHR Technologies of Vehicles and Automotive TEG system

2.1 Introduction

In 2015, the Paris Agreement sets out the common goal to limit global warming and identifies ways in which this might be achieved [41]. It aims to strengthen the global response to the threat of climate change by "Holding the increase in the global average temperature to well below 2 °C above pre-industrial levels and pursuing efforts to limit the temperature increase to 1.5 °C above pre-industrial levels." This aim is an enormous challenge for the researchers because we are using more energy than ever before.

According to the statistics analysis [42], in 2017, the global total energy usage amounted to 13972 million tonnes of oil equivalent (Mtoe). A tonne of oil equivalent (toe) is used here as a unit of energy that is equivalent to the amount of energy released by burning one tonne of crude oil. It is approximately 11630 kilowatt-hours (kWh) and used for measuring large amounts of energy. Figure 2-1 shows a Sankey diagram of the global energy usage by energy sources and end sectors. As shown in the figure, fossil fuel contributed 31.7 % of the total energy, which was the second-largest source of global energy in 2017 [43]. More than 30% of the energy generated by fossil fuel is consumed by the transportation sector, with transportation being the second largest end sector of energy usage among all end sectors. Furthermore, more than 90 % of the energy used by transportation was derived from fossil fuels in 2017, although this number has been decreased over the past few years. Figure 2-2 shows the proportion of transportation in total energy

consumption and the proportion of fossil fuel consumed in transportation energy source from 1973 [44, 45]. As shown in the figures, these two proportions have slightly decreased in the past few years owing to the deterioration of the environmental issues and the development of clean energy sources.

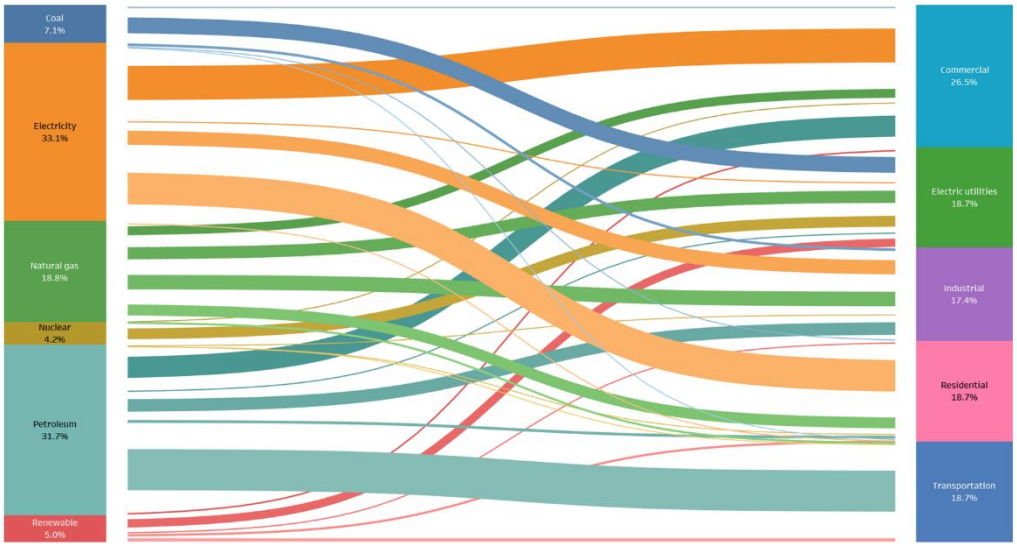


Figure 2-1 Sankey diagram of the global energy usage by sources and end sectors [43]

Yet in the past decade, there has been tremendous growth in the collective number of all registered vehicles. The global light-duty vehicle stock exceeded 1.1 billion in 2015, up from 0.95 billion in 2010 and 0.82 billion in 2005. The energy distribution inside transportation, as shown in Figure 2-3, where it is evident that almost two-thirds of the energy is consumed by light vehicles and 26.3 % of the energy provides the power for passenger cars. This means light-duty vehicles consume a lot of energy every year, equating to roughly the amount used for as residential lighting, according to the statistics analysis [46].

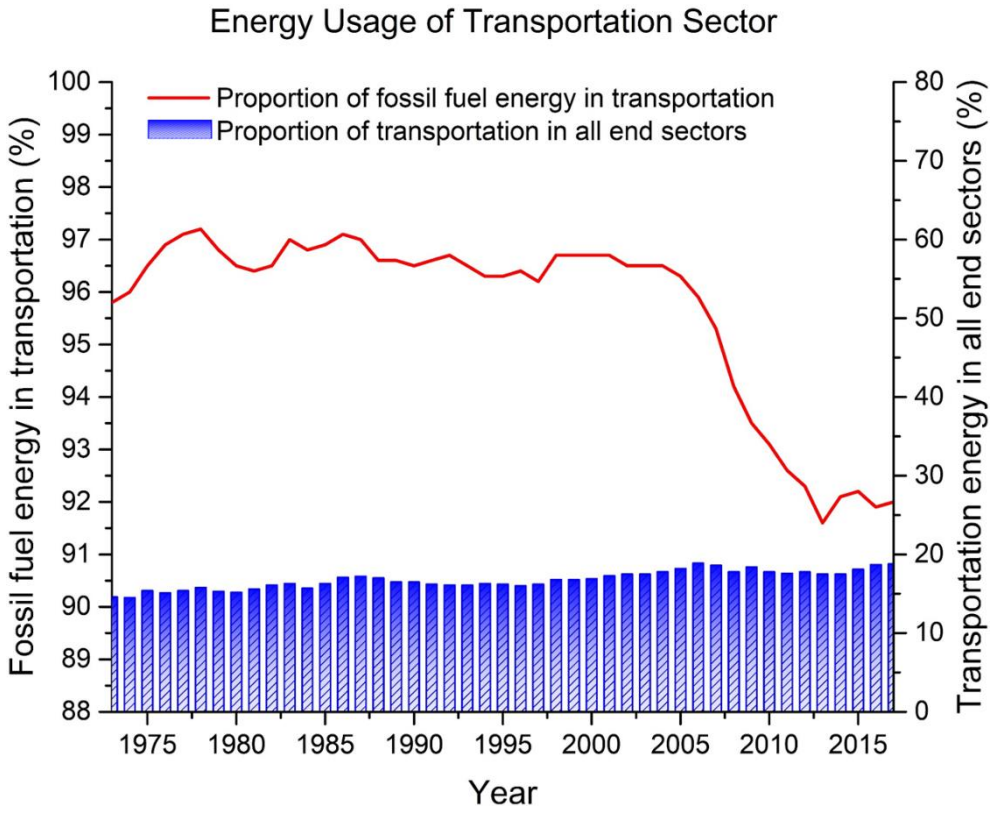


Figure 2-2 Energy usage of transportation sector [44,45]

Therefore, the fuel economy of light-duty vehicles needs to be addressed to achieve the goal of energy saving and adhering to the Paris Agreement. Unfortunately, as indicated in Chapter One, only 30% of the energy generated by the fuel combustion converts into mechanical power, while nearly 35% of the energy is expelled to the ambient through the automotive exhaust system, as shown in Figure 2-4 [47]. In addition, there are several methods to enhance the thermal efficiency of vehicular ICE for improving fuel economy, mentioned in Chapter One as well. However, the fuel economy improvement over the past decade have been significantly lower than the rate of improvement required meeting the 2030 target. There is thus a need for more effective action in the fuel consumption and emission

regulations, which are envisioned to become even stricter and more rigorous in the future.

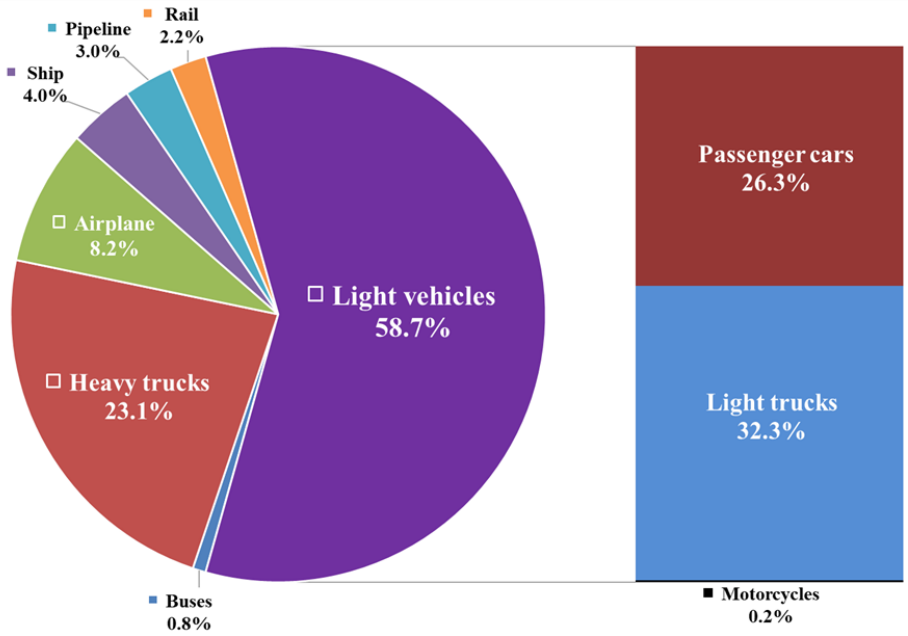


Figure 2-3 Energy distribution within transportation sector [46]

Therefore, finding ways of recovering this lost energy is one of the major goals being pursued by automotive engineers. There is great potential for considerable fuel savings if the electrical energy required by all systems in an automobile can be produced using waste heat rather than relying solely on the vehicle's generator [48-51].

In this chapter, a detailed review of WHR techniques in automobile is provided firstly. By compared these techniques, it becomes evident that the TEG system is the best technique for light-duty passenger vehicles. As such, a literature review about automotive TEG systems is then presented.

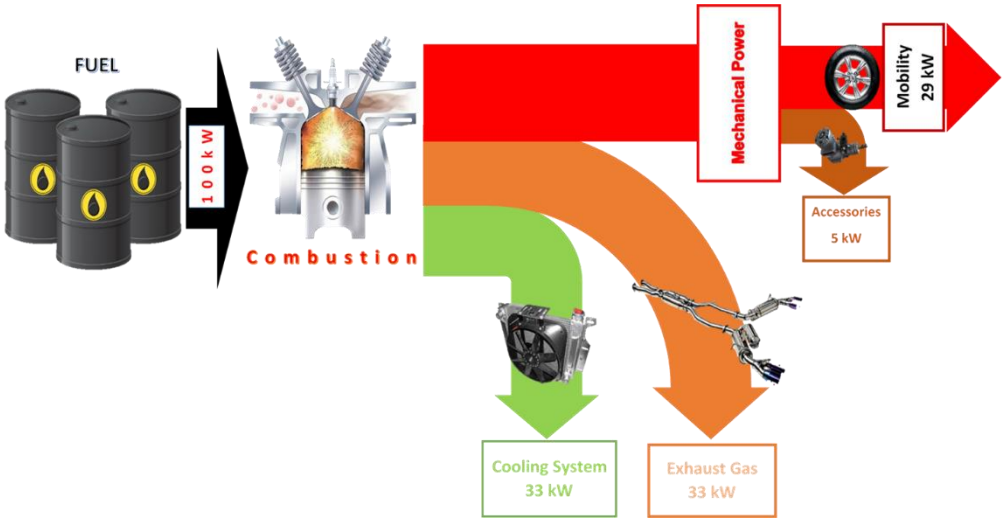


Figure 2-4 Energy distribution of ICE [47]

2.2 WHR Technologies for Light-Duty Passenger Vehicles

2.2.1 Thermoelectric Generator (TEG)

As one of the promising WHR technology, a thermoelectric generator (TEG) is a solid-state device that can convert heat flux directly into electrical energy by means of the Seebeck effect, which was discovered by Thomas Johann Seebeck in 1821 [52]. The Seebeck effect is the direct conversion of temperature differences at the two sides of the TE materials to electric power. Thereby, a TE device can function like heat engines and create voltage potential, which is less bulky and without any mechanical moving component. With this character, TEG systems could be utilised in power plants in order to convert waste heat into additional electrical power and in automobiles to transform the waste heat from the engine exhaust gas directly into electric power and thus increase fuel efficiency [53, 54]. Furthermore, there are two important factors for the automotive TEG system to be efficient: the figure of merit (ZT value) of TE materials and heat transfer efficiency

of heat exchanger [55]. The detailed introduction of TE effects, TE materials and heat exchangers for automotive TEG system will be provided in following part.

Normally, it is better for the TEG system to be closer to the exhaust manifold in order to ensure a higher inlet temperature for the system, which means higher power generation of the system. However, the three-way catalytic converter requires a certain temperature for activating the catalytic reaction, thus the TEG system is located in the exhaust pipe between the three-way catalytic converter and muffler [56, 57]. The major components of TEG system are as follow: a hot-side heat exchanger to absorb the heat from exhaust gas, a cold-side heat exchanger to expel the heat to the engine coolant, a TEG system to generate electrical power with the temperature difference between both sides and a DC-DC converter to adjust the output voltage for matching the vehicle accessories. The operating process of the automotive TEG system can be described as follows [58]:

- During the normal operation of an ICE, the waste heat released through the exhaust pipe is captured by hot-side heat exchanger and expelled via the cold-side heat exchanger.
- Electricity is then generated in TEG system from the temperature difference created by the heat exchangers.
- Power conditioning is performed by the DC-DC converter to achieve a suitable voltage with maximum power transfer.

The advantages of TEG systems are numerous: direct energy conversion, no mechanical moving parts, long lifespan, noiseless operations and high flexibility.

These advantages make the TEG system one of the most suitable techniques for light-duty passenger vehicles.

However, the main issue preventing the TEG system from widespread application is the relatively low heat to electricity conversion efficiency and the high cost of TE materials. The performance of the TE materials has a significant effect on the cost of the TEG recovery system.

Most of the TEMs that are commercially available are based on bismuth telluride (Bi_2Te_3), lead telluride (PbTe), and silicon germanium (SiGe) and the high cost of tellurium and germanium is the main reason for the high cost of TEG system. An early study on the cost of TEG system by Haidar and Ghojel [59] proposed that a full TEG WHR system was still prohibitive in 2001 due to its current price of $175 per TEM for small orders. Yee et al. [60] promoted a cost metric for evaluating the cost effectiveness of TE materials by using $ per W. The results showed that silicide has the lowest raw cost among all the TE materials and the most cost-competitive cooling method is water cooling. However, the development of materials could lead to a significant reduction in the cost of TEG system [61]. In addition to the cost of TE materials, manufacturing costs are also high, particularly owing to the substrates (ceramic plates) and heat exchangers [62].

As the conversion efficiency is relatively low, the system can only become cost effective and more competitive, when lower costs of TEM and a higher-value figure of merit can be achieved.

The detailed analysis of automotive TEG system is presented in the following parts of the review.

2.2.2 **Organic Rankine Cycle (ORC)**

Organic Rankine Cycle (ORC) is considered as a rational solution to convert thermal energy of low and moderate temperature heat sources into mechanical work. It is currently attracting increasing attention as being an effective WHR in ICE [63]. The ORC is named for its utilisation of an organic working fluid with higher molecular mass and a lower boiling point than water, which is used in conventional Rankine Cycle (RC) [64].

A RC system includes four major components: an evaporator, an expander, a condenser, and a pump, as shown in Figure 2-5, which is the flow loop of a typical RC system [65].

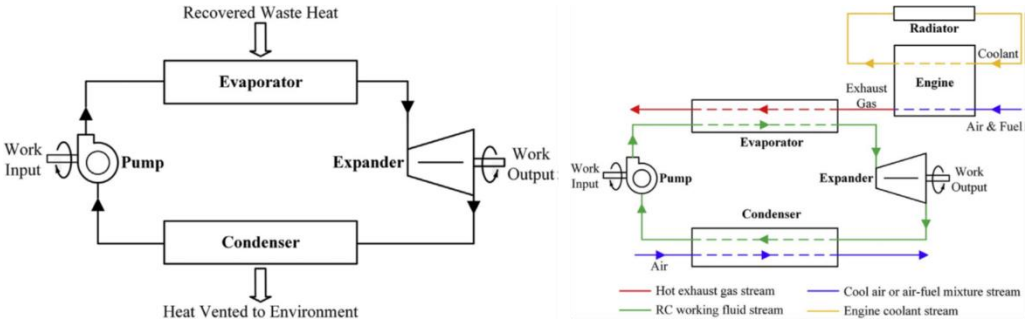


Figure 2-5 Schematic diagram of Rankine Cycle and basic Organic Rankine Cycle [65]

The working fluid is pumped through the whole loop with a water pump and firstly passes through the evaporator boiler where it is evaporated by the thermal energy from waste heat. The expander is at the outlet of evaporator and the evaporated working fluid pushes the turbine in the expander, which converts thermal energy into mechanical power output. Then, the expanded vapour flows through a condenser where it is finally re-condensed, thus completing the cycle. The low-temperature thermal energy is converted into useful work in the expander,

which could be converted into electricity as well. In the ideal cycle described by the theoretical model, the expansion is isentropic and the evaporation and condensation processes are isobaric. Figure 2-6 shows the T–s diagram of a typical Rankine cycle. The working principle of the RC is described as follows [66]:

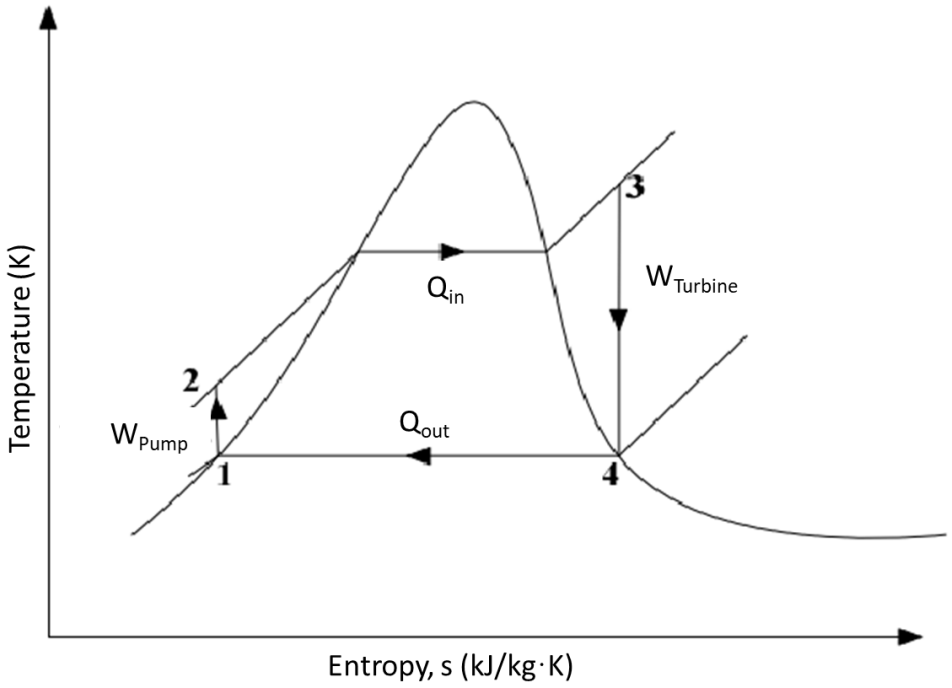


Figure 2-6 T–s diagram of a typical Rankine cycle [66]

- Process 1-2 is isentropic compression in water pump. The low pressure working fluid is pressurized from low to high pressure.
- Process 2-3 is a constant-pressure heat addition in evaporator. The working fluid is vaporised in the evaporator, where it is heated at a constant pressure and becomes a dry saturated vapour, using the thermal energy from waste heat.

- Process 3-4 is an isentropic expansion in the expander. The high-pressure vapour working fluid expands through a turbine and its thermal energy is converted into mechanical energy upon the turbine shaft.
- Process 4-1 is a constant pressure heat rejection in the condenser. The vapour is condensed with coolant into a saturated liquid and a new cycle begins.

The first study examining the application of RC to an automotive application was reported in the 1970s [67]. Since then, extensive work has been done on investigating the feasibility of applying RC to automobiles (with a primary focus on heavy-duty diesel engine trucks [68, 69])

ORC is analogous to the RC as it contains all the main components of the RC such as evaporator, expansion device, condenser and pump with the only difference is that the water is replaced by an organic compound. Figure 2-5 presents a schematic diagram of basic ORC system. Compared to steam RC, the ORC exhibits unique advantages such as high flexibility, high reliability, low maintenance requirements, good thermal performance and low environmental impacts when combined with renewables.

Due to these advantages, the ORC technology has been deployed at a fast pace over the past few years across the globe and experienced remarkable advances due to extensive academic research. Nowadays, the structure of ORC system has been fully developed and there are five different structure in general [65]:

1. Basic structure, which utilises the exhaust gas as the only heat source to evaporate the working fluid.

2. Recuperator structure, in which a recuperator is added before the evaporator. The recuperator uses the steam from the expander to preheat the working fluid.

3. Coolant preheat structure, in which waste heat from the engine coolant is used to preheat the working fluid.

4. Partially evaporative structure, in which the engine block is used at a higher temperature than the coolant to partially evaporate the working fluid.

5. Dual loop structure, which utilises separate system loops and different working fluids to match the specific characteristics of the engine coolant and exhaust gas.

Normally, in ORC system research, more than one of the structures mentioned above would be employed to improve the total efficiency of ORC system. Table 2-1 lists some of recently presented ORC systems in the literatures.

Table 2-1 Recently presented ORC systems in research works

Architect	Working fluid	η_{th} (%)	η_m (%)	Efficiency (%)	Year	Ref
Structure 1	R123 R245fa	0.85-1.2	2.64- 6.96	2.03 9.53	2013	[66]
Structure 5	R134a R245fa	3-6	-	-	2012	[70]
Structure 5	R245fa	1.7-8.2	-	-	2012	[71]
Structure 2&3	R245fa	13	-	5.4%	2014	[72]
Structure 5	Cyclohexane	13.68- 15.62	-	-	2016	[73]
Structure 5	R124 R152a R134a	-	-	23.79 23.38 22.37	2016	[74]
Structure 2&3	Toluene & R143a	9.9	-	16	2016	[75]
Structure 3&4	R143a R245fa	10.7-13 9.9-15.8	- -	9.1-10.8 7.6-10	2016	[76]
Structure 4	Cyclopentane	11.67	-	-	2017	[77]
Structure 2	Toluene MDM MM R245fa	-	-	24.46 21.04 18.96 11.78	2017	[78]

2.2.3 **Exhaust Heat Recovery System (EHRS)**

Exhaust heat recovery system (EHRS) is another guaranteed technology for automotive waste heat recovery, which has been expeditiously developed recently [79]. As stated in Chapter One, there are more than 30 % of engine thermal energy is expelled with exhaust gas, especially during the start-up of the vehicle. During the start-up phase, the temperature of engine coolant and lubricating oil is lower than the optimal working temperature, resulting in a further reduction of the overall thermal efficiency of the engine. Therefore, an effective method for quickly increasing the engine start-up temperature is essential for improving thermal efficiency and fuel economy [80]. The aim of EHRS is to enhance engine cabin warm-up and speeds up coolant and lubricating oil warming through exhaust thermal energy, which would otherwise be wasted [81, 82]. It accomplishes this by capturing the waste thermal energy to warm up the coolant and lubricating oil for reducing parasitic losses in the engine, transmission, and drive shaft. During the engine cold start phase, a valve controls the exhaust gas flow, routing it through a heat exchanger, where the thermal energy of the exhaust gas heats up the vehicle's subsystem fluids. This system can improve fuel economy by up to 8.5 % and significantly reduce emissions. Moreover, EHRS not only improves fuel efficiency by rapidly warming powertrain lubricating oil and coolant but also reduces friction, with minimal impact on backpressure and packaging space.

Normally, the EHRS has two different heat exchangers for coolant and engine lubricating oil, because the engine coolant is less viscous and has better heat transfer properties than engine oil [83]. The exhaust heat warms up the coolant in the gas-liquid heat exchanger firstly and then the coolant heats up the lubricating oil in the

liquid-liquid heat exchanger. Furthermore, the EHRS consists of two parallel flow paths, which are regulated by a double valve, providing two modes of operation: heat recovery and bypass. In heat recovery mode, the exhaust gas passes through the heat exchanger, which then recovers the thermal energy and transfers it to the engine coolant. In bypass mode, the exhaust gasses flow through the bypass and no heat is recuperated. Figure 2-7 presents a schematic diagram of the gas-liquid heat exchanger of EHRS [84]. The EHRS can heat up the engine to optimal working temperature within 2 minutes, therefore an approximate 4 % reduction of fuel consumption on FTP cycle and up to 10 % fuel consumption reduction under cold climate conditions would be achieved. The major features of EHRS are compact structure, high reliability, good temperature adaptability and greater customer comfort.

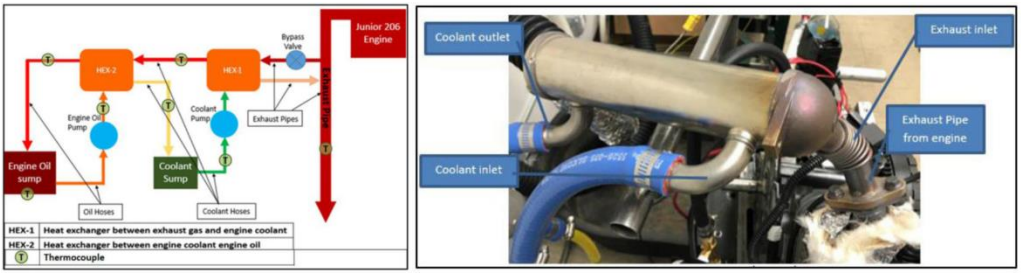


Figure 2-7 Schematic diagram and gas-liquid heat exchanger of EHRS [84]

Uppuluri et al. [81] investigated impact of EHRS on a typical 1.2 L naturally aspirated gasoline engine. The experimental results observed that EHRS captured 26% of available exhaust energy, which resulted in 1% fuel economy benefit. Faurecia [85], in cooperation with Hyundai Motor, presented a 3 kW EHRS in the Hyundai's IONIQ hybrid. This system resulted in a reduction of fuel consumption of up to 7 % and reduced the CO2 emission to 1.5 g/mile in the US.

2.2.4 **Thermoacoustic Converter (TAC)**

Thermoacoustic Converter (TAC) as another recently proposed WHR method that has drawn a lot of attention in the past few years [86-88]. TAC is based on the effect of thermoacoustics (TA), which is the physical phenomenon related to the interaction between temperature, density and pressure variations of acoustic waves. Simply, the TA effect is a physical phenomenon caused by acoustic self-excited oscillations in an elastic medium (high-pressure inert gas). Modern TA theory mainly originates from the works of Rott [89] who has successfully developed linear thermoacoustic theory, which has been validated for application in low-amplitude thermoacoustic oscillation. TA engines can readily be driven using solar energy or waste heat and they can be controlled using proportional control. TA engines provide significant advantages in terms of higher efficiency and lower mechanical complexity.

As in a vehicle engine, the TAC produces electric power where a temperature differential exists, which can be generated with engine exhaust and coolant. Essentially, the TAC converts exhaust waste heat into electricity in two steps: 1) the exhaust waste heat is converted to acoustic energy and 2) the acoustic energy is converted to electrical energy [90]. Figure 2-8 shows a schematic drawing of the TAC [91]. The basic elements comprising the whole system are ambient heat exchanger, hot-side heat exchanger, resonator and stack, which is core components of TAC. Heat is supplied to the TAC via hot-side heat exchanger and released by an ambient heat exchanger. This process results in a temperature difference over the stack. Generally, TAC systems are associated with two distinct types of oscillations: convection-driven or conduction-driven [92].

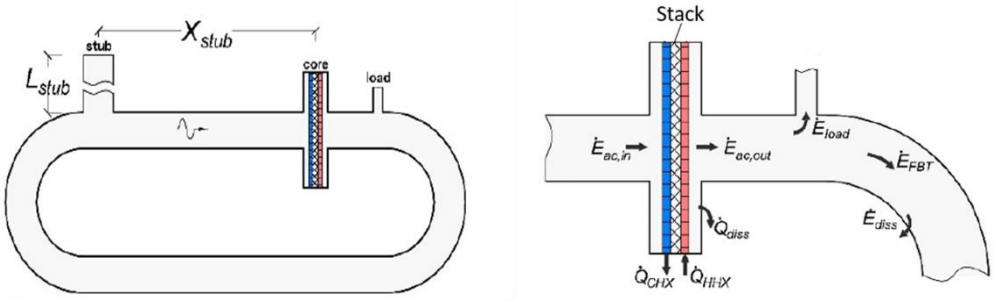


Figure 2-8 Scheme of the TAC and detailed view on core component [91]

In 1998, Yazaki et al. [93] practically demonstrated the first running travelling wave thermoacoustic engine. However, this engine proved to have a very low efficiency. In order to overcome the efficiency limitations of the travelling wave TAC, Backhaus and Swift [94] proposed a new type of TAC, which utilises high acoustic impedance to suppress the high acoustic loss. This thermoacoustic engine has a much higher thermal efficiency of 30 %. Tijani and Spoelstra [95] presented a TAC whose exergetic efficiency can reach 52 % by enhancing construction details. Blok [96] presented a novel TAC under a low operating temperature in the range 70-200 ℃. This system combines the bypass geometry with a loss travelling wave feedback loop which can enhance the overall performance of the system. The travelling-wave TAC with a looped tube configuration was numerically investigated by Ruziewicz et al. [97]. They assumed that the engine was operating under low-grade heat condition (150 °C) and concluded that the single-stage TAC had an exergetic efficiency of 40 % to utilise waste heat under low-grade heat. Although many studies have been carried out in terms of both engine developments and basic understanding of TAC, further efforts are still needed to promote their applications.

Table 2-2 compares the advantages and disadvantages of these four WHR techniques. As shown in the comparison, TEG is the most suitable method for WHR in a light-duty passenger vehicle. Therefore, in the next section, detailed information about the TEG system will be provided.

Table 2-2 Comparison between four WHR technologies

WHR method	Advantages	Disadvantage
Thermoelectric Generator (TEG)	• No mechanically rotating parts • Compact package • No noise and vibration • High reliability	• Relatively low conversion efficiency • Relatively high costs of TE materials
Organic Rankine Cycle (ORC)	• Can utilise at both low and medium temperature • Regardless of ICE load or drive cycle	• Response to transients • Efficiency tend to be low • Large space needed
Exhaust Heat Recovery System (EHRS)	• Low impact on backpressure • Simple system structure • Good temperature adaptability • Reduce emissions	• Only operating during start-up phase • Need to increase power for water pump
Thermoacoustic Converter (TAC)	• High efficiency • Good noise characteristics	• Extra component to exhaust system • Low operating range

2.3 Introduction of Thermoelectric Effects

In 1821, Thomas Johann Seebeck discovered that a thermal gradient formed between two dissimilar conductors could produce electricity. At the atomic scale of the thermoelectric effect is the fact that a temperature difference in a conducting material results in the diffusion of charge carriers. The flow of charge carriers between the hot and cold regions in turn creates a voltage difference. In 1834, Jean Charles Athanase Peltier discovered the reverse effect, where running an electric current through the junction of two dissimilar conductors could cause it to act as a

heater or cooler, depending on the direction of the current [98]. Figure 2-9 presents a schematic diagram of a single TEM and TE leg.

Normally, the thermoelectric effect encompasses three separate effects: the Seebeck effect, the Peltier effect, and the Thomson effect. The Seebeck and Peltier effects are different manifestations of the same physical process [99]. The Thomson effect is an extension of the Seebeck-Peltier effect and credited to Lord Kelvin Thomson. Joule heating is generated whenever a current is passed through a resistive material, which is accessary effect to TE materials. The Seebeck, Peltier and Thomson effects are thermodynamically reversible, whereas Joule heating is not. The following section provides the basic equations for each effect and discusses the relations among them.

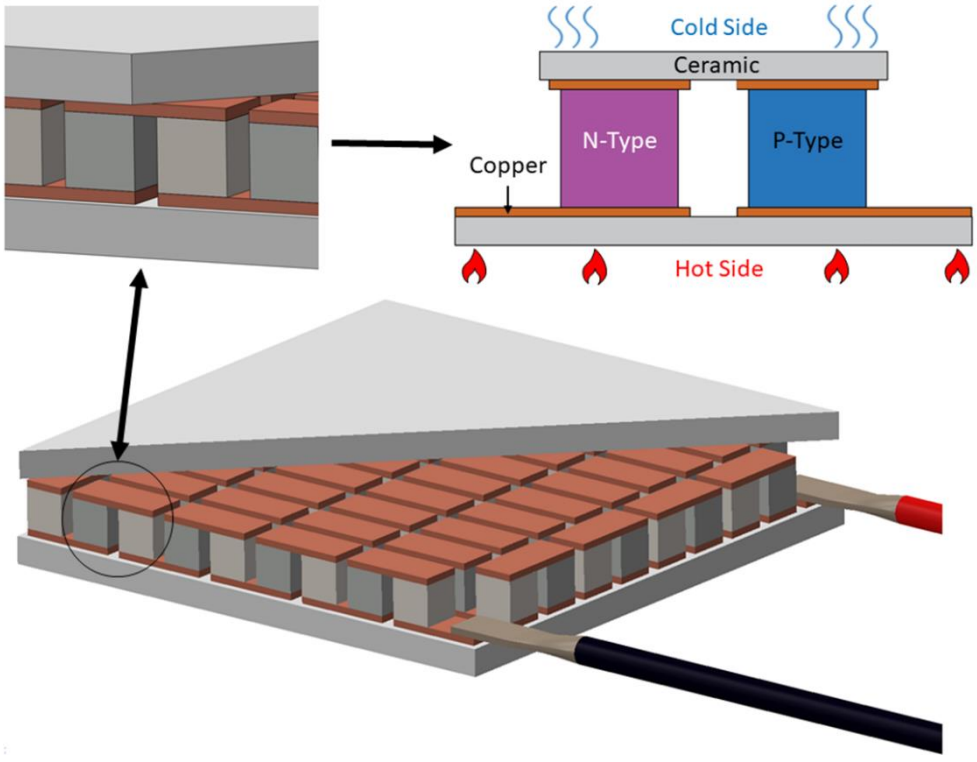


Figure 2-9 Schematic diagram of a single TEM and TE leg

2.3.1 **Fundamental Theory of Thermoelectric**

2.3.1.1 Seebeck Effect

The Seebeck effect is the conversion of heat directly into electricity at the junction of different types of wire. Originally discovered in 1794 by an Italian scientist, it is named after the German physicist Thomas Johann Seebeck, who rediscovered it independently in 1821. It was observed that a compass needle would be deflected by a closed loop formed by two different metals joined in two places, with a temperature difference between the joints. The Seebeck effect is a classic example of an electromotive force and leads to measurable currents or voltages in the same way as any other electromotive force. In general, the Seebeck effect can be described as the creation of an electromotive field [100]

$$E = -S\nabla T \qquad \text{Eq. 2-1}$$

where S is the Seebeck coefficient, a physical property of the material, and ∇T is the temperature difference.

The Seebeck coefficient of a thermoelectric material depends on temperature, as well as on other two physical properties: thermal conductivity and electric conductivity. For ordinary materials at room temperature, the Seebeck coefficient may range in value from μV/K to mV/K.

2.3.1.2 Peltier Effect

The Peltier effect is the presence of heating or cooling at an electrified junction of two different conductors and is named after French physicist Jean Charles Athanase Peltier, who discovered it in 1834. When a current flows through a

junction between two conductors, A and B, heat may be generated or removed at the junction. The Peltier heat generated at the junction per unit time is [100]

$$\dot{Q} = (\Pi_A - \Pi_B) \cdot I \qquad \text{Eq. 2-2}$$

where Π_A and Π_B are the Peltier coefficients of conductors A and B; I is the electric current through A and B. It is worth mentioning that the total heat generated is not determined by the Peltier effect alone, because it may also be influenced by Joule heating.

The Peltier coefficients represent how much heat is carried per unit charge. Since charge current must be continuous across a junction, the associated heat flow will develop a discontinuity if Π_A and Π_B are different. The Peltier effect can be considered as the back-action counterpart to the Seebeck effect: if a simple thermoelectric circuit is closed, then the Seebeck effect will drive a current, which, in turn, will always transfer heat from the hot to the cold junction. The relationship between Seebeck and Peltier effects will be discussed below.

2.3.1.3 Thomson Effect

In different materials, the Seebeck coefficient is not constant in temperature, so a spatial gradient in temperature can result in a gradient in the Seebeck coefficient. In any conductive material in which the electrical current flows in the presence of a temperature difference between two ends, heat is also released or absorbed. This is called the Thomson effect and was first observed by Lord Kelvin (William Thomson) in 1851. The term describes the heating or cooling of a current-carrying conductor with a temperature difference. If an electrical current is passed through a

homogeneous conductor, the Thomson effect predicts a heat production rate per unit volume [100]

$$\dot{q} = -\kappa \cdot J \cdot \nabla T \qquad \text{Eq. 2-3}$$

where ∇T is the temperature difference, J is the current density and κ is the Thomson coefficient. The sign convention of the Thomson coefficient is considered to be positive when the current flows from the low-temperature side to the high temperature side of the conductor and the heat is absorbed through it and negative when the current flows inversely and the heat is rejected from it.

However, the equation above neglects Joule heating and ordinary thermal conductivity. As aforementioned, Joule heating occurs when an electric current that flows through a conductor produces heat. According to the characteristics of Joule heating, Eq. 2-3 changes into

$$\dot{Q} = \rho \cdot J^2 - \kappa \cdot J \cdot \nabla T \qquad \text{Eq. 2-4}$$

where ρ is the electrical resistivity.

2.3.1.4 Full Thermoelectric Effects Equations

As stated above, more than one of the above effects is involved in the operation of a real TE device. The Seebeck effect, Peltier effect, and Thomson effect can be combined, together with the effects of Joule heating and ordinary heat conduction. The Seebeck effect generates an electromotive force, leading to the current equation:

$$J = \sigma \cdot (-\nabla V - S\nabla T) \qquad \text{Eq. 2-5}$$

The full thermoelectric equation for the energy accumulation is

$$\dot{Q} = J \cdot [\nabla \cdot (\rho + \Pi) \cdot J - \nabla \cdot (\kappa \nabla T)] + \dot{q_{ext}} \qquad \text{Eq. 2-6}$$

where $\dot{q_{ext}}$ is the heat added from an external source.

2.3.1.5 Onsager Reciprocal Relations

In 1854, Lord Kelvin found relationships between the three coefficients, implying that the Seebeck, Peltier, and Thomson effects are different manifestations of one effect. The Thomson relations are [100]

$$\Pi = T \cdot S \qquad \text{Eq. 2-7}$$

$$\kappa = \frac{d\Pi}{dT} - S \qquad \text{Eq. 2-8}$$

This relation expresses a subtle and fundamental connection between the Peltier and Seebeck effects. It is worth noting that this first equation is only guaranteed for a time-reversal symmetric material. If the material is placed in a magnetic field or is itself magnetically ordered (ferromagnetic, antiferromagnetic, etc.), then the first equation does not take the simple form.

2.3.2 **Thermoelectric Materials**

Based on the thermoelectric effects described above, TE materials transfer thermal energy into productive applications as efficiently as possible. The efficiency of conversion of heat is characterized by the dimensionless figure of merit ZT, which is related to the Seebeck coefficient *S*, thermal conductivity *k*, electrical conductivity σ and absolute temperature *T* by the following relation [101]:

$$ZT = \frac{\sigma S^2 T}{k} \qquad \text{Eq. 2-9}$$

Moreover, in the equation above, the product of the squared Seebeck coefficient and electrical conductivity is defined as the power factor, which determines the usefulness of the material in a TEG:

$$Power\ fator = \sigma S^2 \qquad \text{Eq. 2-10}$$

Figure 2-10 [102] shows the Seebeck coefficient *S*, electrical conductivity σ, power factor σS^2 and electronic (k_e) and lattice (k_l) thermal conductivity as a function of free-charge-carrier concentration *n*, which is distinguished by the class of materials.

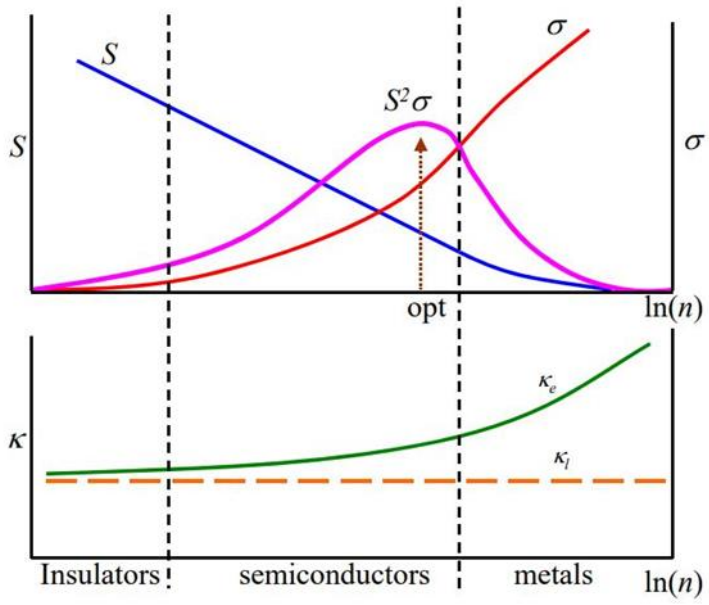


Figure 2-10 Relationship between Seebeck coefficient, electrical conductivity and thermal conductivity [102]

Materials with low thermal conductivity and high electrical conductivity are desirable in order to obtain high ZT or higher efficiency of the material. Presently, the conventional TE materials, which are used in large-scale commercial application, are Bi_2Te_3 and PbTe with ZT value around 1. These materials are not environment-friendly and have low stability at high temperature. Currently, intensive research is being carried out to search for eco-friendly and economical TE materials that are stable at high temperatures.

So far, there has been progress on synthesising new TE materials [103-106]. As a result, there are plenty of categories of TE materials, which are widely classified as intermetallic, skutterudite, clathrates, Half-Haussler alloy, oxides, rare earth chalcogenides, Zintl-phase materials, nanomaterials and superlattices materials. All these materials are degenerate semiconductors, with each having a complex band structure. Carbon nanomaterials, such as carbon nanotubes and graphene, and electronically conducting polymers, such as polyaniline and poly, have also been shown to be useful in TE devices [107-109]. Recently, flexible TE materials combined with the advanced techniques of 3D printing have been obtained, which can greatly broaden the application of the TE materials and improve overall efficiency of energy conversion [110, 111]. Figure 2-11 shows the ZT value of different types of TE materials [112].

2.3.2.1 Syntheses of Thermoelectric Materials

The methods of synthesising TE materials are various and depend on material properties such as melt and growth, mechanical alloying, single-crystal growth, polyol process, hydrothermal, microwave synthesis and other methods [113]. As the methods determine the thermoelectric properties of the materials, the selection of the preparation method is critical. Therefore, these methods can normally be divided into two different categories: powder and crystal growth based techniques. Powder based techniques show an excellent ability to control and maintain desired carrier distribution, particle size, and composition [114]. In powder techniques, either different powders are mixed with a varying ratio before being melted or they are distributed in different layers before pressing and melting. In crystal growth-based techniques, dopants are often mixed with melt, but diffusion from the gaseous

phase can also be used [115]. In addition, disks of different materials are stacked on top of others and then materials are mixed with each other when a traveling heater causes melting [116, 117].

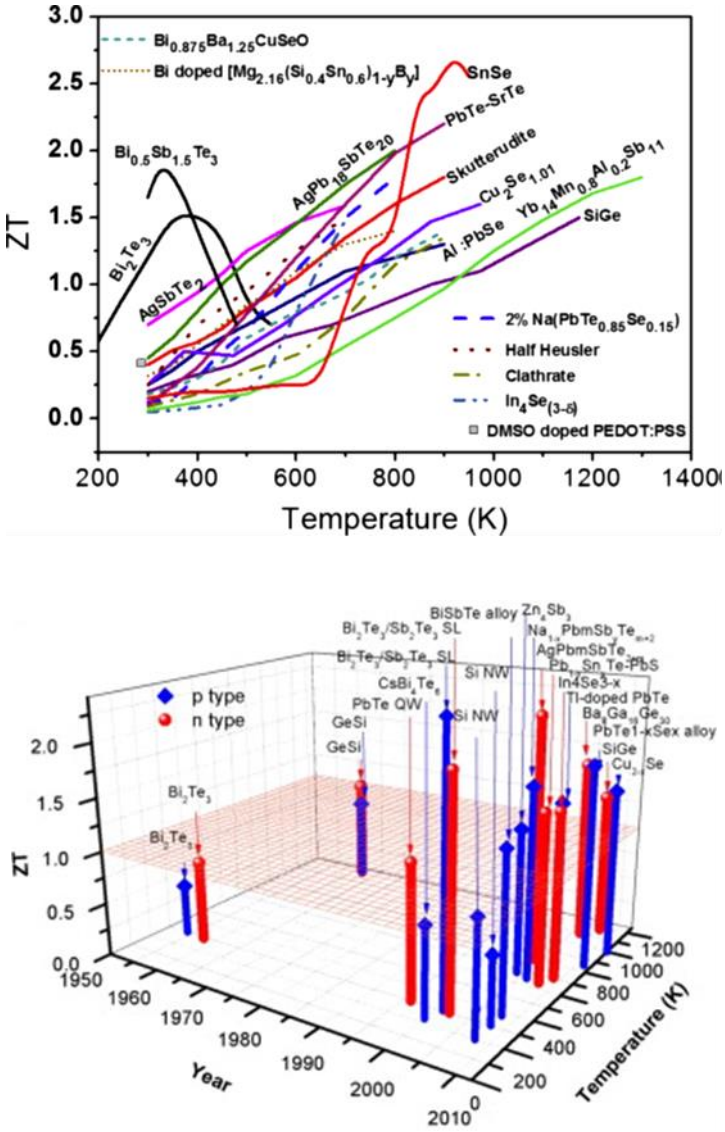


Figure 2-11 ZT value of different types of TE materials in recent research [112]

Significant improvement in 3D printing skills has made it possible for thermoelectric materials to be prepared from 3D printing inks, which are usually synthesised by dispersing inorganic powders in an organic solvent or making a suspension [118]. Because 3D printing is based on complex geometries that fit in

tightly constrained spaces, it is an ideal manufacturing technique. Furthermore, printable materials that demonstrate good mechanical flexibility could be utilised for wearable thermoelectrics, which convert body energy to electricity [119].

2.3.2.2 Strategies for Enhancing Figure of Merit

In the introduction, it was explained that a TE material with a high figure of merit provides a relatively high heat for electricity conversion and is desirable for practical application. Ideally, TE materials should possess charge carriers with optimised motilities, carrier concentration and effective mass. According to Eq. 2-10, materials with a low thermal conductivity as well as high power factor can achieve a high figure of merit. Strategies for enhancing the figure of merit are focusing on improving the power factor, reducing thermal conductivity or both [120-122].

The first strategy is doping. When doping is utilised, suitable doping elements can enhance the carrier concentration in a TE material by modifying the electronic band structure. Consequently, at an optimal carrier concentration, a higher Seebeck coefficient or ZT value could be obtained for semiconductors [123].

The second strategy is alloying. In a complex material system, alloying elements adjust the performance of TE materials in a different way to the doping method. Alloying increases the power factor while reducing the thermal conductivity. Ideally, such effects are employed in most Half-Haussler alloys as well as in skutterudite and clathrates [124].

The third strategy is nanostructure. Nanostructure is found to be effective in reducing the thermal conductivity by introducing nanoscale heterogeneities and

nanodispersions. When the grain size decreases, the density of states increases, which could eventually improve the Seebeck coefficient. Conversely, the thermal conductivity decreases with the scattering of the grain boundary [125].

The fourth strategy is the utilisation of nanocomposite. Nanocomposite strategies that control phonon and electron transport are known to be effective in enhancing the thermoelectric performance of bulk materials with high thermal conductivity, such as skutterudite and Si–Ge systems. Strategies involving nanocomposites are more effective due to the reduction in lattice thermal conductivity via phonon scattering from the grain boundaries and interfaces [126].

The fifth strategy is the utilisation of superlattices. Superlattices are periodic layers of two or more materials with each layer of nanoscale thickness. The thermal conductivity along the thin film could be reduced by creating diffuse interface scattering and by reducing the interface separation distance, which are both caused by interface roughness. The major drawbacks of using superlattices include the complexity synthesis procedure, high cost, and inability to support a large temperature difference through the TE material [127].

2.4 TEG for Automotive Waste Heat Recovery

2.4.1 Heat Exchanger for Automotive TEG system

In addition to research on TE materials, the optimisation of the heat exchanger for automotive TEG system is another vital direction for improving system efficiency. Because the thermal energy, which can be utilised by the TEM, depends on the energy absorbed by the heat exchanger from the exhaust gas. Therefore, a

high performance compact heat exchanger for an automotive TEG system should have the following characteristics:

- High heat transfer coefficient at average flow rate
- High heat transfer surface area or Dual surface configuration
- Meet pressure drop requirements at max flow
- Geometrically compatible with vehicle and scalable manufacturing design

Furthermore, the major challenges in design of heat exchanger for automotive TEG system are summarised as follows:

- Minimize heat loss between exhaust gas and TEG system

As discussed previously, the thermal energy in engine exhaust gas is low-grade energy, which is a production of fossil fuel combustion. Therefore, the total exergy of exhaust gas is much lower and it is more difficult to utilise this part of energy owing to energy devaluation. As a result, it makes the heat exchanger the most important component in automotive TEG system. A decent heat exchanger must obtain energy from the engine exhaust gas as much and as efficiently as possible. Moreover, the exchanger needs to be situated between the exhaust gas and TEG system, thus in a limited installation space.

- Efficient heat transfer

In order to minimize heat loss between exhaust gas and the TEG system, an efficient method for heat transfer is essential. The heat transfer enhancement is required not only from the exhaust gas flow to TEMs but also from the TEMs to the cooling system. There has been plenty of research on the heat transfer

enhancement for automotive TEG system in the past decade. For instance, Wang et al. [128] evaluated the performance of an inserted fins or dimpled-surface hot heat exchanger. Results showed that the pressure drop with dimpled surface was reduced by 20.57 %, and the power output was increased by 173.60 %. Su et al. [129] studied the thermal characteristics of heat exchangers, such as internal structure, material and surface area, in order to achieve uniform temperature distribution and higher interface temperature. Among all the structures, a plate-shaped heat exchanger made of brass with an accordion-shaped internal structure was shown to achieve a relatively ideal performance. Deng et al. [130] compared the performance between plate-shaped and hexagonal-prism-shaped heat exchangers. Results revealed that the plate-shaped heat exchanger was better than the hexagonal-prism-shaped heat exchanger because there was less heat loss with the smaller heat transfer area.

- Thermal contact resistance between interface

In addition to the enhancement of heat transfer between exhaust gas and TEG system, the thermal contact resistance between the interface of the components is another crucial challenge. The major thermal contact resistance within automotive TEG system occurs at the interface between the TEM and heat exchanger. Effective methods for reducing thermal contact resistance include utilising thermal grease and reducing surface roughness on the interface [131].

- Minimize the impact to engine efficiency

Another challenge is reducing the impact to engine efficiency. Any insertion in the exhaust system would generate backpressure increment in the vehicle engine, which would curtail engine performance and vehicle fuel economy. Moreover, the

cooling for TEG system requires additional power and larger radiator. Last but not least, the heat exchanger would increase the total vehicle weight. Therefore, a compact and effective design of heat exchanger is desirable in practical application.

- Reliability and durability

The reliability of the heat exchanger is a challenge, which is also worthy of attention. There should be no significant degradation over the lifecycle of the automotive TEG system (approximately 10 to 20 years). The potential in this regard include mechanical or chemical degradation of heat exchanger surfaces and sedimentation of foreign material that degrades heat transfer. These problems are related to the large vibration of the exhaust system during driving and remaining particles in exhaust gas and need to be taken into consideration at the beginning of design process. Love et al. [132] conducted a series of experimental investigations on the TEG system with clean and fouled heat exchangers of different materials. The power output and system efficiency of the fouled heat exchangers was observed to be 5–10 % lower than in clean heat exchangers.

2.4.2 **Prototypes of Automotive TEG system**

The first attempt at automotive TEG system was undertaken by the University of Karlsruhe in association with Porsche on the Porsche 944 model, using $FeSi_2$ as the TE material, in 1988 [133]. From then on, researchers and original equipment manufacturer (OEM) also began to investigate integrating TEG systems with vehicles. In the first fifteen years of the 21st century, prototypes of automotive TEG systems were developed by many car manufacturers, OEMs and research institutions. Nissan Motor, Hi-Z Technology, Cummins, Renault, Fiat, BMW, Ford

Motor, Gentherm, General Motors, Jaguar Land Rover, Eberspacher and Fraunhofer presented automotive TEG systems in various production vehicle platforms with gasoline or diesel engines. Moreover, Yonsei University, Wuhan University of Technology and Korea Institute of Machinery and Materials presented and tested some novel design of automotive TEG system for practical application.

All these TEG systems used exhaust gases as the heat source and engine coolant as the cooling method. Moreover, the output power of each TGE system ranged from tens of watts to over 1 kW, depending on the amount and type of TE material for each TEM. These automotive TEG prototypes employed uniquely designed heat exchangers, which often used heat transfer enhancement to improve system efficiency. Unfortunately, the power density of these prototypes is still low due to the relatively low heat to electricity conversion efficiency of TE materials. The model with the highest calculated power density is the prototype from Cummins, at 0.521 kW/m^3, using in a heavy-duty diesel engine. Table 2-3 shows the properties and comparison of each prototype of automotive TEG system.

Table 2-3 Prototypes of automotive TEG system

Year	Institution	Vehicle/Engine	Heat Exchanger	Number of TEMs	TE Material (ZT Value)	Power Rating	Power Density (kW/m^3)	Ref
1988	Porsche	Porsche 944	-	90	$FeSi_2$	58 W (average)	0.064	[133]
1998	Nissan	3000cc gasoline engine	Finned heat exchanger	72	SiGe	35.6 W (average)	0.123	[134]
2004	Hi-Z/Clarkson University	Sierra Pick-up Truck	Flat heat exchanger	16	Bi_2Te_3	300 W (peak)	0.18	[135]
2007	Cummins/JPL	Cummins ISX diesel engine	Flat heat exchanger	72	TAGS & PbTe	1068 W (peak)	0.521	[136]
2008	RENAULT	2 L passenger car/11 L Heavy duty truck	Crossflow heat exchanger	38	Mg_2Si (0.99) $MnSi_{1.77}$ (0.72)	500 W- 800 W (peak)	0.083	[137]
2009	FIAT/BOSCH	Light Duty Truck with 2.3L diesel engine	Finned-tube heat exchanger	16	Bi_2Te_3	200 W (average)	0.18	[138]
2011	Yonsei University	SUV with 2 L engine	Flat heat exchanger	72	Bi_2Te_3	75 W (peak)	-	[139]
2011	BSST / BMW / Ford	BMW X6 / Lincoln MKT	Cylindrical heat exchanger	-	Bi_2Te_3	720 W (peak)	0.096	[140]

2012	General Motors	Chevy Suburban	Flat heat exchanger	42	Bi_2Te_3 & Skutterudite (1.2)	350 - 600 W (average)	0.062	[141]
2013	Gentherm	Ford F350	Cartridge heat exchanger	252	Skutterudite (0.9-1.1)	1100 W (peak)	-	[142]
2014	Jaguar Land Rover	SUV with petrol engine	Crossflow heat exchanger	96	Bi_2Te_3 (0.95) &Mg_2Si (0.24)	379 -588 W (peak)	0.152	[143]
2014	GMZ / Eberspacher	Bradley Fighting Vehicle	Flat heat exchanger	400	Half-Haussler material (0.65)	1002.6 W (peak)	0.343	[144]
2014	DLR/Fraunhofer	Opel Ampera Hybrid	Crossflow heat exchanger	60	Skutterudite	400 W (peak)	0.13	[145]
2015	Wuhan University of Technology	Warrior	Flat heat exchanger	240	Bi_2Te_3	944 W (peak)	0.1	[146]
2016	Korea Institute of Machinery & Materials	4 L diesel engine	Flat heat exchanger	40	Bi_2Te_3	119 (peak)	0.153	[147]

2.5 Challenges of TEG Systems for Light-Duty Passenger Vehicles

2.5.1 Pressure Drop Control

Engine exhaust backpressure is defined as the exhaust gas pressure that is produced by the engine to overcome the hydraulic resistance of the exhaust system in order to discharge the gases into the atmosphere. The backpressure is a key feature that influences the engine performance as well as the fuel consumption of the vehicle. While backpressure considerations have always been the first factor considered by designers of exhaust systems, the increment of backpressure has been caused by the introduction of complex after treatment systems in general [148]. Increased exhaust pressure can have a number of effects on all engines, such as:

- Increased pumping work
- Reduced intake manifold boost pressure
- Cylinder scavenging and combustion effects
- Turbocharger problems

At increased backpressure levels, the engine has to compress the exhaust gases to a higher pressure, which involves additional mechanical work and affects intake manifold pressure. This can lead to an increase in fuel consumption, emissions and exhaust temperature. The increased exhaust temperature can result in overheating of exhaust valves and the turbine. By inserting a TEG system to the exhaust system, the engine backpressure would eventually increase, thus it would cause scavenging loss and reduction in power output from the piston.

A bypass [149]valve is an effective solution for this problem, which allow the exhaust gas to flow through another path with low flow resistance, during a certain period of engine operation. Merging TEG system with other components in exhaust system, such as catalyst or muffler, is another solution to decrease the negative effect on backpressure [150]. However, because of the complex structure of three-way catalytic converter and muffler, it is challenging to merge the TEG system with these two components. According to the research results [151, 152], by combining the catalyst with TEG system, the thermal energy of the exhaust gas during the cold-start process boost the average efficiency of catalyst. Moreover, in the WLTC driving cycle, the combined system can reduce the emissions of NOx, HC, and CO, respectively. Therefore, it is mutual benefit for the thermal efficiency and emission of the automotive engine.

On the other hand, the heat exchanger of TEG system is another direction for controlling the increased backpressure. Although the backpressure increment of TEG system would be considered during the engine design process, a large increment in back pressure, cannot be tolerated, because all engines have a maximum allowable engine backpressure. As a result, the structure of the TEG system must be carefully considered to regulate the pressure drop of the system. In order to minimize the backpressure when inserting the TEG system, it is critical to optimize the structural design of the system.

2.5.2 **Variable Driving Condition**

The main purpose of the automotive TEG system is to transfer the waste heat from exhaust into electricity and the power is related to the energy input from waste heat. Therefore, the power output of TEG system is thus strongly associated with

the mass flow rate and temperature of engine exhaust gas. Because these two parameters represent the amount of energy contained in the exhaust gas, it is important to evaluate these two parameters before system design [153]. Normally, the mass flow rate and temperature of exhaust gas are influenced by the driving condition of the vehicles. During the driving, as traffic and road condition will oscillate, the vehicle has to start-stop, accelerate and decelerate regularly. As a result, engine speed and torque will also fluctuate in the same pattern, consequently, the mass flow rate and temperature of engine exhaust gas will not be consistent. This fluctuation will have a negative effect on the power output of the TEG system. Even worse, during the most of the time, the temperature of the TEM will be lower than its optimum working temperature, thus the power output of the TEG system will be lower than the simulated expectation. The performance variation of TEGs becomes more significant with faster acceleration or deceleration and the transient response of the hot and cold side temperatures, voltage and power in deceleration is less significant than acceleration.

Despite the effect of traffic and road condition, the load of the vehicle is another key factor for the mass flow rate and temperature of engine exhaust gas as well. The mass flow rate and temperature of exhaust gas will increase with the increment of vehicle load, but the fuel consumption will increase at the same time. A higher vehicle load can increase the power output of TEG significantly, and lead to a faster transient response.

According to the analysis above, it is important that an energy storage system or temperature steady system could be employed in the TEG system for automotive

WHR. Thus, the details of utilising energy storage system is discussed in following section.

2.5.3 **Energy Storage**

Nowadays, the commonly used TE martial is Bi_2Te_3 or PbTe based TE material in industrial application, according to the introduction above. However, there is a problem that has been plaguing researchers for a long time, which is the efficiency of TE material is parabolic to the operating temperature, which means it is sensitive to the temperature on both sides of the TEM. Correspondingly, as aforementioned, the exhaust temperature fluctuates in a range from a few dozen degrees to several hundred degrees Celsius. Regrettably, the best operating temperature for TEM is around 200 ℃, so for most of the time, the TE material is not as efficient as it could be, which affects the efficiency of the whole system. It is a challenge to keep the temperature of both sides of the TEM in a relatively stable state. For this reason, a thermal energy storage system is often desirable, as it can improve the overall efficiency of the TEG system.

A thermal energy storage system could store the thermal energy from the exhaust gas when the exhaust temperature is too high to be utilised by TEG system, during vehicle acceleration or cruising at high speed. Moreover, the thermal energy storage system could release this stored energy when the exhaust temperature is too low to be utilised by TEG system, during vehicle deceleration or idling at low engine speed. With this method, the temperature difference through each TEM in the TEG system would be more stable and closer to the optimal operating temperature of TE materials. The thermal energy storage system not only could improve thermal

efficiency of TEG system, but also effectively reduce the thermal stress within the TEG system and extend lifespan.

Phase change material (PCM) is a great potential candidate for the creation of an energy storage system of automotive TEG system, especially solid-solid PCMs [154]. Because the assembly space for TEG system in a vehicle chassis is extremely restricted. The energy storage system for automotive TEG system should have the features of compact structure, high heat capacity and decent thermal conductivity. Additionally, PCMs basically satisfy these requirements. A PCM integrated TEG system could yield approximately 29% higher energy than a conventionally constructed TEG system [155]. As a result, a PCM energy storage system is imperative for the automotive TEG system.

2.5.4 System Matching and Integration

In order to integrate the TEG system to the whole vehicle exhaust system, there are mainly two factors that need to be taken into consideration.

The first factor is the assembly space. Because of the limited space in the vehicle chassis and the distribution of other components in the vehicle exhaust system, the mounting space for the TEG system is restricted. However, a larger heat transfer area will provide better heat transfer in the system and generate more electricity from waste heat. Therefore, it is very important that automotive TEG systems have high thermal efficiency heat exchangers, which could collect as much waste heat as it could in a narrow space within the exhaust system.

Electricity matching is another aspect that need to be concerned about. Because the electrical mismatch will have a negative effect on the efficiency of the whole

TEG system, and reduce the power output of the system. The power lost by mismatched conditions (such as temperature, mechanical load, manufacturing tolerances, aging) can be significant, and it is lower in the series connected array [156]. The series electrical connection enables more of the available power to be captured and minimise Joule heating losses in wiring and the electronics [157].

In addition, a conventional vehicle uses electrical power at 13.5 to 14.5 V depending on the operation temperature, but the voltage generated by automotive TEG system is fluctuating all the time and would not match the required voltage of vehicle accessories. In consequence, the DC-DC converter with maximum power point tracking (MPPT) device is essential for boosting the output voltage to an acceptable value that can be utilised by the vehicle accessories. MPPT is a technique used commonly with wind turbines and photovoltaic (PV) solar systems to maximise power extraction under all conditions. Currently, the application of MPPT algorithms to TEG is booming because the TEG system has similar characteristics to PV systems [158]. Generally, MPPT devices are typically integrated into an electric power converter system that provides voltage or current conversion, filtering and regulation for driving various loads, such as power grids, batteries, or motors[159]. According to the recent research, there are several MPPT methods that can be employed to improve performance of TEG systems and the average efficiency of MPPT is approximately 95 % [160, 161]. It is important to choose a suitable method according to the power rating and operating temperature of the TEG system.

2.5.5 **Efficiency, Cost & Life Cycle**

According to the introduction in Section 2.3 and Section 2.4, the total efficiency of TEG system basically depends on two factors: the ZT value of TE materials and heat transfer efficiency of heat exchanger. Although there is abundant research on improving figure of merit of TE material, the ZT value of most commercially used TE materials, nowadays, is still lower than 1. With this conversion efficiency, the TEG system only can transfer approximately 10 % to 15 % of exhaust thermal energy to electricity, which is far below expectations. Moreover, due to limitations of assembly space and pressure drop, the efficiency of heat exchanger in automotive system is always in a relatively low condition [162]. Therefore, some advanced heat transfer technologies would help to improve the heat transfer enhancement of heat exchanger. The final objective of utilising TEG system in automobile is to achieve a 3 % to 5 % improvement in fuel economy, thus the efficiency of the whole TEG system still needs to boost for accomplishing the goal.

As the vehicle market becomes increasingly competitive, all manufacturers are looking to improve fuel economy while having none or narrow increment in vehicle costs. Regrettably, the automotive TEG system remains relatively high cost because the price of commercial TE materials has not reduced. In addition to the TE materials, the cost of other accessories such as ceramic, copper and aluminium also need to be taken into consideration. Especially for ceramic, the cost of some special shaped ceramic plate would be extremely high, owing to the complex manufacture processing. The price evaluation of an automotive TEG system is based on the cost merit, which is explained in Section 2.2, and acceptable value should be less than 1

$ per W for the automotive TEG system. Therefore, before the TEG system is widely promoted, a lot of research still needs to be accomplished.

The life cycle of an automotive TEG system is another factor that needs attention. Because the TEG system is usually located in the vehicle exhaust system, the TEG system operates under a frequently vibrating condition. Consequently, during the design process of automotive TEG system, the vibration resistance of the entire system needs to be considered. Moreover, the particulate matters in the exhaust gas would generate a fouling layer on the surface of heat exchanger, which would block heat transfer between exhaust gas and the heat exchanger. Generally, the life cycle of an automotive TEG system should match to the lifespan of vehicle, which is from 10 years to 20 years.

2.6 Further Development of TEG Systems for Light-Duty Passenger Vehicles

2.6.1 Application on Different Vehicle Platform

As most EU countries have passed the laws that aim to prohibit fossil fuel vehicles over the next 20-35 years, automotive manufacturers are seeking a new driving system for their future. The global stock [163] of electric cars is envisioned to rise rapidly, from 1.3 million in 2015 to over 30 million by 2025 and more than 150 million by 2040, according to the estimation. Hybrid vehicle, which is the bridge of the conventional internal combustion engine vehicle and fully electrical vehicle, must be seen as a great development in the following decades. Automotive TEG system is a competitive method of WHR for the hybrid vehicles as well.

Compared to conventional vehicle, the electrical energy generated by TEG system can be utilised not only for electrical accessories as well as directly for propulsion in hybrid vehicle. However, because hybrid vehicles use much higher voltages for propulsion, while only 12 V is needed for vehicle accessories, a more complicated voltage conversion system is required in hybrid vehicle [164, 165]. Smith [166] inspected the feasibility of TEG system for WHR in hybrid vehicles. Results exhibited that vehicle fuel savings were approximately 3 % and 5.5 % using TEG systems, which recaptured 5 % and 10 % of the engine's waste heat, respectively. Vijayagopal et al. [167] investigated the potential benefits of TEGs on hybrid vehicles numerically and results showed that the fuel economy is improved from 0.8 % to 1.5 %, depending on the vehicle technology and number of TEMs. Mori et al. [168] explored the effectiveness of TEG system on fuel economy in a series hybrid vehicle and a maximum 3 % fuel economy enhancement could be expected. Hussain et al. [169] established a 1-D model of TEG system for hybrid vehicle, in order to evaluate the transient response under actual driving cycles. The model predicted that the TEG system achieves potential power from 300 W to 400 W under highway driving cycle.

2.6.2 **3D Printing Technology in Automotive TEG System**

As a decent progress in the development of 3D printing technology over the past decade, some researchers have promoted the utilisation of this technique in TEG systems. 3D printing is the process of building a three-dimensional object from a computer-aided design model, usually by successively adding material layer by layer and is unlike conventional machining, casting and forging processes. The

most-commonly used 3D-printing process (46% as of 2018) is a material extrusion technique called fused deposition modelling [170].

TE devices are conventionally made using traditional manufacturing techniques beginning with TE material synthesis via ball milling or melting/heating powders of constituent elements. In general, there are four printing techniques: inkjet printing, direct write, screen printing, and stereolithography, which are currently used in printing 3D TE devices [171]. Compared to the conventional method, the 3D printing technique has the advantages of simple patterning, material compatibility, and reduced energy input and material waste [172]. The most important feature of 3D printing technique in TE devices is the flexibility in the structure of TE materials as well as TE devices. Figure 2-12 [173] shows the schematic and photo for a printed cylindrical TEM, which is supposed to be utilised in WHR. As shown in the figure, the cylindrical TEM could perfectly attach to the outer surface of the exhaust pipe. This could solve the existing challenges of limited assembly space, low heat transfer efficiency and low power density of automotive TEG systems. Therefore, 3D printing technique has great potential in the automotive TEG system market.

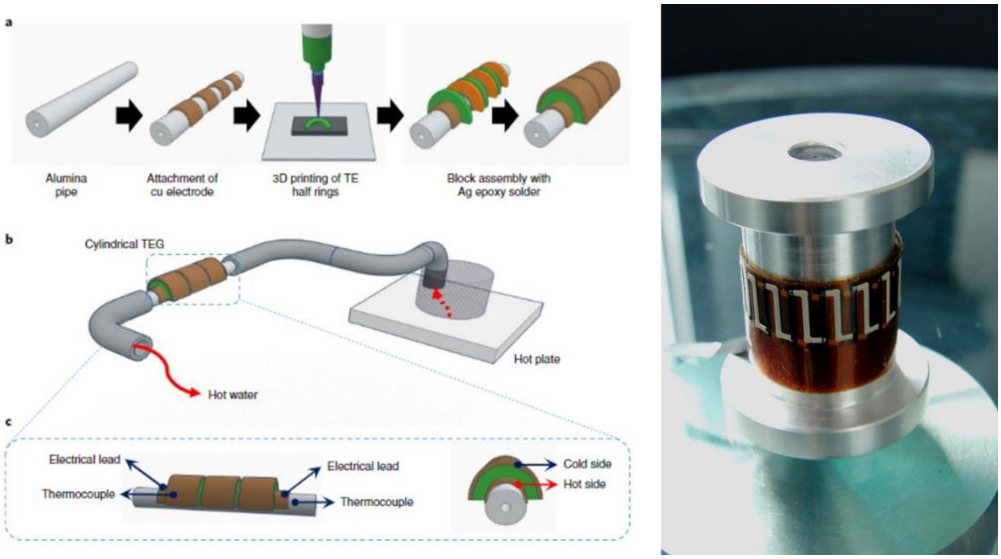


Figure 2-12 Schematic diagram and photo for a printed cylindrical TEM

2.7 Summary

In this chapter, a comprehensive overview of WHR technologies, especially TEG for automobiles has been reviewed. A brief introduction of energy usage in the transportation sector is provided first. Thereafter, an overview of four different technologies for automotive WHR, followed by a detailed information of thermoelectric effects and TE material, is provided as well. The challenges and future development of automotive TEG system is summarised at the end of this review. The notable conclusions of this literature review are as follows:

- The transportation sector is the second highest energy consumption sector in 2017 and light-duty vehicles consume more than half of the energy in transportation sector.
- WHR for automobile is essential for adhering to the emission and fuel economy regulations for vehicles as well as the Paris Agreement regulations to combat climate changes.

- The automotive TEG system is the most suitable method for light-duty passenger vehicles under long-term driving, compared to the other three WHR methods.
- Figure of merit of TE material is the major challenge for preventing TEG system from widespread application. Even though the research of TE materials has seen considerable progress, the ZT value of commercially available TE materials is still around 1.
- Heat exchangers for automotive TEG system yet need to be improved to satisfy the higher requirements of fuel economy enhancement.
- 3D printing technique is a potential method for improving efficiency of automotive TEG system in both material level and system level.

In response to these findings, this project presents a novel design of automotive TEG system and the research will be expanded as: investigation into conductive heat transfer within the TEG system, the convective heat transfer within TEG system, fuel economy improvements and performance enhancement are presented in the proceeding chapters.

Chapter 3. Model Description and Research Methodology

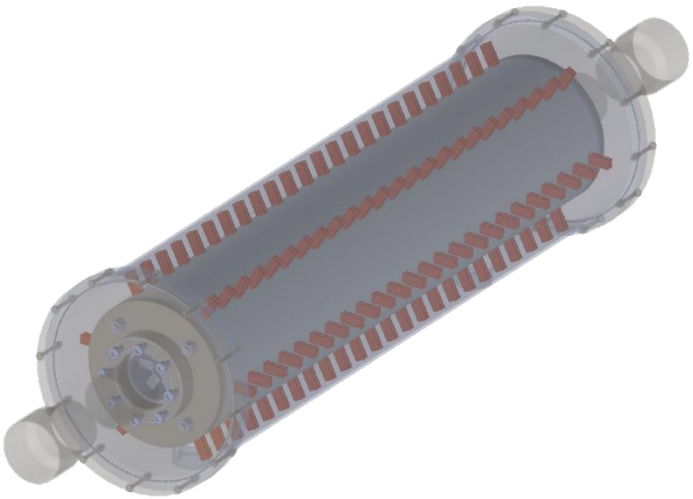
3.1 Model Description of Concentric Cylindrical TEG System

By analysing the existing TEG system reviewed in Chapter Two, it is evident that most of these TEG systems are not efficient regarding space utilisation. Most of these systems have a bulky and flat heat exchanger, in order to enhance the heat transfer within the system and absorb more waste heat from engine exhaust gas. However, the space in the exhaust system under vehicle chassis limits the design of heat exchangers for TEG systems. Moreover, the heavy weight of TEG systems prevents the TEG system from broad commercial applications. Taking account of the drawbacks of TEG system, this project presents a novel structure design of concentric cylindrical TEG system. In order to absorb more waste heat from exhaust gas, a super thermal conductive device, the heat pipe, is employed in the hot and cold sides of concentric cylindrical TEG system to enhance the heat transfer. A heat pipe is a heat-transfer device that combines the principles of both thermal conductivity and phase transition to effectively improve heat transfer. At the hot interface of a heat pipe a liquid in contact with a thermally conductive solid surface turns into a vapour by absorbing heat from that surface. The vapour then travels along the heat pipe to the cold interface and condenses back into a liquid – releasing the latent heat. The liquid then returns to the hot interface through either capillary action, centrifugal force, or gravity and the cycle repeats. Due to the very high heat transfer coefficients for boiling and condensation, heat pipes are highly effective thermal conductors. The effective thermal conductivity can approach 100 kW/m•K for long heat pipes, in comparison with approximately 0.4 kW/m•K for copper.

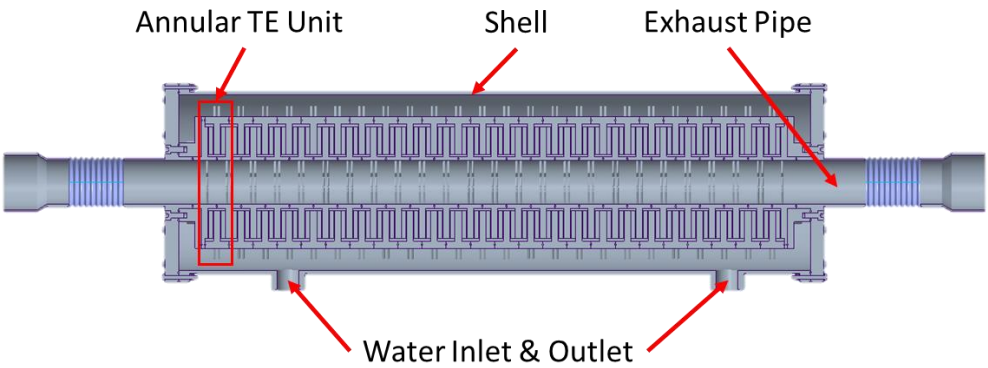
As shown in Figure 3-1, the concentric cylindrical TEG system consists of a series of annular TE units that are segregated to adapt for the practical exhaust pipe. The annular TE unit is made up of four annular TEMs, three heating plates and two cooling plates including twelve heat pipes in each plate as highlighted in blue and red in Figure 3-2 a and Figure 3-2 b. The exhaust stream interacts with heat pipes and transfers the heat into the TEG system in the radial direction of the exhaust stream. The channel spaces of both the exhaust and the coolant are constrained by the heat pipes, the surface of the cooling plates and the shell of the heat exchanger. This configuration can be easily adapted according to the demands of power outputs by exchanging the channels of exhaust and coolant flows and adjusting the number of annular TE units. In reality, each unit has all different flow parameters regarding coolant temperature and exhaust temperature. These differences result in decreasing the temperature of the exhaust and increasing the temperature of the coolant. Therefore, the specific configuration of flow patterns will have a great effect on TE power generation.

Compared with some commonly used TEMs, an annular TEM is applied instead of square-shaped TEM, and the method of self-clamping by adjacent TEMs is introduced to further reduce the need for the single clamp on each TEMs. In this model, the primary assumption of constant temperature in the exhaust and coolant flow is made for simulation purposes. Moreover, a parallel link inside each annular TE unit is set so that the total internal electrical resistance is equal to a quarter of an individual TEM's resistance. Parameter analysis of matched load resistance is conducted to track the maximum power point when the external load fluctuates. Assuming the same power output of each unit, the total power generation of the

whole system is calculated by multiplying the number of units used in the exhaust pipe.



(a) Assembly diagram of the concentric cylindrical TEG system



(b) Longitudinal section of the concentric cylindrical TEG system

Figure 3-1 Schematic diagrams of the concentric cylindrical TEG system

Specifically, in Figure 3-2 (a), the coolant flow can be allocated to an inner axial flow by moving the exhaust flow to outer axial flow channel in respect of utilising the merit of the higher heat capacity of the water coolant. In addition, extruded fin stacks can be installed on heat pipes to enhance heat transfer in the exhaust streams.

Unlike the conventional square-shaped TEMs, the concentric cylindrical TEG system can be easily accommodated with round exhaust pipe. Given that the alteration of clamping method in this newly design, the uneven thermomechanical stress on the components is expected to be minimised by replacing the individual clamps into four simple self-locking metal cables through the internal holes of TEG modules.

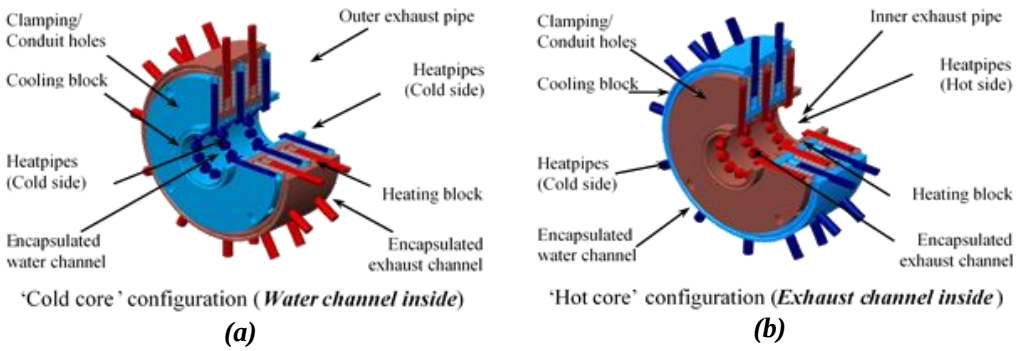


Figure 3-2 Schematic diagram of the single unit in concentric cylindrical TEG system

3.2 Heat Transfer Model of Concentric Cylindrical TEG System and Heat Exchanger

As shown in the description of the model in Section 3.1, heat transfer within the concentric cylindrical TEG system can be separated into two parts, shown in Figure 3-3. The first part is the conductive heat transfer within TEMs and heating or cooling plates. The second part is the convective heat transfer between the exhaust pipe and heat pipes of concentric cylindrical TEG system. The following part will discuss these two different heat transfer methods in detail.

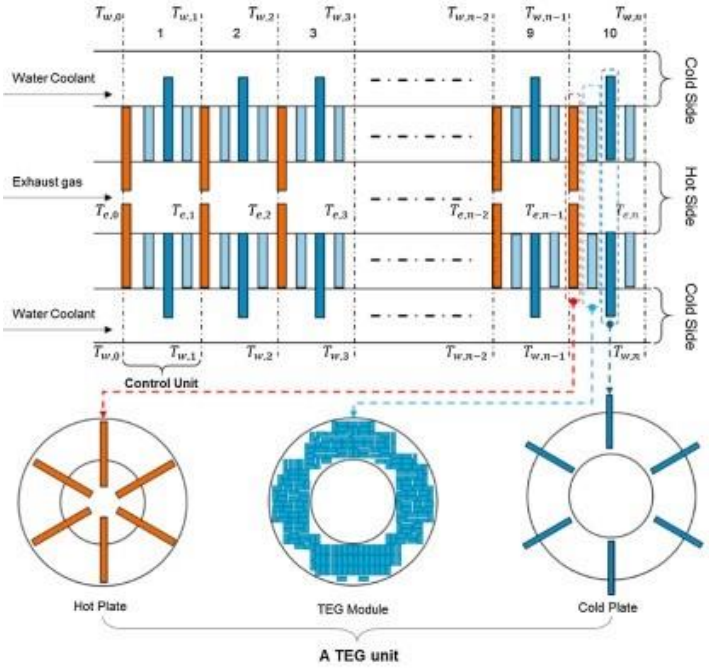


Figure 3-3 Heat transfer within the concentric cylindrical TEG system

3.2.1 **Conductive Heat Transfer in TEM and Heating or Cooling Plate**

The conductive heat transfer in the concentric cylindrical TEG system is basically within the TEM and heating and cooling plate, which is the single annular TE unit of this TEG system. Typically, commercial TE modules consist of several positive-type (P-type) and negative-type (N-type) semiconductor legs that are connected by copper conducting strips in serials to increase the total voltage, combined with the cold and hot ceramic plates. The conductive heat transfer within the annular TE unit of concentric cylindrical TEG system is shown in Figure 3-4. Normally, the space between the hot and cold ceramic plates is filled by air. As shown in the figure, the heat transfer, in the TE module, from the hot side to the cold side should obey the following equation:

$$Q_{con} = Q_{leg} + Q_{air} \qquad \text{Eq.3-1}$$

where Q_{leg} and Q_{air} are the heat flux through the thermoelectric legs and air, respectively, and Q_{leg} is given by:

$$Q_{leg} = n\left(k_P \frac{L_P^2}{H_P} + k_N \frac{L_N^2}{H_N}\right)(T_{hj} - T_{cj}) \qquad \text{Eq.3-2}$$

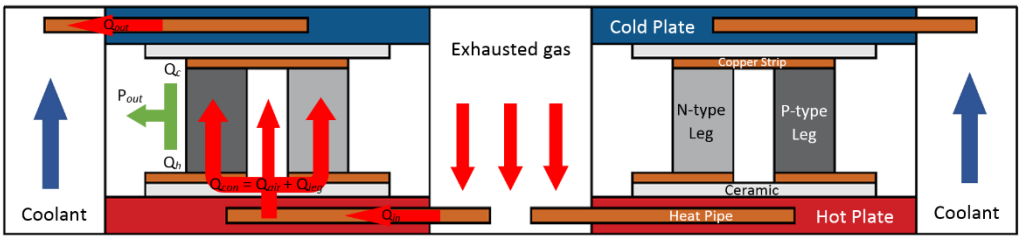


Figure 3-4 Conductive heat transfer within the concentric cylindrical TEG system

Despite the heat flux through the thermoelectric legs, the heat flux through the air among the thermoelectric legs is non-negligible and possible mechanisms of heat transfer through the air are natural convection, conduction and radiation. However, as the corresponding Grashof number and Rayleigh numbers are much smaller than threshold criteria of natural convection heat transfer in an enclosed space, the natural convection is negligible, and heat transfer through the air Q_{air} can be expressed as $Q_{cd} + Q_{rd}$.

$$Q_{cd} = k_{air}\left(\frac{0.5S_{TEM} - nL_P^2}{H_P} + \frac{0.5S_{TEM} - nL_N^2}{H_N}\right)(T_{hj} - T_{cj}) \qquad \text{Eq.3-3}$$

$$Q_{rd} = S_{air} S_b \left(T_{hj}^4 - T_{cj}^4\right)/(2/\varepsilon - 1) \qquad \text{Eq.3-4}$$

where k_{air}, S_{TEM}, L_P, L_N, H_P, H_N T_hj, T_{cj} are the thermal conductivity of air, cross section of TEM, the length of the thermoelectric legs, the height of thermoelectric legs and the temperature at hot and cold junction, respectively, and S_b is 5.67 x 10^{-8} $W \cdot m^{-2} \cdot K^{-4}$.

As the heat pipe is involved in the concentric cylindrical TE system, the temperature at the hot and cold junction can be calculated by using the following equations:

$$T_{hj} - T_{HP} = {}^{Q_{in}}/_{A \cdot k_{HP}} \quad \text{Eq.3-5}$$

$$T_{cj} - T'_{HP} = {}^{Q_{out}}/_{A \cdot k_{HP}} \quad \text{Eq.3-6}$$

where T_{HP}, T'_{HP}, and k_{HP} is the temperature of heat pipe on the hot side, temperature of the heat pipe on the clod side and the equivalent heat transfer coefficient of heat pipe, respectively. The detailed calculation process for the temperature of heat pipe is presented in Section 3.2.2.

As discussed in Chapter Two, a TEM consists of three effects: Seebeck effect, Peltier effect and Thomson effect, and the thermoelectric generator involve all the three basic effects. Besides, there are two accessorial effects, Joule effect and Fourier effect. Seebeck effect is the conversion of temperature different into an electric current. Peltier effect, Thomson effect and Joule effect lead to Peltier heat, Thomson heat and Joule heat, respectively. Therefore, the TEG inner heat generation includes Peltier heat, Thomson heat and Joule heat. As such the heat input to the heating plate can be expressed as:

$$Q_h(I, T_{hj}, T_{cj}) = Q_{Peltier_h} + Q_{cd} - 0.5Q_{Joule} \quad \text{Eq.3-7}$$

$Q_{Peltier_h}$ and Q_{Joule} can be expressed as:

$$Q_{Peltier_h} = nI(\alpha_P - \alpha_N)T_{hj} \quad \text{Eq.3-8}$$

$$Q_{Joule} = I^2 n\left(\frac{H_P}{\sigma_P L_P^2} + \frac{H_N}{\sigma_N L_N^2}\right) \quad \text{Eq.3-9}$$

Substituting the equation above, the heat input to the heating plate then can be expressed as:

$$Q_h(I,T_{hj},T_{cj}) = \mathrm{nI}(\alpha_\mathrm{P}-\alpha_\mathrm{N})\mathrm{T_{hj}} + \left[n\left(k_P\frac{L_P^2}{H_P}+k_N\frac{L_N^2}{H_N}\right)+k_{\mathrm{air}}\left(\frac{0.5\mathrm{S_{TEM}}-\mathrm{nL_P^2}}{\mathrm{H_P}}+\frac{0.5\mathrm{S_{TEM}}-\mathrm{nL_N^2}}{\mathrm{H_N}}\right)\right]\times\left(\mathrm{T_{hj}}-\mathrm{T_{cj}}\right)+\mathrm{S_{air}S_b}\left(\mathrm{T_{hj}^4}-\mathrm{T_{cj}^4}\right)/(2/\varepsilon-1)-0.5\,\mathrm{I^2n}\left(\frac{\mathrm{H_P}}{\sigma_\mathrm{P}\mathrm{L_P^2}}+\frac{\mathrm{H_N}}{\sigma_\mathrm{N}\mathrm{L_N^2}}\right) \quad \text{Eq.3-10}$$

Without loss of generality, we can set L_N=L_P=L and H_N=H_P=H. The equation can be simplified to the form:

$$Q_h(I,T_{hj},T_{cj}) = \mathrm{nI}(\alpha_\mathrm{P}-\alpha_\mathrm{N})\mathrm{T_{hj}} + \left[n\frac{L^2}{H}(k_P+k_N)+k_{air}\left(\frac{S_{TEM}-2nL^2}{H}\right)\right]\times\left(\mathrm{T_{hj}}-\mathrm{T_{cj}}\right)+\mathrm{S_{air}S_b}\left(\mathrm{T_{hj}^4}-\mathrm{T_{cj}^4}\right)/(2/\varepsilon-1)-\frac{0.5I^2nH}{L^2}\left(\frac{1}{\sigma_\mathrm{P}}+\frac{1}{\sigma_\mathrm{N}}\right) \quad \text{Eq.3-11}$$

Based on the same principle, heat output from cold side of the TE modules can be expressed as:

$$Q_c(I,T_{hj},T_{cj}) = \mathrm{nI}(\alpha_\mathrm{P}-\alpha_\mathrm{N})\mathrm{T_{cj}} + \left[n\frac{L^2}{H}(k_P+k_N)+k_{air}\left(\frac{S_{TEM}-2nL^2}{H}\right)\right]\times\left(\mathrm{T_{hj}}-\mathrm{T_{cj}}\right)+\mathrm{S_{air}S_b}\left(\mathrm{T_{hj}^4}-\mathrm{T_{cj}^4}\right)/(2/\varepsilon-1)+\frac{0.5I^2nH}{L^2}\left(\frac{1}{\sigma_\mathrm{P}}+\frac{1}{\sigma_\mathrm{N}}\right) \quad \text{Eq.3-12}$$

The power output of the whole TE module corresponding to ΔT_{leg} is calculated as:

$$P_{TEG}(I,T_{hj},T_{cj}) = Q_h - Q_c = nI(\alpha_P-\alpha_N)(T_{hj}-T_{cj}) - \frac{I^2nH}{L^2}\left(\frac{1}{\alpha_P}+\frac{1}{\alpha_N}\right) = nI(\alpha_P-\alpha_N)\Delta T_{leg} - \frac{I^2nH}{L^2}\left(\frac{1}{\alpha_P}+\frac{1}{\alpha_N}\right) \quad \text{Eq.3-13}$$

3.2.2 **Convective Heat Transfer between Exhaust Pipe and Heat Pipes**

According to the model description in Section 3.1, the cross section of the concentric cylindrical TEG system is shown in Figure 3-5. Because the major objective of the heat exchangers for TEG systems is to absorb more waste heat from exhaust gas, the important issue to solve is to enhance the heat transfer in the hot sides of TEG systems. As mentioned, the concentric cylindrical TEG system integrates heat pipes in order to reduce the conductive thermal resistance in the system. Apart from this, the convective thermal resistance between heat pipe and exhaust gas is pivotal in enhancing the heat transfer of the concentric cylindrical TEG system. In this section, the heat transfer model for convective heat transfer between heat pipe and exhaust gas will be established.

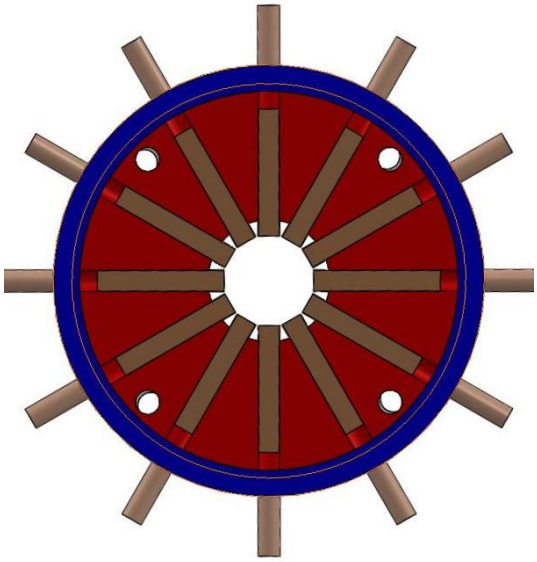


Figure 3-5 Cross section of the concentric cylindrical TEG system

As shown in Figure 3-5, the convective heat transfer problem of the concentric cylindrical TEG can be treated as convective heat transfer problem in an internally

finned tube. Internally finned tubes are effective components for enhancing convective heat transfer. Normally, the dimensional parameters of fins, such as the height of fins or the number of fins, and the thermal boundary condition are two crucial factors regarding temperature distribution in internally finned tubes. In order to reduce the time of calculation, there are several assumptions in this heat transfer model:

- The physical properties of the exhaust gas are constant
- Axial heat conduction in the exhaust gas is negligible
- The viscous dissipation in exhaust gas is not calculated
- The heat flux density on the surface of heat pipes is uniform

For calculating the temperature and velocity field in exhaust pipe, the energy equation and momentum equation, neglecting axial conduction and heat generation due to viscous dissipation, is calculated by [174]

$$\rho\omega C_p \frac{\partial T}{\partial z'} = k\left(\frac{\partial^2 T}{\partial x'^2} + \frac{\partial^2 T}{\partial y'^2}\right) \quad \text{Eq.3-14}$$

$$\frac{dp}{dz} = \eta\left(\frac{\partial^2 \omega}{\partial x'^2} + \frac{\partial^2 \omega}{\partial y'^2}\right) \quad \text{Eq.3-15}$$

where T and ω are the local exhaust gas temperature and velocity, respectively.

The detailed equation of convective heat transfer in the concentric cylindrical TEG system is discussed in Chapter Five.

With the analysis above, in this project, the heat transfer at hot side of the concentric cylindrical TEG system is forced convection in turbulent flows through the enclosed exhaust gas pipe. Therefore, in order to calculate the convective heat

transfer coefficient according to the Dittus-Boelter empirical correlations in Eq. 3-16, the heat pipe temperature on the hot side can be obtained by [175]:

$$Nu = 0.023 \cdot Re^{0.8} \cdot Pr^{0.3} \quad \text{Eq.3-16}$$

where *Nu* , *Re* and *Pr* are the Nusselt number, Reynolds number and Prandtl number, respectively.

$$Nu = \frac{hL_c}{k} \quad \text{Eq.3-17}$$

$$Re = \frac{\rho \omega L_c}{\mu} \quad \text{Eq.3-18}$$

$$Pr = \frac{C_p \mu}{k} \quad \text{Eq.3-19}$$

According to the Dittus-Boelter empirical equation, the convective heat transfer coefficient between exhaust gas and heat pipes can be achieved. Then, according to Newton's law of cooling, the heat pipe temperature T_{HP} on the hot side of the concentric cylindrical TEG system is calculated as:

$$h \cdot A \cdot \Delta T_m = q_m \cdot C_p \cdot (T_{EX_{out}} - T_{EX_{in}}) \quad \text{Eq.3-20}$$

$$\Delta T_m = \frac{T_{EX_{out}} - T_{EX_{in}}}{ln\frac{T_{HP} - T_{EX_{in}}}{T_{HP} - T_{EX_{out}}}} \quad \text{Eq.3-21}$$

where *h* is the heat transfer coefficient calculated by Eq. 3-20, $T_{EX_{in}}$ and $T_{EX_{out}}$ are the average gas temperature at the inlet and outlet of the TEG system, respectively.

This is the heat transfer model for convective heat transfer in concentric cylindrical TEG system and the heat pipe temperature T_{HP} is applied in the conductive heat transfer model to calculate the temperature distribution in annular TEM in Section 3.2.1.

3.3 Conjugate Heat Transfer and Lumped Parameter Analysis in Conjugate Heat Transfer

3.3.1 Conjugate Heat Transfer Process

As known to all, the thermal differential equation is a mathematical expression describing the commonality of the heat transfer process and the solution for the heat transfer problem can be attributed to the solution of the thermal differential equation. In order to solve the thermal differential equation for the steady-state temperature distribution, there must be given some boundary condition, which is called a definite condition. The common boundary conditions for thermal differential equation can be summarised into the following three categories [176-178]:

(1) Dirichlet boundary condition

In thermodynamics, the Dirichlet boundary condition is defined as a surface temperature is held at a fixed value, for example the boundary temperature remains constant, $t_w = C$. The relational expression of Dirichlet boundary condition can be expressed as:

$$when\ \tau > 0,\ t_w = f_1(\tau) \qquad \text{Eq.3-22}$$

(2) Neumann boundary condition

In thermodynamics, a prescribed heat flux from a surface would serve as the Neumann boundary condition. For example, a perfect insulator would have no flux while an electrical component may be dissipating at a known power, $q_w = C$. The relational expression of Neumann boundary condition can be express as:

$$when\ \tau > 0, -\lambda\left(\frac{\partial t}{\partial n}\right)_w = f_2(\tau) \qquad \text{Eq.3-23}$$

where n is the normal direction of the surface.

(3) Robin boundary condition

In thermodynamics, a defaulted heat transfer coefficient h and the temperature of surrounding fluid t_f are defined as the Robin boundary conditions. The relational expression of Robin boundary condition can be express as:

$$-\lambda\left(\frac{\partial t}{\partial n}\right)_w = h(t_w - t_f) \qquad \text{Eq.3-24}$$

The heat transfer coefficient h here, is the heat transfer coefficient between surrounding fluid and boundary, but not the heat transfer coefficient within the solution area.

However, the heat transfer problem in this research does not match the three boundary conditions mentioned above. As shown in Section 3.2, there are two main reasons for this. First, the boundary condition of the concentric cylindrical TEG system is unpredictable, because the heat transfer within the exhaust pipe and heat exchanger is constrained by the interaction between exhaust gas and exhaust pipe wall. Second, the heat transfer within the concentric cylindrical TEG system is time dependent, owing to the fluctuating properties of exhaust gas. The whole heat transfer process is non-steady, which is a transient heat transfer problem. As a result, either the temperature at the interface or the heat flux is regarded as a part of the thermal differential equation solution, not a given boundary condition. In other words, this kind of heat transfer problem whose boundary conditions are dynamically determined by the heat transfer process and cannot be pre-specified is called conjugate heat transfer.

The conjugate heat transfer model was developed after computers came into wide use in numerical heat transfer [179]. This model substitutes the empirical relation of proportionality of heat flux to temperature difference with heat transfer coefficient and describes the heat transfer between a solid body and a fluid flowing over or inside the body, because of the interaction of two objects. The physical processes and solutions of the governing equations are considered separately for each object in two subdomains [180, 181]. Matching conditions for these solutions at the interface provide the distributions of temperature and heat flux along the body–flow interface, eliminating the need for a heat transfer coefficient.

3.3.2 **Methods of Numerical Solution for Conjugate Heat Transfer**

Most of the actual conjugate heat transfer problems cannot be addressed using analytical solutions, but rather by using numerical analysis. Generally, there are two available methods: boundary coupling and whole field solution [177]:

(1) Boundary coupling

One simple way to realise conjugate heat transfer is to apply the iterations. The idea of this approach is that each solution for the solid body or the fluid produces a boundary condition for other subdomains of the system. The process of this method is shown below:

1. Establish governing equations according to physical processes in each subdomains
2. Give boundary conditions for each subdomains
3. Assume the temperature distribution exists on the interfaces of subdomains

4. Solve the governing equation for one subdomain with the hypothetical boundary condition and uses the result as a boundary condition for solving the governing equation for another subdomain
5. If this process converges, the desired accuracy may be achieved

However, the rate of convergence highly depends on the first hypothetical boundary condition and there is no way to find a proper one, except through trial and error.

(2) Whole field solution

Another numerical conjugate heat transfer procedure is based on whole field solution. The heat transfer processes in each subdomains are combined as a simultaneous heat transfer process. Each subdomain applies a general governing equation and the differences in general governing equation for each subdomain are a generalised diffusion coefficient and generalized source term. The coupled boundaries become the interface within the solution area. When using finite volume method to solve this general governing equation, the continuity on the interface can be satisfied. This eliminates the iterative process between each subdomains, therefore, it shortens the calculation time significantly.

3.3.3 **Lumped Parameter Analysis**

As mentioned in Section 3.2 and Section 3.3.1, the temperature in the WHR system fluctuates all the time, thus the heat transfer in the heat exchanger of the concentric cylindrical TEG system is transient conjugate heat transfer process in most of the time. In order to solve this problem in a timesaving way, lumped parameter method is employed in this research.

In a conjugate heat transfer process, the temperature varies with time, as well as the location within the solid object . However, some solid objects are observed to behave as a "lump" whose interior temperature remains essentially uniform, which means the temperature distribution within the solid object is solely varying with time and irrelevant with the location within the solid object during heat transfer process [182, 183]. In other words, the temperature of this solid object can be expressed as a function of time alone, as shown in Eq. 3-25.

$$T(\vec{r}, t) \approx T(t) \qquad \text{Eq.3-25}$$

This heat transfer analysis method that utilises this idealization is called the lumped parameter method. The lumped method is the most simple and efficient way used to determine temperature distribution within the system in conjugate heat transfer process. Because the temperature distribution in the solid object is close to being uniform, there is no need to consider spatial thermal conduction inside, which means the heat transfer from/to the solid body via both convection and radiation is equal to heat loss/gain of the solid body. Therefore, according to first law of thermodynamics, the energy balance expression of a solid body could be written as:

$$\dot{E}_{st} = -\dot{E}_{out} \qquad \text{Eq.3-26}$$

As convective and conductive heat transfer are considered in this research, Eq. 3-26 then becomes:

$$\rho c V \frac{dT}{d\tau} = -hA(T - T_{\infty}) \qquad \text{Eq.3-27}$$

where A and V are effective heat transfer area and volume of solid object, T is temperature of solid object, h is surface convective heat transfer coefficient, T_{∞} is

ambient environment temperature, ρ and c are density and heat capacity of solid object and τ is time variable.

By substituting excess temperature θ as $\theta = T - T_\infty$, this ordinary time differential equation could be written as:

$$\rho cV \frac{d\theta}{d\tau} = -hA\theta \qquad \text{Eq.3-28}$$

The initial condition expressed as excess temperature is:

$$\theta(0) = T_0 - T_\infty \qquad \text{Eq.3-29}$$

By integrating the Eq. 3-28 from *t=0* at which *T= T_0* to any time *t* , at *T= T_i* and rearranging it, gives:

$$\frac{\theta_i}{\theta_0} = \ln\frac{T_i - T_\infty}{T_0 - T_\infty} = -\frac{hA}{\rho cV}\tau \qquad \text{Eq.3-30}$$

Once the temperature T_i at time *t* is available, the rate of convection heat transfer between the solid object and the ambient at that time can be determined from Newton's law of cooling as:

$$\dot{Q}_i = hA(T_i - T_\infty) \qquad \text{Eq.3-31}$$

The total amount of heat transfer between the solid body and the ambient is the change in the energy content of the body. Therefore, the amount of heat transfer reaches its upper limit when the solid object reaches the ambient temperature and the maximum heat transfer between the solid object and the ambient is:

$$Q_{max} = mc_p(T_\infty - T_i) \qquad \text{Eq.3-32}$$

where c_p is the heat capacity of solid object.

3.3.4 **Criteria for Lumped Parameter Analysis**

According to the assumption of lumped parameter analysis, the thermal conductivity of solid object should be infinitely large which is impossible to achieve. However, the condition is closely approximated if the thermal resistance of conduction within the solid object is small enough compared with the thermal resistance of convection heat transfer, then the hypothesis is still valid. Therefore, small solid objects with high thermal conductivities and low convection coefficients are most likely to satisfy the criterion for lumped parameter analysis.

The first step in establishing a criterion for the applicability of the lumped parameter analysis is dimensionless parameter Biot number, *Bi*, given as a ratio of conductive thermal resistance to convective thermal resistance:

$$Bi = \frac{L_c/k}{1/h} = \frac{hL_c}{k} = \frac{conductive\ thermal\ resistance}{convective\ thermal\ resistance} \qquad \text{Eq.3-33}$$

where L_c is characteristic length and expressed as:

$$L_c = {}^{V}/_{A} \qquad \text{Eq.3-34}$$

where A and V are effective heat transfer area and volume of solid object, respectively.

It is generally accepted that lumped parameter analysis is applicable if *Bi* is much less than 1. However, due to the 20 % error in calculating convective heat transfer coefficient of the conjugate heat transfer, in most cases, the critical value of *Bi* is usually less than 0.1 [184]. When this criterion is satisfied, the excess temperature within the solid body and surrounding ambient should remain within 9 % for a cylinder as used in this research.

The numerical analysis in Chapter Five employs the lumped parameter analysis method and the detailed figure will be presented in following section of Chapter Five. The heat pipe with a 6.0 mm diameter was tightly embedded into exhaust pipe and well contacted to the hot side of the annular TEM. Moreover, there is a thermal insulation layer made by glass fibre to minimize heat transfer from the exhaust gas to coolant directly. With known the averaged heat transfer coefficient with in the engine exhaust pipe, ranging from 5000 to 12000 $W/m^2 \cdot K$ and the L_c of the heat pipe is 3 mm. The Biot number of the heat exchanger for concentric cylindrical TEG system ranges from 0.00375 to 0.009, which is less than critical value 0.1.

3.4 Test Rig and Experiment Set Up

3.4.1 Experimental Test Rig for Investigation of Convective Heat Transfer

Figure 3-6 and Figure 3-7 show the schematic layout and photo of the experimental apparatus for convective heat transfer test rig, respectively. As shown in the figures, in order to simulate the exhaust flow, the air is supplied by two 750 W blowers whose speeds are controlled using frequency inverter simultaneously. The air from the blower is ducted into a 9 kW in-line heaters and heated up. The heater is controlled by an integrated PID controller to modify the temperature of the air flow through the test rig. A hot wire flow meter (Quadra Therm780i) is placed at the outlet of the heater to measure the velocity and mass flow rate of the air. The major test section is located on the first floor of the test rig and the test section consists of a series of 17 square TEMs and two heat transfer boxes for hot air and water. Because manufacturing an annular TEM is difficult, all TEMs used in the experiment are square shape, instead of annular shape. The detailed pictures for the

major test section are shown in Chapter Five. For the purpose of measuring the power output of this test section, an electronic load (BK8540) is wired to these 17 TEMs. Moreover, there are 10 thermocouples to measure the temperature of TEMs and 2 thermocouples for measuring the temperature of inlet and outlet water through data logger (DT85M). On the ground floor, the coolant system of this rig is consist of a 900 W water bath, a float flowmeter (IFM SU7000), a 1.5 kW water pump and two ball valves to control the water flow in the major test section. In order to imitate engine exhaust gas, the frequency of two blowers are varying from 35 Hz to 75 Hz, but the temperature is fixed at 200 ℃ due to the limitation of the hot wire flow meter. The water flow ranges from 4 L/min to 9 L/min to adjust the cold side temperature of the major test section.

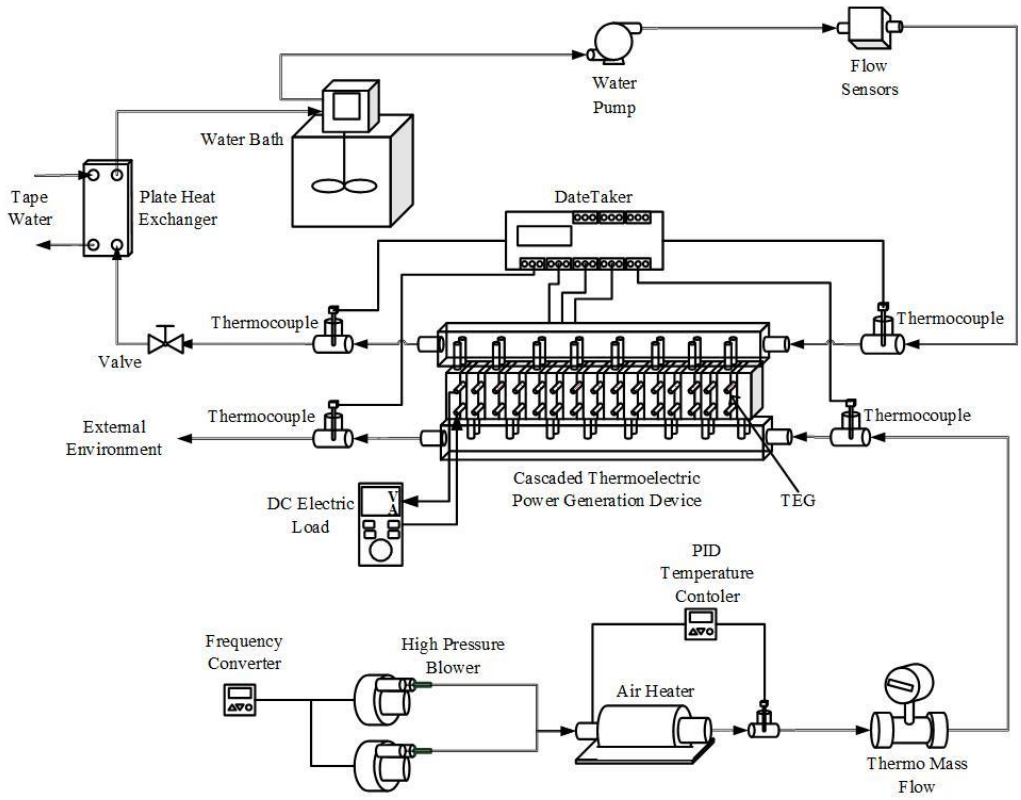


Figure 3-6 Schematic diagram of convective heat transfer test rig

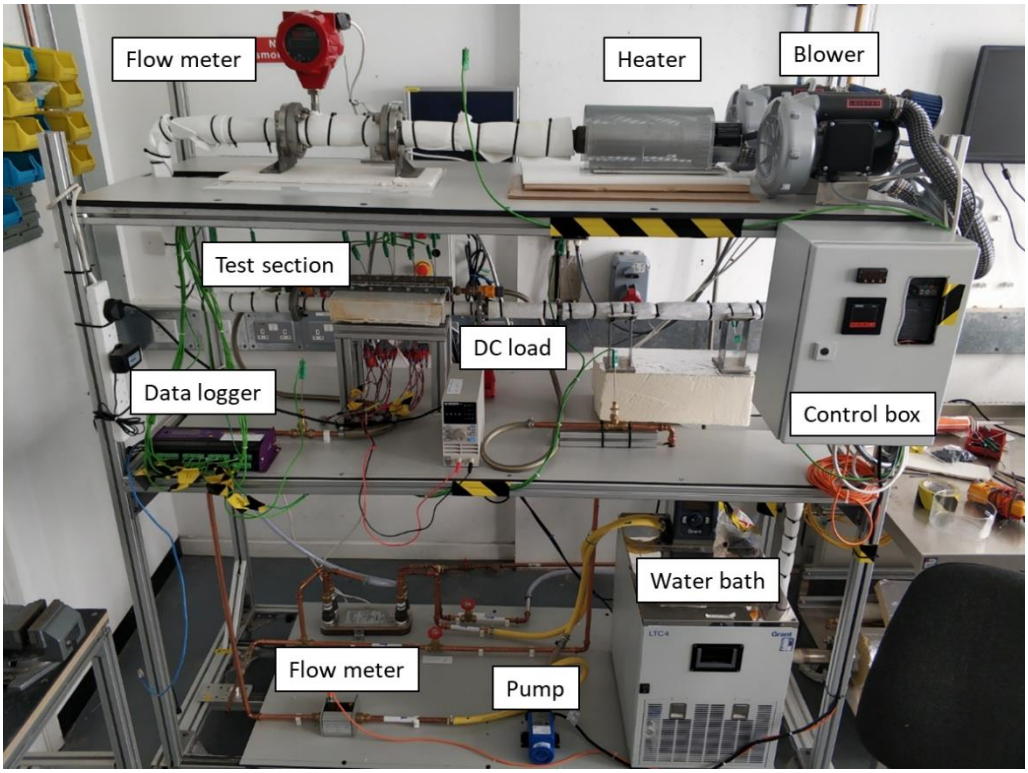


Figure 3-7 Photo of convective heat transfer test rig

3.4.2 **Experimental Test Rig for Transient Performance Improvement**

In order to investigate the performance of PCM integrated TEG system, a single TEM with PCM test rig was established. The schematic diagram of experiment set up and photo of the main test section are shown in the Figure 3-8 and Figure 3-9, respectively. For the purpose of heating the PCM and TEM, three 150 W AC cartridge heaters are placed in the base of heating plate and connected in series for easy control. In order to simulate the fluctuating temperature of exhaust gas, an AC voltage regulator and a voltage meter are employed to adjust the voltage of the three cartridge heaters, which will change the power supply to the test section. This means the temperature on the hot side of TEM is adjustable and the range of power supplied to the test section is 60 W to 80 W. In order to measure the power output

and open-circuit voltage of TEM, a DC electronic load (BK8540) is connected to the TEM. On the cold side of TEM a cooling plate in connected to the water both, in order to circulate the cooling water and maintain the temperature. There are several thermocouples to measure the temperature of the hot and cold side of TEM, the detailed distribution of thermocouples will be presented in Chapter Eight.

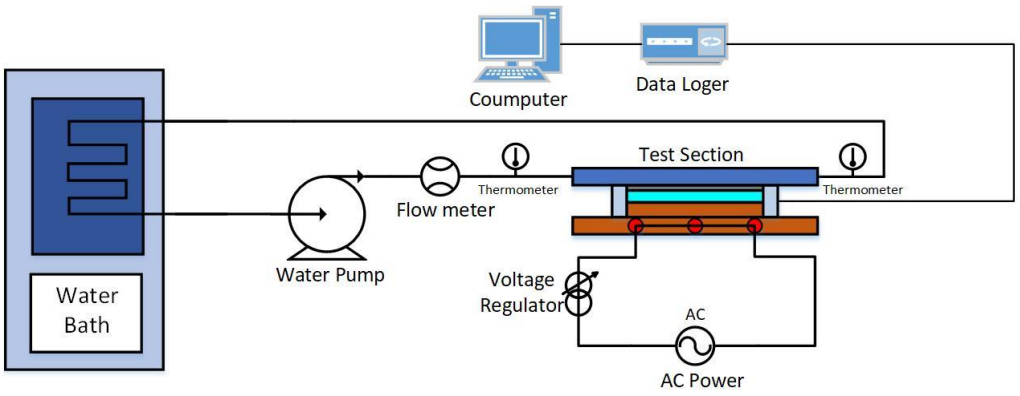


Figure 3-8 Schematic diagram of transient performance improvement set up

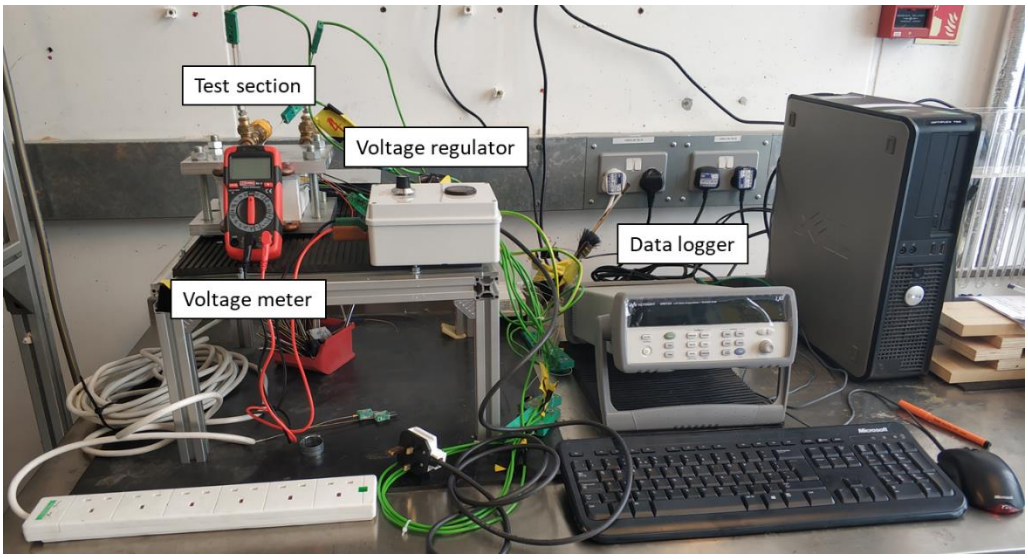


Figure 3-9 Photo of the main test section in transient performance improvement set up

The thermocouples utilized in the experiment were calibrated by the thermo bath method and adjusted according to the temperature range of measurement by using

the curve-fitting method. During the experimental test, there was no obvious drift in temperature measurement. Due to eh time limitation, only three multiple tests for each experimental investigation were carried out, in order to check the repeatability. The uncertainty of these two experiments are discussed in the following Chapter Five and Chapter Eight, respectively.

Chapter 4. Numerical Investigation on Conductive Heat Transfer within Concentric Cylindrical TEG System

4.1 Introduction

As discussed in the previous chapter, a TE system is composed of several thermal and mass transport processes which store and exchange heat through conduction, convection and radiation. Figure 4-1 shows the overall architecture of a TE power generation system in the form of heat energy flow.

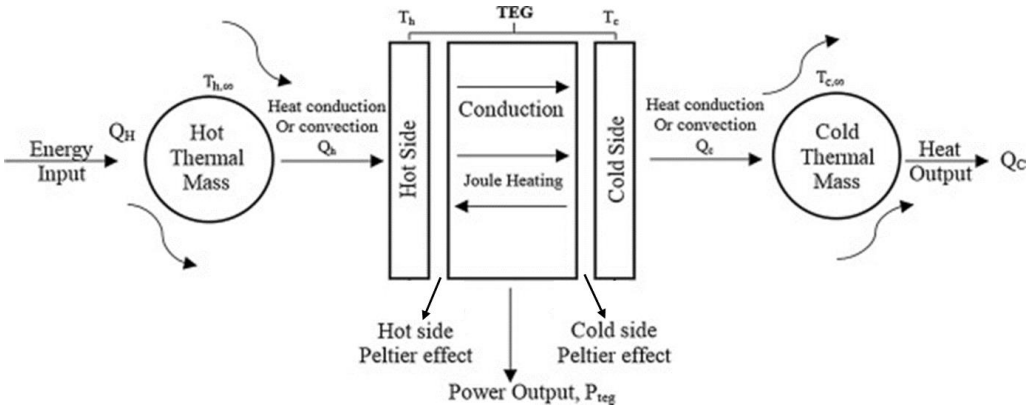


Figure 4-1Overall architecture of a thermoelectric power generation system in the form of heat energy flow

The TEG is connected with thermal masses on both hot and cold sides. Energy conversion in the TEG system takes place in the form of electrical and heat power, leading to changes in the thermal energy stored inside the thermal masses towards the downstream. Meanwhile, parasitic heat loss is inevitable within the TEG due to the Peltier effect (at interfaces) and resistive Joule heating. In addition to the improvements of TE ZT value, the heat conduction and convection processes at both sides of TEM are also the major parameters to consider in maintaining the performance of power generation. Regarding the economics of thermoelectric

power generation, the cost mainly depends on the nature of the heat source in place whereby adequate heating is necessary by the relatively low efficient TE materials. To develop a thermoelectric system including heat exchangers, heat flux through the TE system should be sufficient to maintain the appropriate temperature difference.

The conductive heat transfer within TEG system mainly occurs in the components in TEM such as ceramic plates, copper conductors and TE legs, as well as the copper plates and heat pipes for transferring the heat from exhaust gas to TEM. Because of heat flux through TE materials, it drives the electrons flowing to one end, which causes a voltage potential across the material. In other words, the heat transfer within TEG system is the driving force for generating electricity. Therefore, it is important to investigate the conductive heat transfer within TEG system and optimise the conductive heat transfer within the system through different methods.

The typical heat flux through the TE legs is maintained at around 10 kW/cm^2, assuming that the legs thickness is 1 mm and the temperature difference is 373 K. One can potentially deliver this heat flux by concentrating heat through conduction in the device's hot and cold sides using fins or any other heat transfer enhancement methods. System optimisation, especially for automotive applications, is crucial, hence both the TE device and the heat exchangers should be developed together to match heat flux requirements. Constantly varying heat source temperatures over the hot and cold sides of the TEMs is also a problem in the exhaust heat recovery system. In a typical exhaust heat recovery system, heat source (usually exhaust gas) temperature varies significantly along the flow direction. Therefore, a proper

thermal limiting or flattening component may be needed to solve the heating mismatch along the exhaust pipe. Therefore, in this project, heat transfer enhancement method in radial direction is proposed by the deployment of the heat pipe arrays. The merits of utilising heat pipes in the concentric cylindrical TEG system are explored regarding the improvement of heat flux and the ease of system integration. A better filling ratio of the whole power generation system is achieved by such configuration for engineering and fabrication.

In the following content of this chapter, three three-dimensional models are established in COMSOL Multiphysics with the purpose of investigating the conductive heat transfer within TEG system numerically. The performance of annular TEM is compared with square TEM under different thermal boundary conditions. Moreover, the simulation results are compared with experimental data from a model-scale test rig and Hi-Z performance calculator.

4.2 Model Description and Governing Equation

4.2.1 3D Model of Annular TEM and Annular TE Unit

According to the literature review in Chapter Two, the previous studies of TEG system mainly focused on the heat transfer enhancement and the improvement of TE materials, but the influence of the topological shape of TEMs has not attracted much attention by the researchers.

In this part of research, a novel design of annular TEM is presented and the aim of this novel structured module is to match the novel design of concentric cylindrical TEG system. Compared to the conventional square TEM, the annular TEM has more heat transfer area with same amount of TE unit. The two different

shape of TEMs utilised in this simulation are shown in Figure 4-2. Both modules share the same amount of TE unit and the same material properties. The geometric details of the TEMs are listed in Table 4-1. Moreover, a single annular TE unit of concentric cylindrical TEG system is made up of four annular TEMs, three heating plates and two cooling plates including twelve heat pipes in each plate, as explained in Chapter Three. In addition, the configuration of exhaust could be mutative according to the introduction in Chapter Three as well. The geometric details of major components in single annular TE unit of concentric cylindrical TEG system are listed in Table 4-2.

Each TEM in this study contains same number of TE units. These units are electrically connected in series implying that the electrical currents through them are the same. On the other hand, the heat passes through these units simultaneously, they are thermally connected in parallel. A single TE unit includes a P-type and an N-type leg, connected together with copper strips. The electrical insulation of the TEM units is achieved by placing two aluminium nitrate (AlN) ceramic plates on the top and bottom sides of modules.

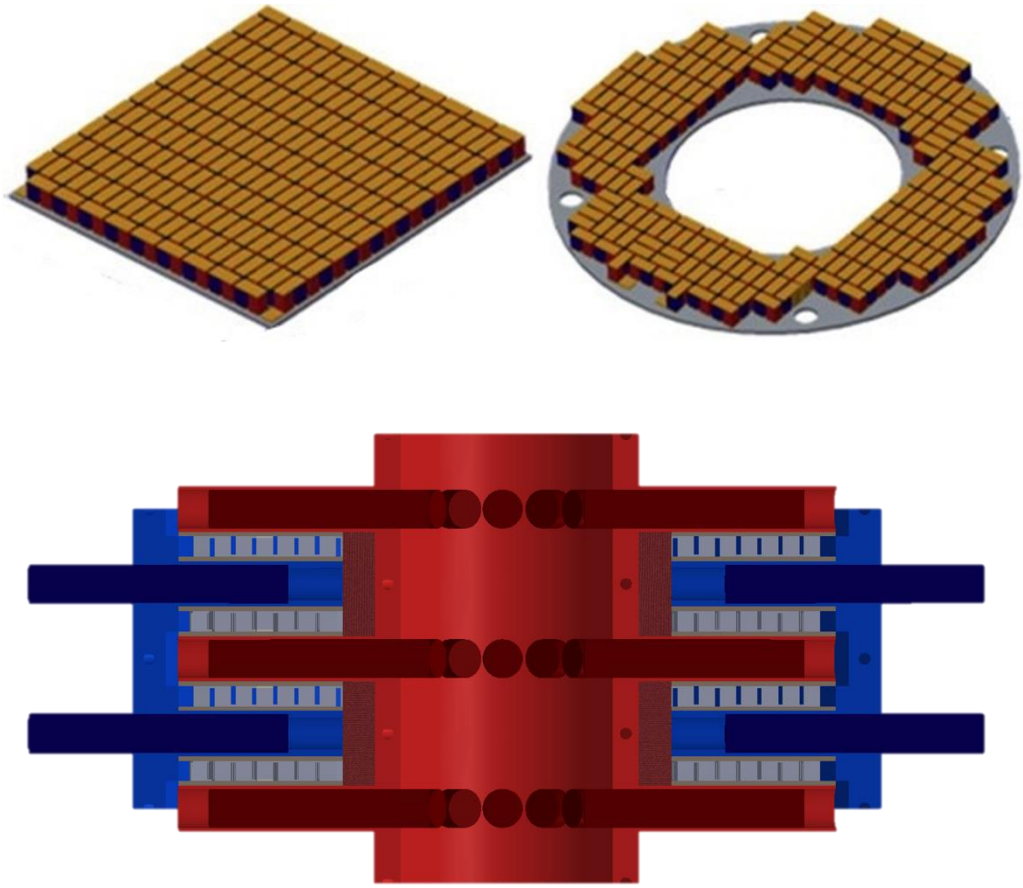


Figure 4-2 3D model of square TEM and annular TEM and single annular TE unit

Table 4-1Geometric details of two TEMs

Parameters	Thermoelectric leg	Copper connector	Ceramic plate	
			Square TEM	Annular TEM
Length (mm)	2.55	5.8	40	-
Width (mm)	2.55	2.55	40	-
Height (mm)	2.55	0.3	0.7	0.7
Inner diameter (mm)	-	-	-	60.8
External diameter (mm)	-	-	-	161.6

The 3-D models of square TEM, annular TEM and single annular TE unit are created and analysed in a commercial software, COMSOL Multiphysics. Both thermal and thermoelectric performance of these two models are simulated in COMSOL Multiphysics.

Table 4-2 Geometric details of major components in annular TE unit

Parameters	Heat pipes	Insulation ring	Internal copper plate	External copper plate
Height (mm)	40	16	23.1	7
Diameter (mm)	6	-	-	-
Inner diameter (mm)	-	50.8	60.8	60.8
External diameter (mm)	-	60.8	175.6	161.6

The detailed mesh figure for annular TE unit is shown in Figure 4-3 and the mesh was conduct in the COMSOL Multiphysics as well. In order to achieve more accurate simulation result, each component in the annular TE unit was meshed separately, during the meshing process. The grid at the surface between each component was converted to the same rate to gain a good coincidence. The increment ratio of the grid was controlled from 1.0 to 6.0 and the grid was adjusted to satisfy the criteria of each function. In order to establish grid convergence, a grid-independent test has been carried out with three types of mesh which grids are 1.01 million, 1.65 million and 2.38 million. The medium level of grid refinement was chosen and the corresponding grid for this model has been generated at the average quality of 0.9995.

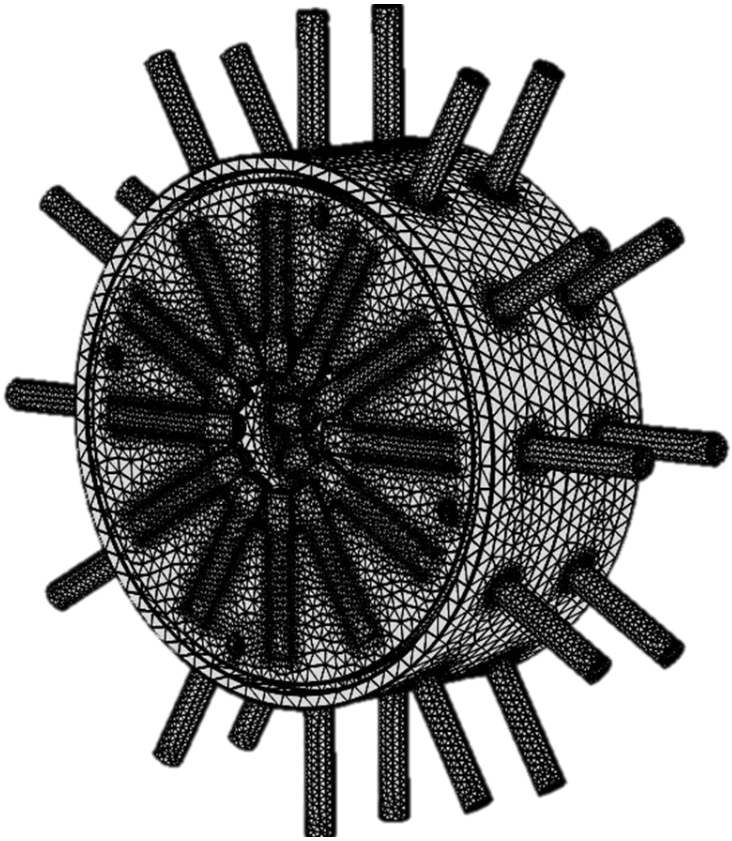


Figure 4-3 Detailed mesh model for single annular TE unit

4.2.2 **Materials Properties in Simulation**

In order to simplify the simulations, some assumptions are made to reduce the computational time. Firstly, the thermal resistance associated with the coolant is much smaller than that caused by exhaust convective heat transfer. Therefore, the heat transfer coefficient of the cold-water is assumed to be a constant value. Also given that the complexity of the exhaust mixer and the combustions, air properties are used as an approximation. The error associated with neglecting the combustion products is usually no more than about 2% [185]. As shown in Table 4-3, the primary assumption regarding the heat pipes is the thermal conductivity which is assumed to be 400 W/m·K in the radial direction (same as copper) and 4000 W/m·K [186] in the axial orientation of each component. This setting is widely used in the

engineering for simplifying the simulation calculation though with acceptable accuracies.

Table 4-3 Materials properties of major components in annular TE unit

Parameter	Copper plate	Copper connector	Ceramic plate	Insulation material	Heat pipe
Thermal conductivity (W/m·K)	400	400	180	0.022	400(Radial) 4000(Axial)

The thermal conductivity of heating and cooling plates is set at 400 W/m·K. The dielectric material, AlN ceramic, whose thermal conductivity is assumed to be 180 W/m·K, is designed concentrically to separate the copper plates and the TE legs. The MicroFoam® insulation material, whose thermal conductivity is set as constant at 0.022 W/m·K, is installed to prevent the heat loss between the exhaust and the coolant, This insulation material is used in this case due to its stable thermal performance across the high-temperature range.

The TE material utilised in this simulation is Bismuth Telluride (Bi_2Te_3), which is widely available in the common market, which is electrically connected in series. Since the TEG thermal properties highly vary under changing temperature conditions, all the relevant properties are set as temperature-dependent variables as shown in Table 4-4. The interpolations are employed here to estimate the Seebeck coefficient, thermal conductivities, and electrical conductivities of the N-type and P-type TE legs.

Table 4-4 Temperature-dependent polynomials of TE materials properties

Thermoelectric leg	Seebeck coefficient (V/K)	Thermal conductivity (W/m·K)	Electrical conductivity (S/m)
N-type	$2.0 \times 10^{-13}\,T^3 + 1.0 \times 10^{-9}\,T^2 - 9.0 \times 10^{-7} T + 8.0 \times 10^{-6}$	$-4.0 \times 10^{-8}\,T^3 + 5.0 \times 10^{-5}\,T^2 - 2.6 \times 10^{-4} T + 5.1$	$-2.6 \times 10^{-3}\,T^3 + 4.60\,T^2 - 2.7 \times 10^{3} T + 5.8 \times 10^{5}$
P-type	$-3.0 \times 10^{-14}\,T^3 - 3.0 \times 10^{-9}\,T^2 + 2.0 \times 10^{-6} T - 0.20 \times 10^{-4}$	$2.0 \times 10^{-7}\,T^3 - 0.20 \times 10^{-4}\,T^2 + 8.0 \times 10^{-4} T - 7.8$	$-2.6 \times 10^{-3}\,T^3 + 4.60\,T^2 - 2.7 \times 10^{3} T + 5.8 \times 10^{5}$

4.2.3 **Boundary Conditions and Heat Transfer Equation**

4.2.3.1 Governing Equation within Annular TEM

In this section, the comparison between the performance of annular TEM and square TEM is presented. When simulating the TE effects within TEM, the following fluxes are the quantities of interest [174]:

- Heat flux q, defined by

$$q = -k\nabla T + \Pi J \qquad \text{Eq.4-1}$$

where Π is the Peltier coefficient and k is the thermal conductivity.

- Electric current density J, defined by:

$$J = -\sigma(\nabla V + S\nabla T) \qquad \text{Eq.4-2}$$

where σ is the electrical conductivity and S is the Seebeck coefficient.

TE efficiency is measured by the figure of merit ZT, defined as:

$$ZT = \frac{S^2\sigma}{k} \qquad \text{Eq.4-3}$$

Some other quantities of relevance are the electric field E and the Joule heat source Q:

$$E = -\nabla V \qquad \text{Eq.4-4}$$

$$Q = J \cdot E \qquad \text{Eq.4-5}$$

From these definitions, conservation of heat energy and electrical current in an immobile solid reads:

$$\rho C_p \frac{\partial T}{\partial t} + \nabla \cdot q = Q \qquad \text{Eq.4-6}$$

$$\nabla \cdot J = Q_j \qquad \text{Eq.4-7}$$

where ρ is the density, C_p is the heat capacity, and Q_j is the current source.

As for the steady-state conditions, the governing equations for constant current and heat transfer of inhomogeneous TE material can be described by

$$\nabla \cdot J = 0 \qquad \text{Eq.4-8}$$

$$\nabla \cdot (k\nabla T) + J^2 \cdot P - TJ\left[\left(\frac{dS}{dT}\right) \cdot \nabla T + \nabla S|_T\right] = 0 \qquad \text{Eq.4-9}$$

where $\nabla S|_T$ is the gradient of Seebeck coefficient at a given temperature.

4.2.3.2 Governing Equation within Annular TE Unit of Concentric Cylindrical TEG System

The second section in this part of simulation is the conductive heat transfer within a single annular TE unit of concentric cylindrical TEG system. In this section, the annular TE unit is treated as one whole system that only has conductive heat transfer and the contact thermal resistance between each components is ignored.

Many topologies and shapes of TEG systems have been reviewed in Chapter Two (longitudinal, hexagonal transverse, circular, etc.). However, the basic models of heat transfer are not improved fundamentally through such differences.

Accordingly, the annular TE unit of concentric cylindrical TEG system is fully assessed in this section. Considering the function of TEG, the exhaust heat is needed to be extracted from the heat sinks of TEG system, resulting in exhaust temperature reduction at every annular TE unit implying that $T_{e,i} > T_{e,i+1}$. In other words, the later performance is lower than at the previous instance. On the other hand, in the coolant loop, the temperature rise is usually within 3 ˚C due to the high mass flow rate. The coolant should be heated by the heat sinks of the TEG, which means $T_{w,i} < T_{w,i+1}$ in the direction of the coolant flow. Considering the cases in this simulation, it is assumed that the annular TE unit of concentric cylindrical TEG system share the same hot source and cold source temperature for power output evaluation only. The assumption is not considered in the investigation of convective heat transfer. Therefore, the heat extraction by heat pipes per unit due to the power generation can be expressed as:

$$\sum_{i=1}^{n} Q_h^i(t) \qquad \text{Eq.4-10}$$

where i is the number of annular TE unit, n is the number of segregated annular TEM placed in series. And Q_h is the usable heat from the exhaust gas which is absorbed by the heat sinks and heat pipes. Q_h can be obtained by applying the heat transfer equations under the Cauchy boundary condition:

$$Q_h^i(t) = h_e^i \cdot A_e^i \cdot \left(T_{e,avg}^i(t) - T_e^i(t)\right) \qquad \text{Eq.4-11}$$

where h_e^i, A_e^i and T_e^i are heat transfer coefficients, interfacial area and surface temperature of hot side heat sinks, respectively. $T_{e,avg}^i$ is the average fluid temperature on the hot side and it is the value used to solve the one-dimensional temperature distribution on each TEM, expressed as:

$$T_{e,avg}^{i}(t) = \left(T_{e,in}^{i}(t) + T_{e,out}^{i}(t)\right)\Big/_{2} \qquad \text{Eq.4-12}$$

where $T_{e,in}^{i}(t) = T_{e,out}^{i-1}(t)$ and $T_{e,out}^{i}(t) = T_{e,in}^{i+1}(t)$, which means that the exhaust inlet temperature $T_{e,in}^{i}(t)$, at each unit, is depended on the previous exhaust outlet temperature from the upper stream. The outlet temperature $T_{e,out}^{i}(t)$ subsequently become the inlet boundary condition for the lower streams in turn. The same settings can be applied at the coolant side, the heat that is extracted from exhaust is eventually applied in heating up the coolant which can be expressed as:

$$\sum_{i=1}^{n} Q_{c}^{i}(t) = \sum_{i=1}^{n} h_{w}^{i} \cdot A_{w}^{i} \cdot \left(T_{w}^{i}(t) - T_{w,avg}^{i}(t)\right) \qquad \text{Eq.4-13}$$

where h_{w}^{i}, A_{w}^{i} and T_{w}^{i} are heat transfer coefficients, interfacial area and surface temperature of hot side heat sinks, respectively. Therefore in the annular TE unit, the power output, P_{teg}^{i} obtained by four parallel-linked concentric TEMs, expressed as:

$$P_{teg}^{i} = Q_{h}^{i}(t) - Q_{c}^{i}(t) = h_{e}^{i} \cdot A_{e}^{i} \cdot \left(T_{e,avg}^{i}(t) - T_{e}^{i}(t)\right) - h_{w}^{i} \cdot A_{w}^{i} \cdot \left(T_{w}^{i}(t) - T_{w,avg}^{i}(t)\right) \qquad \text{Eq.4-14}$$

Totally, the power output of the configured system can be summed up as:

$$P_{tot} = \sum_{i=1}^{n} P_{teg}^{i} = \sum_{i=1}^{n} \left[h_{e}^{i} \cdot A_{e}^{i} \cdot \left(T_{e,avg}^{i}(t) - T_{e}^{i}(t)\right) - h_{w}^{i} \cdot A_{w}^{i} \cdot \left(T_{w}^{i}(t) - T_{w,avg}^{i}(t)\right)\right] \qquad \text{Eq.4-15}$$

It is worthwhile to note that both h_{e}^{i} and h_{w}^{i} are local averaged values which are reciprocally associated with engine load and exhaust conditions. These parameters are not only sound indicators of heat transfer enhancement but also used to identify

the type of available enhancement methods. Therefore, in this simulations, both h_e^i and h_w^i are varied from 50 W/m^2·K to 1200 W/m^2·K and from 1000 W/m^2·K to 20000 W/m^2·K, respectively. In addition, the temperature of the exhaust source and the coolant is set as 750 ℃ and 90 ℃, respectively. The parameter analysis of external load resistance, R_{ex}, is carried out by varying the value from 0 Ω to 7.5 Ω at a step of 0.1 Ω.

Besides the classical heat transfer equations, the TE effect is integrated and simulated by using the coupled-field equation as:

$$-\vec{\nabla}\left((\sigma\alpha^2 T+\lambda)\vec{\nabla}T\right)-\vec{\nabla}(\sigma\alpha T\vec{\nabla}V)=\sigma\left(\left(\vec{\nabla}V\right)^2+\alpha\vec{\nabla}T\vec{\nabla}V\right) \quad \text{Eq.4-16}$$

$$\vec{\nabla}(\sigma\alpha T\vec{\nabla}V)+\vec{\nabla}(\sigma\vec{\nabla}V)=0 \quad \text{Eq.4-17}$$

where σ, α, and λ are the electrical conductivity, Seebeck coefficient and the thermal conductivity of TE legs, respectively. In order to solve these partial differential equations (PDE) [187], the weak form PDE function is coded into a physical model builder in the COMSOL Multiphysics. Therefore, a 3D geometry of the annular TE unit is discretized, and the coupled solutions can be solved based on the above boundary conditions.

4.3 Results and Discussion

4.3.1 Simulation Model Verification

In order to test and verify the COMSOL Multiphysics model utilised in this part of simulation, the results are compared with the data of a proof-concept experiment, which is carried out in a model-scale test rig. In addition, Hi-Z performance

calculator [188] for TEM is utilised during the comparative analysis of the experimental and simulation results.

Figure 4-4 shows the schematic diagram and photo of the model-scale experimental test rig for the COMSOL Multiphysics model, under various boundary conditions. The main test section was composed of 16 TEMs in four layers, with cooling plates and heating plates. Thermal interface materials are placed at the interface of solid surfaces to enhance the heat transfer. Two 100 W controllable cartridge heaters were utilised to supply heat on the hot side and the heat supply could be adjusted by changing the voltage of cartridge heaters. The value of temperature, water flow rate and output voltage were recorded by a DT500 data logger. A rheostat resistance ranging from 0 Ω to 40 Ω was connected to the main test section to provide the adjustable external load.

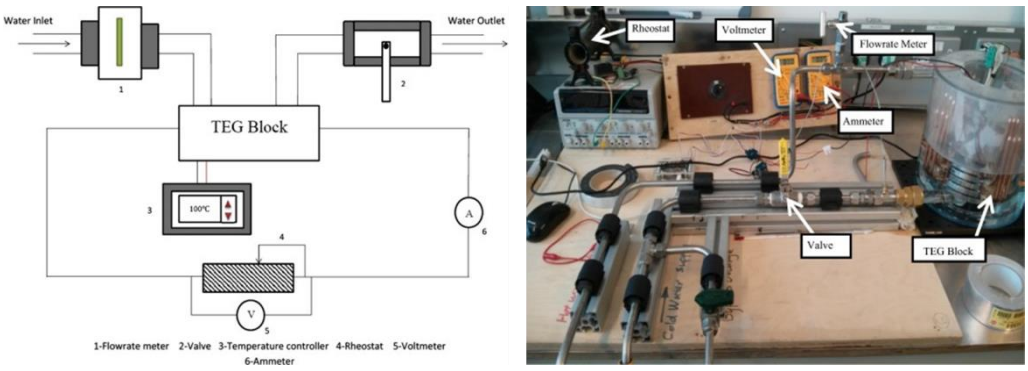
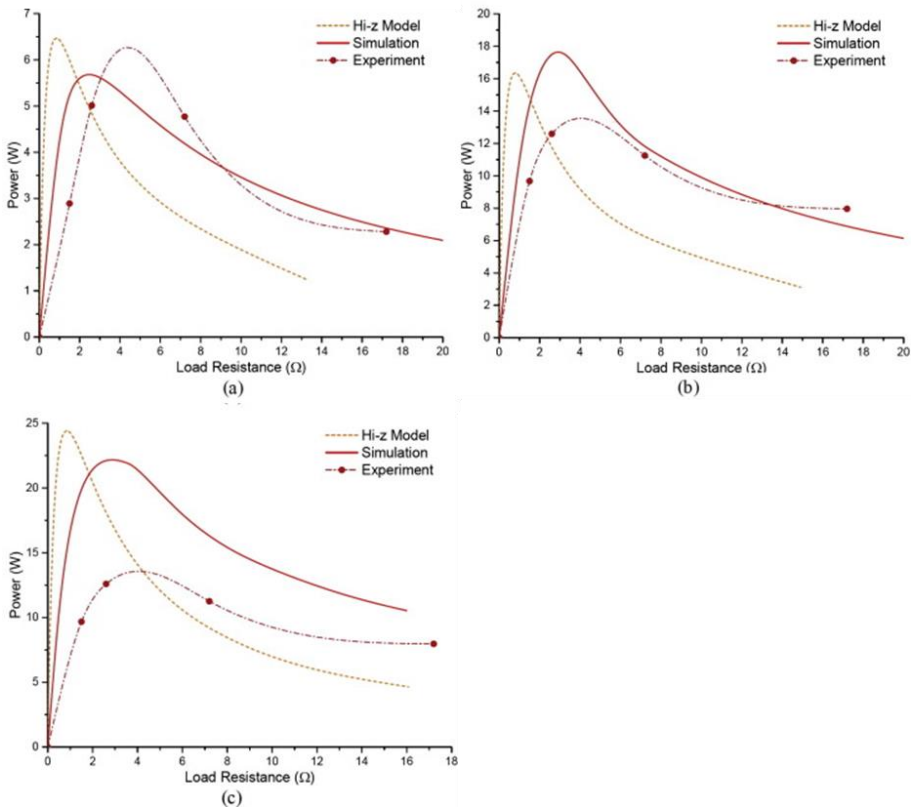


Figure 4-4 Schematic diagram and photo of the model-scale experimental test rig

Figure 4-5 shows the variation in power output versus varying load resistance (R_L) under different hot side temperature. As shown in figure, three load curves exhibit the same trends though they have a marginal difference under different load resistance conditions. The curves of simulation and Hi-Z calculator in Figure 4-4 (a)–(c) are a similar at a lower load resistance but slightly deviate from each other

at a higher load resistance. These differences could be caused by the difference in accuracies and errors during calculations of the internal electric resistance and the heat flux. In Hi-Z performance calculator, there is an egg crate area, which has a lower heat transfer coefficient than other areas. Besides, the internal electric resistance in the simulation was calculated by continuous integration method, which is different from Hi-Z performance calculator [188]. In addition, the application of different input heating power may also cause the difference seen in these curves.



(a) under 353 K of the hot side temperature; (b) under 393 K of the hot side temperature; (c) under 423 K of the hot side temperature

Figure 4-5 Comparison of numerical model, Hi-Z model and experiment

Nevertheless, the trend of these three power output curves is practically the same, even though different hot-side temperatures are applied. The peak point of each curve occurs when the inner resistance of the TEM matches the external load

resistance. The power output increases sharply at lower load resistance and declines slowly at a higher load resistance, which seem to be relatively levelling off afterwards. In Hi-Z Model, the increment and reduction of the power output are more noticeable due to the differences in the calculation method. The agreement between the simulation results and the experimental data is better than that of Hi-Z Model.

Figure 4-5 (a) is the comparison of the results of simulation, Hi-Z calculator and experiment at hot-side temperature of 353 K. The hot-side temperature is because of different inward heat fluxes used in simulation, and varies from 353 K to 384 K representing an increment of 31 K. The comparisons of the different hot side temperatures are shown in Figure 4-5 (b) and (c). These results show good agreement with the result at hot-side temperature of 353 K in Figure 4-5 (a). When the hot-side temperature and temperature difference become larger, the results predicted by the Hi-Z and simulation deviate from each other where the deviation increases with the increment of hot side temperature and temperature difference. Such discrepancies could be caused by using the different temperature-dependent material properties and the difference of the temperature variation within the TE unit.

Figure 4-5 also shows the variation for power output with the load resistance in the experimental test under different conditions of hot-side temperature. In these three figures, the experimental curve is in reasonable agreement with the other two curves. However, actual results of the experiment have a minor difference with simulation and Hi-Z calculator, particularly at the higher hot side temperature. There are two main reasons which lead to such a discrepancy. Firstly, the

discrepancy is caused by the instrumental errors. The difference between the expected and actual maximum power obtained is dependent on the errors in both voltage and current measurements. The error in the heat flux temperature set-point was based on the thermocouple accuracy and the errors in the temperature controller. The errors in the temperature controller were a combination of the indication error of the thermocouple temperature and the overshoot deviation from the set-point temperature. Secondly, due to the thermal loss in the test, the actual heat transfer to the test prototype is not as much as the cartridge heaters supplied. When the temperature increase, the temperature difference between test rig and ambient becomes larger, thus the heat loss was exacerbated. In Figure 4-5 (c), the experiment data shows the obvious difference with the other two curves.

4.3.2 **Performance Comparisons of Single TEM**

Assuming that the inward heat flux of each TEM remains constant, the total inward heat flow is proportional to the heat transfer area. Based on the geometric comparisons in Table 4-1, the main difference between these two TEMs is the heat transfer area. The available heat transfer areas for the square TEM and annular TEM are found to be 1600 mm^2 and 17598 mm^2 respectively.

The total power output of annular TEM also could be calculated according to Eq. 4-15.

Furthermore, the power generated at the external load in a closed circuit can be is expressed as [189, 190]:

$$P_L = \left(\frac{S \cdot \nabla T}{R_L/R+1}\right)^2 \frac{R_L}{R} \qquad \text{Eq.4-18}$$

The maximum power efficiency is the specific conversion rate at which the power reaches its maximum efficiency. In addition, the maximum power is obtained when the external resistance equals to internal resistance of TEM $R_L = R$ and by inserting this relation into Eq. 4-18, it gives:

$$P_{L-max} = \frac{(S \cdot \nabla T)^2}{4R} \qquad \text{Eq.4-19}$$

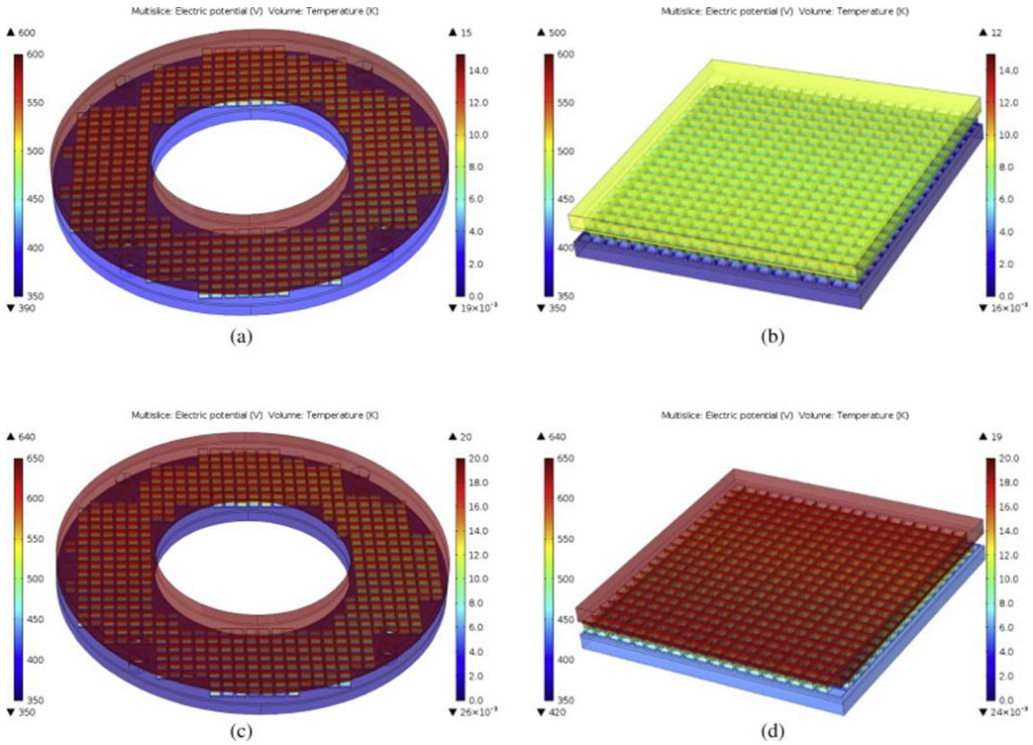
According to the Carnot's theorem, the conversion efficiency of the TEG is in the form of,

$$\eta = \frac{W}{Q_h} \qquad \text{Eq.4-20}$$

Figure 4-6 shows the performances of each TEM, under the same inward heat flux at 5 W/cm^2 and same hot-side temperature. From Figure 4-5 (a) and (b), the heat transfer area has a considerable level of influence on the temperature distribution on the hot side of the TEM. Since the heat exchange area of annular TEM is larger than that of square TEM, annular TEM can conduct more heat with the same inward heat flux. In this case, a higher temperature difference between the hot and cold side of annular TEM results into a higher open circuit electric potential. These two figures also indicate that the average hot-side temperature of annular TEM is 602 K, which is higher than the average hot-side temperature of the square TEM that is 500 K. The temperature difference between each side of annular TEM and square TEM is 213 K and 150 K respectively. As a result, the annular TEM generates a 14.5 V of open circuit electric potential, which is 2.1 V higher than that of square TEM under the same heat flux condition.

Figure 4-6 (c) and (d) show the simulation result of both TEMs operating at the same hot side temperature of 643 K. The figures indicate that the annular TEM

module performs better than square TEM at the same hot-side temperature. As long as the hot-side temperature is maintaining at the same value for each TEM, a lower average cold side temperature for annular TEM is achieved due to the larger heat transfer area enabling it to acquire a higher heat dissipation rate. Consequently, the respective average cold side temperatures for annular TEM and square TEM are 352 K and 417 K. This difference obviously affects the open circuit electric potential generated by TEM because the Seebeck effect responsible for generating this potential is actuated by the temperature difference on the two sides of the TEM. Therefore, the open circuit electric potential for annular TEM is higher at 19.6 V than that for square TEM at 18.9 V.



(a and b) under inward heat flux q = 50,000 W/m^2; (c and d) at hot side temperature T_h = 643 K

***Figure** 4-6 Performances of each TEM under different hot-side condition*

As mentioned above, two kinds of boundary conditions are adopted. The first one is Neumann boundary condition on the hot side and Cauchy boundary condition on the cold side. The second one is Dirichlet boundary condition on the hot side and Cauchy boundary condition on the cold side The reason for specifying these two different sets of boundary conditions is that the various measurements of the hot-side temperature in practical and simulation are taken. In some situations, it is difficult to obtain the exact value of the hot-side temperature, so the temperature is often calculated by the heat flux on the hot side, which is the Neumann boundary condition. During simulation, the hot-side temperature is often specified for a more accurate simulation. As a result, Dirichlet boundary condition is also applied in the next part of the simulation.

4.3.3 Influence of Heat Transfer Area

Under the same inward heat flux, the primary difference of these two TEMs is the heat transfer area, which leads to higher surface temperature distribution of annular TEM than that of square TEM. As a result, the different temperature distributions of the two TEMs influence their power generation capabilities represented by their open circuit electric potential values. In this part of simulation, the influence of engine speed is taken into consideration, as the variation of engine speed affects the total inward heat flux of TEM. In this way, the influence of automotive driving cycle to the performance of TEM is investigated.

Figure 4-7 shows the average temperature and open circuit voltage of both TEMs under different inward heat flux, which is calculated at various engine speed. The curves indicate that the hot-side average temperature of annular TEM is higher than that of square TEM due to the larger heat transfer area of annular TEM. Furthermore,

the hot-side average temperature is in direct proportion to inward heat flux. Under the same inward heat flux, the hot side average temperature of annular TEM is 20 to 25 K higher than that of square TEM. This difference results in a considerable variation in the temperature difference so that the open circuit electric potential of annular TEM is again greater than that of square TEM.

Since the temperature difference of annular TEM is higher than that of square TEM, the open circuit voltage generated by annular TEM is also higher in general. Under various inward heat fluxes caused by different engine speed, the open circuit voltage generated by annular TEM is 2 to 2.5 V higher than that generated by square TEM. This difference becomes larger when the inward heat flux is lower because the two curves show a parabolic shape.

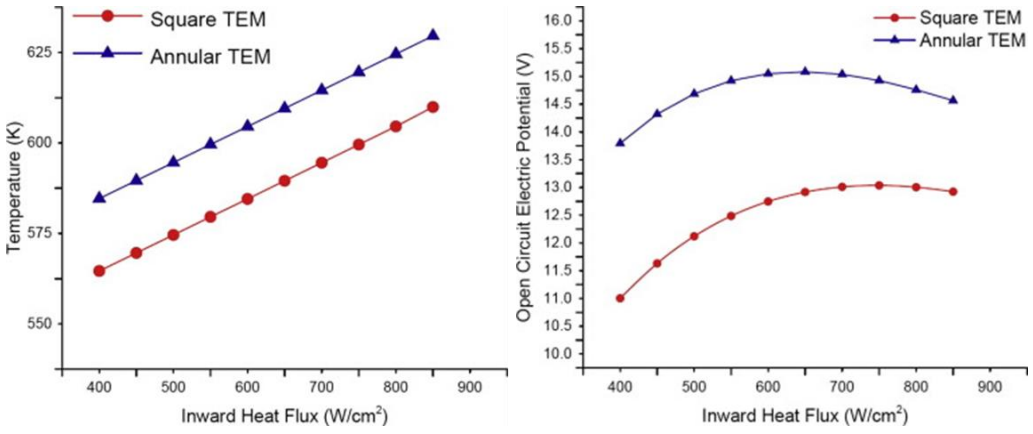


Figure 4-7 Average temperature & open circuit voltage of both TEMs under different inward heat flux

This figure also demonstrates that each TEM has an optimal performance point, which is a function of inward heat flux as observed. Therefore, the automotive driving condition should be taken into account when the TEG system is being designed for a specific vehicle exhaust system. In order to obtain a better output

voltage and power, the position of TEG system in the entire exhaust system also needs to be considered carefully.

4.3.4 Performance of Single Annular TE Unit

In the simulated cases, the best performance results for the single annular TE unit of concentric cylindrical TEG system are shown in Figure 4-8. The major features of the TEG performance are: matched load voltage, matched load current and matched load power as shown in P-I-V curves of Figure 4-8 (b) and (d). The matched load voltage is obtained at 4.5 V when the matched load resistance reaches to 0.7 Ω (which is $R_L/4$, a quarter of each modular resistance of 2.8 Ω). Meanwhile, the maximum output power is achieved at 29.8 W for the same load resistance condition in which the match load output current is 6.62 A, which passes through the terminal connectors. As mentioned in Chapter Three, there are two different exhaust pipe configurations: external exhaust channel and internal exhaust channel. In this figure, the comparison between these two configurations is presented as well. The external-exhaust-channel configuration for the radial direction outperforms the internal-exhaust-channel configuration shown in Figure 4-8 (d), which represents the power rating.

For the internal-exhaust-channel configuration, the matched load power achieved is less than 5 W which is computed for a total of 4 annular TEMs even when the best convective conditions are applied. A limited heat transfer area could be the major reason that causes such undesired results. To compare Figure 4-8 (a) and (c), the temperature at hot side heat pipe are maintained at 555 K and 371 K respectively. There is still room for improvement to increase the hot-side temperature of the TE legs. However, it should be noted that the fin stacks, which are not simulated in this

case, might contribute to higher heat transfer coefficient at the interface of the exhaust and the heat pipes. The main obstacles to applying extra fin stacks are the limited space within the standard exhaust pipe. The advantage of the external-exhaust-channel configuration is that the fin stacks can easily be applied to the hot-side heat pipe at the external channel. Therefore, a higher power rating could be anticipated.

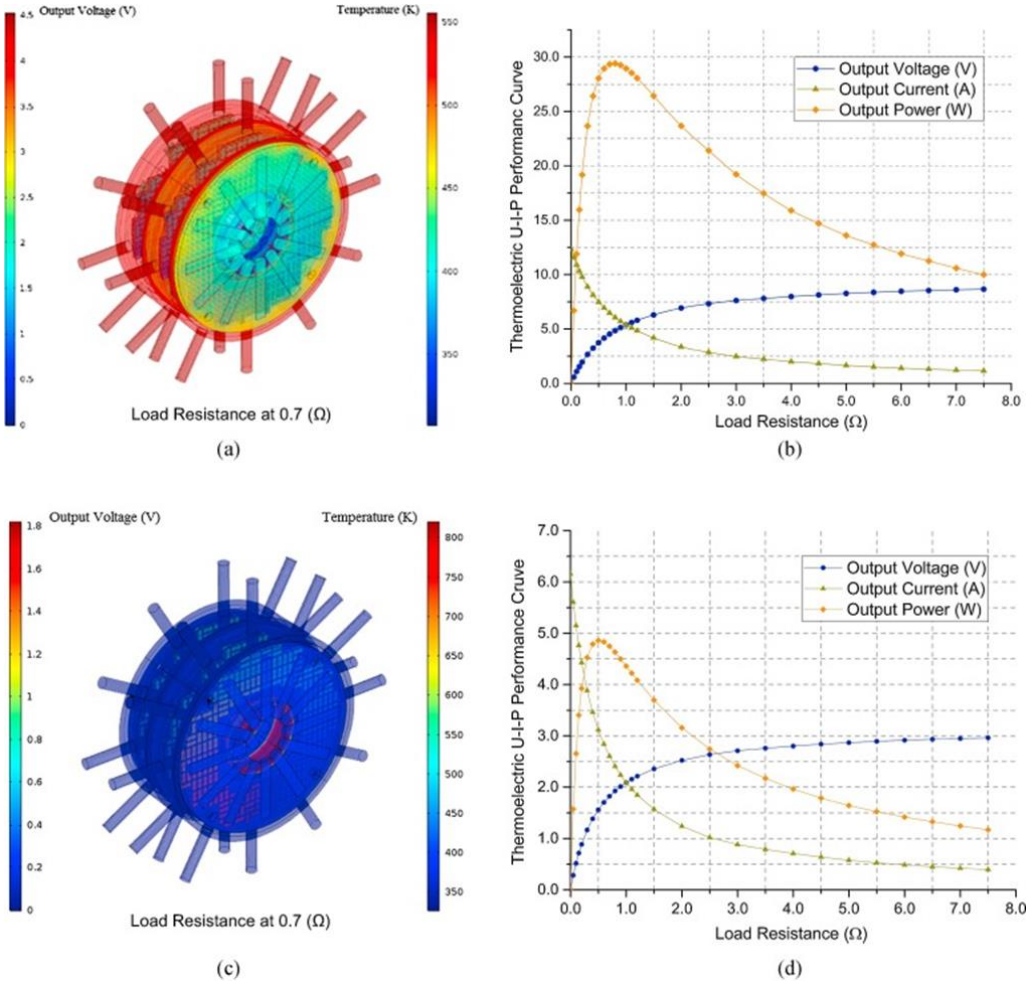


Figure 4-8 Temperature distribution simulation and P-I-V curve of external exhaust channel and internal exhaust channel configuration

Figure 4-9 shows the temperature distribution within the annular TE unit of concentric cylindrical TEG system. To maintain a sustained temperature difference

at both sides of the TEM, heat pipes are deployed in our cases by means of integrating them with the concentric cooling and heating copper blocks. The main reason for such deployment is to reduce the thermal resistance of the heat sinks at both ends of the TEM surfaces. As shown in Figure 4-9 (a) and (b), the cooling block can be maintained at 401.7 K while the heating block can be achieved at 555.7 K. Both copper blocks show excellent temperature and even distribution of temperature which help to maintain the temperature of TE legs within each annular TEM. Therefore, a proper temperature distribution within TE legs can be obtained as seen in Figure 4-9 (c) where the temperature difference within the module is about 20 K in the radial direction of the exhaust flow.

In addition to the arrangement of heat pipes, it is worthy to note that proper insulations around the annular TEM also contribute to maintaining a bigger temperature difference as shown in Figure 4-9 (d). The thermal bridging may happen without sufficient thermal insulation at the junctions between heating blocks and cooling blocks. This may result in undesirable heat loss to the water coolant directly. As seen in Figure 4-9 (d), the TEMs are tightly sandwiched between stacked cooling and heating blocks. Therefore, thermal insulation material with high performance are required and are carefully placed between the blocks to solve such issues. In this case, the TEM operates at its optimal temperature condition ranging from 473 K to 523 K. The figure of merit, ZT value of 0.867 is achieved which is acceptable at the current stage regarding the conversion efficiency.

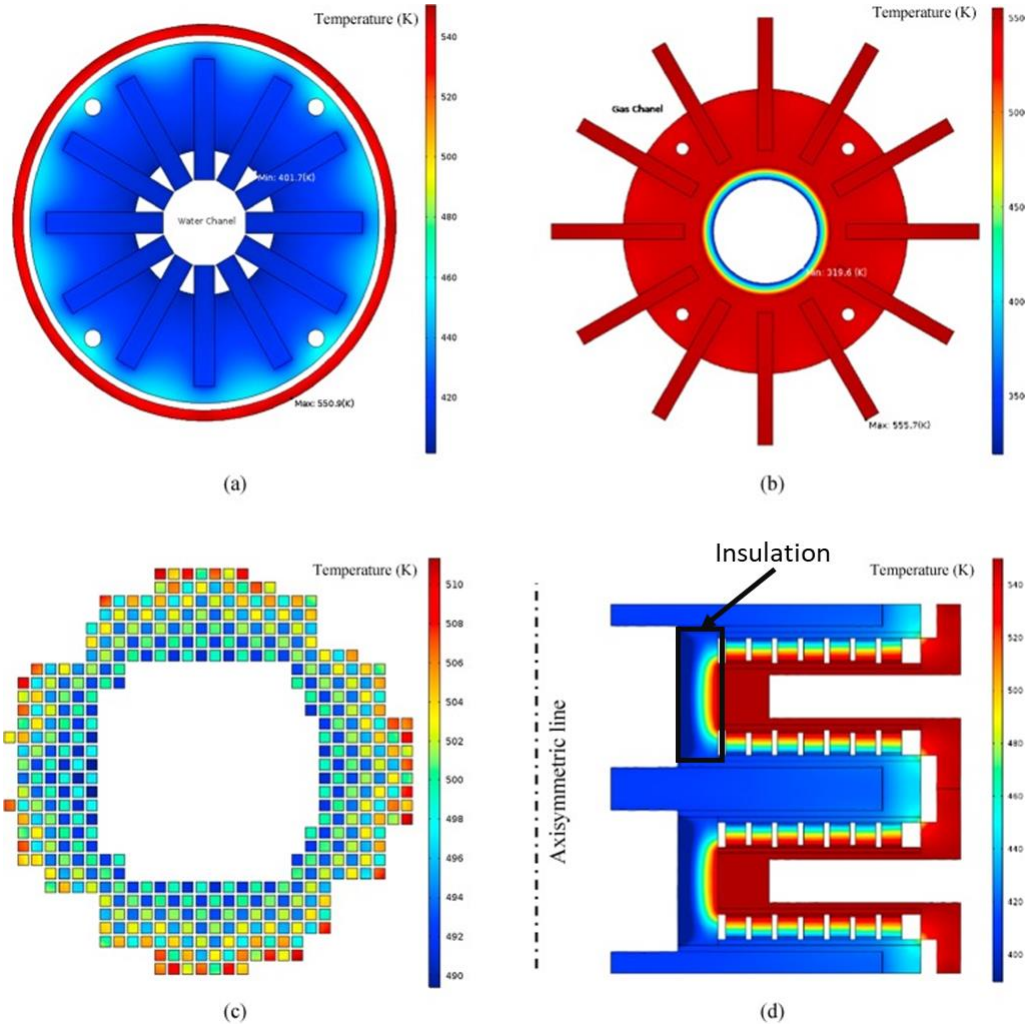


Figure 4-9 Temperature distribution of (a) cooling blocks (b) heating block (c) cross section of TEM and (d) longitudinal section of annular TE unit

Due to the unique characteristic of the flow and heat transfer pattern, the correlations of combined internal and external flow correlations (Aligned or staggered tube banks) cannot be applied in this case [191]. Alternatively, the average heat transfer coefficients value $\bar{h}$ at the local interface is adopted as the indicators of heat transfer enhancement.

As can be seen from the curves of Figure 4-10, the increases of heat transfer coefficient of either exhaust gas or coolant reveal a general trend of steady rise of

the power output though the margins of the rises varied. In addition, the trends of improvement in power generation could be recognised in two stages from both curves. Below the value of 10000 W/m^2·K for the water coolant heat transfer coefficient, the power output increase rapidly with coolant side heat enhancement. However, the power out of a single annular TE unit increases at a slower rate when it comes to the later stage. Same as the water coolant side, there are upward trends in power generation of a single annular TE unit, and the curves become more linearly when the heat transfer coefficient increased.

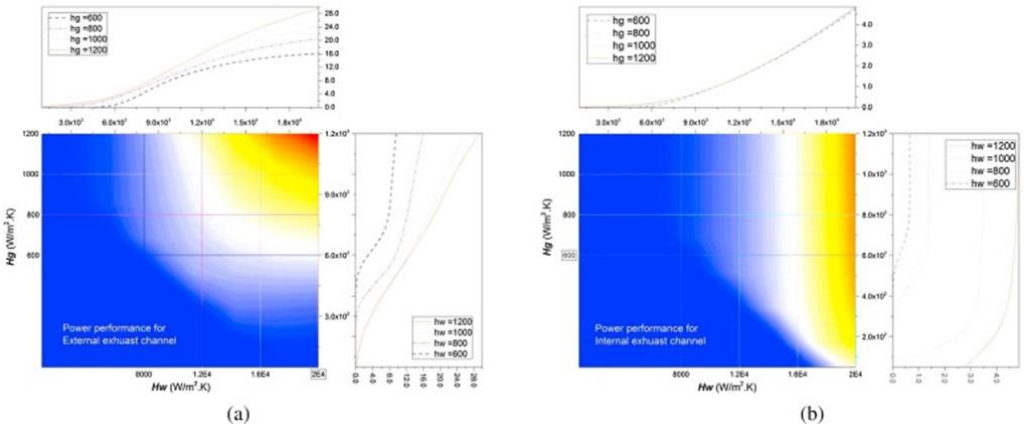


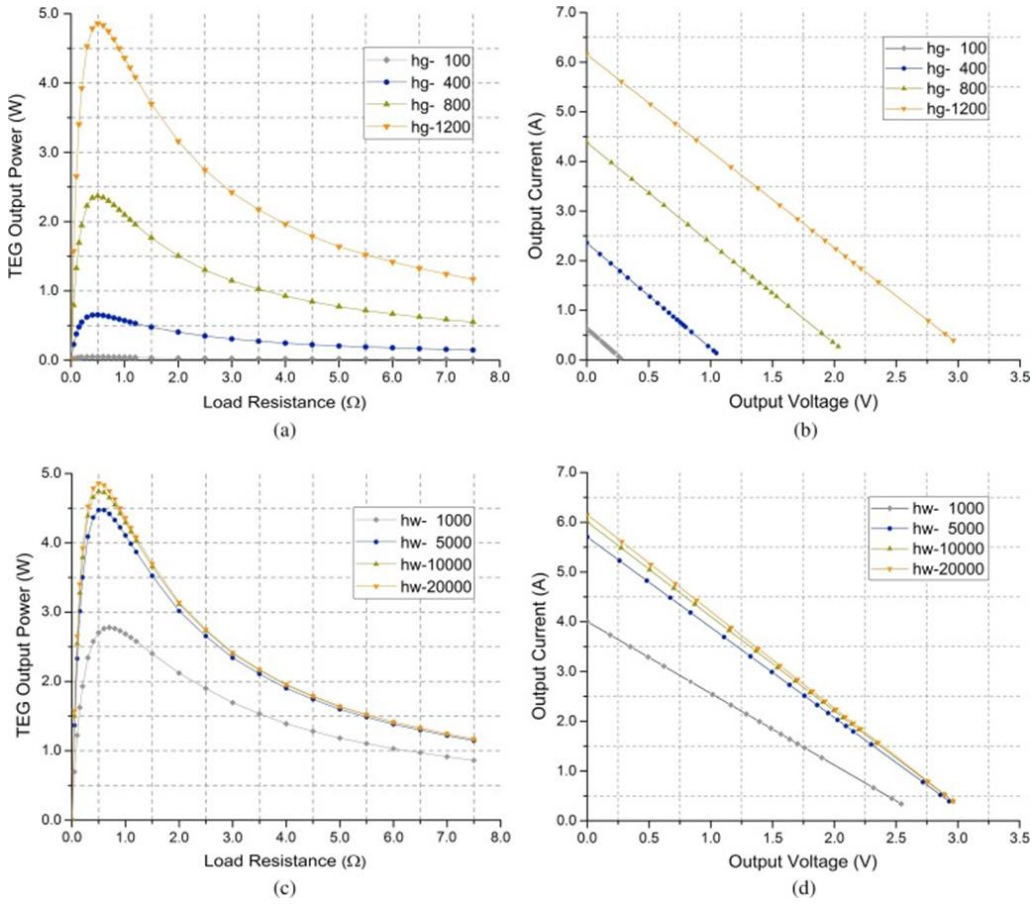
Figure 4-10 Power output contour of annular TE unit under different heat transfer coefficient for (a) external and (b) internal exhaust channel.

4.3.5 Performance Comparisons of Two Different Exhaust Configurations

In the exhaust pipe of modern vehicles[185], heat transfer coefficient ranges from 100 W/m^2·K to 1500 W/m^2·K according to the practical engine performance. The exhaust flows steadily in the turbulent region. On the other hand, the heat transfer coefficient of the water coolant in vehicle radiators is in the range of 5000 W/m^2·K to 15000 W/m^2·K within the fin stacks. Nevertheless, the performance of the TEG

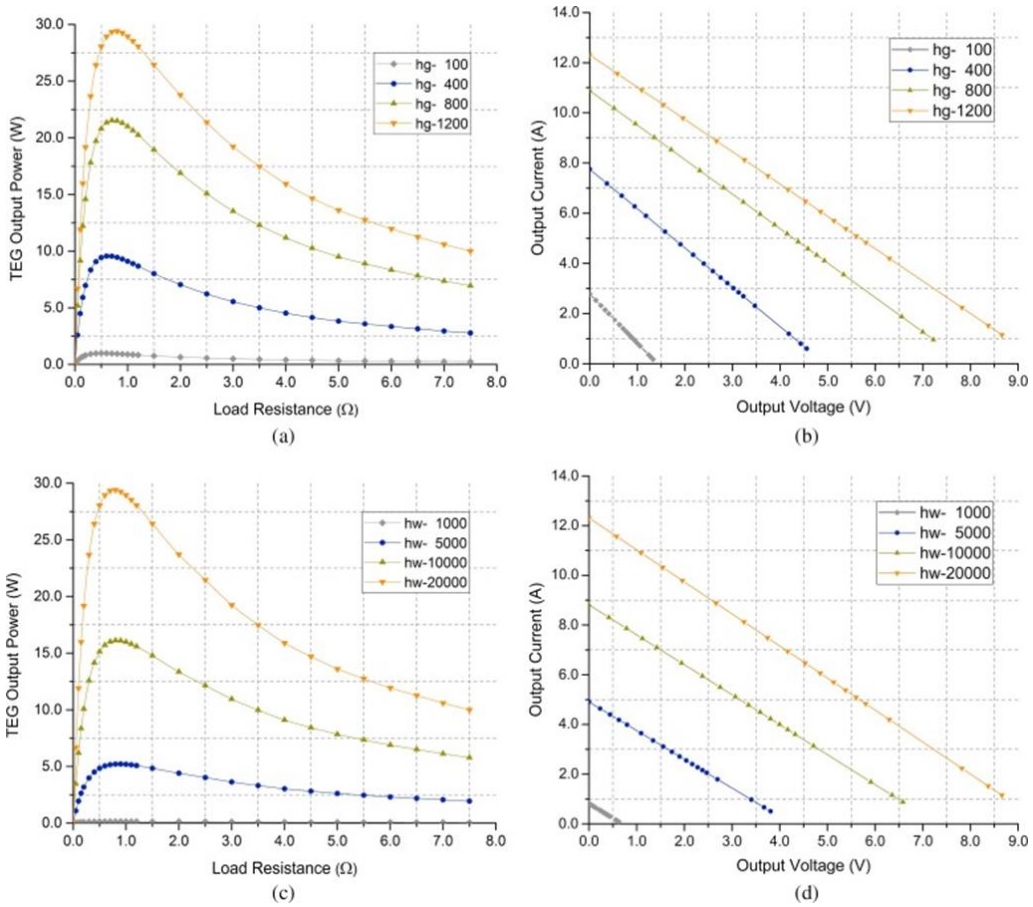
is closely related to the layout of the heat source and heat sinks, thus designs of the TEG heat exchanger should be focussed on efficient heat transfer.

In this section, the performance comparison between two different exhaust configurations is discussed. As shown in Figure 4-11 and Figure 4-12, both heat source and cold source impose enormous impacts on the output power of the TEGs. However, the overall power rating of the external-exhaust-channel configuration is much better than the internal-exhaust-channel configuration.



(a) and (b) electrical performance under enhanced heat convection of the exhaust gas, (c) and (d) electrical performance under enhanced heat convection of the coolant.

Figure 4-11 Performance curves of internal-exhaust-channel configuration



(a) and (b) electrical performance under enhanced heat convection of the exhaust gas, (c) and (d) electrical performance under enhanced heat convection of the coolant.

Figure 4-12 Performance curves of external-exhaust-channel configuration

In Figure 4-11 (a), the output power is shown to increases significantly with higher exhaust gas heat transfer coefficient. The V-I profile changes correspondingly under the same trend as seen in Figure 4-11 (b). Interestingly, the trend in heat transfer improvement at cold side, which is presented in Figure 4-11 (c), shows a disproportional increase in output power for the internal-exhaust-channel configuration. Although the output power of the annular TE unit still increases, a weaker impact of higher heat transfer coefficient is noted in Figure 4-11 (c) and (d). The growth of both output voltage and output current become inactive as shown in Figure 4-11 (d). The resistance of an annular TE unit, as

presented as the slope of the curves in Figure 4-11 (d), are affected by the enhanced coolant flow. The results of V-I curves in Figure 4-11 (d) tend to be normalised to an upper limit when the heat transfer coefficient increases.

In comparison to with the results of internal-exhaust-channel configuration in Figure 4-11, the external-exhaust-channel configuration shows better performance in terms of power output, which is consistent with heat transfer coefficient improvement. This result is mainly attributed to the larger surface area of the external channel. More heat flux can be transferred into the heating blocks under same heat transfer coefficient conditions. Another main benefit of this setting is that extra fin stacks can be configured on the heat pipes due to the ample space available in the exhaust channel. In such contexts, the higher heat flux can be achieved.

4.3.6 **Temperature Distribution**

A temperature distribution in the radial direction of concentric cylindrical TEG system is shown in Figure 4-13. The two different configurations result in different heating impacts on the components in the TEG system. With the higher heat transfer coefficient at the exhaust channel, the TEG system exhibits a higher temperature profile at the hot side heat pipe. This is consistent with other investigations where a major decline of hot-side temperature and temperature difference are noted in both Figure 4-13 (a) and (b) due to the parameter variations at the hot side of the TEG module. The largest temperature difference at hot side heat pipe is 225.8 K while the difference of temperature difference is maintained at 144 K. This decline inevitably contributes to adverse effects on the power output of the TEG system. Therefore, extra heat enhancement measures are needed in this regard. The optimal temperature of Bi_2Te_3 based TEG should settle in the range of 450 K to 520 K

according to the current material development. Any temperature rise above this region will make TEG legs less efficient and a higher risk of thermal shock to the solder materials. Additionally, the conventional copper-water heat pipe here may be challenged by such temperature rise and therefore could not adhere to the operational temperature ranges. As shown in hw-20000-hg-1200 curve of Figure 4-13 (a), only such case is suitable for the optimal condition of both the heat pipes and the TEG. The overall temperature profile can be improved and reduced by the application of fins stacks in the future.

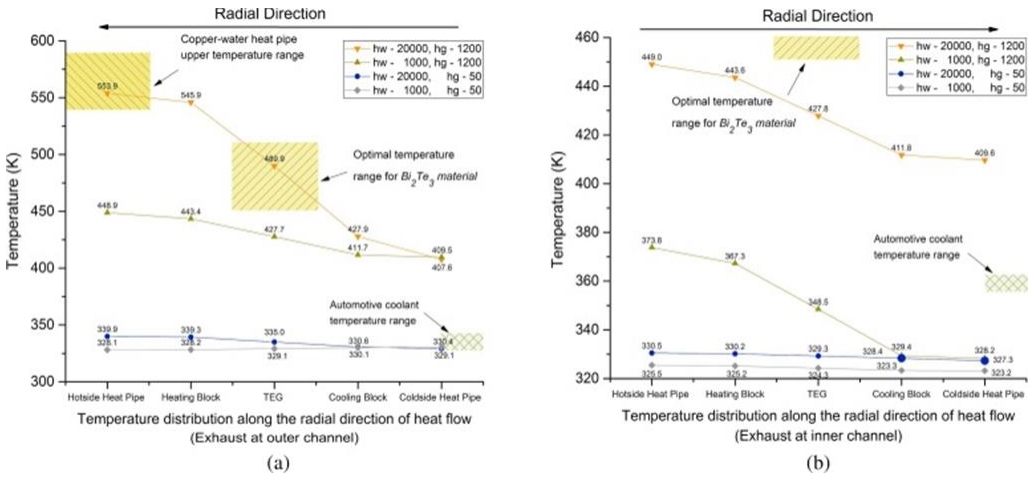


Figure 4-13 Temperature distribution in radial direction of concentric cylindrical TEG system

On the cold side, the heat transfer coefficient of water coolant has minimal effects on the temperature distribution of the TEG system. It is also noted that the temperature distribution of the external-exhaust-channel configuration is generally higher than that of the internal-exhaust-channel configuration with different heat transfer coefficient, which is well consistent with the previous results in terms of the power output for these two systems. In contrast, the maximum difference of hot-side temperature between these two systems is 104.9 K, but the maximum

difference of the cold-side temperature between these two systems is merely 2.6 K. Furthermore, the highest temperature difference of the external-exhaust-channel configuration is 300.7 K, which is higher than that of the internal-exhaust-channel configuration. The reason for such a variance is the enhanced exhaust heat exchange that is arranged in the external channel.

In addition to these four curves in each schematic, there are three shadow parts in these two figures, which indicate the copper-water heat pipe upper-temperature range, including the optimal temperature ranges for Bi_2Te_3 material and automotive coolant temperature range. In practice, these three areas are the optimum working temperature for TEG system when it is assembled in the automotive. Among all these eight curves, it can be noted that the temperature distribution is located at the optimal temperature range for Bi_2TE_3 material and copper-water heat pipe upper-temperature range only when the exhaust is arranged at external channel and the heat transfer coefficient when water and exhaust side is set at 20000 $W/m^2 \cdot K$ and 1200 $W/m^2 \cdot K$ respectively. In Figure 4-13 (b), none of the four curves is located in the optimal temperature range for Bi_2TE_3 material in the schematic of the temperature distribution of the internal-exhaust-channel configuration, which means this kind arrangement is not suitable for the concentric cylindrical TEG system, or an enhancement for heat transfer is needed.

4.3.7 **Heat Transfer Filling Factor**

In practice, the installation space for TEG system is highly restricted, which means delicate considerations of location and configuration should be taken into account. Especially, there is little room for such an auxiliary system in the existing passenger car platform. On the other hand, the whole TEG system needs to take in

more heat from the exhaust gas in the same area or length for higher recuperation performance. As the various designs of heat recovery system, the area of the heat exchanger in each TEG system are significantly different. In this part of research, different topological design TEG systems from Purdue University is introduced here as a comparison [192, 193]. Provided that TEG systems can be easily scalable, we consider only the ratio of TEM and heat exchanger areas, rather than their absolute values. A new measurable indicator is described, which is the ratio of TEM to heat exchanger areas is named as the heat transfer filling factor: $f = A_{TEM}/A_{Exchanger}$. The heat transfer filling factors of different TEG systems, including the concentric cylindrical TEG system are shown in Table 4-5.

Table 4-5 Heat transfer filling factor of different topological TEG system

Topological	Longitudinal	Transverse	Hexagonal	Cylindrical	Concentric Cylindrical
Filling Factor	0.458	0.43	0.521	0.575	0.655

The heat transfer filling factor is a measurable indicator of the level of space utilisation in installed place. As seen in Table 4-4, the concentric cylindrical TEG system has the highest heat transfer filling factor, which means that, in the same space, more annular TEMs could be installed in the concentric cylindrical TEG system. Practically, the problem of narrow installation space could be solved for TEG system in existing vehicles without deep modifications. This factor can give guidance for further optimal design of TEG systems.

In most situations, the increment of back pressure in the whole exhaust system has an adverse effect on the fuel economy of the vehicle. By introducing the heat

pipes, the concentric cylindrical TEG system has a higher heat transfer filling factor which means it can transport more heat in the same area. This will also help to reduce the complexity of the exhaust system compare to others and result in the decrease of back pressure increment. Furthermore, due to the high heat transfer filling factor, the same amount of coolant can obtain a better cooling effect. This benefit results in reducing the amount of power supply to the water pump, subsequently improving the fuel economy. Another advantage of applying heat pipes is that they may contribute to the obsolete of mufflers as the noise and vibrations in the exhaust can be absorbed in the heat pipe as protruded pin fins.

4.4 **Summary**

In this part of research, the conductive heat transfer within concentric cylindrical TEG system is investigated numerically in two sections. The first section assesses the performance of annular TEM with different thermal boundary condition and the second section investigated the performance of a single annular TE unit with different thermal boundary condition. The 3-D models of annular TEM, square TEM and annular TE unit is established in COMSOL Multiphysics for simulation. These multiphysics models are developed and simulated in multiscale, in which the heat transfer coefficient of the exhaust and the coolant in channels, as well as the heat conduction and electrical conduction in TE materials, are conjugated and resolved to comprehensible levels. The model is based on an analytical solution of the nonlinear heat transport equation for TE, which enable it to take into account the temperature-dependent material properties. The performance of concentric cylindrical TEG system is studied over a full range of operating parameters regarding the heat transfer enhancements at both the cold and hot sources. Moreover,

the simulation result is compared with the results from module-scale experiment and Hi-Z performance calculator. From these results, it can be concluded as follow:

- Due to its larger surface area, the overall performance of annular TEM is better than square TEM under same inward heat flux and temperature on hot side.
- Both TEMs have an optimal performance point, which is a function of inward heat flux.
- Encapsulated heat pipes arrays in the radial direction of the exhaust pipe help to enhance heat effectively from an external fluid stream.
- The features of heat pipes such as temperature flattening, temperature control and thermal diode may help autonomous, maintenance-free operation of TEMs under fluctuating heating sources in the future. The spatial distribution of the temperature rise is considerately responsive by the variation of heating condition from exhaust streams.
- The electric power generation of the annular TE unit strongly depends on the heat transfer enhancement on hot side.
- The proposed universal structure proved to be useful for systematically providing a broad design and operating parameters that can optimise the performance of TEG system and lower its cost.
- Notably, a new index termed as the heat transfer filling factor f has been introduced that quantities the level of space utilisation by TEMs where they are installed. This index can give guidance for further optimisation design of TEG systems.

- The results in this chapter will provide a guide for the numerical simulation of convective heat transfer in the concentric cylindrical TEG system. It can help to simplify the material properties of the sub-domains in the two-dimensional model in Chapter Five. Moreover, the results will be utilized in the one-dimensional model in Chapter Six for calculating the temperature distribution of annular TEM.
- Endurance tests versus performance test is needed in future experiment due to the over limitation of conventional copper-water heat pipes.
- Further studies on optimal design in heat exchanger should be accomplished to improve the convective heat transfer of TEG system.
- In order to investigate the performance under different vehicle driving conditions, more studies for concentric cylindrical TEG system need to be carried out as well. This could help to optimise the concentric cylindrical TEG system to adapt to variable driving conditions of vehicle.

Chapter 5. Experimental and Numerical Investigation for Convective Heat Transfer Enhancement of Concentric Cylindrical TEG System

5.1 Introduction

As mentioned in Chapter Two, the heat exchanger is a crucial component in TEG systems for automotive WHR. According to the Seebeck effect, the electrical power generation is proportional to temperature difference through the TEM, thus higher hot-side temperature for the TEMs leads to higher power generation for the whole TEG system. Generally, to increase efficiency, heat exchangers are designed to maximise the heat transfer area between the two fluids, while minimizing resistance to fluid flow through the exchanger. The exchanger's performance can also be affected by the addition of fins or corrugations in one or both directions, which increase surface area and may channel fluid flow or induce turbulence. Moreover, in practical application, the relatively high velocity of exhaust gas and limited space in the vehicle chassis set high requirements on designing heat exchangers for automotive TEG systems. During the design process, not only the heat transfer enhancement for heat exchangers but also the pressure drop of the whole system need to be taken into consideration. When the exhaust gas flows through TEG system, it will boost exhaust backpressure and reduce engine efficiency, which is undesirable in terms of fuel economy. Therefore, an effective design of the heat exchanger for automotive TEG system is an important precondition for the large-scale industrial application of automotive TEG system.

Much research has been conducted on the optimisation of heat exchangers for automotive TEG system, in the past few years. Researchers invest a lot of enthusiasm in improving the convective heat transfer while diminishing the pressure drop of heat exchangers for automotive TEG system. It is worth noting that there are several novel designs for heat exchangers and different methods for heat transfer enhancement have been presented in the past decades from different research institutes. Kumar et al. [192] proposed a comprehensive numerical model of a TEG system for automotive WHR and the topological parameters of heat exchanger are evaluated. Results showed all topologies behave somewhat similarly at lower numbers of TEMs in terms of electrical generation, but the performance of the hexagonal topologies suffers when the number of TEMs exceeds 40 owing to large pressure drops. The cylindrical design outperforms other designs in terms of power generation for a given volume and number of TEMs. Liu et al. [146, 194] numerically and experimentally studied the thermal performance of heat exchangers with different internal structures and thickness in automotive TEG. Results showed that a plate-shaped heat exchanger with chaos-shaped internal structure and thickness of 5 mm achieves a relatively ideal thermal performance. Moreover, a maximum power of 944 W was obtained on the revolving drum test. Wang et al. [128] presented a heat exchanger containing cylindrical grooves on the interior surface. Results showed the cylindrical grooves could enhance heat transfer and turbulence intensity, meanwhile there was no additional back pressure for engine. Compared to other structures, heat exchanger with cylindrical grooves could improve the TEG efficiency at low engine speed. Lu et al. [195] explore the feasibility of combining the exhaust heat exchanger with the muffler. The results

demonstrated the symmetrical 1-inlet and 2-outlet structure increased hydraulic disturbance and enhances heat transfer, resulting in the more uniform flow distribution and higher face temperature than the 2-inlet and 2-outlet and empty cavity. He et al. [196] established a complete numerical TEG system model, including the fluid heat transfer and flow resistance characteristics. The results showed in order to obtain the maximum net power with fluid flow resistance, the optimal cross section area should be 0.0056 m^2, with the optimal scales at a height of 0.005 m, and length of 0.56 m.

In order to achieve the purpose of high convective heat transfer coefficient and low pressure drop for the heat changer of concentric cylindrical TEG system, a heat pipe combined cascading structure is employed. As aforementioned, heat pipes are ultra-effective devices that combine the principles of both thermal conductivity and phase transition to transfer heat between two interfaces. Their effective thermal conductivity can range from 10 to 10000 times (4000 W/m·K to 40000000 W/m·K) the effective thermal conductivity of copper, depending on the length of the heat pipe. With this extremely high effective thermal conductivity, there is almost no temperature difference between hot and cold side of heat pipes, which means the hot-side temperature of TEM approximately equals to the local temperature of exhaust gas. This could significantly enhance the heat transfer efficiency of the heat exchanger. Moreover, due to the utilisation of cascading structure, it not only economizes the space in exhaust system but also reduces the exhaust backpressure in the engine.

In this part of research, following the investigation of conductive heat transfer within the concentric cylindrical TEG system in previous chapter, the mechanism

of convective heat transfer within the concentric cylindrical TEG system is experimentally and numerically investigated in this chapter. In the following content, the experimental test section and numerical model are presented first. Thereafter, the experimental results for normal heat exchanger and simulation results for structure-optimized heat exchanger are exhibited and discussed as well.

5.2 Test Section and Numerical Model Description

5.2.1 Experimental Test Section

In this experimental investigation, the square TEM is employed instead of annular TEM due to the difficulty in manufacturing. As shown in Figure 5-1, the annular TE unit of concentric cylindrical TEG system can be divided into approximately six segments and each segment of annular TEM equals to the square TEM employed in this experiment. Therefore, the experimental investigation for concentric cylindrical TEG system is carried out in the square TEM based test rig. Because the details of the test rig was introduced in Chapter Three, the following part will present the arrangement of test section in the test rig.

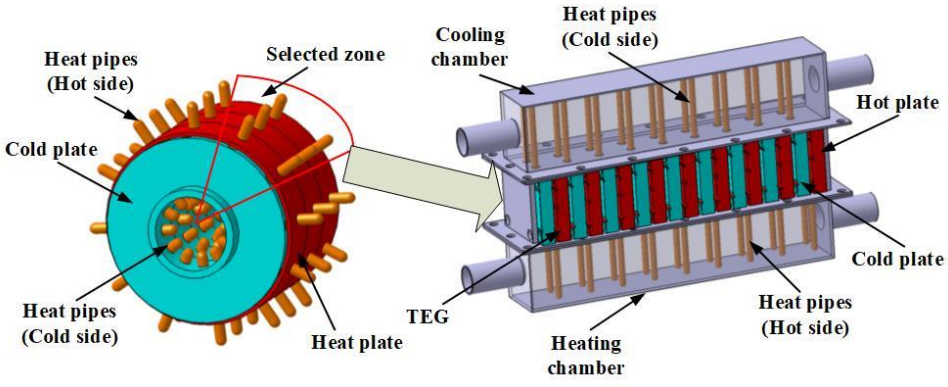


Figure 5-1 Schematic of experimental selection in concentric cylindrical TEG system

The novel cascading structured heat exchanger includes three parts: cooling part, heating part and TEM array. As shown in Figure 5-2, the cooling part of this test section contains a container for coolant in which the water could flow through this container from inlet to outlet for carrying away the heat of TEMs by heat pipes attached on cold side. Similarly, the heating part is a container for hot air in which the hot air could flow through for supplying the heat to those TEMs via the heat pipes on hot side. The TEM array is the core component in this test section where seventeen TEMs are settled in series with cooling plates and heating plates, which are made of aluminium. One TEM is sandwiched between one cooling plate and the heating plate to form a basic unit of this test section. In this experiment, there are seventeen basic units, which are stacked together and form a column as TEM array. Each cooling plate or heating plate has two heat pipes, which are inserted into the plate for absorbing or discharging the heat for TEM.

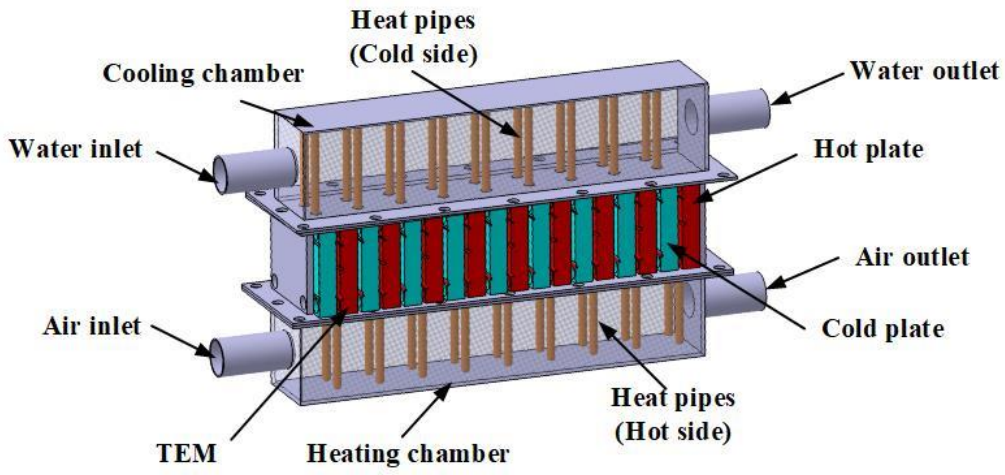


Figure 5-2 Schematic for test section

In the experiment, the thermocouples are arranged in a specified cooling plate and heating plate in order to obtain the temperature of different TEMs, as shown in

Figure 5-3. In a specified basic unit, there are two thermocouples which are utilised to measure the hot-side and cold-side temperatures of TEM. The temperature of five specified basic units are measured by thermocouples which are 1st, 5th, 9th, 13th, and 17th. The cold-side temperature are indicated respectively by T_1, T_3, T_5, T_7, and T_9 and the hot-side temperature are indicated respectively by T_2, T_4, T_6, T_8, and T_{10} in the experimental results. In order to investigate the flow arrangement effect and change the flow direction, the two flange connections are utilised to the hot air container, and hoses are utilised to the coolant container.

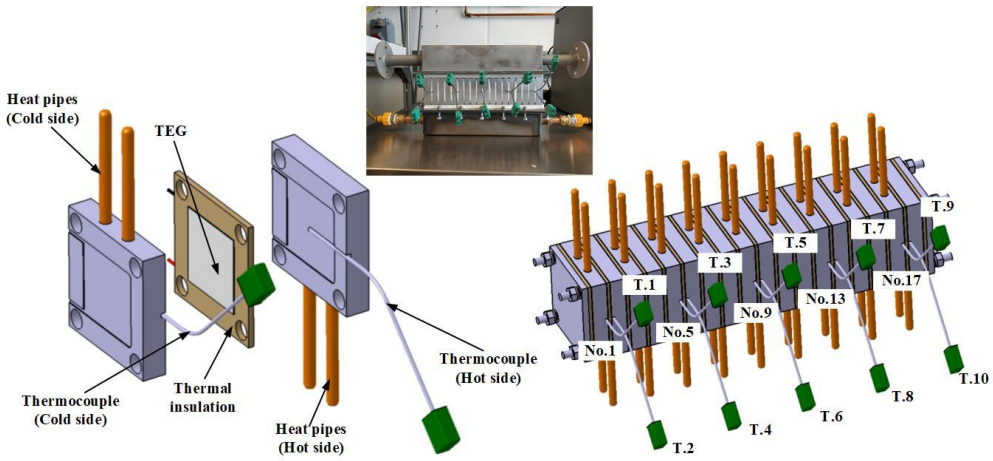


Figure 5-3 Arrangement of thermocouples in test section

During the experimental test, the effects of flow arrangement within the test section is investigated as well. Normally, there are three primary classifications of heat exchangers according to their flow arrangement: parallel-flow, counter-flow and cross-flow. In parallel-flow heat exchangers, the two fluids enter the exchanger at the same end, and travel in parallel to one another to the other side. In counter-flow heat exchangers the fluids enter the exchanger from opposite ends. In a cross-flow heat exchanger, the fluids travel roughly perpendicular to one another through the exchanger. In this part of experimental test, only parallel-flow and counter-flow

arrangements are investigated, as the cross-flow is not possible to be arranged under the vehicle chassis.

Furthermore, as the cascading structured heat exchanger combined with heat pipes, the gravitational effect on heat pipes is an important influencing factor for the heat transfer performance of this heat exchanger, according to the references [197, 198]. Figure 5-4 shows the different arrangement of test section for investigating the gravitational effect on heat pipes within this heat exchanger. The arrangement of gravitational effect is according to the hot-side heat pipes, because the hot-side heat pipes absorb the heat from exhaust gas and play the key role in this heat exchanger.

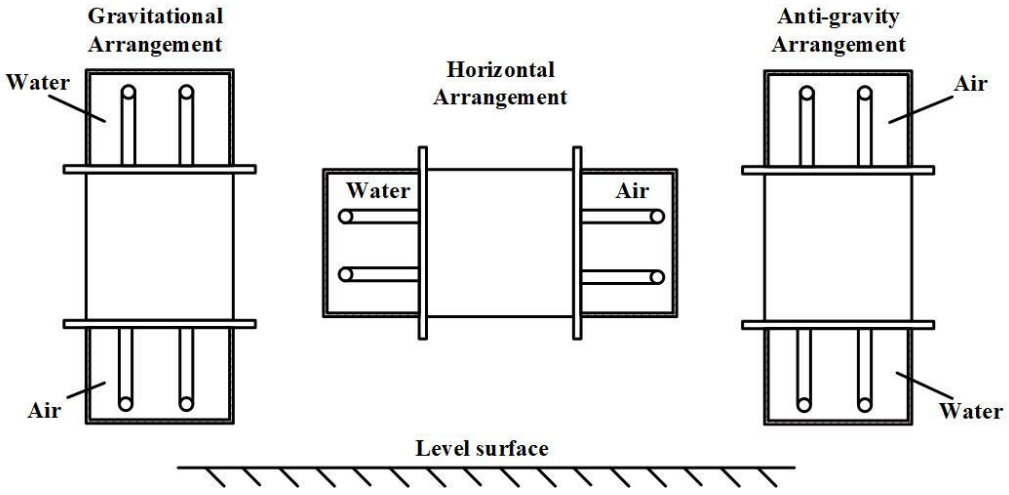


Figure 5-4 Schematic for flow arrangement in experiment test

In order to investigate the influence of air flow rate and water flow rate on the power generation performance of this cascading heat exchanger, the air flow rate and water flow rate are set as various values during the whole test. The air flow rate is controlled by altering the frequency of the two blowers , the frequency is set at 30 Hz, 35 Hz, 40 Hz, 45 Hz, 50 Hz, 55 Hz, 60 Hz, 65 Hz, 70 Hz, and 75 Hz,

respectively. As shown in Figure 5-5, the corresponding air flow rate is changing with the frequency of two blowers. The water flow is respectively set at 3 L/min, 4 L/min, 5 L/min, 6 L/min, 7 L/min, and 9 L/min by controlling the water pump in the test rig.

Due to the limitation of the air and water flow rate meter, the maximum heating temperature of the heater is set at 200 ℃ and the maximum flow rate of water is 9 L/min, during the experimental test. This is not sufficient for simulating the engine exhaust gas at practical driving condition. Therefore, a numerical simulation is essential to investigate the performance of concentric cylindrical TEG system in real-time driving condition.

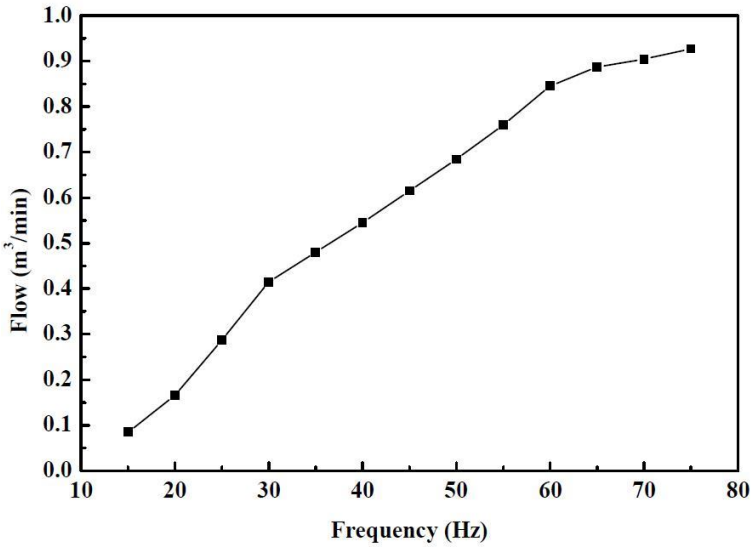


Figure 5-5 Corresponding air flow rate with blower frequency

5.2.2 **Numerical Model Description**

In addition to the experimental investigation of convective heat transfer of concentric cylindrical TEG system, the heat transfer enhancement for concentric cylindrical TEG system by utilising various fins and different heat pipe length are

investigated numerically. By introducing various type of fins, it can enhance exhaust flow and generate more turbulence to force the exhaust gas flowing into the space between heat pipes. Furthermore, the length of heat pipes is another crucial factor for the convective heat transfer in concentric cylindrical TEG system. If all the heat pipes is of the same length, the upstream heat pipes would block the downstream heat pipes within the exhaust pipe, thus hindering their heat transfer with exhaust gas.

In this part of research, for the purpose of studying the influences of fins and heat pipe length on convective heat transfer of concentric cylindrical TEG system, four different type of two-dimensional simulation models are established in COMSOL Multiphysics. As shown in Figure 5-6, there are three models with different angled fins and one model with different heat pipe length and the three different angles are 30°, 45° and 60°, respectively. In order to validate the reliability of the model, a model using the same dimension of test section is established as well to compare the simulation results to the experiment-test results. Moreover, all the dimensions applied in the numerical model are the same as the cross section of test section shown in Figure 5-7. Compared to experiment test section, the inlet and outlet channel extends 20d distance from the main model in order to avoid reversed flow from ambient environment. During the simulation, all the initial values of inlet flow rate and temperature are set according to the engine speed and exhaust gas temperature, in order to simulate the performance of concentric cylindrical TEG system in practical application.

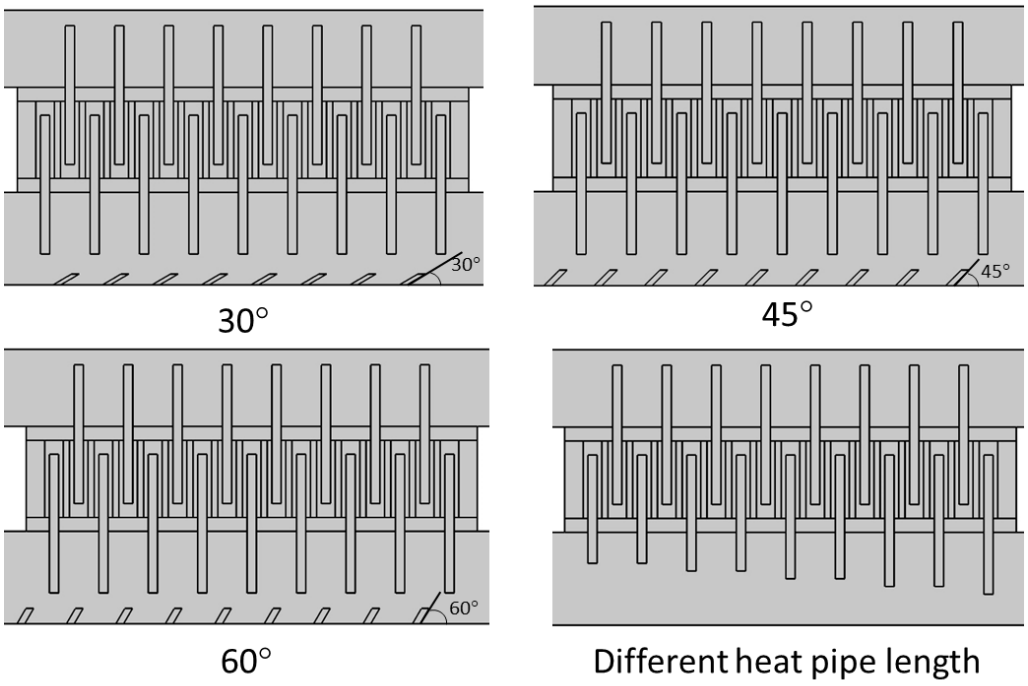


Figure 5-6 Four simulation models with different angled fins and heat pipe length

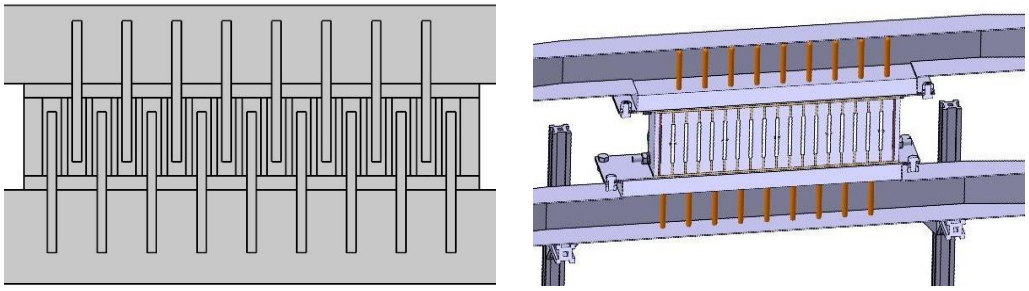


Figure 5-7 Verified simulation model & experimental test section

5.2.3 Governing Equation in Conjugated Heat Transfer

A complete mathematical description of convective heat transfer problems including differential equations and definite solutions is provided here. In this chapter, as mentioned in previous part, the model for simulating the cross section of the heat exchanger is two-dimensional. Therefore, for a two-dimensional convective heat transfer problem, which is incompressible, constant physical

properties and no internal heat source, the governing equations for the flow and heat transfer in this study can be expressed as follows [177]:

- Continuity equation

Increment of mass in the control volume during a certain time interval = net mass flowing into the micro-body at the same time:

$$\frac{\partial u}{\partial x}+\frac{\partial v}{\partial y}=0 \qquad \text{Eq.5-1}$$

- Momentum equation

Increase rate of momentum in the control volume = sum of the forces acting upon the micro-body:

$$\rho\left(\frac{\partial u}{\partial \tau}+u\frac{\partial u}{\partial x}+v\frac{\partial u}{\partial y}\right)=F_x-\frac{\partial p}{\partial x}+\eta\left(\frac{\partial^2 u}{\partial x^2}+\frac{\partial^2 u}{\partial y^2}\right) \qquad \text{Eq.5-2}$$

$$\rho\left(\frac{\partial v}{\partial \tau}+u\frac{\partial v}{\partial x}+v\frac{\partial v}{\partial y}\right)=F_y-\frac{\partial p}{\partial y}+\eta\left(\frac{\partial^2 v}{\partial x^2}+\frac{\partial^2 v}{\partial y^2}\right) \qquad \text{Eq.5-3}$$

These two equations are also known as Navier-Stokes equations (N-S equations)

- Energy equation

Increase rate of thermodynamic energy in the control volume = net heat flux into the control volume + body force and surface force acted upon the control volume:

$$\frac{\partial t}{\partial \tau}+u\frac{\partial t}{\partial x}+v\frac{\partial t}{\partial y}=\frac{\lambda}{\rho c_p}\left(\frac{\partial^2 t}{\partial x^2}+\frac{\partial^2 t}{\partial y^2}\right) \qquad \text{Eq.5-4}$$

From equation 5-1 to equation 5-4, there are four variables (u, v, p, t) and four equations and this equation system is closed-form expression and can be solved, in principle. However, due to the complexity and nonlinearity of N-S equations, it is extremely difficult to solve the above equation system for practical problems. As a

result, there are different models for solving this convective heat transfer problem by simplifying N-S equations.

As per the review of internal finned heat exchanger simulations [199-202], the realizable k-ε model is commonly recommended to simulate the coupling between heat transfer and fluid flow within the internal finned heat exchanger. It couples the heat transfer and flow interfaces and provides options to include flow heating in the model. Turbulence effects are modelled using the standard two-equation k-ε model with realizable constraints. Flow close to walls is modelled using wall functions. A fluid model is active by default on all the interface selection. The heat transfer in solids interface provides features for modeling heat transfer by conduction and convection. Its selection should be modified to match the domain selection used for the flow interface. A solid model is active by default on the non-fluid domains.

According to the Ref [174], the non-isothermal flow and conjugate heat transfer interfaces contain the fully compressible formulation of the continuity and momentum equations:

$$\frac{\partial \rho}{\partial t} + \nabla \cdot (\rho u) = 0 \qquad \text{Eq.5-5}$$

$$\rho \frac{\partial u}{\partial t} + \rho u \cdot \nabla u = -\nabla p + \nabla \cdot \tau + F \qquad \text{Eq.5-6}$$

It also solves the heat equation, which for a fluid is given in Eq. 5-4 by:

$$\rho C_p \left(\frac{\partial T}{\partial t} + u \cdot \nabla T\right) + \nabla \cdot (q + q_r) = \alpha_p T \left(\frac{\partial p}{\partial t} + u \cdot \nabla p\right) + \tau : \nabla u + Q$$

Eq.5-7

where term $\alpha_p T\left(\frac{\partial p}{\partial t} + u \cdot \nabla p\right)$ is the work done by pressure changes, term $\tau : \nabla u$ is the viscous heating and term Q is the heat sources other than viscous heating, respectively.

The physics interface also supports heat transfer in solids can be expressed as:

$$\rho C_p \left(\frac{\partial T}{\partial t} + u_{trans} \cdot \nabla T\right) + \nabla \cdot (q + q_r) = Q \qquad \text{Eq.5-8}$$

The forced convection regime corresponds to configurations where the flow is driven by external phenomena or devices that dominate buoyancy effects. In this case the flow regime can be characterized, similarly to isothermal flow, using the Reynolds number, Re, as an indicator. The Reynolds number represents the ratio of inertial forces to viscous forces. At low Reynolds numbers, viscous forces dominate and laminar flow is observed. At high Reynolds numbers, the damping in the system is very low, giving small disturbances. If the Reynolds number is high enough, the flow field eventually ends up in turbulent regime. The momentum boundary layer thickness can be evaluated, using the Reynolds number, by δ_M.

$$\delta_M = \frac{L}{\sqrt{Re}} \qquad \text{Eq.5-9}$$

In this part of simulation, the Reynolds number of each case is larger than 10000, thus all the cases are conjugate heat transfer problems. Therefore, the temperature equation solved in the turbulent non-isothermal flow and conjugate heat transfer interfaces can be expressed as:

$$\rho C_p \frac{\partial T}{\partial t} + \rho C_p u_j \frac{\partial T}{\partial x_j} + \frac{\partial}{\partial x_j}\left(-(\lambda + \lambda_T)\frac{\partial T}{\partial x_j}\right) = -\frac{1}{\rho}\left(\frac{\partial \rho}{\partial T}\right)_p T\left(\frac{\partial p}{\partial t} + u_j \frac{\partial p}{\partial x_j}\right) + \tau_{ij}\frac{\partial u_i}{\partial x_j}$$

Eq.5-10

The turbulent conductivity is defined by the method provided by Kays-Crawford [203], it is compared to other models for Prandtl number *Pr* and found to be a good approximation for most kinds of turbulent wall bounded flows, except for turbulent flow of liquid metals. The model is given by:

$$Pr = \left(\frac{1}{2Pr_{T\infty}} + \frac{0.3C_p\mu_T}{\lambda\sqrt{Pr_{T\infty}}} - \left(\frac{0.3C_p\mu_T}{\lambda}\right)^2 \left(1 - exp\left(-\frac{\lambda}{0.3C_p\mu_T\sqrt{Pr_{T\infty}}}\right)\right)\right)^{-1} \quad \text{Eq.5-11}$$

where the Prandtl number at T_d is $Pr_{T\infty}$= 0.85 and λ is the conductivity.

The heat flux between the fluid with temperature T_f and a wall with temperature T_w, is:

$$q_{wf} = \frac{\rho C_p C_u^{1/4} k^{1/2}(T_w - T_f)}{T`} \quad \text{Eq.5-12}$$

Moreover, as illustrated in Figure 5-8, the simulation result from realizable k-ε model is compared to experimental data. It can be observed that the hot-side and cold-side temperatures of each TEM show a great agreement between realizable k-ε model and experimental data, especially at the inlet and out let of the heat exchanger, and only the TEMs, located in the middle of the array have minor discrepancy in the results. The average hot-side temperatures for simulation and experiment are 68.11 ℃ and 69.72 ℃; moreover, the average cold-side temperatures for simulation and experiment are 32.51 ℃ and 32.98 ℃, respectively. The average discrepancy of hot-side and cold-side temperatures of each TEM are 2.3 % and 1.4 %, which are within the confidence level of simulation.

From the analysis above, the realizable k-ε model with enhanced wall treatment has decent overall accuracy and acceptable agreement with experimental results for

current study. Therefore, realizable k-ε model with enhanced wall treatment is adopted for following studies.

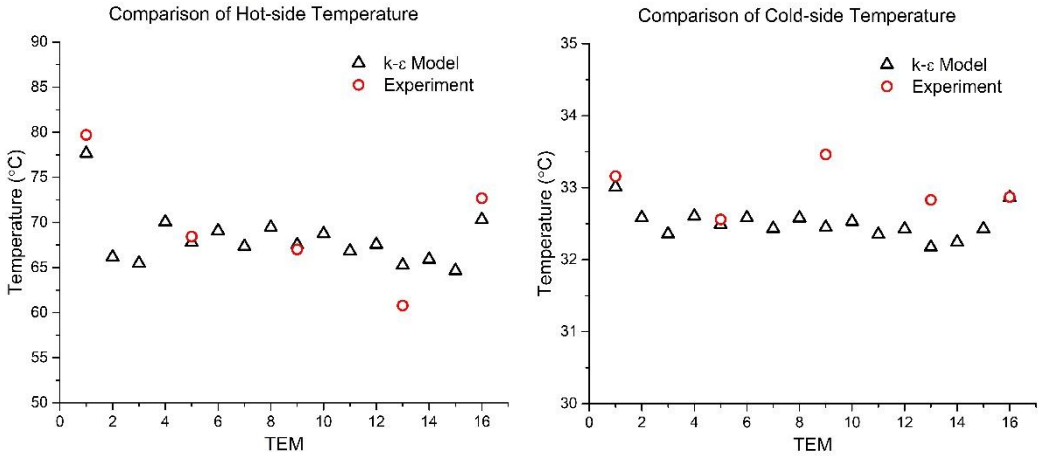


Figure 5-8 Results comparison between realizable k-ε model and experimental data

As it can be seen in the figures, there is an obvious temperature drop and rise at the second and the last heat pipe both in experimental results and simulation results and the reasons for this phenomenon can be concluded as follow. First, the cross-sectional area at the outlet of both exhaust gas and water have a sudden change and the areas are almost half of the cross-sectional area of the heating and cooling chamber. This significant change in the cross-sectional area would cause the reflow and stagnation of the exhaust gas and coolant. This means the heat energy would be stacked at the outlet of the heating chamber and force the temperature of the down-stream heat pipe to rise. As for the cooling side, the stagnation of coolant would reduce the heat transfer capacity of the coolant and cause the temperature increment at the hot side as well. From the aspect of the experimental setup, the heat pipes and thermocouples at the rear of the test section are too closed to the outlet of the heating and cooling chamber, which would intensify the temperature deviation in the results of experimental test. In addition, the heat pipes were located

at the radial tangential direction of the inlets and outlets of the cooling and heating chamber, which could cause the insufficient convective heat transfer in the middle of the section. Therefore, the phenomenon will be exacerbated. During the numerical simulation, in order to simplify the simulation process, a two-dimensional model was employed, which do not have sufficient simulation for the scavenging of exhaust gas around the heat pipes. Moreover, the results in the simulation results are the average temperature, which is not like the temperature at a certain point in experimental results. These two reasons would cause the temperature discrepancy between the experimental and simulation results. Furthermore, with the increment of engine speed, the mass flow rate of exhaust would be increased, which could cause a further stagnation of the exhaust gas and intensify this phenomenon, as shown in the following figures of the simulation results. Although the accuracy of the results in experiment and simulation needs to be improved in the future works, the results in these two methods show good compatibility, which can reflect the overall temperature distribution in the concentric cylindrical TEG system and can provide a reference for future optimization of TEG system.

5.3 **Results and Discussion**

5.3.1 **Uncertainty Analysis**

The uncertainty regarding the experimental results in this part of research rest upon the measured parameters such as temperature, air flow rate and water flow rate. The measurement biases of temperature, air flow rate and water flow rate are

within ± 1.5 ℃, 1 % and 3 %, respectively. Moreover, the ambient temperature during the experiment test would also affect the experimental results. Because the test rig is located in an enclosed room, the ambient temperature would increase by 1 ℃ during the whole test. Some of the results presented below are in the form of dimensionless parameters unless specified, i.e., Reynolds number, Re. The uncertainty analysis with a 95% confidence level on the measured parameters using the method described by Moffat [204]. If R was a function of several independent variables, v_i, each with their own uncertainties, δv_i, the overall uncertainty W_R in R was calculated as

$$w_R = \sqrt{\sum_{i=1}^{n} \left(\frac{\delta R}{\delta v_i}\right)^2 (\delta v_i)^2} \qquad \text{Eq.5-13}$$

In the experimental test, the uncertainties of the hot-side temperature and cold-side side temperature were ± 2.3 % and ± 3.64 %, respectively. The uncertainty of Reynolds number was ± 2.51 %. In addition, the uncertainty of temperature difference is ± 4.31 %.

5.3.2 **Experimental Results**

In order to verify the concept of heat pipe combined cascading structured heat exchanger, a series of experimental tests have been carried out in this part of research. In the following content, the results of experimental tests are presented and discussed.

5.3.2.1 Influence of Air Flow Rate

First, the influence of air flow rate is investigated with the inlet air temperature and water flow rate set at constant 200 ℃ and 9 L/min respectively. Additionally,

the flow arrangement and heat pipe arrangement are parallel flow and gravitational arrangement. The influence of air flow rate on the hot-side temperature and temperature difference of TEMs is presented in Figure 5-9. As shown in the figure, the hot-side temperature and temperature difference of the first TEM in this array is the highest and with the hot air flows, the hot-side temperature and temperature difference of downstream TEMs decreases gradually. However, there is a significant increase in hot-side temperature and temperature difference of TEMs close to the outlet. This is due to the sudden change in diameter at the outlet, which would generate more turbulence for improving convective heat transfer. In addition, the pressure change between the container and outlet pipe driving some hot air flow back into the container to bring a secondary heating for the rear heat pipes. Moreover, with the increment of air flow rate, the hot-side temperature and temperature difference of each TEM is promoted in general. However, the growth rate of hot-side temperature and temperature difference abates with an increasing air flow rate. Compared to the hot-side temperature, the temperature difference at the middle of TEM array has more disparity, which is caused by the increment of cold-side temperature. The coolant is warmed by heat from the hot air though heat pipes and TEMs. Therefore, it has a slight growth in temperature between inlet and outlet of the coolant container.

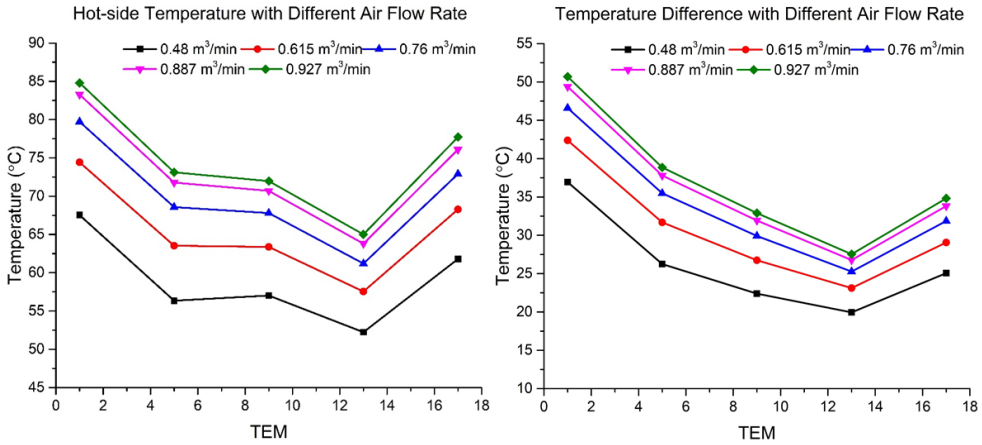


Figure 5-9 Temperature distribution with different air flow rate

5.3.2.2 Influence of Water Flow Rate

The influence of water flow rate is investigated subsequently with the inlet air temperature and air flow rate set at constant 200 ℃ and 0.927 m^3/min respectively. Besides, the flow arrangement and heat pipe arrangement is the same with previous experiment. Figure 5-10 shows the hot-side temperature and temperature difference of TEMs under different water flow rate. It is can be observed that the pattern of each curve is the same with the result of previous experiment, which is a decrement at upstream TEMs and an increment at downstream TEMs. The difference is that, with the increment of water flow rate, the hot-side temperature decreases but the temperature difference increases. However, as shown in the figures, the influence of water flow rate on hot-side temperature and temperature difference of TEMs could barely been observed and the temperature difference of TEMs remains almost the same with different water flow rate.

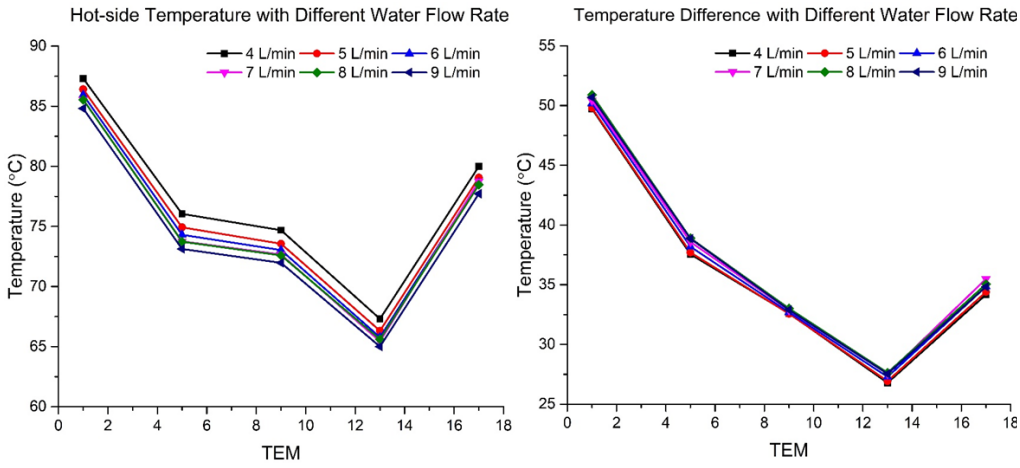


Figure 5-10 Temperature distribution with different water flow rate

There are several reasons for this phenomenon. Firstly, the hot-side temperature of TEMs is determined by the convective heat transfer in hot side of this heat exchanger instead of that in cold side. Therefore, the increment of hot air flow rate has greater impact than that of water flowrate. Moreover, the convective heat transfer coefficient at cooling side is much higher than that at heating side. As a result, the variation in water flow rate would have slight impact on the temperature at cold side of TEMs when the heat transfer coefficient is extremely high compared to the heating side, and the hot-side temperature of TEMs would not have massive change. Furthermore, because the heat capacity of water is higher than that of air, the water flow rate would not have abundant effect on the convective heat transfer coefficient on cooling side. Therefore, the water flow rate is not the main influencing factor on the heat transfer between the heat pipes and the coolant.

With the analysis above, the flow rate of air is a more critical factor, compared to that of water. Therefore, during the design process, the heat transfer enhancement on heating side need more consideration.

5.3.2.3 Influence of Flow Arrangement

In addition to the influence of air and water flow rate, the influence of flow arrangement for water and air is investigated experimentally as well. The experiment is carried out under constant inlet air temperature and water flow rate at 200 ℃ and 9 L/min respectively, as well as, the heat pipe arrangement is gravitational arrangement.

Figure 5-11 shows the average hot-side temperature and temperature difference of TEMs under different air flow rate with parallel flow and counter flow arrangement. As shown in the figure, in general, the counter flow arrangement achieve a better hot-side temperature and temperature difference than parallel flow arrangement. Moreover, with the increment of air flow rate, the improvement on temperature difference becomes larger.

The results mean that the counter flow arrangement is more efficient, in that it can transfer more heat because the average temperature difference along any unit length is higher. According to the investigation from Ramesh [205] and Kuppan [206], the counter flow arrangement has three significant advantages over the parallel flow arrangement. First, the more uniform temperature difference between the two fluids minimizes the thermal stresses throughout the exchanger. Second, the outlet temperature of the cold fluid can approach the inlet temperature (highest) of the hot fluid. Third, the more uniform temperature difference produces a more uniform rate of heat transfer throughout the heat exchanger. In contrast, the parallel flow arrangement is advantageous when two fluids are required to be brought to nearly the same temperature [207].

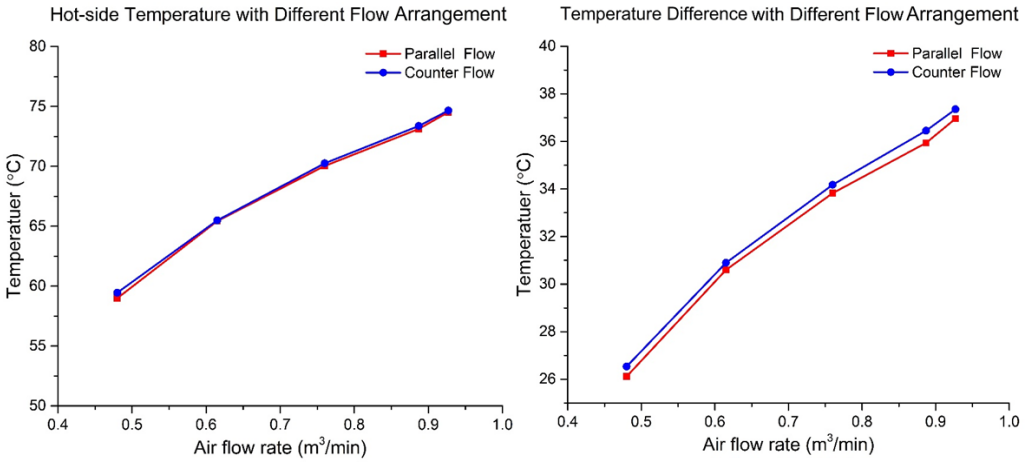


Figure 5-11 Average temperature distribution with different flow arrangement

5.3.2.4 Influence of Heat Pipe Arrangement

Besides all the investigation above, the influence of gravity in heat pipes is inspected as mentioned in the previous part. The experiment is conducted under constant inlet air temperature and water flow rate at 200 ℃ and 9 L/min respectively, as well as, the parallel flow arrangement.

Figure 5-12 shows the average hot-side temperature and temperature difference of TEMs under different air flow rate with gravitational, horizontal and anti-gravity arrangement of heat pipes. Because the arrangement is determined by the gravity effect upon heat pipes on the heating side, the heat pipes in cooling side have the opposite effect of gravity. As shown in the figure, the anti-gravity arrangement has the highest hot-side temperature and temperature difference among all three arrangements, while the horizontal arrangement is lowest.

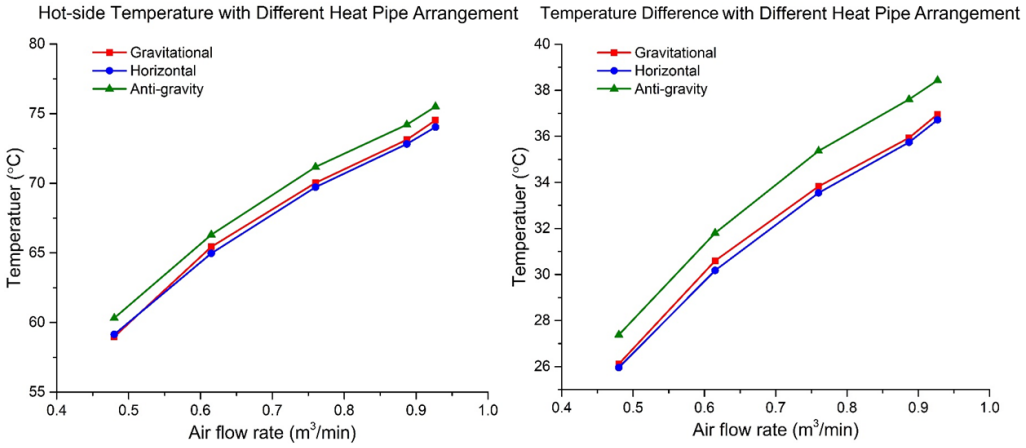


Figure 5-12 Average temperature distribution with different heat pipe arrangement

By compared these three arrangements, the anti-gravity arrangement has better performance than other arrangements, which is not in accordance with theoretical analysis. According to the research of effects of gravity on the performance of heat pipes, the increasing gravity assistance decreases the temperature between evaporator and condenser, which is always a desirable feature. However, the results in this experimental test showed above is different. The reasons for this variation may be explained as follow. Firstly, the heat pipes on the cooling side are subjected to gravity and have more heat transfer capacity. In addition, the convective heat transfer on cooling side is better than that on heating side, Therefore, it can also increase the temperature difference through TEMs. Furthermore, when the heat pipes on heating side is under anti-gravity arrangement, the hot air temperature would not drop as quickly as gravitational arrangement. This would also be helpful for obtaining a higher hot-side temperature.

The horizontal arrangement has the worst performance, because neither the heat pips on the heating side nor the heat pipes on cooling side are subjected to gravity, and they transfer the working liquid by capillary force solely.

5.3.3 **Lumped Parameters Method**

As aforementioned in Chapter Three, during a convective heat transfer process, some objects behave as a "lump" whose interior temperature remains essentially uniform, if the temperature distribution of a solid object is irrelevant to the location within the solid object. In this situation, the lumped parameters method could be the most effective method for analysing this convective heat transfer process and determining temperature distribution within the system. Normally, this solid object is extremely small in dimension or has extremely high thermal conductivity. Coincidentally, the heat pipes utilised in the heat exchanger of concentric cylindrical TEG system has an extremely high effective thermal conductivity, which ranges 10 to 10000 times the effective thermal conductivity of copper. Therefore, in this numerical investigation the lumped parameters method is employed for accelerating the simulation procedure and curtailing the calculation time. During the numerical simulation, the spatial thermal conduction inside heat pipes is neglected, which means the conductive heat transfer in the radial direction of heat pipe is ignored.

However, there is a criterion for utilising lumped parameter analysis, which is the dimensionless parameter Biot number, *Bi*, given as a ratio of conductive thermal resistance to convective thermal resistance, as mentioned in Equation 3-33. Usually, the acceptable criteria value of the Biot number for utilising lumped parameter method is less than 0.1. In this numerical simulation, the highest convective heat transfer coefficient and thermal conductivity of heat pipe is 1200 $W/m^2 \cdot K$ and 4000 $W/m \cdot K$, respectively. In addition, the diameter of heat pipe is 6 mm and the characteristic length for a cylindrical heat pipe is r/2, which is half diameter of the

heat pipe. As a result, the highest value of *Bi* in this numerical simulation is 0.0009 which far more less than the criteria value. Therefore, the lumped parameter method is valid throughout the whole calculation process.

5.3.4 **Simulation Results Presentation**

In this part, in order to simulate the performance of the heat pipe combined cascading structured heat exchanger for concentric cylindrical TEG system, the numerical simulation is carried out according to the real data of an internal combustion engine (ICE). The exhaust temperature varies from 300 ℃ to 800 ℃ and the engine speed ranges from 1000 rpm to 6000 rpm and the corresponding air flow rate is calculated by the following equation:

$$V_{air} = \rho \frac{nV_C}{4N_c} \qquad \text{Eq.5-14}$$

where V_c is engine capacity, N_c is number of engine cylinders, n is engine speed and $\rho$is density of exhaust gas, respectively.

In this part of the simulation, the lumped parameter analysis method is employed to simplify the model of the heat pipe. By utilizing the lumped parameter analysis the complex physical process within the heat pipe can be ignored. As a result, the axial thermal conductivity of the heat pipes can be set as a constant value. In the perspective of heating and cooling plates, they are made of copper which has low thermal resistance and the thickness is thin. Therefore, to some extent, the lumped parameter analysis is also feasible in the whole body during the simulation.

The detailed results of simulation for five different types of heat exchanger are presented in the following content. In order to compare the effect of air flow rate and temperature, the results are present in the form of hot-side temperature and

temperature difference of TEMs with different engine speed and exhaust gas temperature. Moreover, the contours of temperature difference, pressure drop and Reynold Number are presented for intuitive analysis of the performance of different heat exchangers.

5.3.4.1 Simulation Results of Heat Exchanger without Fins

Figure 5-13 shows the hot-side temperature and temperature difference of TEMs with different engine speed and exhaust gas temperature for heat exchanger without fins. As shown in the figures, the curves of hot-side temperature and temperature difference are approximately in the same pattern with experimental results, but have higher values due to experimental test could not provide high temperature and air flow rate. However, the hot-side temperature and temperature difference of the last TEM is higher than the first TEM in the array.

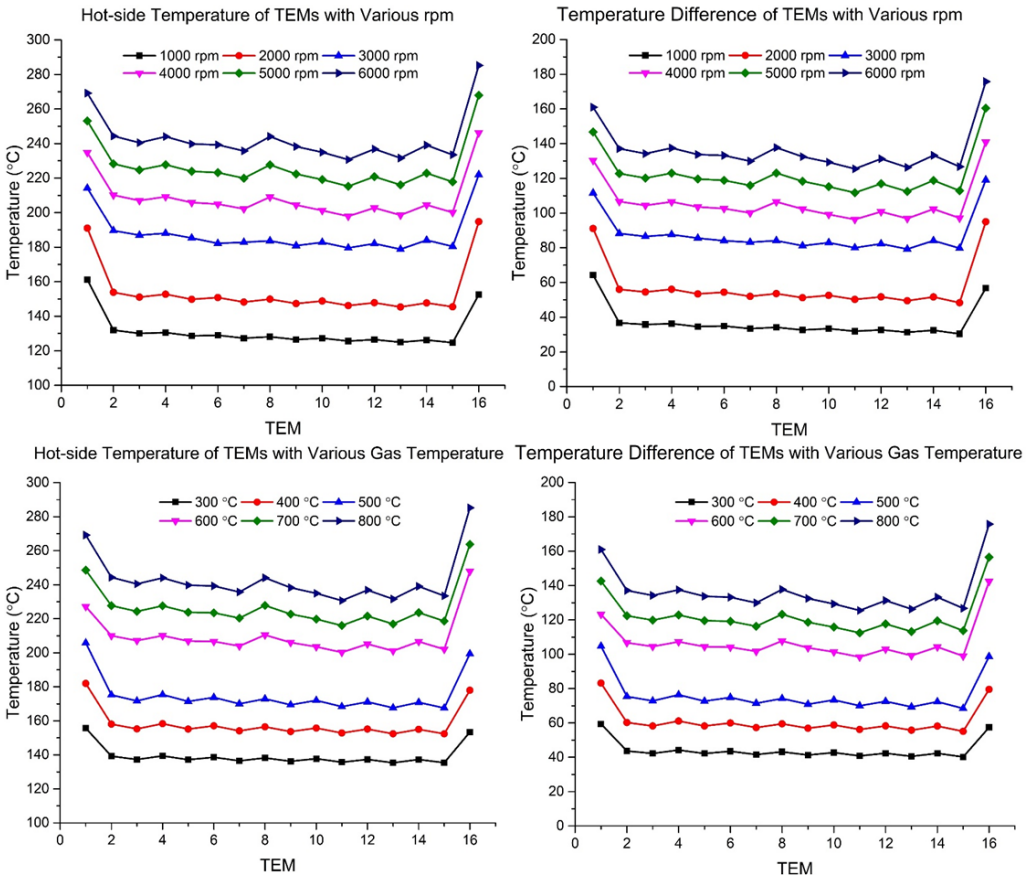


Figure 5-13 Temperature distribution of heat exchanger without fins

In general, the hot-side temperature and temperature difference of TEMs increase with the increment of engine speed and exhaust gas temperature. Nevertheless, with the increment of engine speed and exhaust gas temperature, the fluctuation in the middle TEMs becomes significant. Figure 5-14 to Figure 5-16 show the contours of temperature difference, pressure drop and Reynold Number of heat exchanger without fins. As shown in the figures, the highest temperature difference appears at high engine speed and exhaust temperature, the highest pressure drop appears at high engine speed and low exhaust temperature and the highest Reynold Number appears at high engine speed and low exhaust temperature, respectively.

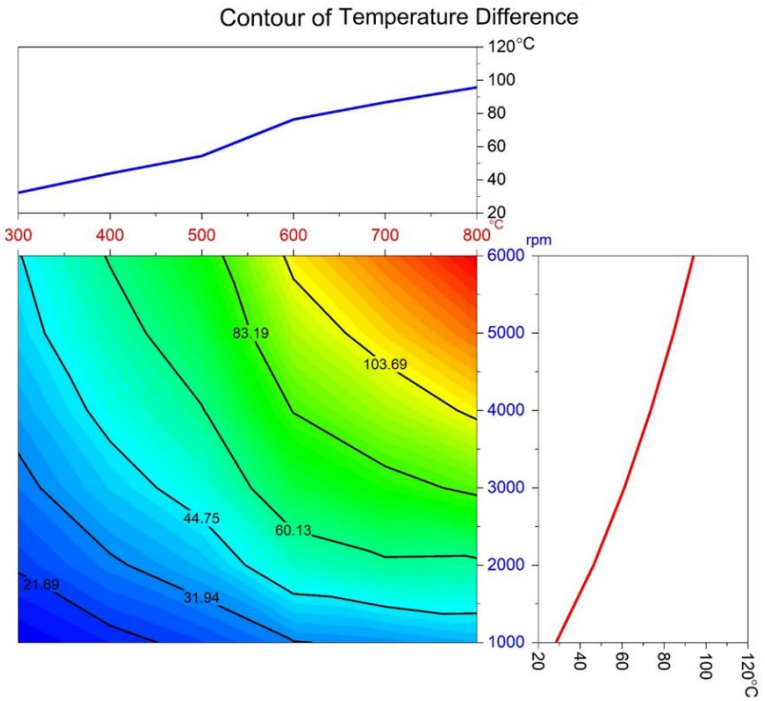


Figure 5-14 Temperature difference contour of heat exchanger without fins

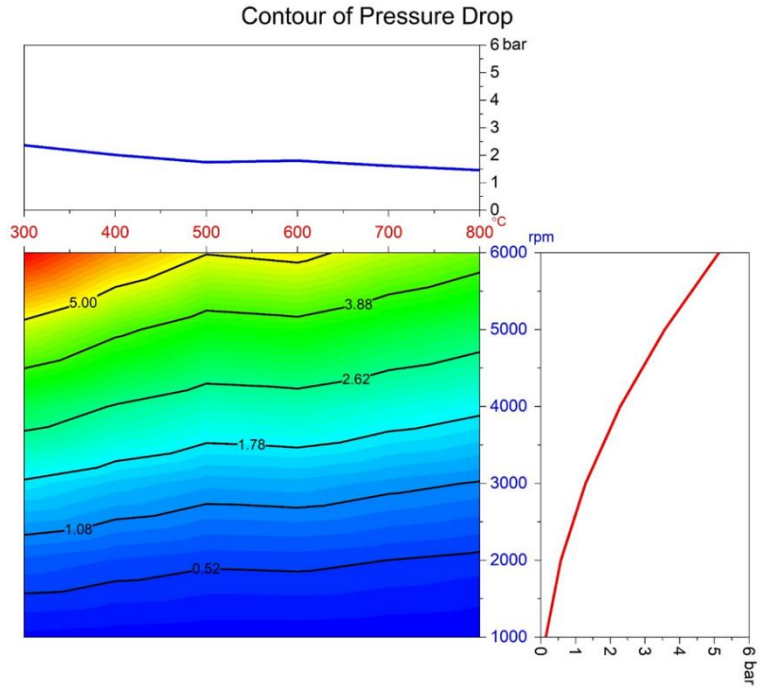


Figure 5-15 Pressure Drop contour of heat exchanger without fins

5.3.4.2 Simulation Results of Heat Exchanger with 30° Fins

Figure 5-17 to Figure 5-20 show the hot-side temperature and temperature difference of TEMs with different engine speed and exhaust gas temperature and contours of temperature difference, pressure drop and Reynold Number for heat exchanger with 30° fins. As can be seen in the figures, the pattern of each temperature curve is the same with that of heat exchanger without fins, but the peak temperature is slightly higher than heat exchanger without fins and the fluctuation is more significant as well. The increment of pressure and Reynold Number at high engine speed demonstrate decelerating trend.

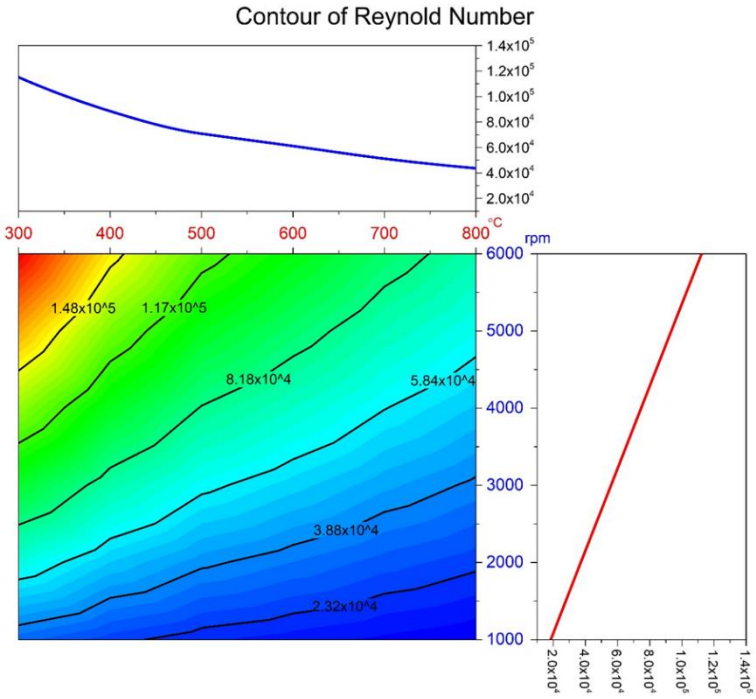


Figure 5-16 Reynold Number contour of heat exchanger without fins

5.3.4.3 Simulation Results of Heat Exchanger with 45° Fins

Figure 5-21 to Figure 5-24 show the hot-side temperature and temperature difference of TEMs with different engine speed and exhaust gas temperature and contours of temperature difference, pressure drop and Reynold Number for heat exchanger with 45° fins. Compared to the previous results, the peak point of hot-side temperature and temperature difference becomes higher, and the fluctuation still improves at high engine speed. Moreover, the pressure drop at low exhaust temperature seems to be more significant than at high exhaust temperature

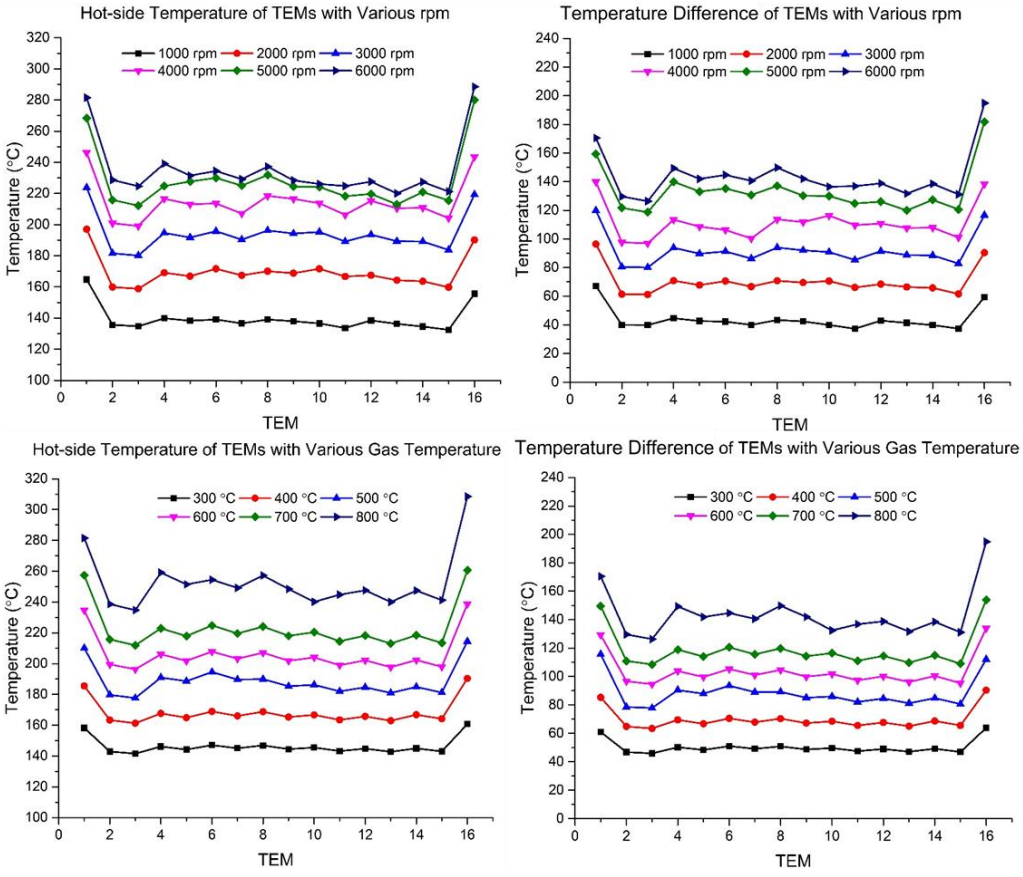


Figure 5-17 Temperature distribution of heat exchanger with 30°fins

5.3.4.4 Simulation Results of Heat Exchanger with 60° Fins

Figure 5-25 to Figure 5-28 show the hot-side temperature and temperature difference of TEMs with different engine speed and exhaust gas temperature and contours of temperature difference, pressure drop and Reynold Number for heat exchanger with 60° fins. Compared to the previous results, the peak point of hot-side temperature and temperature difference increase once again and there is a more obvious fluctuation at high engine speed.

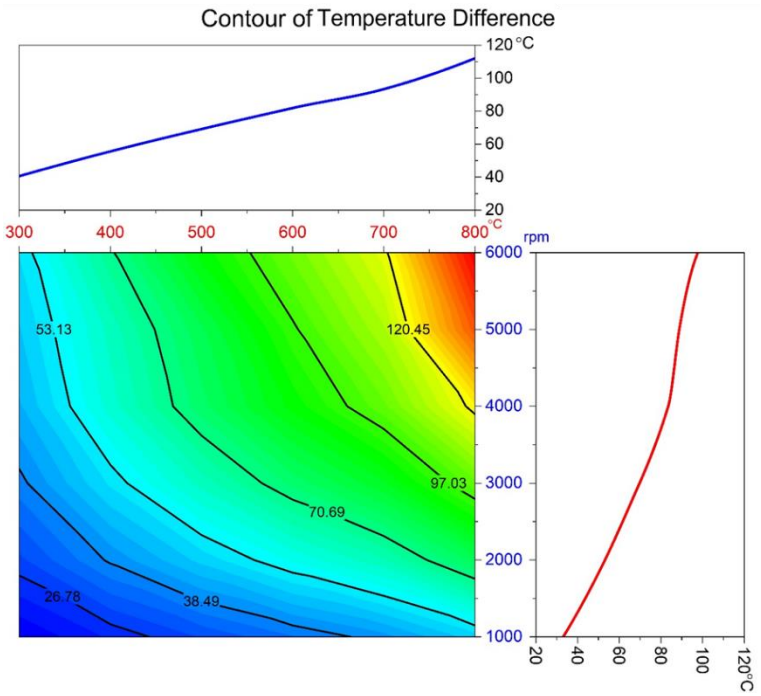


Figure 5-18 Temperature difference contour of heat exchanger with 30° fins

However, because of the relatively larger elevation angle of fins, the heat transfer in the front of TEM array is suppressed. Therefore, the hot-side temperature of the front TEMs is lower than that of rear TEMs, especially the 2nd and 3rd TEMs. There is an obvious temperature difference drop in the front of TEM array, compared to the results of other heat exchangers.

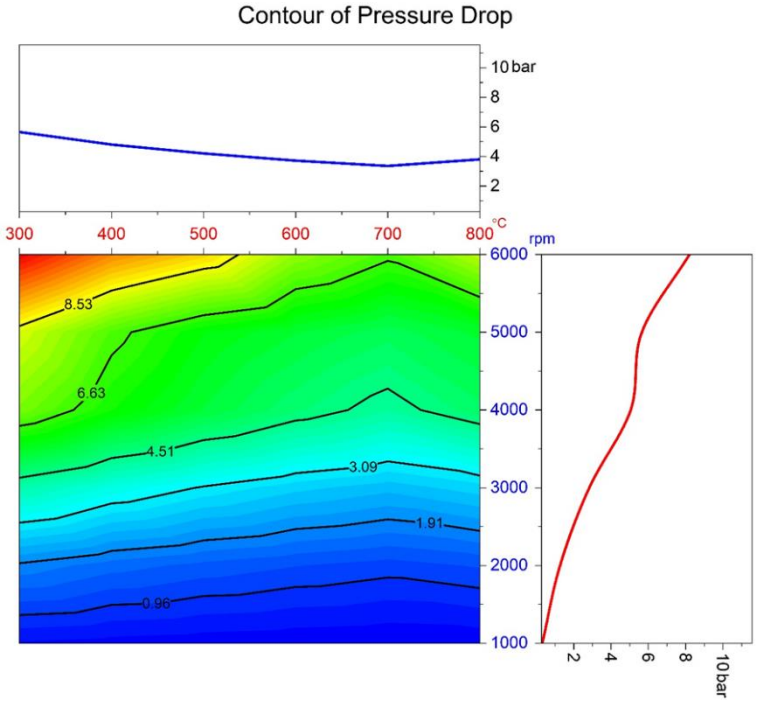


Figure 5-19 Pressure drop contour of heat exchanger with 30° fins

5.3.4.5 Simulation Results of Heat Exchanger with Different Heat Pipe Length

Figure 5-29 to Figure 5-32 show the hot-side temperature and temperature difference of TEMs with different engine speed and exhaust gas temperature as well as contours of temperature difference, pressure drop and Reynold Number for heat exchanger with different heat pipe length. As shown in the figures, the curves of hot-side temperature and temperature difference are different with the results from heat exchanger with fins. Because the length of front heat pipes is shorter than rear heat pipes, the heat transfer area for front heat pipes is smaller. Therefore, the hot-side temperature and temperature difference of front TEMs is generally lower than that of rear TEMs. Moreover, there is apparent temperature drop between two heat pipes of the same length. Furthermore, the peak point of hot-side temperature and temperature difference for heat exchanger with different heat pipe length is

generally lower than that of heat exchanger with fins. In addition, the increment of temperature difference turns into slow growth at high exhaust gas temperature.

Additionally, the velocity and temperature fields of each heat exchanger under different engine speed and exhaust temperature will be exhibited in Appendix II.

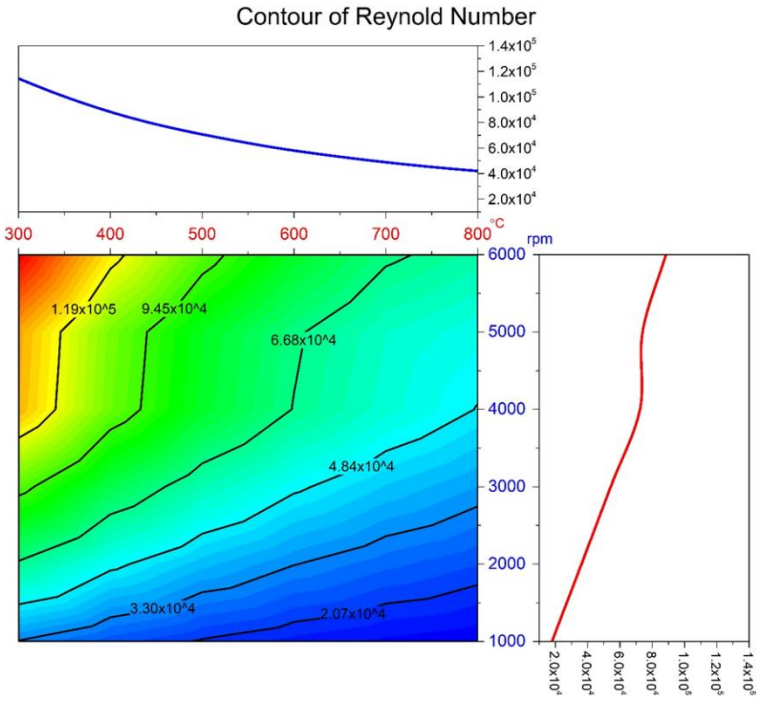


Figure 5-20 Reynold Number contour of heat exchanger with 30° fins

5.3.5 **Discussion on Simulation Results**

In the following section, a comprehensive discussion of the above simulation results and a detailed analysis for the performance of different heat exchangers is provided.

5.3.5.1 Temperature Difference

By compared the contours of temperature difference of each heat exchanger, it is found that the heat exchangers with fins have better performance in heat transfer enhancement. The average temperature difference though TEMs is boosted by

10.8 ℃, 16.1 ℃ and 17.9 ℃ for the heat exchanger with 30° fins, 45° fins and 60° fins, respectively. On the contrary, the average temperature difference though TEMs of heat exchanger with different heat pipe length decrease around 30 ℃, compared to heat exchanger without fins. This is due to the abridged heat pipes in front of the TEMs array, which inhibit the convective heat transfer, and cause lower hot-side temperature of TEM.

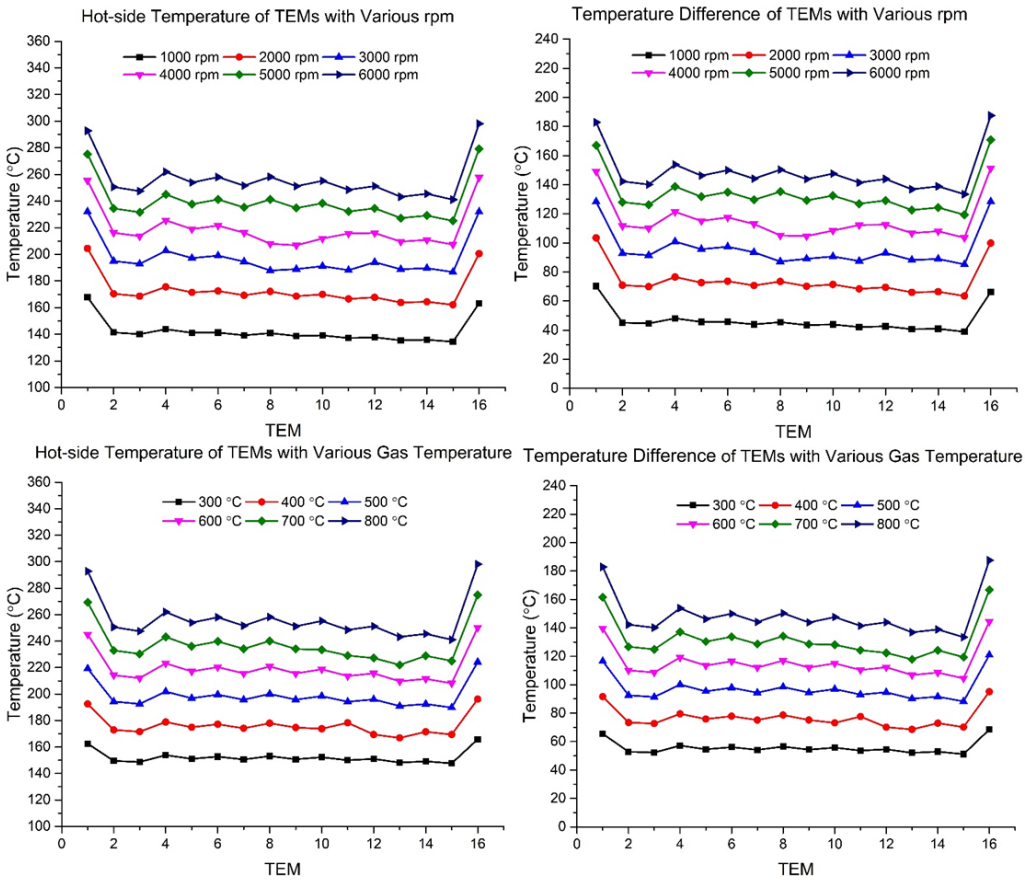


Figure 5-21 Temperature distribution of heat exchanger with 45° fins

Moreover, with the increment of exhaust temperature, the growth of temperature difference is basically in linear relation to the exhaust temperature. Nonetheless, the growth of temperature difference decelerates while the engine speed increase. Because with the increment of engine speed, the air flow rate becomes higher,

according to Equation 5-14. The high-speed exhaust flow would obstruct the efficiency of convective heat transfer, thus less heat is transferred to the hot side of TEMs.

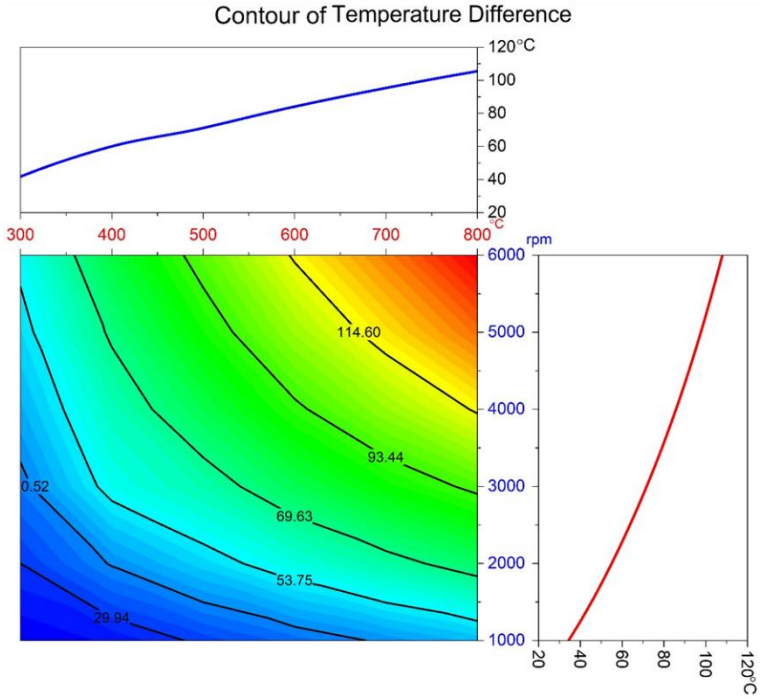


Figure 5-22 Temperature difference contour of heat exchanger with 45° fins

5.3.5.2 Pressure Drop

By compared the contours of pressure drop of each heat exchanger, it shows completely different results relative to temperature difference. With the insertion of different angled fins, the pressure drop of heat exchanger increase apparently and the increment of pressure drop becomes larger as the elevation angle of fins increases. In contrast, the pressure drop of heat exchanger with different heat pipe length is minimal among all these five heat exchangers, even smaller than that of heat exchanger without fins.

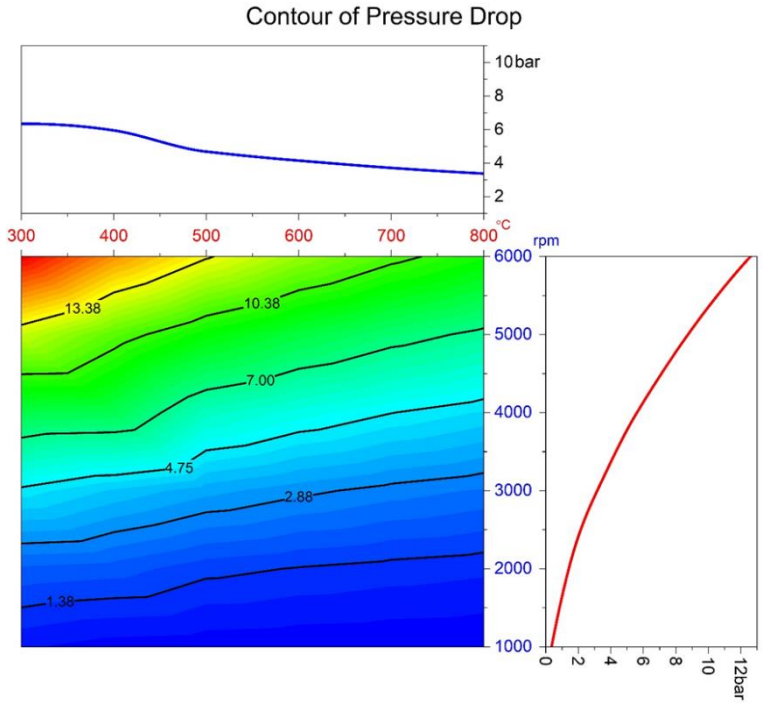


Figure 5-23 Pressure drop contour of heat exchanger with 45° fins

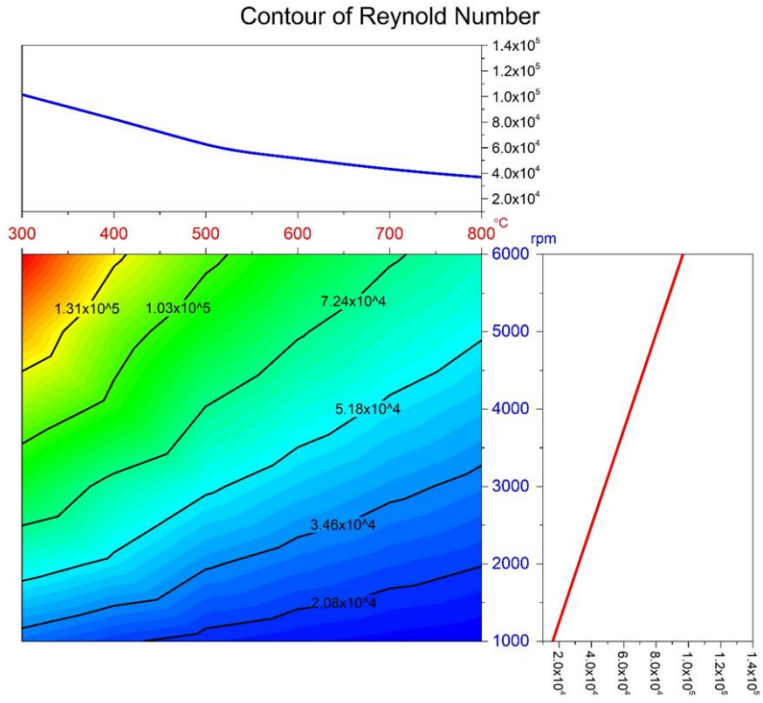


Figure 5-24 Reynold Number contour of heat exchanger with 45° fins

In addition, the increment of exhaust temperature has tiny impact on pressure drop. It only could be noticed in the heat exchanger with 60° fins that the pressure drop is diminished with the increment of exhaust gas. There are two reasons for explaining this circumstance. Firstly, the most important factor of affecting pressure drop is the velocity of exhaust gas. With the increment of elevation angle of fins, the cross section area of heat exchanger is compressed. According to the Bernoulli's principle, the velocity of exhaust gas will be increased with the decrease of cross section area. The second reason is the dynamic viscosity of exhaust gas. As the dynamic viscosity of exhaust gas decreases with the increment of exhaust temperature. According to Darcy–Weisbach equation, the pressure drop of heat exchanger will reduce as the dynamic viscosity of exhaust gas decreased.

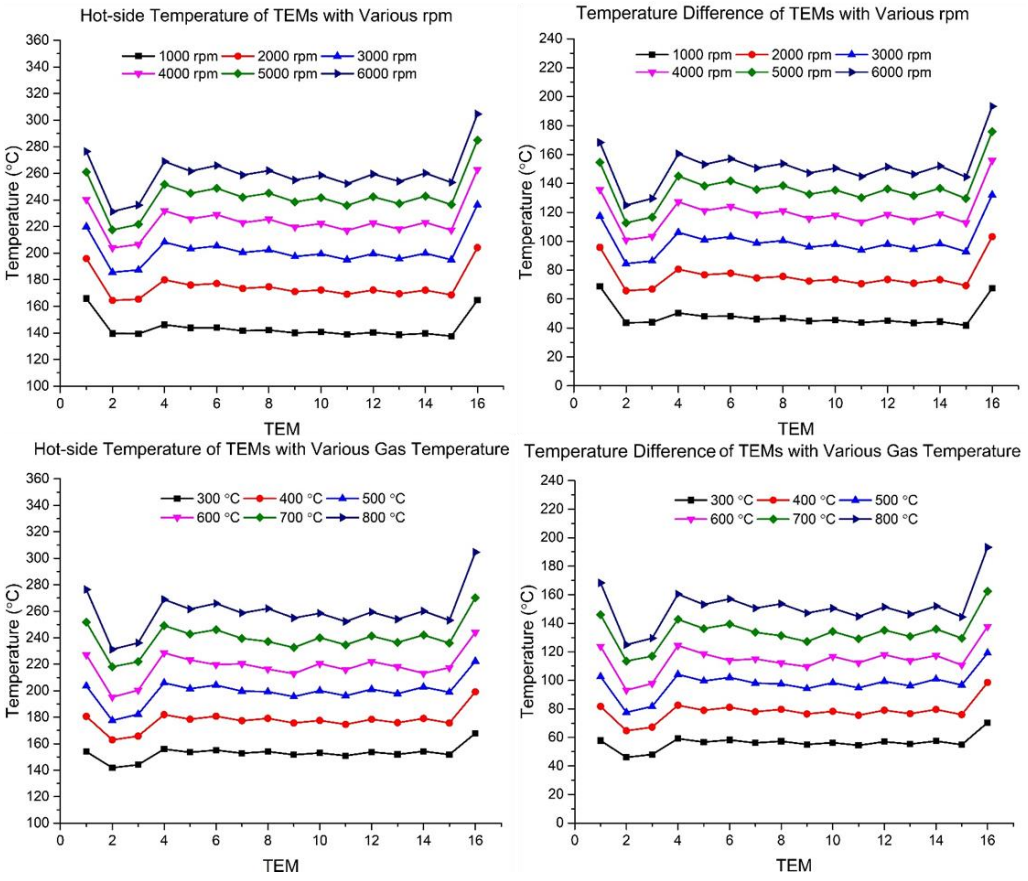


Figure 5-25 Temperature distribution of heat exchanger with 60° fins

Furthermore, with the increment of engine speed, the growth rate of differential pressure drop becomes larger. According to Darcy–Weisbach equation, the pressure drop of heat exchanger is in proportion to the square of air flow rate. Therefore, the curves of pressure drop with engine speed shows in a parabolic shape.

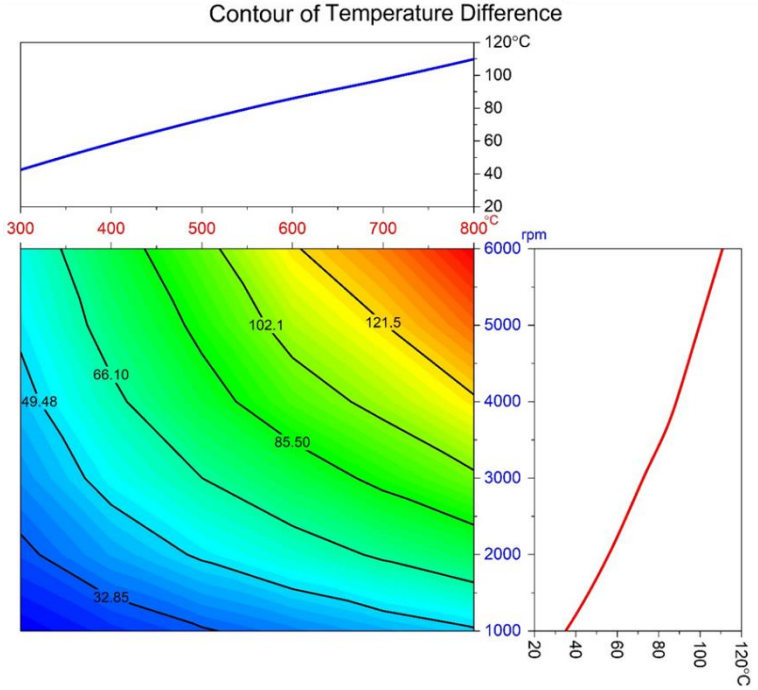


Figure 5-26 Temperature difference contour of heat exchanger with 60° fins

5.3.5.3 Reynold Number

By compared the contours of Reynold Number of each heat exchanger, it shows that the heat exchanger without fins has the highest average Reynold Number among all these heat exchangers. This is because it has the largest cross sectional area and the Reynold Number is in proportion to the cross-sectional area. However, it does not mean the heat exchanger without fins has the best performance in convective heat transfer. Because, by introducing fins, it can generate more turbulence and force the exhaust air flow into the area between heat pipes to

increase the heat transfer coefficient. With the increment of elevation angle, the Reynold Number becomes smaller.

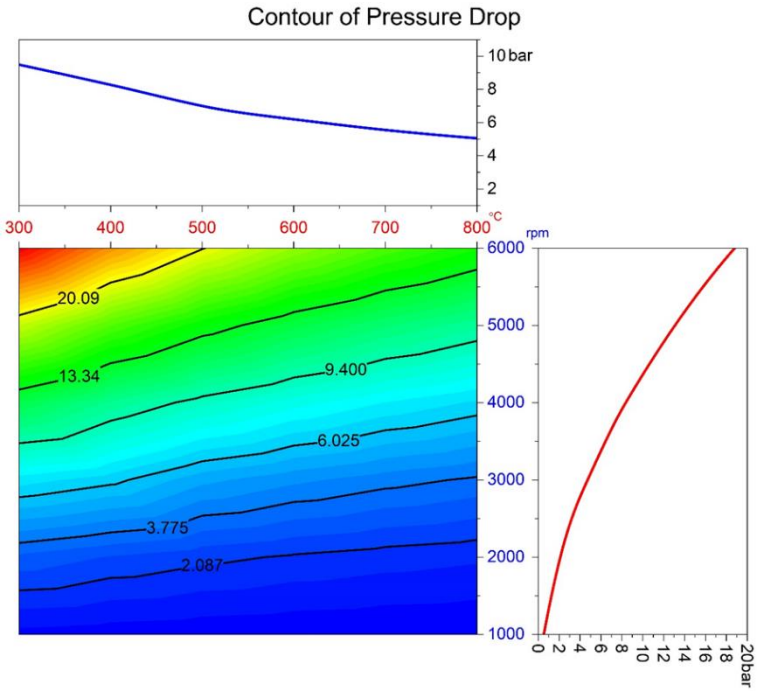


Figure 5-27 Pressure drop contour of heat exchanger with 60° fins

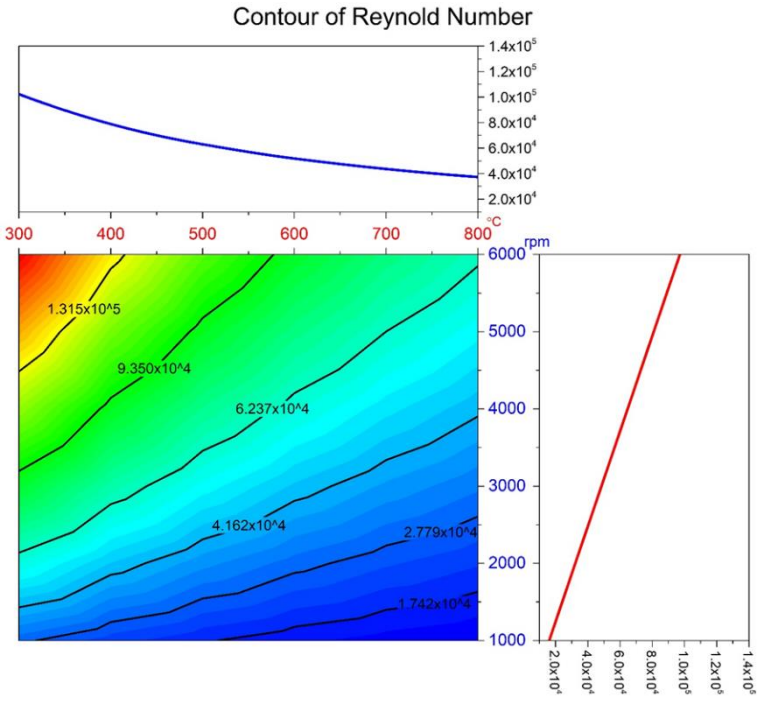


Figure 5-28 Reynold Number contour of heat exchanger with 60° fins

In addition, with the increment of engine speed, the Reynold Number presents a linear growth trend to the engine speed. According to the calculation of Reynold Number, the Reynold Number is in proportion to air flow rate, thus at high engine speed, the relatively high air velocity leads to higher Reynolds Number.

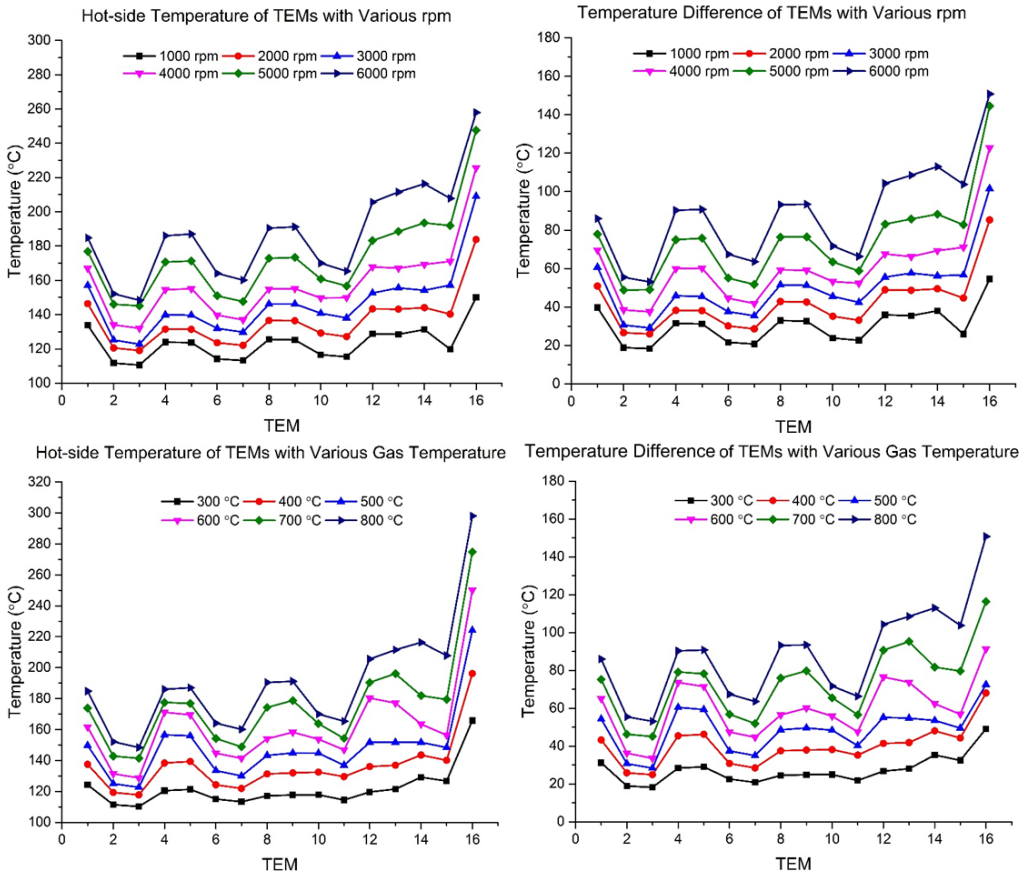


Figure 5-29 Temperature distribution of heat exchanger with different heat pipe length

On the contrary, the increment of exhaust temperature causes the reduction in Reynolds Number, because of the devaluation of exhaust viscosity. The viscosity in gases arises principally from the molecular diffusion that transports momentum between layers of flow. According to the Chapman–Enskog theory based on the Boltzmann equation, the viscosity of gases can be expressed as:

$$\mu_{mix} = \alpha_i \rho_i \lambda \sqrt{\frac{2k_b T}{\pi m_i}} \qquad \text{Eq. 5-15}$$

where k_b is the Boltzmann constant, m is the molecular mass, and α is a numerical constant on the order of 1.

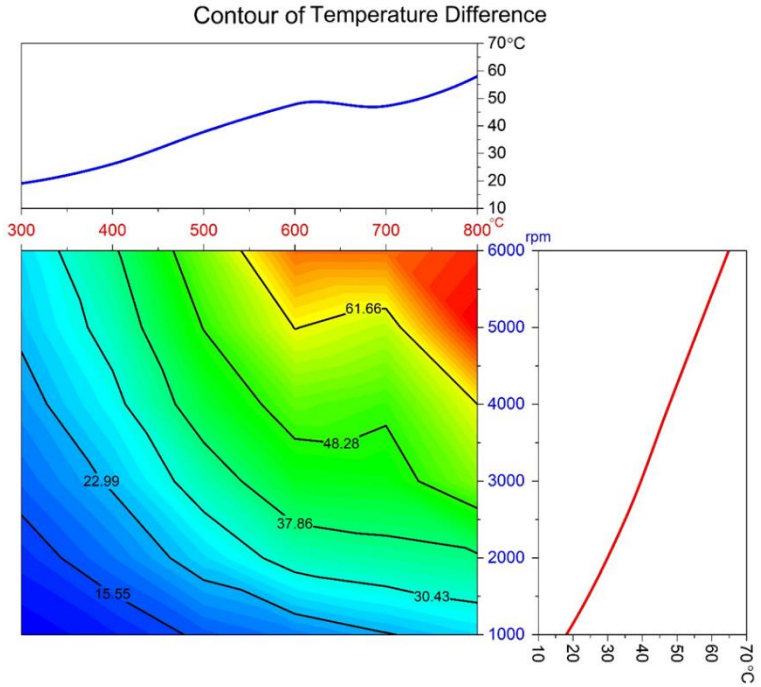


Figure 5-30 Temperature difference contour of heat exchanger with different heat pipe length

When the temperature rises, the thermal motion of the molecule increases, which means the momentum increases, thus the internal friction between layers increases. Therefore, the viscosity of gases increases with the increase of temperature, which is completely opposite to the law of viscosity change of liquids. Furthermore, the viscosity of gases increases as the pressure increases.

According to analysis, the viscosity of exhaust gas declines while the exhaust temperature increasing, which causes the reduction of Reynold Number.

5.3.5.4 Influence of Engine Speed

To summarize the influence of engine speed on temperature difference, pressure drop and Reynold Number of different heat exchanger, Figure 5-33 shows the comparison of each heat exchanger with different engine speed. As shown in the figure, in general, the temperature difference of heat exchangers with fins is higher than that of heat exchangers without fins and with different heat pipe length. In addition, it shows different trend in growth of temperature difference with engine speed between these heat exchangers. For the heat exchanger with different heat pipe length, the growth rate of temperature difference becomes higher with the increase of engine speed, which is opposite to other heat exchangers.

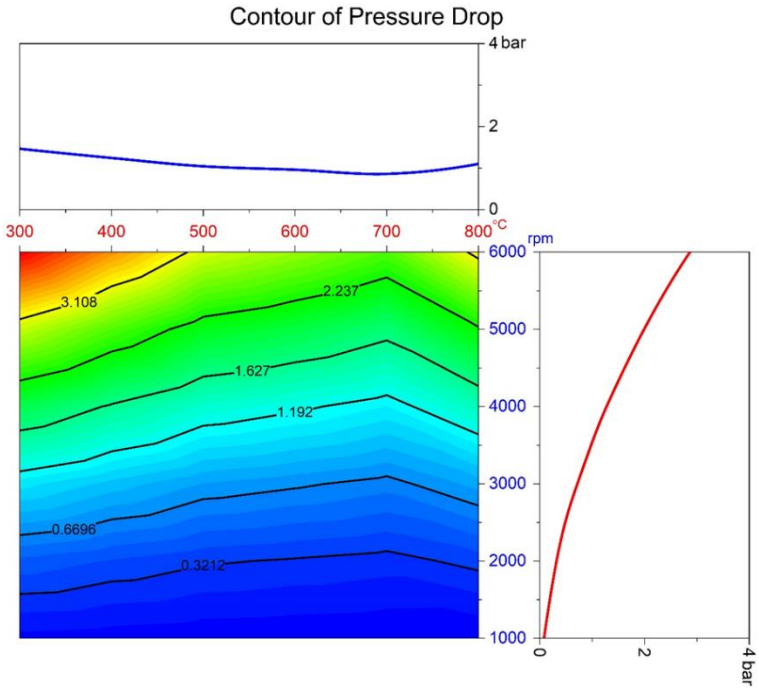


Figure 5-31 Pressure drop contour of heat exchanger with different heat pipe length

In the aspects of pressure drop and Reynold number, all of these five heat exchangers have the same trend. In addition, the heat exchanger with different heat

pipe length has the lowest pressure drop. When the engine speed is 1000 rpm, the pressure drop of each heat exchanger is virtually the same. As the engine speed increases, the gap between each heat exchanger develops more and more obvious.

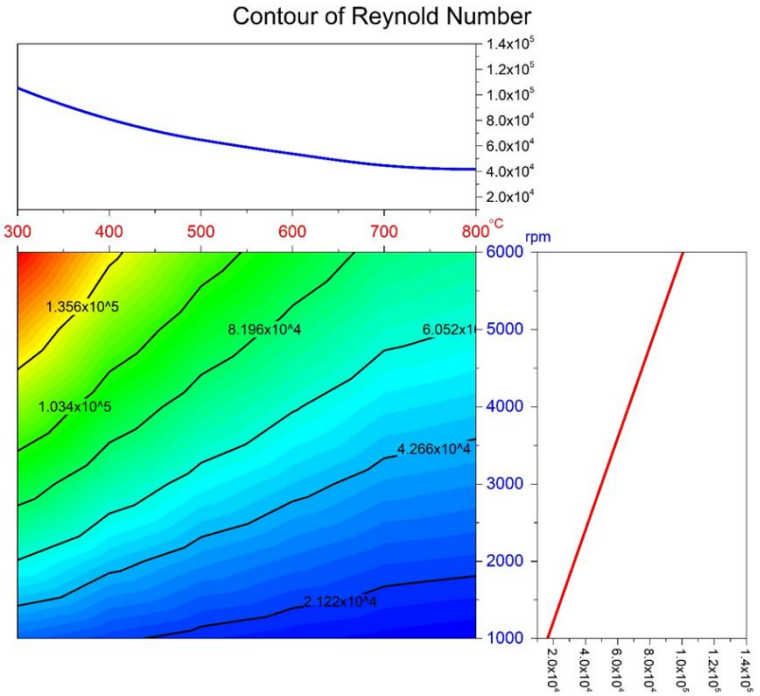


Figure 5-32 Reynold Number contour of heat exchanger with different heat pipe length

5.3.5.5 Influence of Exhaust Gas Temperature

In order to sum up the influence of exhaust temperature on temperature difference, pressure drop and Reynold Number of different heat exchanger, Figure 5-34 shows the comparison of each heat exchanger with different exhaust temperature. The temperature difference of heat exchanger with different heat pipe length is the lowest among all five heat exchangers and the trend of growth rate is contradictory to the curves of different engine speed. Moreover, the change in pressure drop with exhaust temperature is not as obvious as engine speed and the gap of pressure drop between each heat exchanger becomes smaller, with the

increment of exhaust temperature. Furthermore, the influence of exhaust temperature on Reynold Number is also contrary to the effect of engine speed and the change in Reynold Number is nonlinear to exhaust temperature.

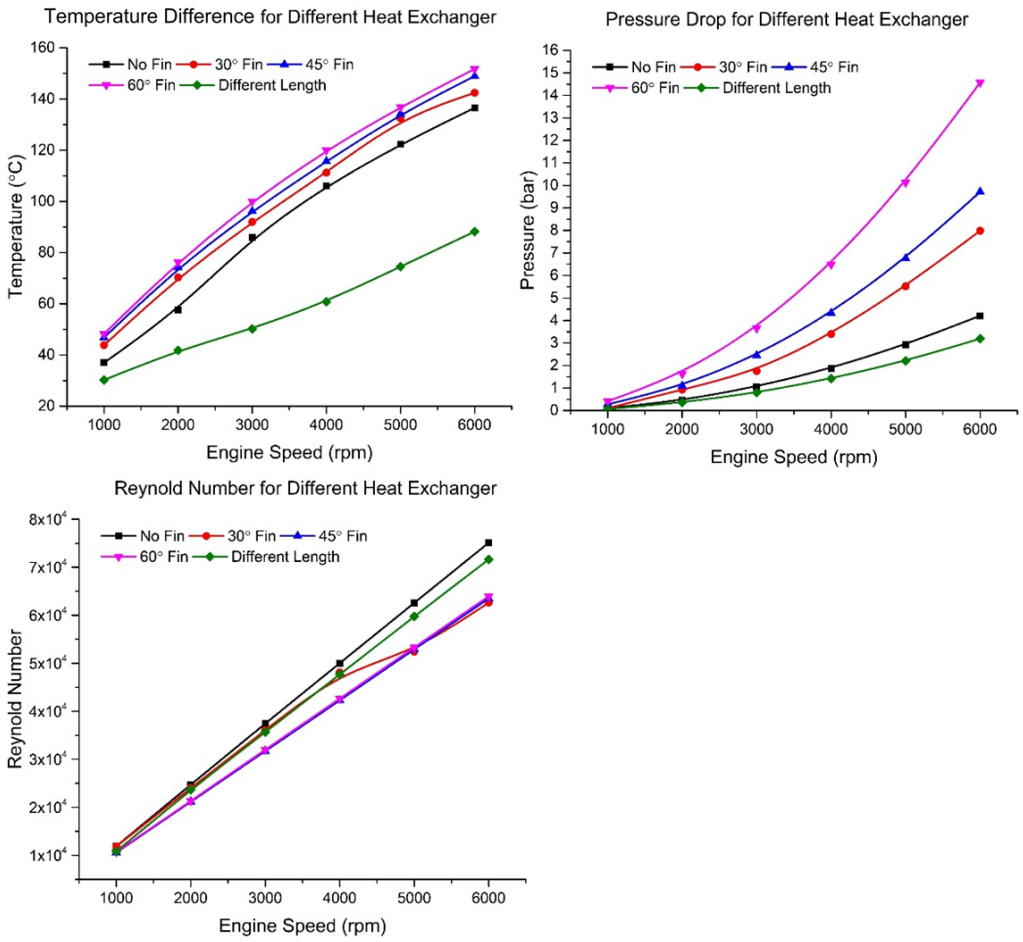


Figure 5-33 Comparison of each heat exchanger with different engine speed

In conclusion, from the temperature distribution of each heat exchange, the heat exchanger with different heat pipe length seems to be the worst in temperature characteristic. However, the metrics of the heat transfer capacity for a heat exchanger is logarithmic mean temperature difference (LMTD) rather than temperature characteristic. Therefore, in the following part, the LMTD of each heat exchanger will be discussed.

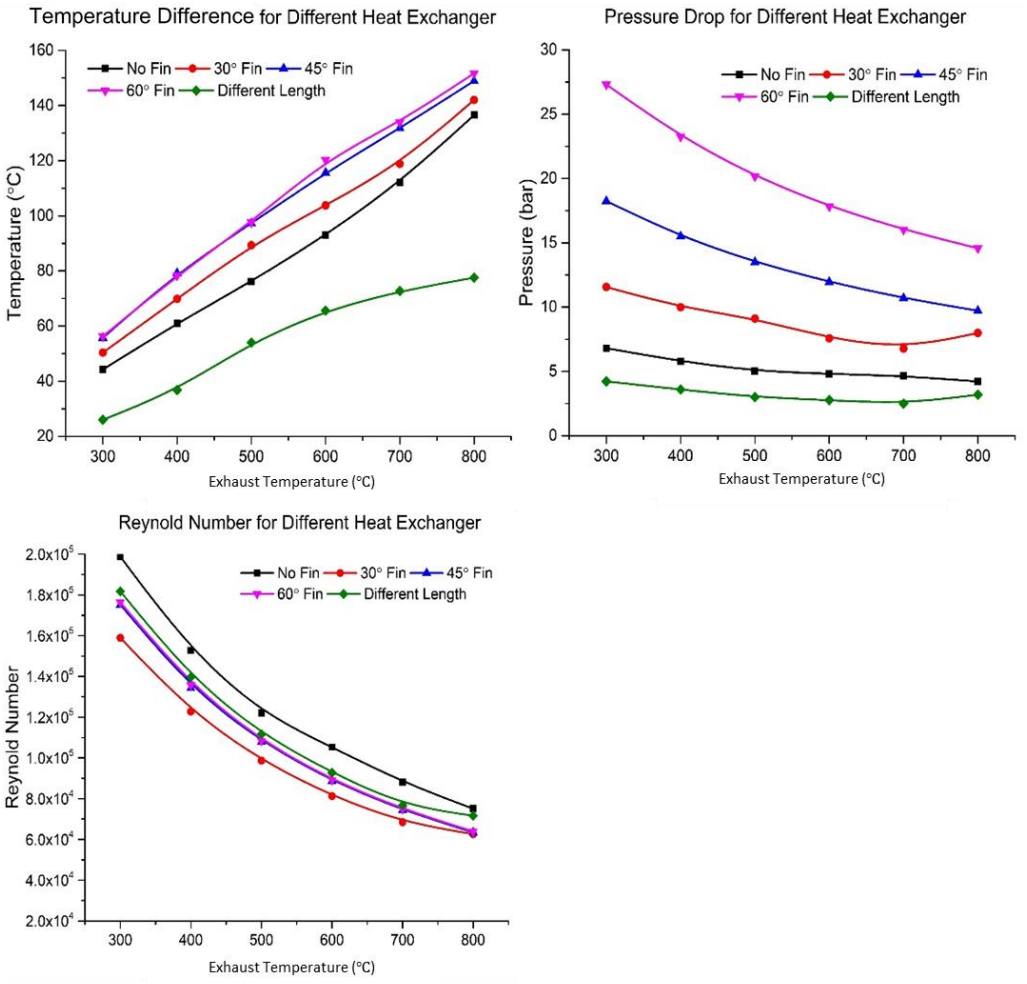


Figure 5-34 Comparison of each heat exchanger with different exhaust temperature

5.3.6 **Log Mean Temperature Difference Analysis**

The driving temperature across the heat transfer surface varies with position, but an appropriate mean temperature can be defined. In most simple systems this is the log mean temperature difference (LMTD) [208, 209]. The LMTD is used to determine the temperature driving force for heat transfer in flow systems, most notably in heat exchangers. The LMTD is a logarithmic average of the temperature difference between the hot and cold feeds at each end of the double pipe exchanger. For a given heat exchanger with constant area and heat transfer coefficient, the

larger the LMTD, the more heat is transferred. The use of the LMTD arises straightforwardly from the analysis of a heat exchanger with constant flow rate and fluid thermal properties [210].

It is assumed that a generic heat exchanger has two ends, named A and B, at which the hot and cold streams enter or exit on either side, then, the LMTD is defined by the logarithmic mean as follows [211]:

$$LMTD = \frac{\Delta T_A - \Delta T_B}{\ln \Delta T_A - \ln \Delta T_B} \qquad \text{Eq.5-16}$$

where ΔT_A is the temperature difference between the two streams at end A, and ΔT_B is the temperature difference between the two streams at end B. With this definition, the LMTD can be used to find the exchanged heat in a heat exchanger:

$$Q = U \times A_r \times LMTD \qquad \text{Eq.5-17}$$

where Q is the exchanged heat duty, U is the overall heat transfer coefficient and A_r is the exchange area. This holds both for parallel-flow and counter-flow of the heat exchanger.

In addition to the analysis for temperature characteristic of each heat exchanger, the LMTD for each heat exchange is also calculated, according to the Eq.5-16 above, to illustrate the heat transfer capacity of each heat exchanger.

Figure 5-35 shows the LMTD of each heat exchanger under different engine speed and exhaust temperature. As shown in the figure, the heat exchanger with different heat pipe length has the highest LMTD among all these heat exchangers either in various engine speed or in various exhaust temperature. This proves that he heat exchanger with different heat pipe length has the best heat transfer capacity,

even though the temperature characteristic is not good enough for this kind of heat exchanger. In general, with the increment of engine speed and exhaust temperature, the LMTD of heat exchanger becomes higher. Moreover, the LMTD for each heat exchanger becomes almost the same under a certain engine speed, which means the engine speed (air flow rate) is the most crucial factor for the heat transfer capacity of heat exchangers. However, with the increment of engine speed, the growth rate of LMTD becomes slower, especially for heat exchangers with fins.

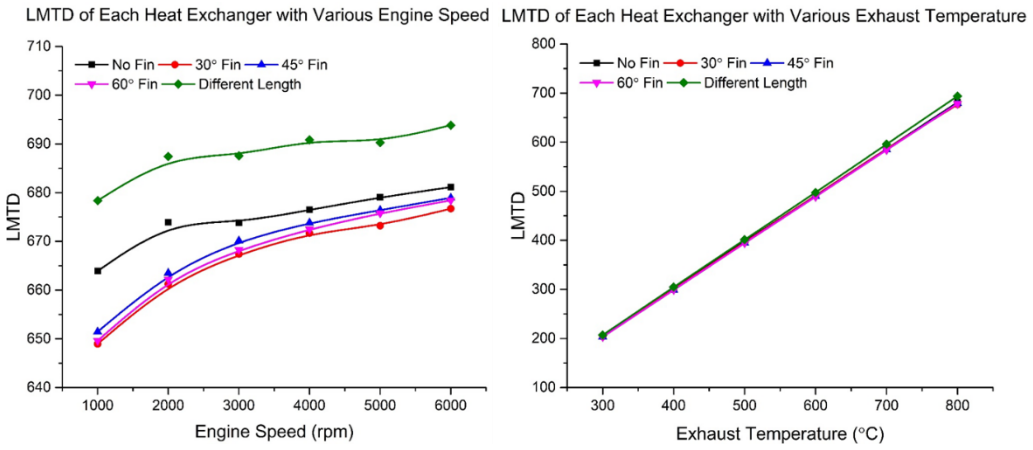


Figure 5-35 LMTD under different engine speed and exhaust temperature

5.4 **Summary**

In this chapter, the convective heat transfer within concentric cylindrical TEG system is investigated experimentally and numerically. As the limitation of manufacturing for annular TEM, the experiment is conducted in an array of square TEMs and heat pipe combined cascading structured heat exchanger. Due to the limitation of air flow meter, the highest operating temperature of experimental test rig is 200 ℃. In order to simulate the practical operating situation for concentric cylindrical TEG system, a numerical simulation is thus carried out using commercial CFD software, COMSOL Multiphysics. Moreover, for the purpose of

studying the enhancement for convective heat transfer within concentric cylindrical TEG system, the performance of five different heat exchangers for concentric cylindrical TEG system are explored simultaneously. Some important results and conclusions are summarised as follows:

- The flow rate of exhaust gas act as more important role than that of coolant. The variation in coolant flow rate has almost no effect on the hot-side temperature and temperature difference of TEMs.
- The performance for counter flow arrangement of exhaust gas and coolant is better than parallel flow arrangement and the performance of anti-gravity arrangement is the best among three different heat pipe arrangement.
- With the insertion of fins, the hot-side temperature and temperature difference of TEMs is enlarged. Furthermore, the enlargement of hot-side temperature and temperature difference improves with the increment of elevation angle.
- The pressure drop of heat exchanger with different heat pipe length is the lowest among all five heat exchangers, which means the influence to the engine backpressure is the lowest.
- The Reynold Number at high engine speed and exhaust temperature is still improved, which means the influence of engine speed is more crucial than exhaust temperature.
- The LMTD of heat exchanger with different heat pipe length is the largest among all five heat exchangers, which means the heat transfer capacity is the best in these heat exchangers.

- The results in this chapter give reference to the temperature distribution of the concentric cylindrical TEG system, along with the direction of exhaust flow. This could benefit the estimation of temperature distribution in the one-dimensional model in Chapter Six, under various vehicle driving condition. Moreover, the investigation of different arrangement will give a guide for the further optimization of the system structure.
- According to the simulation results, the most suitable structure for heat exchanger of concentric cylindrical TEG system should combine the fins with different heat pipe length.
- In this Chapter, the accuracy of the experimental and simulation results need to be improved, due to the structure of the test section and the numerical model in the simulation. Therefore, further experimental and numerical investigation needs to be conducted with the optimized test section and the three-dimensional simulation model.
- It is difficult of manufacturing the different angled fins within the heat exchanger of concentric cylindrical TEG system to achieve better performance in convective heat transfer.

Chapter 6. Comprehensive Model of Fuel Economy Estimation for Vehicles with Concentric Cylindrical TEG System

6.1 Introduction

As explained in the introduction in previous chapters, the main purpose of a TEG system is to recover the waste heat in the exhaust gas and transfer it into the reusable electrical power for vehicle accessories. Through this approach, the vehicle could achieve purposes of improving the thermal efficiency and fuel economy. According to the literature review in Chapter Two, however, the major challenging obstacle for TEG systems from broad commercial application is the relatively low heat-to-electricity conversion efficiency. Regarding this challenge, much research has been conducted in promoting the figure of merit (ZT value) of TE materials and some researchers have achieved a certain breakthrough in material science. However, these TE materials with high ZT value are simply remaining in the lab test phase and would take a long time to implement the practical application. Meanwhile, the research on heat transfer enhancement in system level for automotive TEG received considerable attention as well. Researchers committed numerous energy into the heat transfer improvement, in order to absorb more heat from the exhaust gas, in the past few years.

Aside from this research, it is also important to study the effect of the TEG system on fuel economy, which has received little attention. This aspect is important because the main purpose of the TEG system in automotive vehicles is fuel saving and the insertion of TEG system would have impacts on the various parameters. Moreover, in real-time driving, the properties of exhaust gas have significant

fluctuations, which gives a major impact on the operation of TEG system. According to research for exhaust gas temperature on TEG system performance by He et al. [67], different exhaust temperatures led to significantly different heat transfer and flow resistance characteristics, and thereby led to corresponding differences with respect to the optimal design of exchanger scales. Furthermore, Tang et al. [156] investigated the impact of thermal imbalance on the output power of TEG at module and system level and an 11 % of power loss was spotted under temperature mismatch conditions compared to the theoretical maximum power. In addition, Manikandan et al. [212] explored the influence of Thomson effect in the performance optimisation of a two-stage TEG system. The optimum numbers of thermocouples for the maximum power output and energy/exergy efficiency conditions have been evaluated during the research.

As shown in the analysis above, the performance of automotive TEG systems is interwoven with the driving conditions. However, research on the effects of vehicle driving conditions on the TEG system has rarely seen over the past few years. Comamala et al. [213] develop a new numerical model of calculating the power output and fuel economy improvement of a radial automotive TEG system. Results indicated that the maximum fuel economy improvement of 1.3 % is attained with an efficiency of TEM at 6%. Lan et al. [214] developed a semi-empirical model with quasi-static vehicle model, dynamic exhaust model, dynamic coolant model and dynamic TEG model. By utilising this model, TEG system, controlled by optimised operating conditions delivered a fuel consumption reduction of 4% over a constant speed of 120 km/h. Massaguer et al. [215] presented a method to assess the fuel economy of automotive TEG systems ,and according to this method, a flat

automotive TEG system presented a maximum fuel economy improvement of 0.18%. Among these researches, there are even less researches on the performance of TEG systems under standardized vehicle driving conditions. Yu et al. [216] simply investigated the transient behaviour of TEG systems under different start-up mode, and discovered that the duration to reach a steady-state power output is significantly affected by the start-up current of TEG systems.

In this project, a novel design of concentric cylindrical TEG system is presented and the investigation on fuel economy improvement by utilising this TEG system is essential as well. In the following content of this chapter, a comprehensive fuel consumption model is established. This model combined the engine, vehicle and TEG model in GT-Suite, as well as the estimation model of fuel consumption with TEG system in MATLAB Simulink. In this chapter, the results from Chapter Four and Chapter Five are utilized during the establishment of the one dimensional model of concentric cylindrical TEG system. These results can simplify the structure and material properties of the model and reduce the total time of computation. Moreover, the date from engine and vehicle model is verified by the data of a 1.6 L engine in a test bench experiment. The detailed model description will be provided in the following section. In order to give an accurate estimation of fuel economy improvement, the Worldwide Harmonised Light Vehicle Test Procedure (WLTP) is employed to measure fuel consumption. Furthermore, the fuel consumption improvement is compared with New European Driving Cycle (NEDC) and EPA Federal Test Procedure (FTP-75) as well.

6.2 Engine, Vehicle and TEG Model Description

The first part of the comprehensive fuel consumption model for vehicle utilising concentric cylindrical TEG system includes three GT-Suite models, which are vehicle model, engine model and TEG system model. The vehicle model calculates the engine speed and torque, which gives the boundary condition for the engine model, as well as the specific fuel consumption under WLTP cycle. The engine model calculates the exhaust properties such as mass flow rate and temperature, which gives the boundary condition for concentric cylindrical TEG system. The TEG model is established according to concentric cylindrical TEG system, and calculates the power output of this system. moreover, these three models obtain all the input parameters of the MATLAB model introduced in next part.

Figure 6-1 shows the detailed GT-Suite models of the engine and vehicle as well as the calculating procedure. Figure 6-2 shows the detailed GT-Suite models of concentric cylindrical TEG system and its location in exhaust system.

In order to verify the models of vehicle and engine, experimental data from an engine experimental bench is employed. The experiment was carried out in a 1.6 L turbo-charging engine by a vehicle manufacturer from China. The photo of the test bench is shown in Figure 6-3. Moreover, the detailed specifications of the test vehicle and engine are provided in Table 6-1

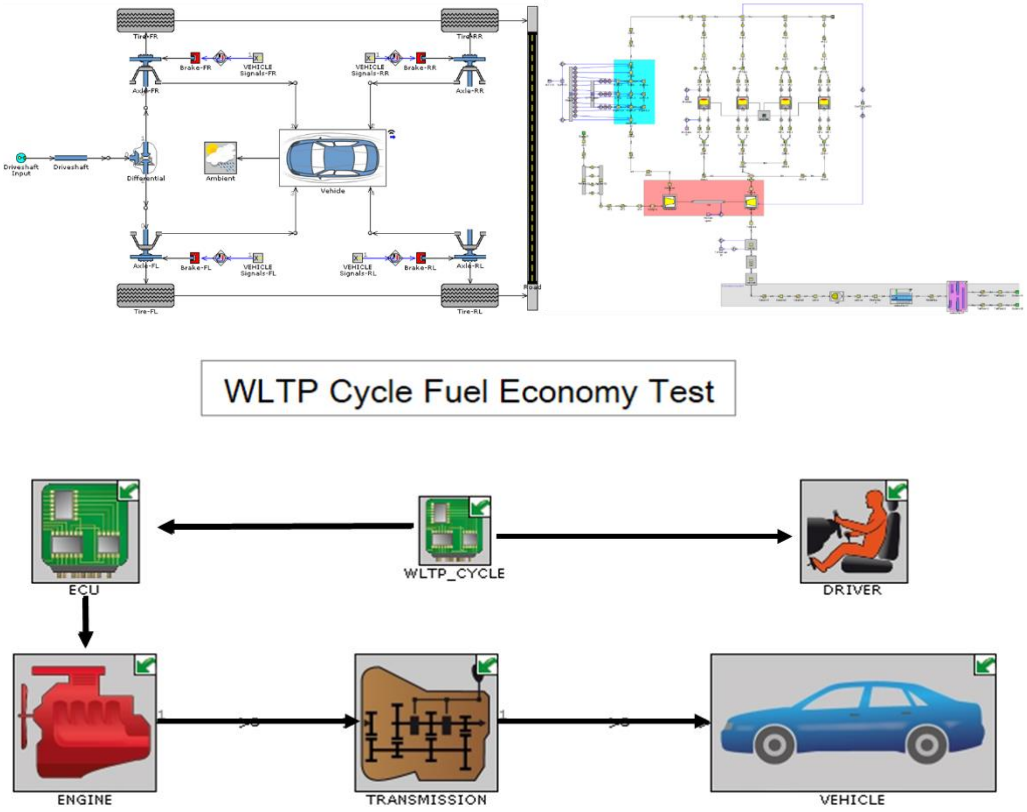


Figure 6-1 GT-Suite models of the engine and vehicle & calculating procedure

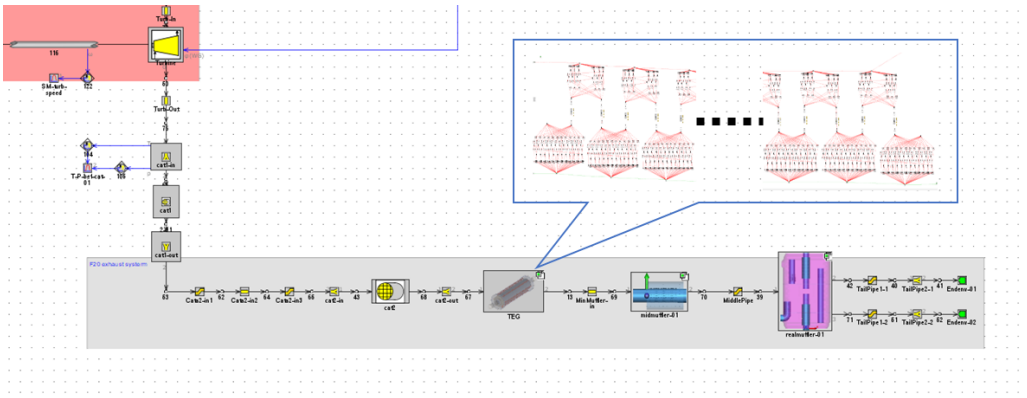


Figure 6-2 GT-Suite models of concentric cylindrical TEG system & location

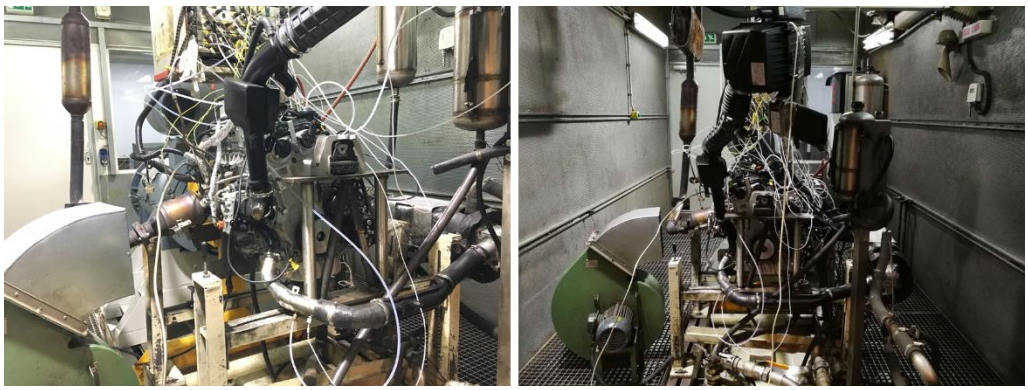


Figure 6-3 Engine experiment test rig for validating GT-Suite models

6.3 **Model for Fuel Economy Estimation**

The second part of the comprehensive fuel consumption model for vehicle utilising concentric cylindrical TEG system is the MATLAB Simulink model of calculating the fuel consumption by the parameters achieved from GT-Suite models.

Table 6-1 Detailed Specifications of Test Vehicle

Vehicle Parameters	Vehicle Weight (Full load) (kg)	1330 (1720)
	Vehicle Dimension (mm)	4240*1803*1600
	Air resistance coefficient	0.36
	Frontal area (m^2)	2.62
Engine Parameters	Bore diameter (mm)	76.5
	Piston stroke (mm)	87
	Compression ratio	9:1
	Engine Displacement (L)	1.6
	Maximum Power (kW)	108.47
	Maximum Torque (Nm)	227.7
	Number of Transmission Ratio	6
Tire Parameters	Rolling radius (m)	0.36
	Moment of inertia (kg*m^2)	1.05
	Resistance coefficient	0.0097

With the purpose of investigating the upgrading of fuel economy with the TEG system, several factors need to be addressed. The improvement of fuel consumption by utilising concentric cylindrical TEG system can be estimated by the electric power generation of the TEG system and the engine performance penalty after utilising the TEG system:

- Increment of back pressure
- Weight of TEG system
- Coolant pumping power
- Efficiency of DC-DC converter

These factors are dependent on the design of the system and will influence the engine performance, therefore determine the fuel saving of the entire vehicle [213]. The electric power generation of the TEG system can be calculated by the model, which is present in Section 6.2. In the following part, the engine performance penalty factors will be discussed in detail, to generate a comprehensive method to calculate the fuel economy improvement by employing TEG system.

6.3.1 **Back Pressure Impact**

Any insertion in the exhaust system will cause an increase of back pressure, which can cause the loss of engine power output and fuel economy consequently. The pressure drop of the TEG system is related to the properties of exhaust gas and the shape of the heat exchanger and can be calculated by the equation below [217, 218]:

$$\Delta P = \frac{1}{2} \cdot k_e \cdot \rho \cdot v^2 \qquad \text{Eq.6-1}$$

where ρ is the exhaust gas density, v is the exhaust gas velocity, k_e is flow loss coefficient which related to the shape of the heat exchanger.

As described in the former part, the structure of the concentric cylindrical TEG system has a hard pipe heat exchange section. According to the reference, the flow loss coefficient of a hard pipe is $k_e = 4fL/D$, where f is the Darcy resistance coefficient; D and L are the hydraulic diameter and length of the pipe, respectively. The press drop for the concentric cylindrical TEG system, then, can be expressed as follow [195]:

$$\Delta P = 2fL/D \cdot \rho \cdot v^2 \qquad \text{Eq.6-2}$$

In this study, the fuel consumption penalty caused by increment of back pressure is presumed in linear relation to the pressure drop of the TEG system. Therefore, it can be expressed as [219]:

$$\Delta F_{BP} = \Delta P / P_{me} \times 100\ \% \qquad \text{Eq.6-3}$$

where ΔF_{BP} is the fuel consumption increase percentage caused by increasing back pressure; P_{me} is the Brake Mean Effective Pressure (BMEP) of the engine.

6.3.2 System Weight Impact

The effect of added weight of TEG system can be easily included in the vehicle model by increasing vehicle weight. In this study, the total weight of concentric cylindrical TEG system is assumed as 40 kg. Because the fuel consumption is related to the vehicle weight directly, and the fuel consumption increase can be expressed as [220, 221]:

$$\Delta F_m = m_{TEG} / m_{Vehicle} \times 100\ \% \qquad \text{Eq.6-4}$$

where ΔF_m is the fuel consumption increase percentage by increasing weight; m_{TEG} and $m_{Vehicle}$ are the weight of the TEG system and vehicle, respectively.

6.3.3 Pumping Power Impact

As the concentric cylindrical TEG system is cooled by the same coolant of the engine, it is necessary to pump the water to the TEG system from the engine cooling system. In other words, there will be an augment in pumping power of the water pump. The power for the water pump is supplied by the engine, as a result, the augment in pumping power will have a negative effect on fuel consumption [222].

Normally, the pumping power P can be calculated using the equation below [223]:

$$P = {Q \times H \times g \times \rho}/{\eta_{pump}} \qquad \text{Eq.6-5}$$

where Q is the flow rate of the water, H is the head of the pump; ρ is the density of the water and η_{pump} is the pump efficiency and usually sets as 95%.

The flow rate Q of water can be calculated by the following equation [224]:

$$Q = {\Phi_w \cdot \eta_V}/{c_w \cdot \rho \cdot \Delta T_w} \qquad \text{Eq.6-6}$$

where Φ_w is the heat carried away within the TEG system; C_w is the specific heat capacity of water; ρ is the density of water; ΔT_w is the temperature difference between water inlet and outlet, in most instances, the difference should keep within 10 ℃; η_V is the volumetric efficiency of the pump rating from 0.6 to 0.85 for the most water pump.

So the percentage of fuel economy penalty for the increment of water pump ΔF_{Pump} can be expressed as:

$$\Delta F_{Pump} = {}^{P_{TEG} - P}/_{P_{TEG}} \times 100\% \qquad \text{Eq.6-7}$$

6.3.4 DC-DC Converter Impact

The insertion of the TEG system is intended to reduce the electrical power, which is generated by the alternator, for supplying the vehicle accessories, thereby conserving the engine power for operating the alternator and achieving the purpose of fuel saving. However, the output voltage of the TEG system is lower than the requirement of vehicle accessories, which is 12 V, during most of the time. Therefore, a DC-DC converter is imperative for the TEG system for matching those accessories for operating at a stable voltage. Furthermore, there will be energy loss between the TEG system and the DC-DC converter, caused by the mismatch of the electrical resistance of these two components. According to the reference, the efficiency of a DC-DC converter η_{DC} is around 85 % to 95 % [225]. These part of energy loss need to be considered in the fuel economy as well.

6.3.5 Fuel Consumption Improvement

Concluding with all the analysis above, the total improvement of fuel economy ΔF_{TEG} by integrating concentric cylindrical TEG system can be expressed as:

$$\Delta F_{TEG} = be \times \left(\frac{P_{TEG} \cdot \eta_{DC}}{P_{alt}} - \Delta F_{BP} - \Delta F_{M} - \Delta F_{Pump}\right) \qquad \text{Eq.6-8}$$

where P_{alt} is the power output for automotive alternator which is relate to the engine speed.

All the parameters that appear in Equation 6-8 vary with the engine speed and torque, so the total improvement of fuel economy ΔF_{TEG} can be defined with engine speed (rpm) and torque (Nm) as $\Delta F_{(rpm,\ Nm)}$. This will be much easier to utilise in

any kind of vehicle platform with the basic information of engine speed and torque, even in the hybrid electric vehicles (HEV).

A comprehensive fuel consumption model is established in MATLAB Simulink, to calculate the fuel consumption under the real time driving cycles. The Simulink model is combined with the results from the vehicle, engine and TEG models built in GT-Suite, in order to get the boundary condition of mass flow rate and temperature of the exhaust gas. The detailed structure of the comprehensive model is presented in Figure 6-4 and the flow chart for calculating fuel consumption is shown in Figure 6-5.

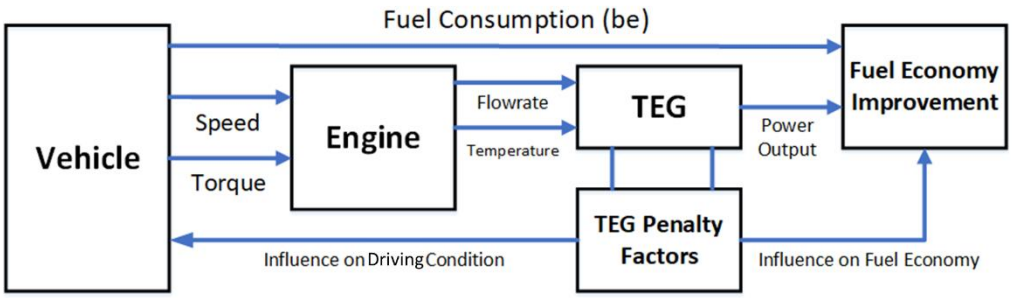


Figure 6-4 Schematic diagram for comprehensive fuel consumption model

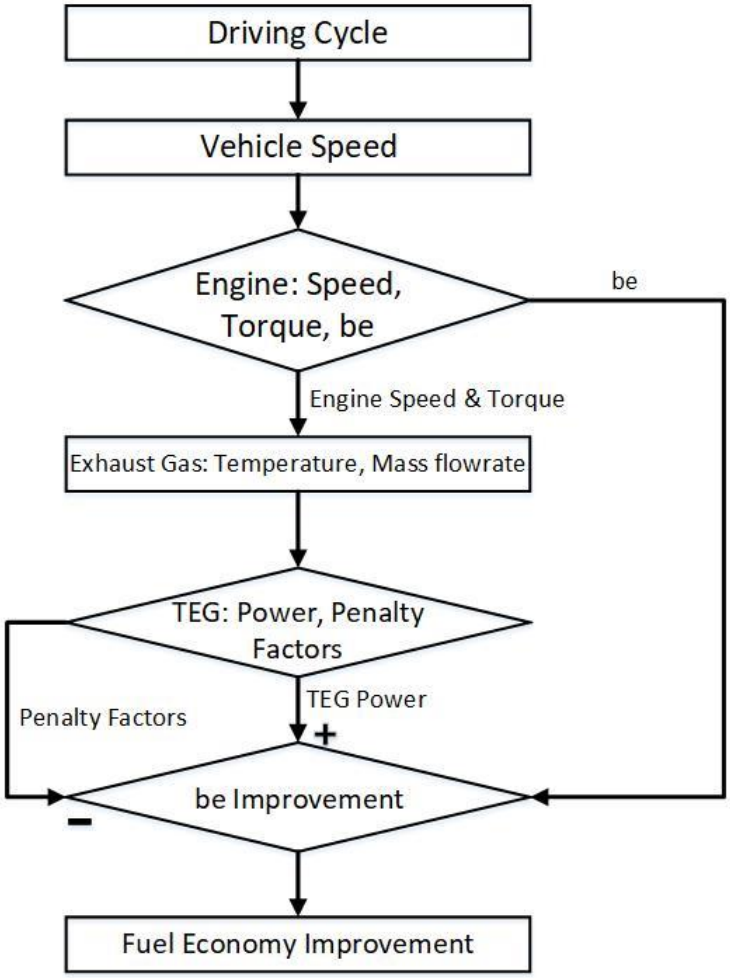


Figure 6-5 Flow chart for calculating fuel economy improvement

6.4 Result and Discussion

In this section, the exhaust gas properties under different engine working condition are discussed at the beginning. These results can demonstrate the exhaust gas energy and give a universal boundary condition for the concentric cylindrical TEG model for calculating its power generation. In addition, the brake specific fuel consumption and power output for concentric cylindrical TEG system with various engine condition is exhibited, as well as, the total electric power generation under real-time driving cycle. The real-time driving cycle employed in this study is WLTP

to meet the real-driving data and better match on-road performance. Furthermore, the fuel economy improvement under WLTP cycle, which is calculated by the comprehensive numerical model, is also analysed in this section.

6.4.1 Engine Performance and Waste Heat

In order to investigate the performance of concentric cylindrical TEG system under standardized driving cycle, the properties of engine exhaust gas were investigated, as the power generated from TEG system is affected by the mass flow rate and temperature of the exhaust gas. Figure 6-6 shows the experimental results for the mass flow rate and temperature of the exhaust gas. As shown in the figure, in general, the temperature and mass flow rate of exhaust gas both increase with the increment of engine speed and torque. The exhaust gas temperature ranges from 452 ℃ to 960 ℃, while the mass flowrate varies from 3 g/s to 133 g/s. Both of these two parameters have a large fluctuation with different engine speed and torque, therefore the exhaust gas energy will have an enormous variation in the daily driving of vehicles. Furthermore, there is a significantly different distribution of these two parameters, caused by the engine calibration for a lower fuel consumption. The mass flowrate is growing smoothly while the engine speed and torque are increasing and reaches the peak point at highest engine speed and torque. However, the highest exhaust gas temperature is concentrated at the middle of the engine torque with high speed or high engine torque and low speed. As shown in Figure 6-6, there are three areas of high exhaust temperature, and these three areas lead to high exhaust energy, which needs to be considered in the calibration of TEG system. Because these two parameters are the contributing factors for TEG system and influence the power output individually, the distributions of these two parameters

with engine torque & speed are important references while designing and matching the TEG system with the vehicles. The detailed effects of these two parameters will be investigated in the further works.

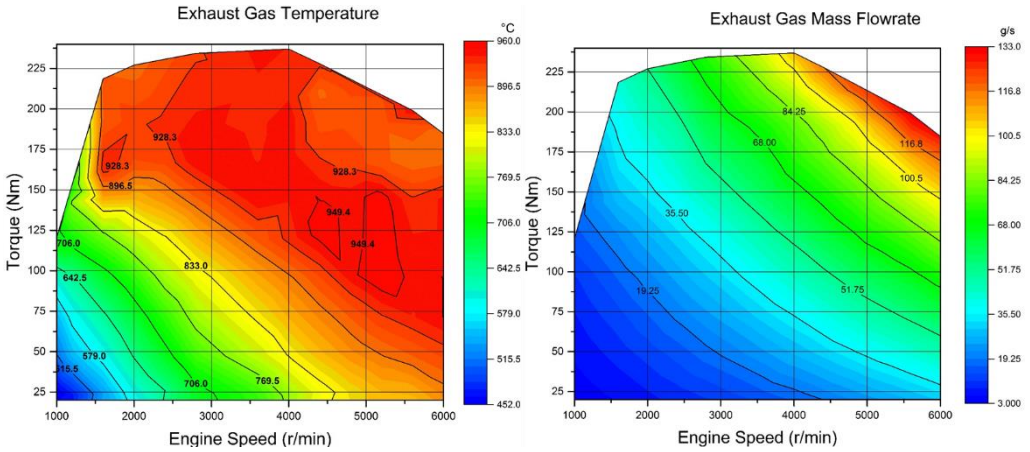


Figure 6-6 Experimental results of contours for exhaust properties

Besides these two figures, the contours of exhaust gas energy and energy percentage, which are calculated by the GT-suite model, are also calculated and displayed in Figure 6-7. These two parameters will give a more intuitive value of the waste heat carried away by engine exhaust gas. The contour of exhaust gas energy gives the specific energy value of the exhaust gas under different engine speed and torque. The energy varies from 1 kW to maximum 117 kW at relatively higher torque and engine speed. In general, the maximum exhaust gas energy of each engine speed occurs at the peak torque point in this speed and vice versa. This contour gives very essential information for the TEG systems when they are matching with vehicle at the different driving condition. Because the complex driving condition vehicle will not allow TEG system operating in the optimum working interval constantly, the connection between each TEM should be adjusted according to the contour of exhaust gas energy. The exhaust gas energy percentage

contour shows a respectable consistent with previous analysis, ranging from 31.1 % to 47.9 %.

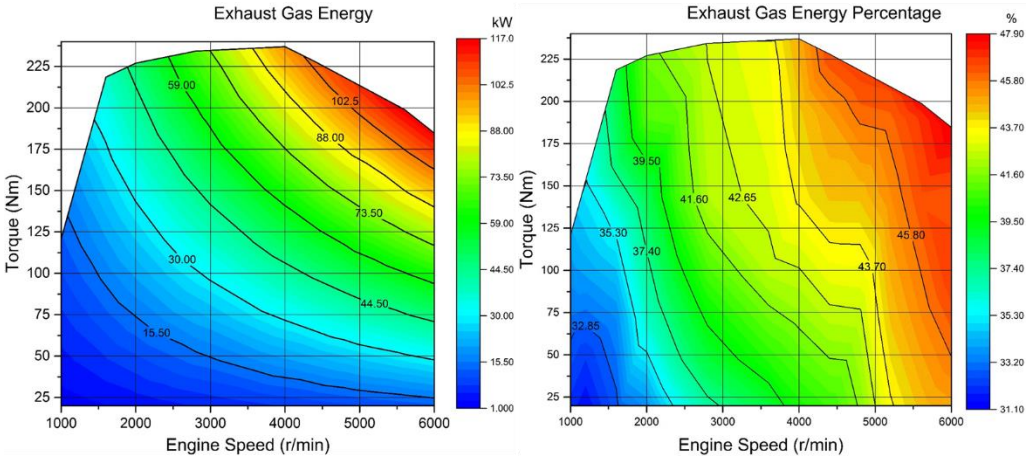


Figure 6-7 Contours of exhaust gas energy and energy percentage

It is obviously from the figure that the exhaust gas energy percentage increases with the increment of engine speed and torque. When the engine is operating at a relatively high load, the combustion is not sufficient, most of the energy generated by combustion cannot be converted into mechanical power, and is expelled with exhaust gas. However, according to the contour, engine speed has more influence on the percentage of exhaust gas energy. This may be because the exhaust gas volume is related to the engine speed. Regarding to the certain specific heat, the higher volume means higher heat. This contour is also a guide for the connection of each TEM and the MPPT unit in the TEG system.

6.4.2 **Power Generation of Concentric Cylindrical TEG System under Standardised Driving Cycle**

From the analysis in part 6.1, the mass flowrate and temperature of exhaust gas will fluctuate all the time during real-time driving, and their fluctuation have a

significant effect on the power output of the concentric cylindrical TEG system. According to the exhaust gas properties, the electric power generated by the TEG system can be calculated by the model mentioned in part 6.3, which is shown in Figure 6-8, the power output contour of TEG system.

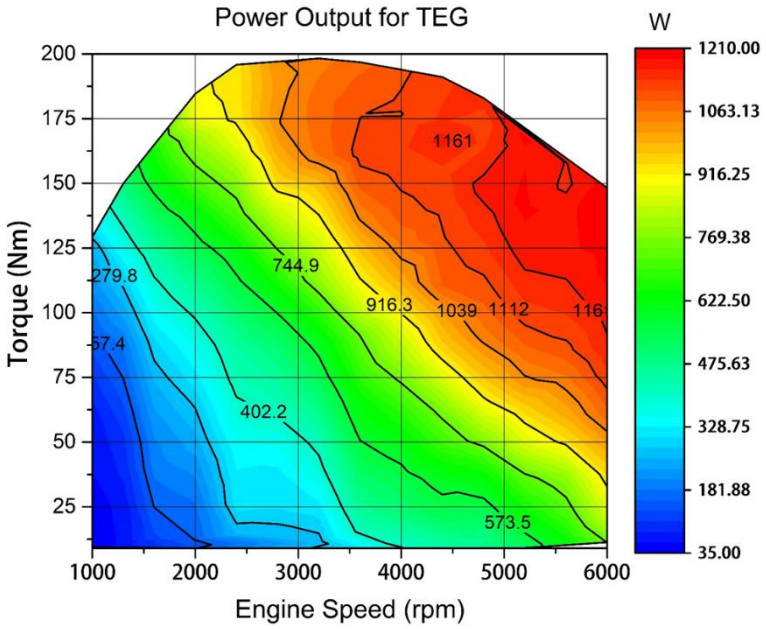


Figure 6-8 Contour of power generation of concentric cylindrical TEG system

As is shown in this figure, the electric power output rises with the increment of engine speed and torque and reaches its peak value with 1210 W around 6000 rpm and 135 Nm. By compared to the contour of exhaust gas energy, the power output of the TEG system shows a decent consistency with the energy of exhaust gas, but there is still some differences between these two contours. Firstly, the exhaust energy in the lower engine torque stays almost the same, because the mass flowrate of the exhaust gas remains nearly in the same level. However, for the power output of TEG system, with the increment of engine speed, the velocity of exhaust gas will boost which will improve the convection heat transfer between exhaust gas and heat

pipe heat-exchanger and broaden the temperature difference between hot and cold side of TEM, so the power output of the TEG system will ascend with engine speed. Secondly, the power output of TEG system at high engine speed and torque is not as stable as the exhaust gas energy. This is because the conviction heat transfer, at high engine speed and torque, becomes more unsteady. The drastic changes in the temperature and velocity of exhaust gas have a substantial effect on convection heat transfer, thus will cause an enormous fluctuation in the temperature difference between hot and cold side of TEM. These two differences will affect the performance of TEG system on the improvement of vehicle fuel consumption.

In order to demonstrate the power output of the concentric cylindrical TEG system under real-time driving, the WLTP class 3 driving cycle is employed in this study. The WLTP class3 driving cycle is used for calculating the fuel economy and emission of a vehicle with a ratio of rated power over 34, and the whole driving cycle has 4 phases in total. Figure 6-9 shows the whole driving cycle in vehicle speed versus time. Normally, the WLTP class 3 driving cycle has 1800 seconds and the cycle is divided into 4 phase: low speed phase, medium speed phase, high speed phase and extra-high speed phase. Each phase has different period of time and maximum vehicle speed. The low speed phase has the longest period of time and the lowest maximum vehicle speed which is similar to the real-time urban driving condition, on the contrary, the extra-high speed phase has the shortest period of time and highest maximum vehicle speed which is similar to the real-time high-way driving condition.

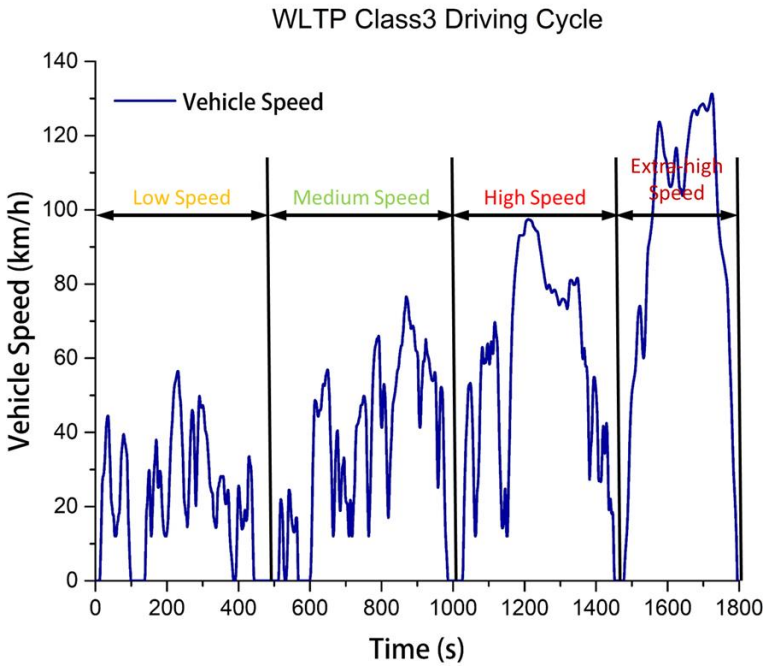


Figure 6-9 Vehicle speed in WLTP class 3 driving cycle

By given the contours of exhaust gas properties and the vehicle speed of WLTP class3 driving cycle, the engine speed and torque can be calculated by the model established in GT-suite. Figure 6-10 shows the engine speed and torque, as well as, the exhaust gas properties under WLTP class3 cycle. As shown in the figure, the engine speed is fluctuating between 946 and 4000 rpm, while the engine torque varies from 12 to 236 Nm. Furthermore, the variation of both two parameters is related to vehicle speed all the time during the cycle and in the same pattern with vehicle speed. This is because the vehicle speed was regarded as a contributing factor in the establishment of the fuel consumption model and other influencing factor, such as road, driver and ambient, was ignored.

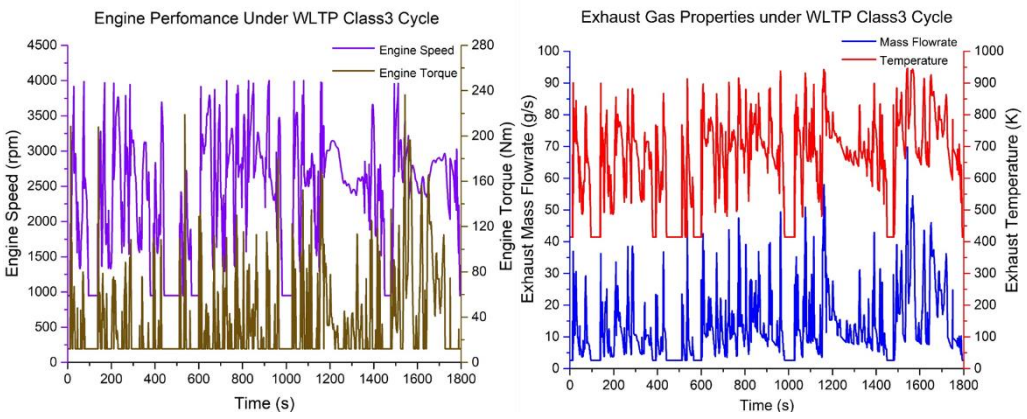


Figure 6-10 Engine speed and torque & exhaust properties under WLTP class3 cycle

The exhaust gas properties for the engine, under WLTP class3 cycle, can be calculated by the established model in GT-suite, mentioned in part 6.1, as well. As these two parameters fluctuate with the change of engine speed and torque, the maximum mass flowrate and temperature of exhaust gas are 69.84 g/s and 945.75 K, respectively, while the minimum mass flowrate and temperature of exhaust gas are 2.6 g/s and 413.72 K, respectively. The lowest mass flowrate and temperature of exhaust gas appears in the idling of the vehicle between each phase of the WLTP class3 cycle, and during these periods of time the power output of TEG system will be lowest. As the power will not cover the penalty from the pumping water and backpressure increment, the fuel consumption will be increased during these periods of time.

The temperature difference between the hot and cold side of TEM and the power output of concentric cylindrical TEG system under WLTP class3 cycle are shown in Figure 6-11. Because the temperature difference will reduce along the direction of the exhaust gas flow, the temperature difference shown here is chosen from the TEG located in the middle of the TEG system, only to represent the tendency of the

temperature difference between the hot and cold side of each TEM in the system. The temperature difference varies from 9.96 K to 162.44 K. Furthermore, because of the employment of water cooling, the cold side of TEM has a limited temperature change of 10 K, which will improve the thermal mismatch of the TEG system.

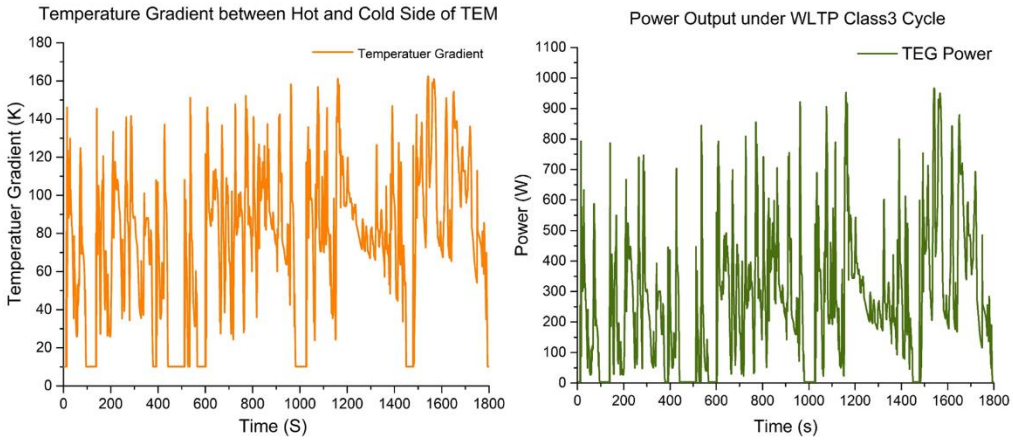


Figure 6-11 Temperature grad difference ient and power output under WLTP class3 cycle

Furthermore, the total power generated is 487.68 kW and the power output varies from 4.03 W to 966.17 W as shown in the figure. The power output is calculated by the TEG system model described in Section 4.3, which has no MPPT circuit for boosting the voltage. The TEG system will not reach its peak point of power output during the whole driving cycle, and will generate more power in the extra-high speed phase, due to relatively high engine speed and torque. Normally, there must be a MPPT circuit for stabilizing the output voltage of the TEG system at 14 V for matching the vehicle accessories, as the actual voltage of the TEG system varies between 4 V to 66 V. As a result, there will be around 5% energy loss in the MPPT circuit as mentioned in Section 6.3, which means the total power charge to the

accumulator will be around 463.3 kJ. In addition, as introduced in Chapter Three, all the TEMs will be connected in series, actually most of the electric power was consumed by the internal resistance of TEMs. In order to improve the total power output of TEG system, the internal electrical connection needs to be taken into account as well during the design stage.

6.4.3 Improvement of Fuel Economy under Standardised Driving Cycle

After getting the power output of concentric cylindrical TEG system under WLTP class3 driving cycle, the fuel economy improvement under WLTP class3 driving cycle can be calculated by the fuel consumption model built in part 6.3.

In the first place, the original fuel consumption of the engine was obtained in the test rig, and Figure 6-12 shows the contour of specific fuel consumption of the vehicle. It is can be found in the figure that the specific fuel consumption ranges from 258 g/kWh to 958 g/kWh and the lowest point is concentrated in the middle of the contour around 3000rpm and 150Nm, which means the engine consume the least amount of gasoline. Because of the engine calibration, the engine will be working in this region in most of the time, during real time driving. The economic mixture will be supplied to the engine on the purpose of reducing fuel consumption. The relatively higher specific fuel consumption is concentrated at low engine torque and the peak point appears at high engine speed and low torque. However, in the real-time driving, the engine basically does not work in this region.

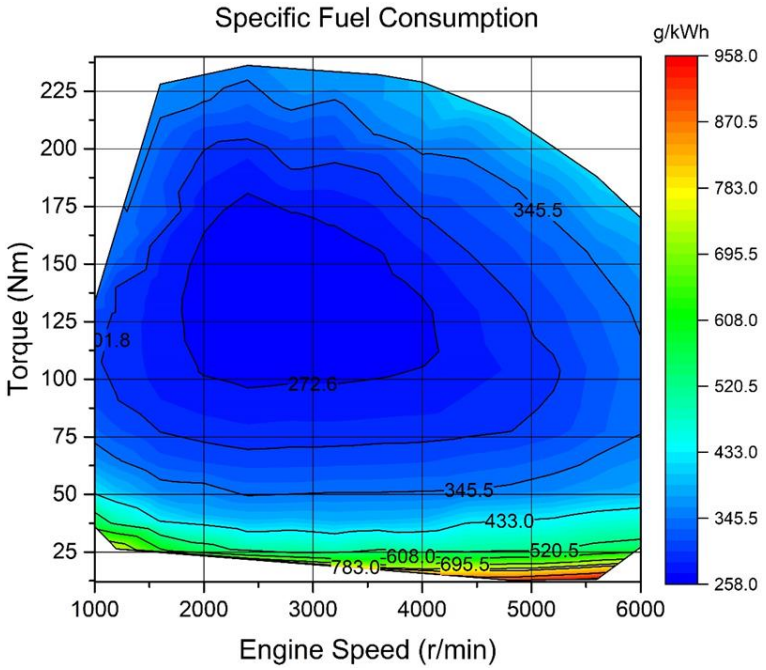


Figure 6-12 Contour of specific fuel consumption of the test vehicle

Figure 6-13 shows the contour for the percentage of fuel consumption improvement by employing concentric cylindrical TEG system. From the figure, it is shown that the highest percentage of fuel economy improvement is 5.22% at high engine speed and low torque. This is because the fuel consumption at this area is the highest as shown in the previous figure, nonetheless, the engine will not be working in these conditions during whole driving cycle. Moreover, the relatively higher fuel saving area is at middle range of engine speed and higher torque. This is because the fuel economy penalty from back pressure is lower and the power generated by TEG system is higher within this area. However, even though the peak power output of concentric cylindrical TEG system is in the high engine speed and high torque area, the improvement of fuel economy is not outstanding due to the substantial penalty from back pressure and water pump.

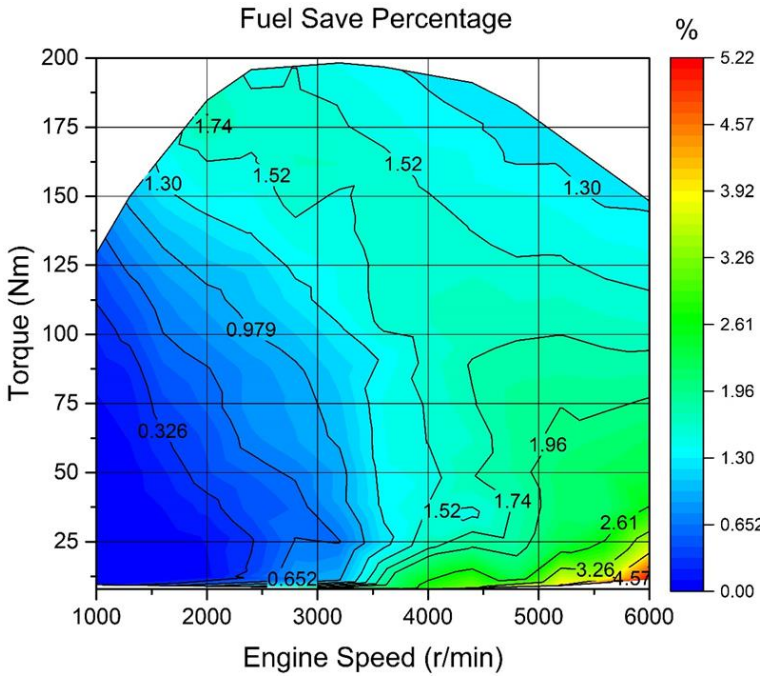


Figure 6-13 Contour of the percentage improvement in fuel consumption by utilising concentric cylindrical TEG system

The total fuel economy improvement under WLTP class3 cycle by employing a concentric cylindrical TEG system can be calculated by having contour for the percentage of fuel consumption improvement. As mentioned in the previous part, during the engine is idling between each phase of the driving cycle, the concentric cylindrical TEG system is barely generating only electric power. As a result, the fuel economy improvement during these periods of time will be negative, as the vehicle accessories are still working. The TEG system also weights about 40 kg, the increment of total weight of vehicle will negate the improvement in fuel economy. The highest decrease in fuel economy improvement will be 1.97 % during the whole driving cycle.

Figure 6-14 shows the total decrement of fuel consumption under different driving cycles. In this present work, the WLTP driving cycle is compared with

Federal Test Procedure (FTP) and New European Driving Cycle (NEDC), which are previous test driving cycles in United States and Europe. From the figure, it can be seen the improvement of fuel economy under FTP and NEDC driving cycles are lower than 1 %, however the improvement under WLTP driving cycle is around 1.64 %. This is because the average vehicle speed of WLTP driving cycle is higher than that of the other two cycles, especially during the high speed phase and extra-high speed phase. Higher speed allows the vehicle works at relatively higher engine speed and torque, which means the concentric cylindrical TEG system will operate within its optimal range and save more gasoline during the WLTP class3 driving cycle.

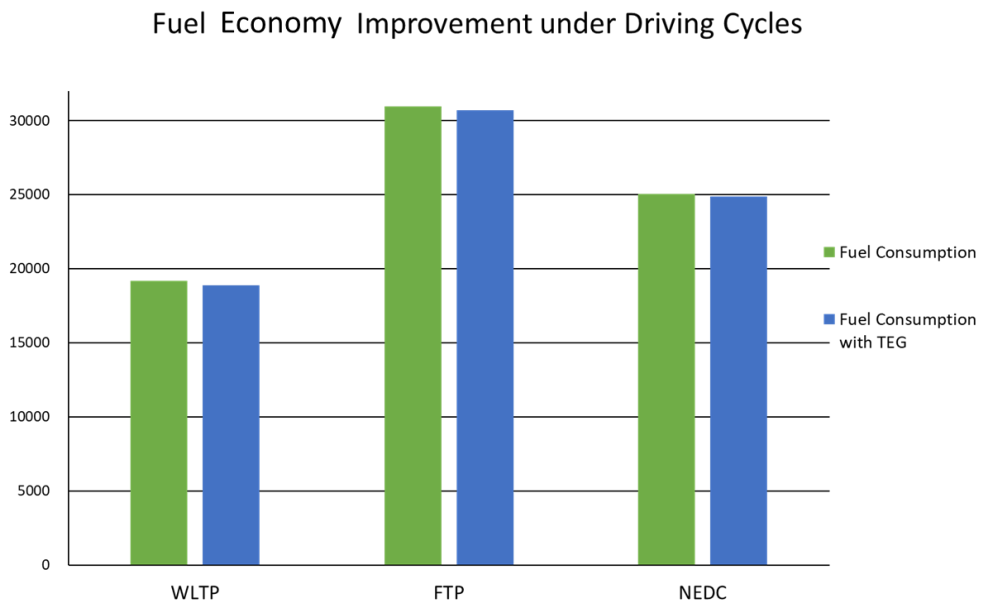


Figure6-14 Fuel economy improvement under different driving cycle

6.5 Summary

In this paper, a conjugated model of fuel consumption for a vehicle with a concentric cylindrical TEG system is established. By taking the negative factors of

water pump, back pressure, weight and alternator, the model is combined two different sub-models. One is the vehicle, engine and TEG system model in GT-suite to calculate the exhaust gas properties under standardised driving cycles. Another is the MATLAB Simulink model to calculate the total improvement of fuel economy. The engine model was also verified by data from an experimental test for giving an accurate boundary condition of the fuel consumption model. The results of the simulation are as follows:

- The exhaust gas energy of the engine tested in the paper ranges from 1 kW to 117 kW, and the percentage of the total energy generated by fuel combustion varies from 31.1 % to 47.9 %. These results prove that, one third of the engine energy generated by combustion is expelled by the exhaust gas. In order to improve fuel economy of vehicle, the WHR is imperative.

- The total electric power generated under WLTP class3 driving cycle is 463.3 kJ, with the peak power output at 966.17 W. During a few periods of time in the driving cycle, the fuel economy improvement is negative due to the penalties from other factors. This result offers a guide for improving the matching between TEG systems and vehicles, in the future research on TEG systems.

- The total fuel economy improvement under WLTP class3 driving cycle is 1.64 %, compared to 0.74 % for FTP driving cycle and 0.75 % for NEDC driving cycle, respectively.

- Because of the fluctuation of exhaust temperature during the real-time driving, the temperature between hot and cold side of each TEM is unstable. In order to boost the efficiency of the whole system, an energy storage system is needed

for stabilizing the temperature of TEG system. Further investigation will be conducted in the future research.

- The electric connection between each TEM in the concentric cylindrical TEG system still need to be improved, because most of the power generated by TEM is consumed by the internal resistance of themselves. In order to achieve a higher efficiency, a more rational connection between each TEM is necessary.

Chapter 7. Experimental Investigation for Transient Performance Improvement of TEG by Integrating Phase Change Material

7.1 Introduction

As aforementioned, the properties of exhaust gas such as temperature and mass flow rate are fluctuating according to the driving condition of vehicle in real-time application. It is unpredictable of the temperature distribution within TEG systems during its design process. As a result, an accessional energy storage system for accumulating thermal energy from exhaust gas, and improves transient performance of TEG system is necessary in practical application of TEG system. In this part of research, a brief introduction to energy storage systems and phase change materials (PCM) is presented at the beginning. Thereafter, the feasibility of a latent thermal energy storage system for Bismuth-Telluride (Bi_2Te_3) based TEM is investigated experimentally. The results of the experimental study show an acceptable potential of improving transient performance for TEG systems by integrating PCMs.

7.1.1 Background

According to the analysis in Chapter Six, the temperature of engine exhaust gas is varying from under 300 ℃ to over 800 ℃, hence the hot-side temperature of concentric cylindrical TEG system is fluctuating from under 100 ℃ to over 240 ℃. The most commercially used TE material is Bi_2Te_3 whose optimal working temperature is around 190 ℃. Although the optimal working temperature of Bi_2Te_3 TEM is located within the hot-side temperature of the concentric cylindrical TEG system, the fluctuating driving conditions will curtail the efficiency of the system.

Moreover, in most periods of urban driving conditions, the hot-side temperature will not achieve more than 180 ℃, except during vehicle accelerating process. Therefore, an energy storage system is improving not only the transient performance of concentric cylindrical TEG system, but also the total efficiency of the system.

The most suitable thermal energy storage system for automotive WHR is a latent thermal energy storage system such as PCM [226, 227]. However, not much research into PCM integration in the automotive TEG system has been conducted. Altstedde et al. [155] carried out a numerical investigation on integration of PCM into automotive TEG for stabilising transient amounts of heat. Results showed that automotive TEG system with PCM has a 29% higher energy yield than a conventionally constructed TEG system. Additionally, most of the existing research about PCM and TEG system is focusing on the cold side of the system with paraffin and its derivatives. Jo et al. [228] conducted a series of experiments on a TEG system embedded in paraffin for waste heat harvesting. Results showed that the TEG continuously produced electrical power after the heat source was removed. Yin et al. [229] studied the performance of photovoltaic and PCM-TEG hybrid system. A series of comparative experiments are carried out to reveal the effects of different PCM containers on thermal resistances. Results showed that copper foam has a better effect on decreasing the thermal resistance of paraffin than the expanded graphite. Moreover, paraffin/expanded graphite composite and fins has the best performance in the coupling system among researched PCM containers.

Nonetheless, improving the hot-side heat flux of the TEG system is the vital issue for improving total efficiency of TEG system, because the hot side is the energy

source of the system and enhancement of hot-side heat flux means more energy is absorbed. Therefore, a suitable PCM for TEG hot-side application is more pivotal than that for cold-side application. One drawback of PCM integrated TEG system is the low thermal conductivity of PCM as its own physical property. There are some investigations on improving the thermal conductivity of PCM by metal foam or mixing powder of high thermal conductivity substance.

The following content will be a brief literature review on energy storage systems, PCM for thermal energy storage and heat transfer enhancement for PCMs.

7.1.2 Energy Storage System

In order to rationally use energy and improve energy utilisation, energy storage is the capture of temporarily excess energy for a certain period of time with a sort of method and extract it during the peak usage or in a place where energy is scarce [230]. A system with this kind of function, which can store energy for later usage, is generally called an energy storage system. The basic purpose of an energy storage system is to overcome the temporal or local differences between energy supply and demand and there are two situations responsible for causing these differences. One is a sudden change in energy demand and the other is the energy conversion devices for primary energy. Therefore, an energy storage system can accumulate excess heat energy, kinetic energy, electric energy, potential energy or chemical energy and adjust energy output capacity, location and time. Some technologies provide short-term energy storage, while others can endure for much longer.

Energy storage systems often involve multiple energies, devices, substances and processes and usually includes the inlet and outlet of energy and mass and complex

energy conversion and storage equipment. There are different requirements for different energy storage application purposes. In summary, the common characteristics of energy storage system are as follows [231]:

- High rate of energy stored per unit volume
- Good regulation performance for different load
- High efficiency in energy storage
- Low cost and long-term reliability

The energy storage mainly includes the storage of energy such as thermal energy, kinetic energy, electric and electromagnetic energy, chemical energy and electrochemical energy. The different energy storage technologies are shown in Table7-1. At present, the research, development and application of energy storage technologies are mainly based on thermal energy and electric energy. It is widely used in field of solar energy, power plant, air conditioning and WHR. The following part gives a brief introduction for different energy storage system and their advantages and disadvantages are listed in Table 7-2.

7.1.2.1 Mechanical energy storage

The most commercially applied mechanical energy storage system is pumped-storage hydroelectricity, which uses mechanical energy to pump the water to a higher elevation or move solid matter to higher locations (gravity batteries). At times of low electrical demand, excess generation capacity is used to pump water from a lower source into a higher reservoir. When demand grows, water is released back into a lower reservoir (or waterway or body of water) through a turbine, generating electricity. Nearly all facilities use the height difference between two

water bodies. Pure pumped-storage plants shift the water between reservoirs, while the “pump-back” approach is a combination of pumped storage and conventional hydroelectric plants that use natural stream-flow [232].

Table 7-1 Energy storage technologies

Mechanical	Electrical	Electro-chemical	Thermal	Chemical
• Compressed air • Flywheel • Pumped-storage hydroelectricity	• Capacitor • Super capacitor • Superconducting magnetic	• Flow battery • Rechargeable battery • Ultra Battery	• Cryogenic energy storage • Phase-change material • Seasonal thermal energy storage	• Biofuels • Hydrogen storage • Power to gas

Other commercial mechanical energy storage methods include compressing air and flywheels that convert electric energy into kinetic energy and then back again when electrical demand peaks. Compressed air energy storage system uses surplus energy to compress air for subsequent electricity generation. Small scale systems have long been used in such applications as propulsion of mine locomotives. The compressed air is stored in an underground reservoir, such as a salt dome. Flywheel energy storage system works by accelerating a flywheel to a very high speed, holding energy as rotational energy. The flywheel energy storage system is employed to recover and reuse kinetic energy captured during braking. When energy is extracted, the flywheel’s rotational speed declines as a consequence of conservation of energy; adding energy correspondingly results in an increase in the speed of the flywheel [233, 234].

7.1.2.2 Thermal energy storage

Thermal energy storage system is the temporary storage or removal of heat and normally there are two different type of thermal energy storage system. The first type is sensible thermal energy storage system, which allows heat, or cold to be used months after it was collected from waste energy or natural sources. The material can be stored in contained aquifers, clusters of boreholes in geological substrates such as sand or crystalline bedrock, in lined pits filled with gravel and water, or water-filled mines. Seasonal thermal energy storage projects often have paybacks in the four-to-six year range [235, 236].

Another type of thermal energy storage system is latent thermal energy storage systems, which works with materials with high latent heat capacity, known as PCM. The main advantage of these materials is that their latent heat storage capacity is much more than sensible heat. Latent-heat thermal energy storage system consists of a process by which, energy in the form of heat, is either absorbed or released during the phase-change of a PCM. During the phase change process, a PCM has the capacity to absorb large amounts of thermal energy for later usage in a specific temperature range due to its high latent heat [237, 238].

7.1.2.3 Electrochemical energy storage

The most commonly used electrochemical energy storage system is the rechargeable battery, which is used in our daily life. A rechargeable battery, comprises one or more electrochemical cells. It is known as a 'secondary cell' because its electrochemical reactions are electrically reversible. Rechargeable batteries come in many different shapes and sizes and have lower total cost of usage

and environmental impact than non-rechargeable batteries. Common rechargeable battery chemistries include: lead–acid batteries, nickel–cadmium batteries, nickel–metal hydride batteries and lithium-ion battery [239].

A flow battery is another type of electrochemical energy storage system, which operates by passing a solution over a membrane where ions are exchanged to charge/discharge the cell. Cell voltage is chemically determined by the Nernst equation and ranges, in practical applications, from 1.0 to 2.2 V. Its storage capacity is a function of the volume of the tanks holding the solution. A flow battery is technically akin both to a fuel cell and an electrochemical accumulator cell. Commercial applications are for long half-cycle storage such as backup grid power [240].

Supercapacitor, also called electric double-layer capacitor or ultra-capacitor, is a generic term for a family of electrochemical energy storage systems that do not have conventional solid dielectrics. Capacitance is determined by two storage principles, double-layer capacitance and pseudo capacitance. Supercapacitors bridge the gap between conventional capacitors and rechargeable batteries. They have the highest energy density among capacitors. They support up to 10,000 farad/1.2 V, which is about 10,000 times that of electrolytic capacitors, but deliver, or accept less than half as much power density. While supercapacitors have specific energy and energy densities that are approximately 10% of batteries, their power density is generally 10 to 100 times greater. This results in much shorter charge/discharge timing and they will tolerate many more charge and discharge cycles than rechargeable batteries [241].

7.1.2.4 Chemical energy storage

Power to gas technology is a certain kind of chemical energy storage method, which converts electricity into a gaseous fuel such as hydrogen or methane. There are three commercial methods that use electricity to decompose water into hydrogen and oxygen by means of electrolysis. In the first method, hydrogen is injected into the natural gas grid or is used in transport or industry. The second method is to combine the hydrogen with carbon dioxide to produce methane using a methanation reaction. The third method uses the output gas of a wood gas generator or a biogas plant to upgrade the quality of the biogas. Power to liquid is similar to power to gas, however the hydrogen produced by electrolysis from wind and solar electricity isn't converted into gases such as methane but into liquids such as methanol. Methanol is easier to handle than gases, and requires fewer safety precautions than hydrogen. It can be used for transportation, including aircraft, but also for industrial purposes or in the power sector [242, 243].

7.1.2.5 Electrical energy storage

The most common electrical energy storage system is the capacitor with a passive two-terminal electrical component used to store energy electrostatically. A capacitor can store electric energy when disconnected from its charging circuit, so it can be used like a temporary battery, or like other types of rechargeable energy storage system. Capacitors are commonly used in electronic devices to maintain power supply while batteries charge and this prevents loss of information in volatile memory [244, 245].

Table 7-2 Comparison between different energy storage system

Category	*Type*	*Advantages*	*Disadvantages*
Mechanical energy storage	Pumped-storage Hydroelectricity	High efficiency around 75%	Difficulties in site selection
	Compressing Air	Without secondary conversion	Low energy storage efficiency
	Flywheel	High reliability	Low energy density
Thermal energy storage	Sensible Heat Thermal Storage	Very large thermal storage Low cost	Location restriction Long storage cycle
	Latent Heat Thermal Storage	Temperature feasibility Higher energy density	Corrosive Decomposition Complex system
Electrochemical energy storage	Rechargeable Battery	Most Cost-effective High efficiency	Low energy storage capability Explosive at high temperatures
	Flow Battery	Energy store for hours to days	Large size Expensive Complex system
	Super Capacitor	Long life-cycle Short charging time	Low energy density High material cost
Chemical energy storage	Power to Gas	Facile raw materials	Low cycle efficiency High requirement in gas storage
	Power to Liquid	Facile raw materials	Low cycle efficiency High safety requirement
Electrical energy storage	Capacitor	Low cost Compact volume	Low energy storage capability
	Superconducting	Minimal energy loss Quick response	High material cost Low reliability

Superconducting magnetic energy storage systems accumulate energy in a magnetic field created by the flow of direct current in a superconducting coil that has been cooled to a temperature below its superconducting critical temperature. A typical superconducting magnetic energy storage system includes a superconducting coil, power conditioning system and refrigerator. Once the

superconducting coil is charged, the current does not decay and the magnetic energy can be stored indefinitely. The stored energy can be released to the network by discharging the coil. The associated inverter/rectifier accounts for about 2–3 % energy loss in each direction. Superconducting magnetic energy storage systems lose the least amount of electricity in the energy storage process compared to other methods of storing energy by offering round-trip efficiency greater than 95 % [246, 247].

7.1.3 PCM for Thermal Energy Storage

In this project, in order to improve the transient performance of TEG system under real-time driving conditions especially during vehicle deceleration, a thermal energy storage system is imperative. With the additional thermal energy storage system, the excess thermal energy during car acceleration or high speed driving could be collected and released when the vehicle decelerates. This could diminish the temperature fluctuation on both sides of the concentric cylindrical TEG system, but specifically hot-side temperature. As a result, the transient performance of the concentric cylindrical TEG system can be enhanced by obtaining a higher hot-side temperature.

As mentioned above, there are two different kinds of thermal energy storage system: sensible thermal energy storage and latent thermal energy storage. Compared to sensible thermal energy storage, latent thermal energy storage has the advantages of bigger energy storage density, smaller volume, higher efficiency, fixed temperatures for charging and discharging, etc. These advantages make latent thermal energy storage more suitable for the application in waste heat recovery. The

commonly known latent thermal energy storage system is PCMs. PCMs as reliable methods of thermal energy storage have broad applications in multiple area.

A PCM is a substance with a high heat of fusion, which is capable of storing and releasing large amounts of thermal energy, during melting and solidifying at a certain temperature [248]. Heat is absorbed or released when the material changes from one phase to another and vice versa. The thermal energy storage in PCMs can be achieved through phase changes such as liquid to solid, solid to solid and liquid to gas. Initially, PCMs behave like sensible thermal energy storage materials and their temperature rises as they absorb heat. With the temperature continuously increasing, unlike sensible thermal energy storage materials, PCMs absorb large amounts of heat at an almost constant temperature when they reach their phase conversion temperature. The PCM continues to absorb heat without a significant rise in temperature until all the material is transformed to another phase. The storage capacity Q_s of a PCM medium [249] is given by

$$Q_s = \int_{t_i}^{t_m} mc_p dt + mf\Delta q + \int_{t_m}^{t_f} mc_p dt \qquad \text{Eq. 7-1}$$

$$Q_s = m\left[c_{ps}(t_m - t_i) + f\Delta q + c_{pl}\left(t_f - t_m\right)\right] \qquad \text{Eq. 7-2}$$

where t_m is the melting temperature; m is the mass of PCM; c_p is the average specific heat of PCM; f is the melt fraction and Δq is the latent heat of fusion.

A large number of phase change materials are available in any required temperature range. A general duty classification of PCMs is given in Figure 7- 1 [236] and the temperature range of different PCMs is shown in Figure 7-2 [250]. Nowadays, the most widely used PCMs are solid-liquid PCM and solid-solid PCM, and solid-liquid PCM includes organic, inorganic and eutectic categories. In general,

inorganic PCMs have almost double the volumetric latent heat storage capacity than the organic PCMs. For their very different thermal and chemical behavior, the properties of each sub classification, which affects the design of latent heat thermal energy storage systems using PCMs of that sub classification, are discussed in detail below.

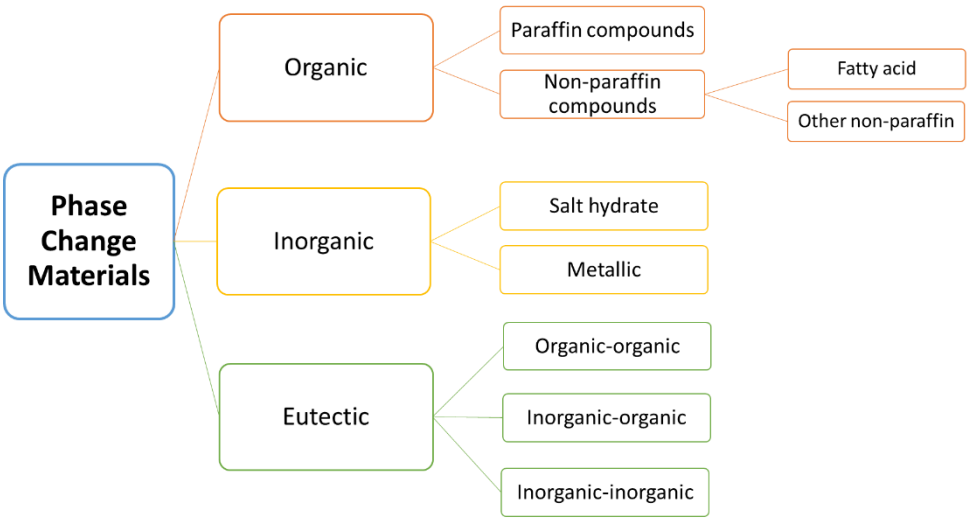


Figure 7- 1 General classification of PCMs

1. Organic PCMs

Organic PCMs can melt and solidify many times without phase segregation, and because of the degradation during their melting, they crystallize with little or no super-cooling and are usually non-corrosive. Organic PCMs are further described as paraffin material and non-paraffin material.

(1) Paraffin waxes consist of a mixture of mostly straight chain n-alkenes CH_3-(CH_2)-CH_3. The crystallization of the CH_3 chain releases a large amount of latent heat. Both the melting point and latent heat of fusion increase with chain length. Due to cost consideration, however, only technical grade paraffin may be used as

PCMs in latent heat storage systems. Paraffin is safe, reliable, predictable, less expensive, non-corrosive, and available in a large temperature range (5 - 200 ℃).

(2) Non-paraffin organic PCMs are the most numerous of the PCMs with highly varied properties. A number of esters, fatty acids, alcohols, and glycols suitable for energy storage have been identified [251]. Main features of these organic materials include high heat of fusion, inflammability, low thermal conductivity, low flash points, and instability at high temperatures.

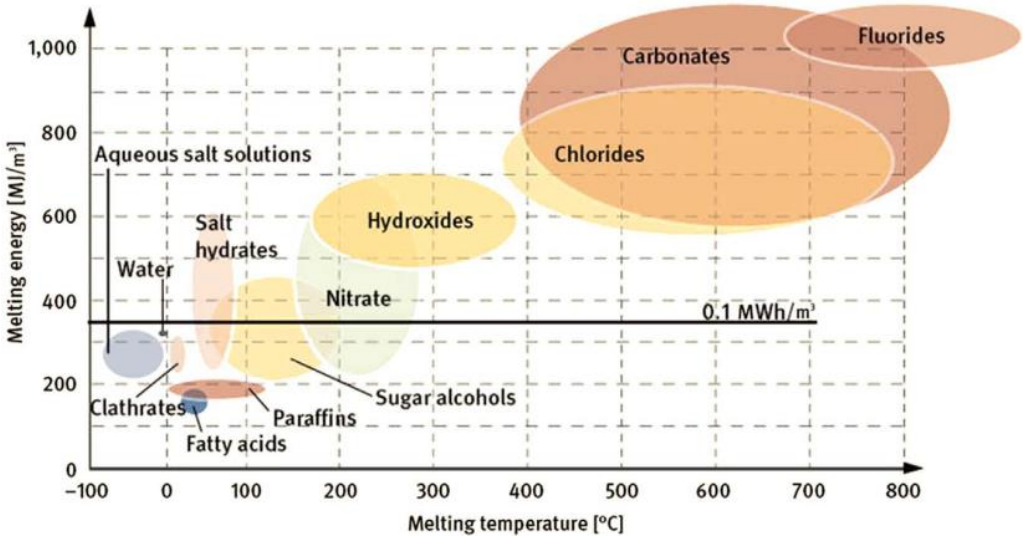


Figure 7-2 Temperature range of different PCMs [250]

2. Inorganic PCMs

Inorganic PCMs are mostly used in high-temperature applications and one of the most reported challenges is their maintenance. These PCMs do not super-cool appreciably and their melting enthalpies do not degrade with cycling. Inorganic PCMs are further classified as salt hydrate and metallic.

(1) Salt hydrates are alloys of inorganic salts and water, forming a typical crystalline solid of general formula AB_nH_2O, whose solid–liquid transition is

actually a dehydration and hydration of the salt. Salt hydrates have been extensively studied in heat storage applications because of their positive characteristics: high latent heat of fusion per unit volume, a relatively high thermal conductivity (almost double that of paraffin), low corrosiveness, and compatibility with plastics. Some disadvantages include incongruent melting and super-cooling, spontaneity of salt hydrates and lower number of water moles during the discharge process. Adding chemicals can prevent the nucleation of lower salt hydrates, which preferentially increases the solubility of lower salt hydrates over the original salt hydrates with a higher number of water moles.

(2) Metallic includes the low melting point metals and their alloys. They are scarcely used in heat storage applications because of their low melting enthalpy per unit weight, even if they have high melting enthalpy per unit volume and high thermal conductivity [252]. Some of the features of these materials are as follows: low heat of fusion per unit weight, high heat of fusion per unit volume, high thermal conductivity, high specific heat and relatively low vapour pressure. Such materials are utilised for their ability to help meet the high demands of large capacity power plants. An inorganic mixture based on an industrial by-product was developed and characterized for its application as a PCM for low-temperature thermal energy storage [253].

Normally, organic PCMs have many advantages over inorganic PCMs, but they are flammable and have low thermal conductivity. On the other hand, inorganic PCMs are cheaper, abundant, non-flammable and have high heat storage capacity and thermal conductivities.

3. Eutectics PCMs

A eutectic PCM is a combination of two or more low melting materials with similar (congruent) melting and freezing points. Eutectic nearly always melts and freezes without segregation since they freeze to an intimate mixture of crystals, leaving little opportunity for the components to separate. The weight percentage of each material can be varied to obtain variations in the melting point of the resulting eutectic mixture. For this reason they are a promising type of PCM, even if they are actually less diffused than the other groups. However, they have low latent and specific heat capacities [251].

The advantages and disadvantages of each PCM are listed in the Table 7-3.

At present only solid-liquid phase changes are most practical application in PCMs. Although liquid to gas transitions have a higher heat of transformation than solid-liquid transitions, liquid to gas phase changes are impractical for thermal energy storage because large volumes change or high pressures are required to store the materials during their gas phase.

Besides the normal classification of PCMs mentioned above, a specialized group of PCMs undergo a solid-solid phase transition with the associated absorption and release of large amounts of heat. These materials change their crystalline structure from one lattice configuration to another at a certain temperature, and the transformation can involve latent heats comparable to the most effective solid-liquid PCMs. Such materials are valuable because, unlike solid-liquid PCMs, they do not require nucleation to avoid supercooling. Additionally, because the phase change process is simply transformation in the solid state, there is almost no volume

change during the transformation, and there are no issue of material encapsulation due to no liquid phase of the PCM.

Table 7-3 Advantages and disadvantages of different type of PCM

PCM	Advantages	Disadvantages
	Organic	
Paraffin	• Cost Effective • Non-corrosive • Large Temperature Range	• Low Thermal Conductivity • Low Melting Point • Highly Volume Change • Flammable
Non-paraffin	• High Heat of Fusion • Low Flash Points	• Low Thermal Conductivity • High-temperature Instability
	Inorganic	
Salt hydrate	• High Heat of Fusion • High Thermal Conductivity • Non-flammable • Good Compatibility	• Phase Segregation • Super-cooling • Corrosiveness
Metallic	• High Thermal Conductivity • High Specific Heat	• Low Heat of Fusion • Expensive
	Eutectic	
Eutectics	• High Latent Heat • Sharp Melting Point	• High Volume Change • Super-cooling

However, solid-solid PCMs are not given enough attention due to their smaller latent heat and higher phase change temperatures, which are undesirable in low-temperature heat storage applications. Solid-solid PCMs, when compared to solid-liquid PCMs, have the advantages of a smaller volume change, no leakage, smaller erosion, longer lifespan. Nonetheless, the higher phase change temperature of solid-solid PCMs is desirable for automotive waste heat recovery. Moreover, the low

volume change ratio is exactly suitable for vehicles, due to the limited space availability in vehicle chassis. Most promising materials are organic solid solution of Pentaerythritol, Pentaglycerine, Li_2SO_4 and KHF_2 [254].

7.1.4 **Heat Transfer Enhancement for PCM**

As discussed in the previous section, most PCMs have relatively low heat transfer coefficient due to their own physical properties. However, this is contradictory for their application in thermal energy storage, because in heat transfer application the materials are expected to have high thermal conductivity. As a result, the heat transfer enhancement for PCM is essential for all the practical application [255].

In the past few years, there are plenty of studies on the heat transfer enhancement for PCM either in material aspect or in heat exchanger aspect. Lin et al. [256] reviewed the methods of thermal conductivity enhancement for PCM in thermal energy storage. The methods are roughly divided into two types: adding substances with high thermal conductivity and microencapsulated. Substances with high thermal conductivity include carbon-based materials, metal-based materials and other materials. Microencapsulated is made up of PCM shelled by emulsion polymerization, interfacial polymerization, mini-emulsion polymerization and other methods. Velraj et al. [257] investigated three different methods of heat transfer enhancement for paraffin, which are internal finned tube, Lessing-ring filling and water-poured tube. Results showed heat transfer enhancement with fin configuration and by using Lessing-ring in storage tanks is appreciable and these two methods are highly suitable for solidification enhancement. Rehman et al. [258] investigated the effect of heat transfer enhancement for copper foam and paraffin composites heat sinks. Results indicated that higher volume fraction of PCM

resulted in more decline in base temperature. Sohif et al. [259] numerically investigated the melting process in a triplex-tube heat exchanger with PCM and results showed that melting time of triplex-tube heat exchanger with fins is reduced by 56.7 % than that of triplex tube without fins. Stritih [260] carried out series experiment about heat transfer enhancement in rectangular PCM and gave a new correlation between the dimensionless numbers (Nusselt number as a function of Rayleigh number). The fin effectiveness showed that heat transfer during solidification is improved and about 40% reduction in the solidification time.

7.2 Test Section

In this part of project, an experimental investigation on transient performance improvement for TEG system by integrating PCM is carried out. As explained in Section 7.1, the solid-solid PCM is most suitable for TEG system in automotive WHR. In the following part, the criteria of PCM selection is discussed firstly. The material properties of Pentaerythritol (PE), which is used in this project, is presented. Moreover, the experimental test section applied in this project is given in detail and different cases are employed to compare the heat transfer improvement of PCM.

7.2.1 PCM Selection

A large number of PCMs are known to melt with a heat of fusion in any required range. However, for their employment as latent heat storage materials these materials must exhibit certain desirable thermodynamic, kinetic and chemical properties. Moreover, economic considerations and easy availability of these materials has to be taken into consideration. The PCM to be used as thermal-storage

systems should possess desirable thermal, kinetics and chemical properties, which are as follows [261, 262]:

- Thermal properties

When selecting a PCM for a particular application, the phase-changing temperature of PCM should be within in the operating temperature of the system. The latent heat should be as high as possible, especially on a volumetric basis, to minimize the dimension of the storage. Moreover, high thermal conductivity would be desirable for assisting the heat transfer within the energy storage system.

- Physical properties

Phase stability during liquefaction and solidification would help for the life cycle of the entire system and high density is desirable to reduce the size of the storage container. Small volume changes on phase transformation and small vapor pressure at operating temperatures could minimise the challenge for constraint problem.

- Kinetic properties

Supercooling has been a troublesome aspect of PCM development, particularly for salt hydrates. Supercooling of more than a few degrees will interfere with proper heat extraction from the system to device, and a 5–10 ℃ supercooling can prevent this process entirely.

- Chemical properties

PCM can suffer from degradation by loss of water for hydration, chemical decomposition or incompatibility with materials of construction. Moreover, PCMs should be non-toxic, nonflammable and non-explosive for safety.

- Economics

Low cost and large-scale availability are crucial when selecting a PCM for practical application.

In addition to the PCM selection, the design of containers for PCMs is another critical issue for thermal energy storage system, because during the phase-change process, the containers for PCMs will suffer variety of complex situations and maintain good sealing. Normally, the volume changes of the PCMs would also necessitate special volume design of the containers. It should be able to absorb these volume changes and should be compatible with the PCM used as well. Any latent heat energy storage system therefore, possess at least following three components:

- A suitable heat exchange surface
- Compatible with the PCM

According to the analysis above, in order to choose a suitable PCM for concentric cylindrical TEG system, the optimal operating temperature of the TEM should be discussed at first. Table 7-4 [263] shows the properties of mostly commercial Bi_2Te_3 TEM, which is utilised in this part of experimental investigation as well.

From the table, the optimal operating temperature for N-type and P-type leg is 162.4 ℃ and 221.1 ℃, respectively. Therefore, the suitable phase-changer temperature range for the employed PCM should be within 170 ℃ to 190 ℃. Moreover, considering the precise space requirements of the TEG system for automotive waste heat recovery, a solid-solid PCM is more desirable than liquid-solid PCM, because of the advantages of minimal volume change and simple sealing condition.

Table 7-4 Properties of Bi_2te_3 TEM

Properties	Value	Tolerance
Dimensions		
Width & Length	40 x 40 mm	± 0.02
Thickness	4.1 mm	± 0.1
Thermal Properties		
Max Hot Side Temperature	250 ℃	± 10
Max Cold Side Temperature	175 ℃	± 5
Thermal Conductivities	N: $k_n = 0.00003345 \times T^2 - 0.0233503 \times T + 5.60633$	
	P: $k_p = 0.00003638 \times T^2 - 0.0263513 \times T + 6.221262$	
Heat Flux	8.74 W/cm2	± 0.5
Electrical Properties		
Match Load	3.5 Ω	± 15 %
Match Load Power	6.99 W	Min.
Match Load Voltage	5.05 V	± 0.1
Match Load Current	1.38 A	± 0.05
Open Circuited Voltage	10.11 V	± 0.3
Seebeck coefficient	N: $\alpha_n = 0.00153074 \times T^2 - 1.08058874 \times T - 28.3381$	
	P: $\alpha_p = -0.0036381 \times T^2 + 2.7438095 \times T - 296.21439$	

7.2.2 **Material Properties and Preparation**

According to the analysis in previous part, a solid-solid PCM, Pentaerythritol (PE), is selected for the experimental test in this part of research. PE [2,2-bis(hydroxymethyl)-1,3-propanediol], is an organic compound with the formula

$C_5H_{12}O_4$ [264, 265]. The earliest research on PE as a PCM was in 2000 and this polyalcohol shows a phase transition in the solid state between 187- 189 ℃ (tetragonal to cubic structural change) [266]. Moreover, PE has small degree of supercooling and shows a decent thermal cycle stability [267]. The properties of PE is given in Table 7-5 [268] and Figure 7-3 [269] shows the chemical structure and molecule model of PE and the heating and cooling curves.

Table 7-5 Properties of Pentaerythritol

Properties		Value
Phase-change Temperature	Heating	183.8 ℃
	Cooling	167.2 ℃
Latent Heat	Heating	244.5 J/g
	Cooling	225.6 J/g
Molar Mass		136.15
Density		1.396 g/cm^3
Melting Point		260.5 ℃
Boiling Point		276 ℃

The material utilised in the experiment is Pentaerythritol (analytical reagent grade, purity 98.0%) in powder form which is purchased from Sigma Aldrich. For preparing the bulk material for experiment, PE powder is firstly weight by an electronic weight scale and spread evenly in a container. Then, locate the container on an electric heating plate and control the heating temperature between 260 ℃ to 276 ℃. While heating PE, continuing add PE powder to ensure the volume of bulk material, because there will be small amount of volatility. After the entire PE powder is liquefied, stop heating and place the container in an environment without

ventilation for solidification. Moreover, it should be ensured a uniform crystallisation during the solidification.

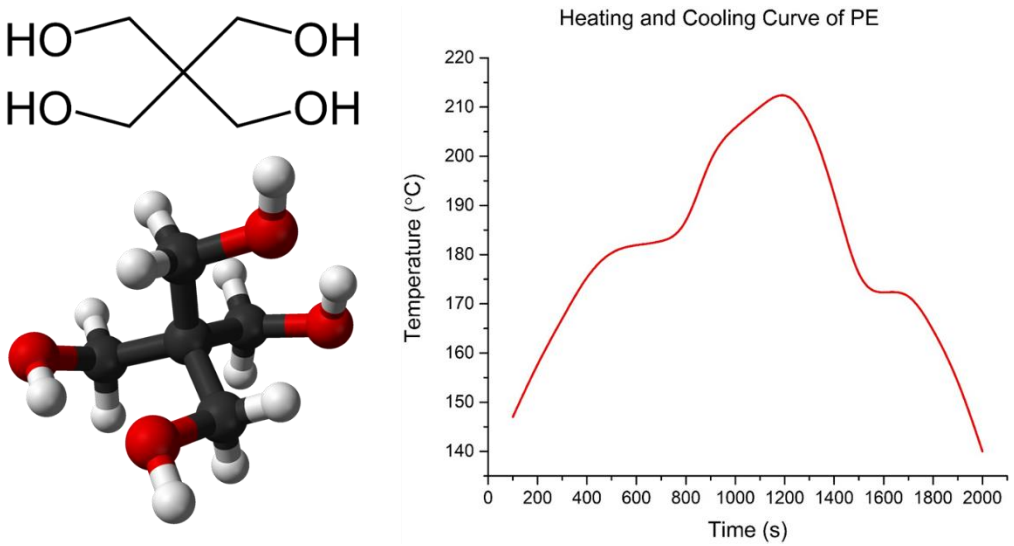


Figure 7-3 PE's chemical structure and molecule model of & heating and cooling curves

7.2.3 **Experimental Test Section**

In order to investigate the heat transfer enhancement for PE, four containers with different internal ribs are utilised during the experimental test. Figure 7-4 shows the photo of four different containers. As shown in the figure, the four containers have the same dimension and the volume ratio of PE is 50 %, 65 %, 80 % and 100 %, respectively. Moreover, the dimension of internal ribs is dissimilar with each other for investigating the effectiveness of internal rib on heat transfer enhancement.

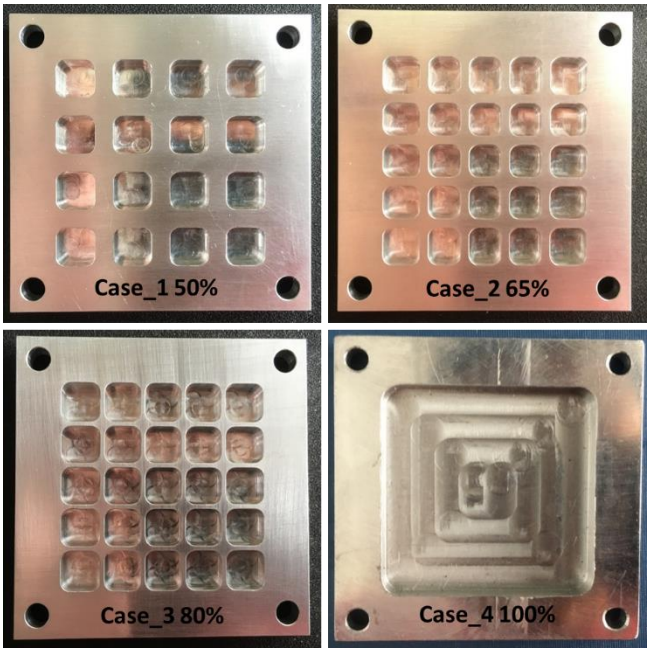


Figure 7-4 Photo of four different containers

Figure 7-5 shows the containers with PE before and after experiment. Because the detailed description of test rig is introduced in Chapter Three, Figure 7-6 shows the arrangement of thermocouples in the main test section exclusively.

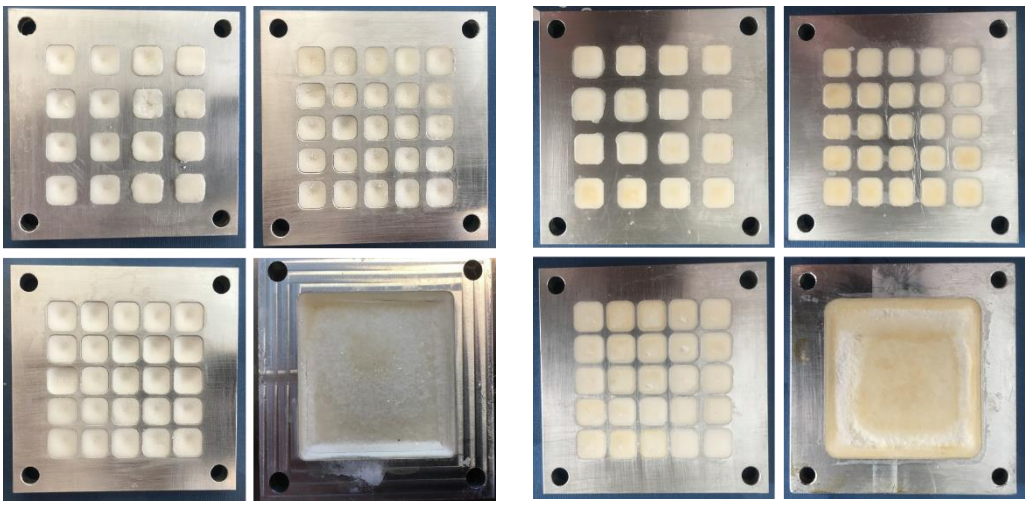


Figure 7-5 Containers with PE before and after experiment

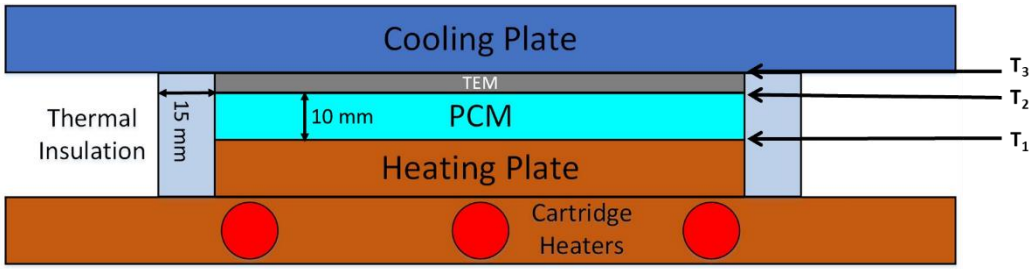


Figure 7-6 Arrangement of thermocouples in the main test section

7.3 Result and Discussion

7.3.1 Uncertainty Analysis

Experimental uncertainty analysis provides a method for predicting the uncertainty of experimental results based on its variable uncertainties which is also known as analysis of the propagation of uncertainty. Unless otherwise specified, each of these uncertainties has a confidence level of 95% on each measured parameters. The uncertainty of experimental results in this part of research originates in from the measured parameters such temperature, voltage and electrical power. The measurement biases of temperature, voltage and electrical power is within ± 1.5 ℃, ± (0.05 % + 0.1 % FS) and ± (1 % + 0.8 % FS), respectively. During the experimental test, the external electrical resistance is provided by a DC electronic load. Therefore, the errors of electrical resistance in the DC electronic load, which is 0.01 Ω, also need to be taken into consideration. As the tightening force of the cooling plate and the contact thermal resistance between each component would affect the power output of TEM, the tightening force needs to be set in a constant value during the experimental test.

Moreover, according to the theory from reference [270, 271], if the experimental result R is a function of n independent variables, v_i

$$R = R\ (v_1, v_2, \dots \dots v_n) \qquad \text{Eq.7-3}$$

For small variations in the variables, this relation can be expressed in linear form as

$$\delta R = \frac{\delta R}{\delta v_1}\delta v_1 + \frac{\delta R}{\delta v_2}\delta v_2 + \cdots + \frac{\delta R}{\delta v_n}\delta v_n \qquad \text{Eq.7-4}$$

If each variable is normally distributed, the relation between the interval for variables w_i, and the interval of the result w_R, which gives the same odds for each of the variables and for the results is

$$w_R = \sqrt{\sum_{i=1}^{n}\left(\frac{\delta R}{\delta v_i}\right)^2 (\delta v_i)^2} \qquad \text{Eq.7-5}$$

In the experimental test, the uncertainties of hot-side and cold-side temperature measurement were ± 1.07 % and ± 3.19 %, respectively. The uncertainty of power output and voltage were ± 2.5 % and ± 1.82 %, respectively.

7.3.2 **Performance of Single TEM with Different Match Load**

In order to compare the transient performance of TEM, its electrical performance under steady working conditions is investigated first. Figure 7-7 show the I-V characteristics and V-I-P characteristics of a single TEM under constant temperature situation with different matched load resistance. According to the introduction in part 7.2, the electrical resistance of TEM is a temperature related function and the functional relationship is parabolic. Therefore, according to the Ohm's law of closed circuit, there is an optimal external resistance for matching this TEM to get the highest power output for the TEM.

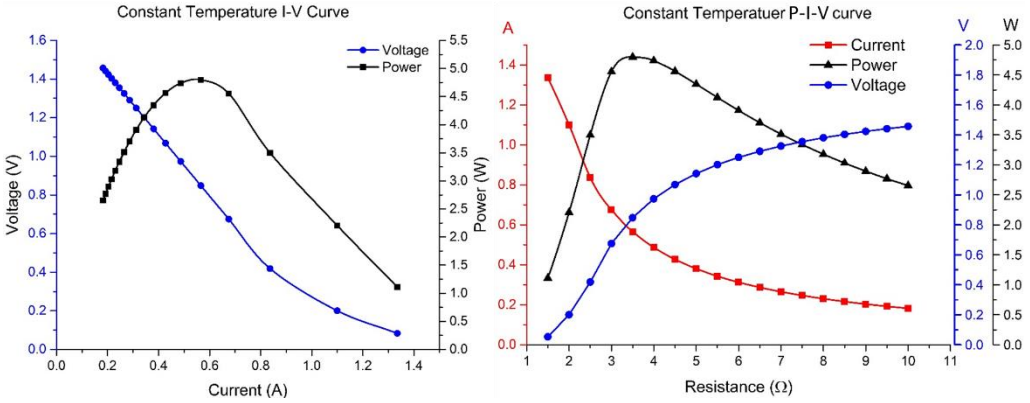


Figure 7-7 I-V characteristics and P-I-V characteristics of a single TEM

From Figure 7-7, it can be seen that at the matched load of around 3.5 Ω, the power output of TEM achieves its peak value. This result is confirmed by the data sheet of TEM in Table 7-4, in which the matched load is 3.65 Ω. Furthermore, with the increment of external resistance, the matched load voltage decreases while the current increases slightly and the power output is in a parabolic shape. According to the Ohm's law of closed circuit, this can be explained by a reduction in voltage with applied current due to the internal resistance of the thermoelectric material. At zero current, the open circuit voltage is high but no power is produced. As the current is increased, the power increases to a maximum. At high currents, the voltage drops to zero or below and the power produced drops to zero or becomes negative, which means the power is being consumed by the TEM instead of producing power from TEM.

Figure 7-8 shows the power output of a single TEM with different matched load resistance at different temperature difference from 100 ℃ to 160 ℃. As shown in the figure, each curve is almost in the same parabolic shape of which the peak value of power output is varying around 3.5 Ω. because, there is a variety in the internal

resistance of TEM with temperature, the peak value of different temperature difference is achieved with different external match load. The power generated by the TEM significantly decreases when the matched load resistance keeps growing after reaching the internal resistance of TEM. Importantly, the slope before external resistance equals to internal resistance of TEM is much steeper than that after external resistance equals to internal resistance and becomes larger. Moreover, with the increment of temperature difference, the growth rate of power output becomes higher. Even if the temperature difference of each test varies by 20 ℃, the growth rate of power output at 160 ℃ is almost 25 % higher than that of 100 ℃.

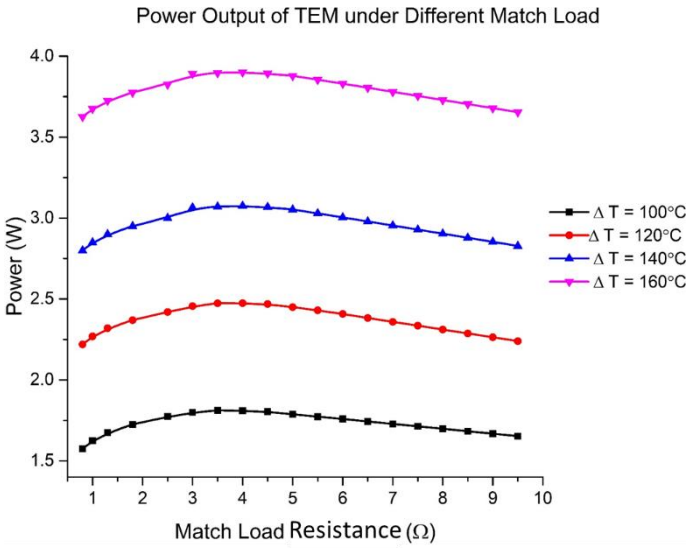


Figure 7-8 Power output of a single TEM with different match load resistance

In addition, during the experimental test, the hot-side temperature of TEM is different between open circuit and close circuit. When applying a load to the TEM, a closed circuit is established, the hot-side temperature decreases compared to open circuit. This is caused by the Peltier effect in that a current flow through a TEM would decrease the hot-side temperature and increase cold-side temperature.

Therefore, the Peltier effect is undesirable for a TEM to generate power due to decrease the temperature difference across the TEG and reduce the power generated by the Seebeck effect.

7.3.3 **Transient Performance Comparison by Integrating PCM**

From the analysis in Chapter Six, the transient performance is an important factor for automotive TEG systems, as the exhaust gas temperature varies significantly during real-time driving. In order to improve the transient performance, a PCM, Pentaerythritol, is employed as an energy storage system to enhance total thermal efficiency of the concentric cylindrical TEG system. In this part, the comparison of transient performance, such as temperature distribution, open circuit voltage and power output, between the sample of TEM with PCM and the sample of TEM without PCM is carried out.

7.3.3.1 Temperature Distribution

Figure 7-9 shows the comparison of temperature distribution of TEM with PCM and TEM without PCM. From the figure, it can be seen a significant difference in hot-side temperature of the two samples. First of all, the temperature difference between the hot side and heating plate in the sample with PCM is around 55 ℃, which is much larger than 5 ℃ in the sample without PCM with the same heating power. This is due to low heat transfer coefficient of PCM that prevent heat from transferring to the hot side of TEM. Furthermore, the slope of T_1 and T_2 for sample without PCM is much steeper than that for sample with PCM during heating process. This is caused by phase change process in PCM, which would accumulate the heat and spend more time for heating process. It nearly takes 3 to 5 times of duration to

heat sample with PCM to the same temperature of sample without PCM under different heating power. On the contrary, during the cooling process, the duration is almost the same between the two samples. However, the temperature slope of T_1 and T_2 for sample without PCM is flat and an obvious change in slope can be observed at the phase change point of PCM. Because PCM releases the energy accumulated during heating process, the temperature change range on heating plate is higher than that of TEM hot side. This could stabilise the temperature, especially during cooling process, and allow TEM to generate more power in a transient condition.

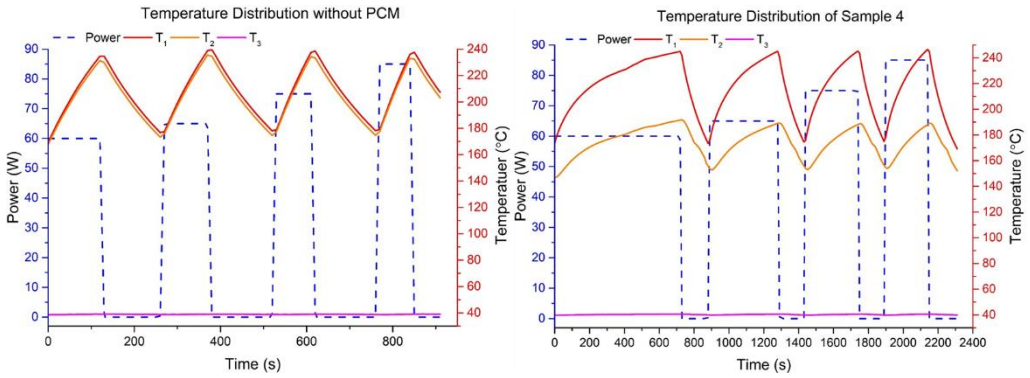


Figure 7-9 Comparison of temperature distribution of TEM with and without TEM

In addition, the response to the heating power between these two samples is also different. As shown in the figure, when the heating power is changing from 60 W to 0 W, the temperature at heating plate changes immediately. However, for the hot-side temperature of TEM, there is a 20 s delay after the heating power turned off. The reason for this delay is the higher heat capacity and low heat transfer coefficient of PCM.

7.3.3.2 Open Circuit Voltage

Figure 7-10 shows the comparison of open circuit voltage and the temperature difference between hot and cold side of TEM for these two samples. As shown in the figure, it is almost the same with temperature distribution curve that the slope of temperature difference and open circuit voltage for sample with PCM is more flat than that of sample without PCM. Furthermore, there is a noticeable slope change of open circuit voltage during cooling process as well. By compared these two samples, the heating process of sample without PCM is longer than cooling process, however, it is exactly the opposite in sample with PCM. Which means the sample with PCM will absorb more heat and release to TEM for generating more power. The average open circuit voltage for sample with PCM is 6.288 V with the average temperature difference of 135.94 ℃. It is 0.7 % higher than the average open circuit voltage for sample without PCM of 6.251 V with the average temperature difference of 134.54 ℃.

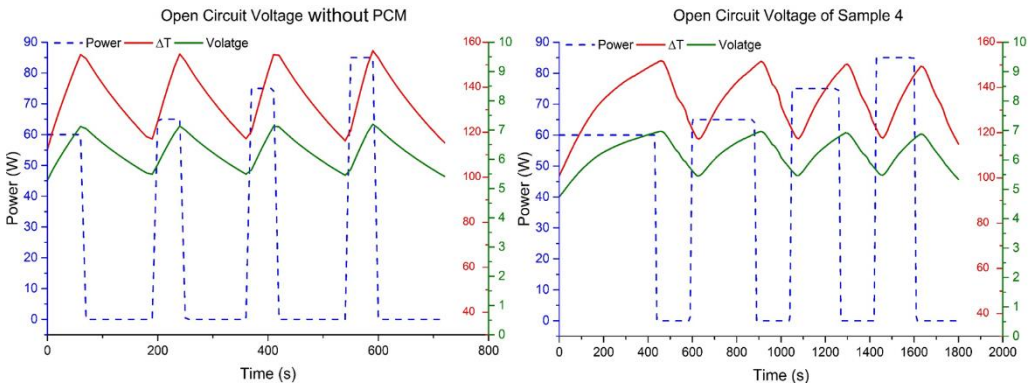


Figure 7-10 Comparison of open circuit voltage and temperature difference

7.3.3.3 Power Output

Figure 7-11 shows the power output for these two samples at 3.5 Ω, as well as, the temperature difference between hot and cold side of TEM. According to the analysis in Section 7.3.2, the optimal matched load for TEM employed in this experimental test is 3.5 Ω. Therefore, the resistance of DC electronic load is set at 3.5 Ω during all the power output test afterwards. As shown in the figure, the slope of temperature difference and power output for sample with PCM is more flat than that of sample without PCM which is the same with the previous two figures. The temperature difference for sample with PCM varies from 151.14 ℃ to 107.11 ℃ and the range for sample without PCM is from 156.77 ℃ to 111.54 ℃. There is more than 1 ℃ difference between these two samples. Moreover, the power output for sample with PCM varies from 3.423 W to 1.984 W and that for sample without PCM is 3.622 W to 2.065 W. The average power output for sample with PCM is 2.892 W, which is 0.033 W higher than that for sample without PCM and the improve percentage is 1.16%.

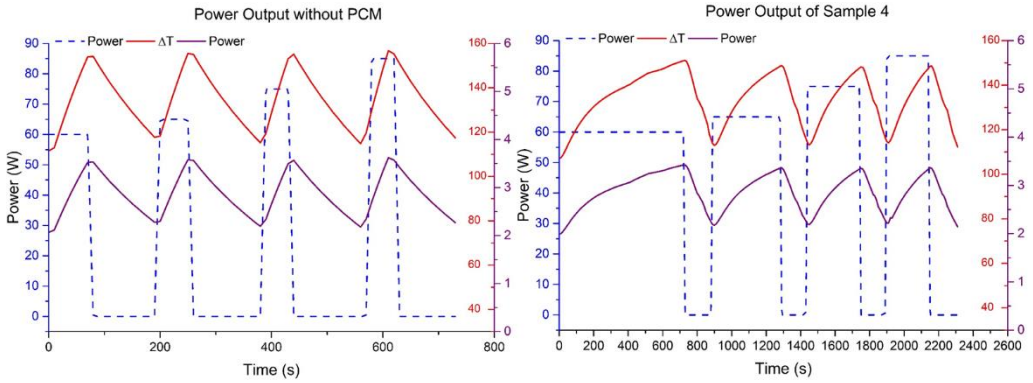


Figure 7-11 Power output and temperature difference at 3.5 Ω match load resistance

According to the analysis above, it appears that integrating PCM into the TEM system could solve the issue of transient performance. However, the improvement is not satisfactory due to the low heat transfer coefficient of PCM. Therefore, the heat transfer enhancement for PCM is investigated in the following part, by combining PCM with internal ribbed boxes as previous mentioned.

7.3.4 Temperature Distribution of Different Experimental Test Case

According to the comparison between the sample without PCM and the sample with 100 % PCM, the improvement for transient performance is significant. In the project, three different types of internal ribbed box are employed to enhance the heat transfer in PCM. As aforementioned, the volume ratio of PCM for each box is 50 %, 65 % and 80 %, respectively. The effect of these three internal ribbed boxes compared to the 100 % sample will be presented in this and following part.

In order to compare the heat transfer enhancement with different type of internal ribbed box, namely the different percentage of PCM volume, the temperature distribution between the hot side and cold sides of TEM is investigated firstly. Figure 7-12 shows the hot-side and cold-side temperature distribution of TEM with each PCM sample. The volume percentage of sample 1, 2, 3 and 4, as mentioned in Section 7.2, is 50 %, 65 %, 80 % and 100 %, respectively. Moreover, the heating power is varying from 60 W to 85 W to simulate the fluctuating heat source temperature in practical application. In order to achieve the same temperature at the hot side of TEM, the temperature at the heating plate is particular due to the different volume of TEM. It is can be seen from the figures that the hot-side temperature of TEM is fluctuating with the heating power, but the cold-side temperature remains almost the same during the experimental test.

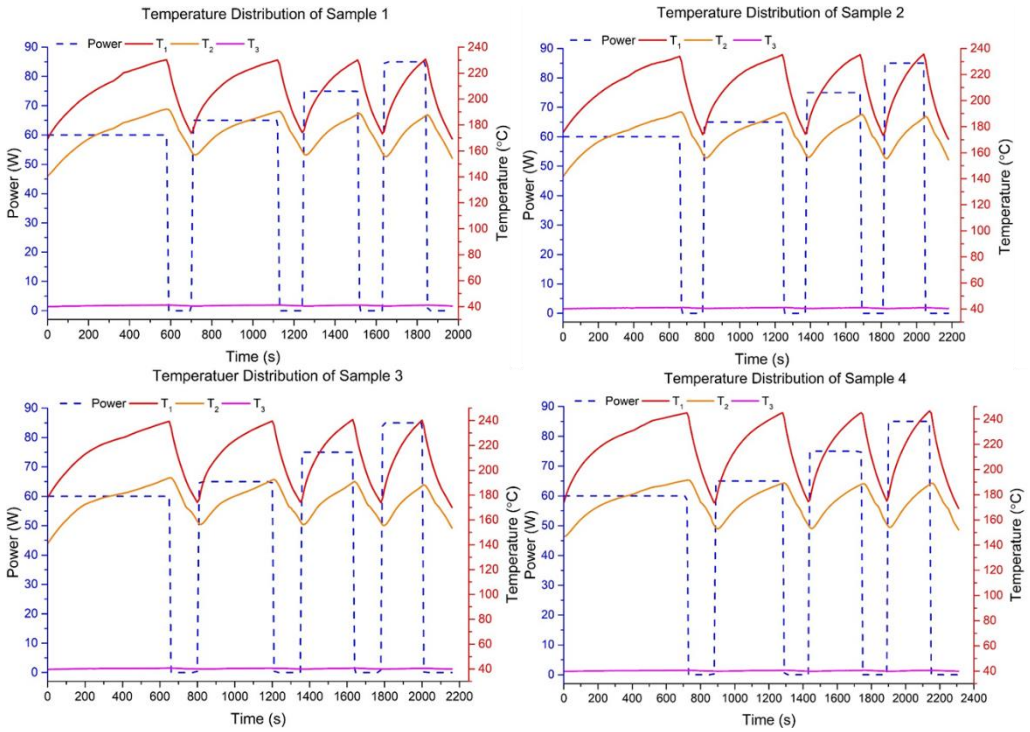


Figure 7-12 Hot-side & cold-side temperature distribution of TEM with each sample

These figures also exhibit that there is a gap between the temperature of heating plate and TEM hot side in each sample test. The temperature of heating plate is higher than that of TEM hot side by 40 ℃ to 60 ℃. This temperature difference is caused by low heat transfer coefficient of PCM and phase-changing process in PCM. Even the phase-changing process of heating process is not obvious, it still can be seen an unequal slope during temperature increment. For all the samples, the slope of temperature increment at heating plate is larger than that of TEM hot side, during the heating process and there are two reasons to explain this difference. The first one is the phase-changing process happened in PCM. When the heating temperature reach the phase change point, the heat is absorbed and kept within the PCM rather than transferring to the hot side of TEM. This part of thermal energy will be held in PCM and released later in cooling process. Another reason for this difference is the

high heat capacity of PCM, which means the PCM need more thermal energy for heating to the same temperature compared with aluminium. However, there is no obvious temperature slope change in the temperature of TEM hot side, like the curve in the part 7.2. As a result, the phase change process can not be identified in the heating process of temperature and performance curves for each sample. This is because the limited amount of PCM in the internal ribbed box compare to the heat supplied from the heater. Furthermore, due to the low heat transfer coefficient of PCM, it is easy to build a thermal bridge though the aluminium encapsulation. The thermal bridge allows the heat conductive directly to the hot side of TEM avoid PCM and increase the average hot-side temperature.

During the cooling process, there is a significant change in the slope of the temperature at TEM hot side for each sample, which is around the phase change point of PCM at around 172 ℃. It is the evidence for the phase change process happening in the internal ribbed boxes with PCM. Moreover, with the increment of PCM volume, the phase change duration becomes longer, from less than 20 s in sample1 with 50 % PCM to over 40 s in sample 4 with 100 % PCM. Furthermore, the temperature decline at TEM hot side is lower compared to that of heating plate during the cooling process. On one hand, the phase change process in PCM will release the stored thermal energy to TEM hot side for preventing the reduction of temperature. On the other hand, the high heat capacity also lessen the temperature decline within the PCM, hence it adjusts the temperature-varying trend between heating plate and TEM hot side.

In addition to the temperature-varying trend in heating and cooling process, the heating and cooling duration of each sample also has divergence, even though they

are all longer than that of non-PCM sample. Figure 7-13 shows the comparison of temperature at TEM hot side for each sample.

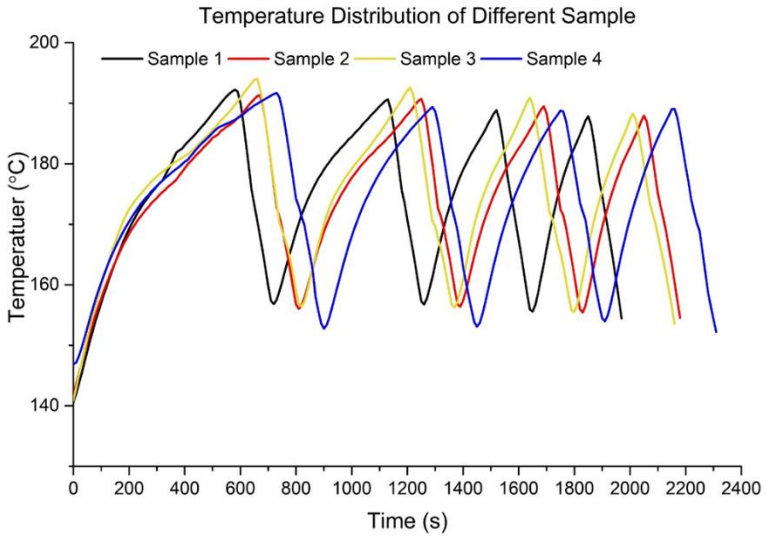


Figure 7-13 Comparison of hot-side temperature for each sample

In general, with the increase in the PCM volume, the heating process become longer as well as cooling process. Moreover, the duration of heating process becomes shorter while the heating power increase from 60 W to 85 W for each sample. From the figure, sample1 with 50 % PCM has the shortest duration of 1970 s for completing all the cycles and sample4 with 100% PCM has the longest duration of 2310 s for completing all the cycles. However, by compared sample 2 with 65 % PCM and sample 3 with 80% PCM, a difference can be found that sample2 costs more time for completing all the cycles. The reasons causing this diversity can be summarised in two aspects. The first reason is the heat transfer area within sample 3 is larger than that of sample 2. In order to obtain a higher volume percentage of PC, there are more ribs arranged in the box and the ribs become thinner. As a result, the total heat transfer area in the rib becomes larger, which helps the conductive heat transfer within the internal ribbed box and reduce the

duration of heating and cooling process. The second reason is the larger sub volume within the sample 2. In order to enhance the heat transfer, the ribs will divide the PCM into several small pieces. With an increased number of ribs, the volume of each small piece is curtailed. The decline in sub volume would help all the PCM reach the phase change point in a shorter time, according to law of specific heat capacity.

In addition to the analysis above, the characteristic of each sample for eliminating temperature difference is investigated as well. From Figure 7-12 and 7-13, it is can be seen that with the increment of volume percentage, the characteristic of eliminating temperature difference becomes stronger. The average deviation of temperature difference between TEM hot side and heating plate of sample1, 2, 3 and 4 is 22.16 ℃, 26.46 ℃, 29.48 ℃, 34.29 ℃, respectively. The deviation increase about 54.74 % by compared sample1 with 50 % PCM with sample4 with 100 % PCM. This is caused by the more volume of PCM could store more thermal energy during heating process and release to TEM in cooling process. This deviation means the temperature at hot side of TEM becomes more stable with the same fluctuating temperature of heat source. This could benefit for improving the transient performance of TEG system applied in automotive waste heat recovery. Moreover, the heating power is another influencing factor of the characteristic of eliminating temperature difference. With the increment of heating power between 60 W to 75 W, the average deviation of temperature difference between TEM hot side and heating plate in each sample increase correspondingly. However, when the heating power reach 85 W, the deviation becomes lower. Take sample1 as an example, the deviation with heating power of 60 W, 65 W, 75 W and 85W is 24.83 ℃, 26.57 ℃,

27.78 ℃ and 26.64 ℃, respectively. The explanations for this phenomenon are as follow. The increasing heating power would generate higher heat flux through internal ribbed box to PCM, which boosts the phase change process of PCM and leads to lower hot side temperature afterwards. The relatively lower hot side temperature is the reason for increasing deviation. On the other hand, the supercooling within the PCM would obstruct the phase change during cooling process of PCM and has a negatively affects the functionality of this PCM. That is because the phase change does not start at the expected phase change point, but only way below, with a practical requirement of a large operating temperature range. This is the reason of the decreasing deviation at 85 W. Therefore, it has to consider this phenomenon during the design and matching process of automotive TEG system.

7.3.5 **Voltage and Power Comparison of Different Samples**

In addition to the analysis of temperature distribution of different sample, the open circuit voltage and power output of TEM will be presented in this part. Moreover, a comprehensive comparison of the transient performance between each sample will be carried out.

7.3.5.1 Open Circuit Voltage Comparison

Figure 7-14 shows the open circuit voltage and temperature difference of the TEM for the different samples. As shown in the figure, the curve of the open circuit voltage has the same pattern as the curve of temperature difference for each sample. The duration of completing all the cycles for each sample is same as that in the temperature curves. Sample1 with 50 % PCM is the shortest and sample4 with 100 %

PCM is the longest, among all the samples. The average temperature difference of each sample 1, 2, 3 and 4 is 134.49 ℃, 137.42 ℃, 138.58 ℃ and 135.94 ℃, respectively. This is another evidence for the heat transfer enhancement in sample3 is the best among all these four samples, because of the larger heat transfer area and smaller sub volume.

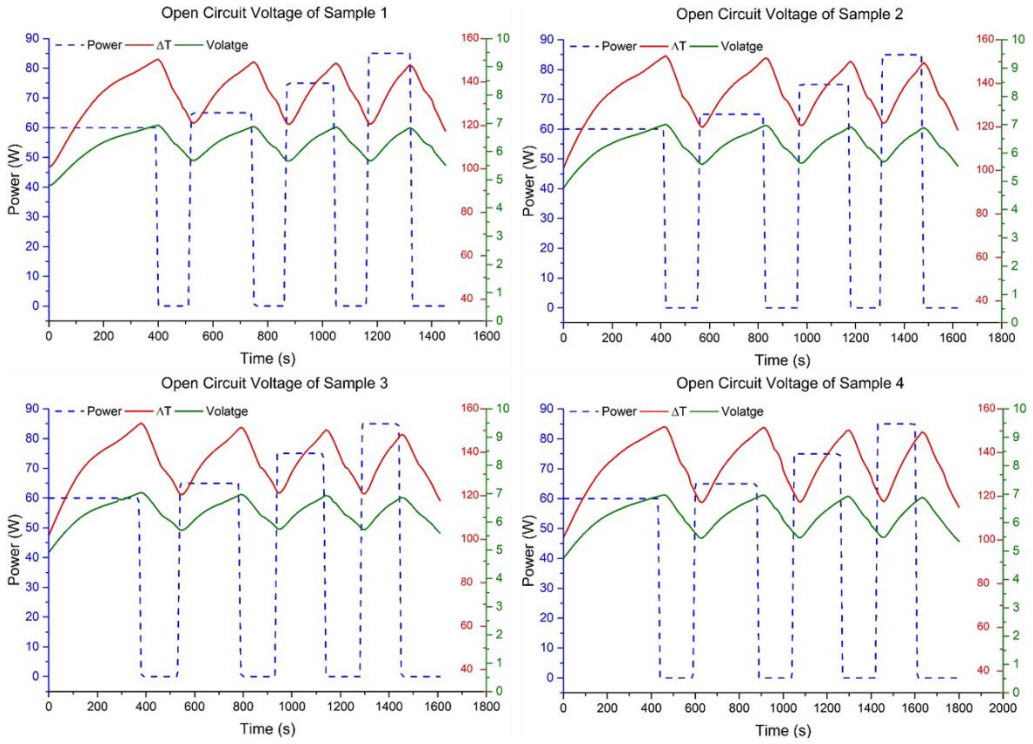


Figure 7-14 Open circuit voltage and temperature difference of different sample

Figure 7-15 shows the comparison of open circuit voltage for each sample. According to the average temperature difference of each sample, the average open circuit voltage of sample 1, 2, 3 and 4 is 6.245V, 6.375 V, 6.412 V and 6.288V. Compared to the average open circuit voltage of sample without PCM at 6.251 V, the average open circuit voltage of sample 2, 3 and 4 is higher and sample1 is lower. Even though the internal ribs in sample1 improve the heat transfer of PCM, the low heat transfer coefficient and large sub volume of PCM still obstruct the transient

performance of TEM, therefore, the average open circuit voltage of sample1 with 50 % PCM become lower than that of sample without PCM. Moreover, the variation of average open circuit voltage for each sample is – 0.1 %, 1.98 %, 2.4 % and 0.7 %, respectively. The variation of sample3 with 80 % PCM is the highest among all these samples. Furthermore, the variation of hot-side temperature and open circuit voltage for sample 3 with 80 % PCM is 34.06 ℃ and 1.438 V, respectively, which is also the lowest among all the samples. This also demonstrates that sample 3 with 80 % PCM is more effective in stabilizing the temperature fluctuation from heat source.

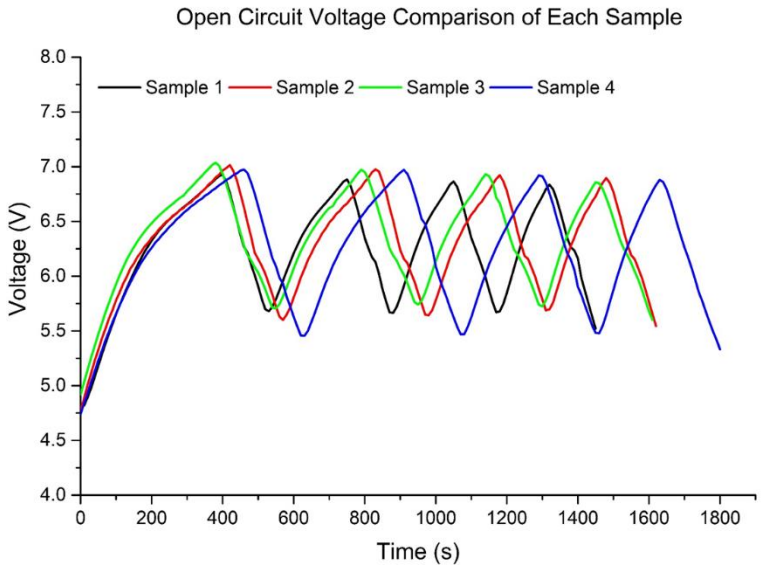


Figure 7-15 Comparison of open circuit voltage for each sample

7.3.5.2 Power Output Comparison

Figure 7-16 show the power output and temperature difference through TEM of each sample. Generally, the curves are in the same pattern with those of open circuit voltage, but it takes longer duration for completing all the cycles. This is caused by Peltier effect which decrease the hot-side temperature during the test, as mentioned

in Section 7.3.2. As shown in the figures, the average temperature difference of each sample 1, 2, 3 and 4 is 134.63 ℃, 135.53 ℃, 136.47 ℃ and 135.21 ℃, which are all higher than that of sample without PCM at 134.62 ℃. Once again, the average temperature difference of sample3 with 80 % PCM is the highest and sample1 with 50 % PCM is the lowest, among all the samples.

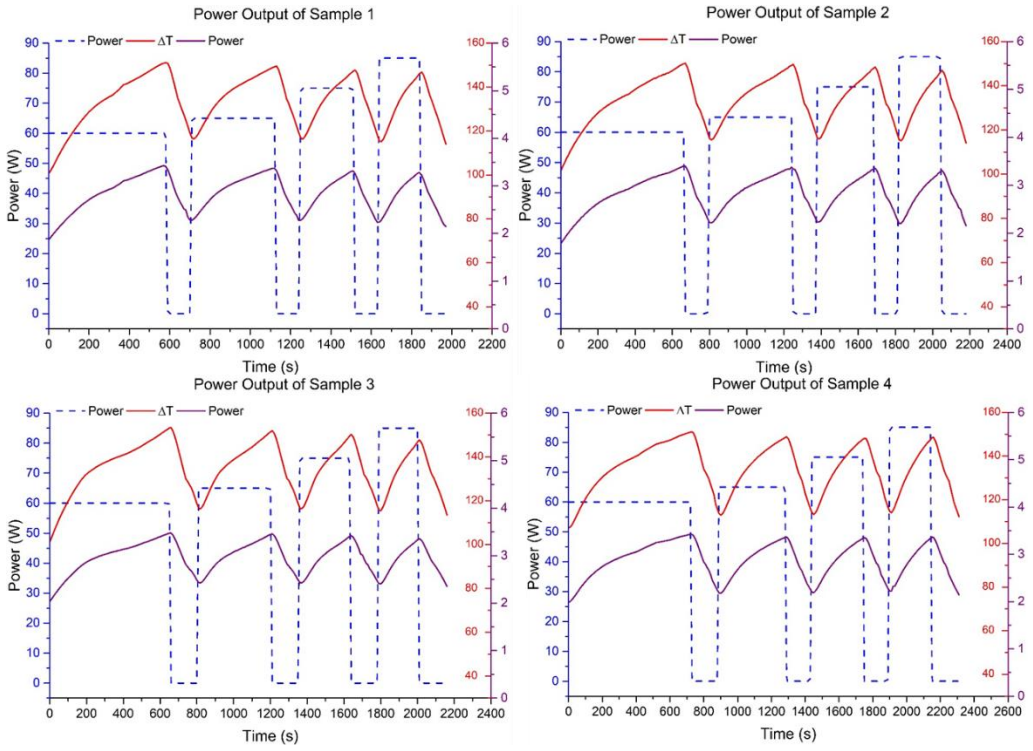


Figure 7-16 Power output and temperature difference of each sample

Figure 7-17 shows the comparison of power output for each sample. According to the average temperature difference of each sample, the average power output of sample 1, 2, 3 and 4 is 2.864 W, 2.965 W, 3.007 W and 2.892 W, respectively. Compared to the 2.859 W power output of sample without PCM, the PCM integrating TEM system generates more power under fluctuating heating power, and achieves a better transient performance. The reason for this improvement is mainly contributed by the thermal energy released by PCM at phase change point

during cooling process, which provide more heat to TEM and stabilizes hot-side temperature. Even though the total amount of PCM in each sample is not numerous, it still can act as a good energy storage system under complicated working conditions and improve the transient performance of TEM. Moreover, the variation of average power output for each sample is 0.17 %, 3.71 %, 5.18 % and 1.16 %, respectively. Similarly, the variation of sample 3 with 80 % PCM is the highest among all these samples and variation of sample 1 with 50 % PCM is the lowest.

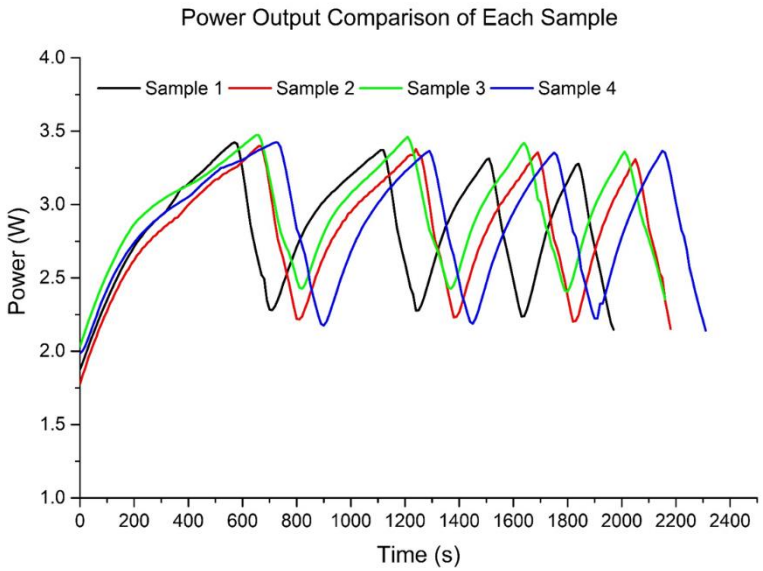


Figure 7-17 Comparison of power output for each sample

According to the analysis above, sample 3 with 80 % PCM has the best performance under transient condition, even if the volume ratio of PCM is higher than sample1 with 50 % PCM and sample 2 with 65 % PCM. The main reason is the internal structure of the box which has the highest heat transfer area and enhance the conductive heat transfer within PCM.

7.4 Summary

In this chapter, to improve transient performance of the concentric cylindrical TEG system under real-time driving condition, a solid-solid PCM, Pentaerythritol, is introduced as an energy storage system for automotive TEG system. Furthermore, in order to enhance the heat transfer within PCM, different type of internal ribbed boxes are employed. A simple proof-concept test rig is set up to investigate the feasibility of integrating PCM with TEG system experimentally. Temperature distribution, open circuit voltage and power output are the main metrics for this experimental test and the crucial experimental results and further works are listed as follows:

- Pentaerythritol is the most suitable PCM of thermal energy storage system for automotive waste heat recovery due to its phase change temperature and extremely low volume change ratio.
- By integrating PCM, the fluctuating temperature of the heat source is stabilized, but the heating process is extended due to the phase change process and low thermal conductivity of PCM.
- In order to enhance heat transfer within PCM, samples with different volume ratios of aluminium rids are manufactured. According to the experimental results, sample 3 with 80 % PCM has the best transient performance among all the samples because of the larger heat transfer area and relatively smaller sub volume.

- The improvement of open circuit voltage for each sample is – 0.1 %, 1.98 %, 2.4 % and 0.7 %, respectively. The improvement of power output for each sample is 0.17 %, 3.71 %, 5.18 % and 1.16 %, respectively.
- The investigation of heat transfer enhancement within PCM needs to be studied in detail, in order to give a comprehensive guidance for automotive TEG systems.
- Metal foams could be a good method to enhance heat transfer within PCM, and the thermal properties of PCM combined with metal foams need to be investigated in the further works.
- The main disadvantage of integrating PCM is the activation for PCM, which requires longer duration for samples with PCM heated to the same temperature than samples without PCM.
- Another disadvantage of integrating PCM is the relatively low thermal conductivity of PCM would negatively impact the total thermal efficiency of the whole system. This needs further investigations about improving overall thermal efficiency for different TEG systems.

Chapter 8. Conclusions and Further Work

8.1 Conclusions of Current Work

This presented thesis presents a novel design of concentric cylindrical TEG system and offers an in-depth investigation about the performance of this novel structured TEG system. A comprehensive literature review covering from early stage to up-to-date research works in WHR technologies and TEG systems for automobiles has been presented in Chapter Two. The heat transfer performance of the concentric cylindrical TEG system is investigated in two separate aspects: conductive heat transfer and convective heat transfer. In addition, the system-level performance of concentric cylindrical TEG system, such as power output, open circuit voltage and fuel economy improvement is studied numerically. According to the results of the system-level investigation, the novel concept of integrating PCM as thermal energy storage system is proposed. Pentaerythritol (PE), as a potential PCM for thermal energy storage in automotive TEG systems, is presented and investigated experimentally at the end of this research work.

In this thesis, the investigation on the performance of the concentric cylindrical TEG system divides into two main part, the thermal performance and electrical performance which are related to the properties of TE devices, and the investigation is expended from component level to system level. Chapter Four and Chapter Five are focused on the heat transfer performance of the concentric TEG system which is separated into two aspects: conductive heat transfer and convective heat transfer. Chapter Four provides the investigation on conductive heat transfer of annular TE unit, which is the component-level heat transfer. The results describe the

temperature distribution in a single annular TE unit with various temperature boundary condition. In addition, they give a basic guide for the numerical simulation and support to simplify the model of numerical simulation in Chapter Five. The numerical investigation of convective heat transfer in the concentric cylindrical TEG system is conducted in Chapter Five. The numerical model contains several annular TE units, therefore, the numerical simulation focuses on the component-level heat transfer as well. The simulation results can give an insight into the hot-side and cold-side temperature of annular TEMs in the concentric cylindrical TEG system. These results can be utilized in the establishment of fuel consumption model in the system-level investigation. Chapter six, as core content in this thesis, investigates the electrical performance of concentric cylindrical TEG system in system-level and gives one-dimensional models of the vehicle and TEG system, as well as, fuel consumption model for calculating the fuel economy improvement. By using the results from Chapter Four and Chapter Five, the temperature distribution within the TEG system, under different vehicle driving condition, can be calculated and then utilized in the one-dimensional model to calculate fuel consumption. Chapter Seven delivers a potential mothed for improving the transient performance of the concentric cylindrical TEG system. According to the results of Chapter Six, if the extra energy during vehicle accelerating can be reserved and released during vehicle deaccelerating, the temperature distribution of concentric cylindrical TEG system would be closer to the optimal operating temperature for TE materials. This can enhance the transient performance of the TEG system and the fuel economy improvement. Therefore, PCM is purposed as an energy storage system for vehicle TEG system.

The conductive heat transfer within concentric cylindrical TEG system occurs between annular TEMs and heat exchanger of this system. The investigation of conductive heat transfer focus on the thermal characteristics of annular TEM and annular TE unit of concentric cylindrical TEG system under different thermal boundary conditions. The research works conducted in COMSOL Multiphysics and results show that annular TEM has approximately 20 % better performance than conventional square TEM due to larger heat transfer area. Additionally, the concentric cylindrical TEG system has the highest TEM filling factor of 0.655, compared to other structures.

The convective heat transfer with concentric cylindrical TEG system occurs between the engine exhaust gas and heat exchanger of this system. In order to enhance heat transfer, an advanced heat transfer technology, heat pipe, is introduced into this system. The research work is carried out both experimentally and numerically. A test rig is established for verifying the feasibility of heat pipe combined heat exchanger for automotive TEG system. The additional numerical simulation is to explore the heat transfer enhancement with fins and different heat pipe lengths. According to the results, a counter flow arrangement and an anti-gravity arrangement for heat pipe are the best arrangement of heat exchanger of concentric cylindrical TEG system. The heat exchanger with different heat pipe lengths has the highest heat transfer capacity among all the optimized structure.

In order to explore the system-level performance of the concentric cylindrical TEG system, a comprehensive fuel consumption model is presented in this thesis. The model take not only the power generated by TEG system but also the penalty factors of integrating TEG system into consideration. Experimental data from a car

manufacturer is employed to verify the reliability of this model. By utilising this model to calculate the performance of concentric cylindrical TEG system, the total power generated is 463.3 kJ, with the peak power output at 966.17 W, under WLTP class3 driving cycle. Furthermore, the total fuel economy improvement is 1.64 %, which is higher compared to other TEG systems of 1.4 % and 0.7 %, respectively.

Based on the investigation on TEG system performance under standardized driving cycle, a potential PCM for thermal energy storage in TEG system is proposed and the performance is investigated experimentally as well. PE has the phase changing temperature around 180 ℃, which is also the optimal operating temperature of commercially used TE material Bi_2Te_3. By integrating PCM, the power output of a single TEM could be boosted by 1.16 %. With the purpose of improving heat transfer in PE, different structured containers are employed in the experiment. Sample3 with 80 % PCM has the best transient performance among all the samples because of the larger heat transfer area and relatively smaller sub volume.

8.2 Future Work

There are several possible future works regarding the concentric cylindrical TEG system and PCM integrating automotive TEG systems, which are recommended based on current work as follows:

- One of the most important future works is to find a solution for manufacturing annular TEMs for concentric cylindrical TEG system. because all the experimental investigation in this thesis is based on square TEMs, due to the limitations of cost and processing technology for annular TEM.

- With the manufacturing of annular TEM, the heat transfer performance within the concentric cylindrical TEG system could be investigated experimentally. Moreover, the experiment of system-level performance could be carried out in the engine test rig.
- The structure of the test section in convective heat transfer experimental test need to be improved and the three dimensional model for concentric cylindrical TEG system need to be established for more accurate experimental and numerical results.
- The structure of heat exchanger in concentric cylindrical TEG system could be optimized further for achieving higher heat transfer coefficient with lower pressure drop. Processing method for implementing such structure is also a direction that needs to be considered.
- A heat pipe, operating at the medium temperature range (250 ℃ to 500 ℃), is desirable in concentric cylindrical TEG system, in order to replace the copper-water heat pipes, whose operating temperatures are around 300 ℃, located upstream of the system. This could improve the total efficiency of concentric cylindrical TEG system.
- The investigation of different PCM for automotive TEG system needs to continue, with the purpose of seeking a PCM with higher latent heat and better thermal performance for automotive TEG system.
- The heat transfer enhancement of PCM could be combined with metal foams. Even though the some initial research has begun, further analysis is essential, as the metal foam is a decent method for improving heat transfer.

- The investigations on reducing costs and improving efficiency of TE materials are urgent for promoting TEG system in automotive WHR market.

References

[1] H.N. Gupta, Fundamentals of internal combustion engines, PHI Learning Pvt. Ltd., 2012.

[2] K. Mollenhauer, H. Tschöke, K.G. Johnson, Handbook of diesel engines, Springer, 2010.

[3] J.B. Heywood, Internal combustion engine fundamentals, (1988).

[4] R. Van Basshuysen, F. Schäfer, Internal combustion engine handbook-basics, components, systems and perspectives, 2004.

[5] A.J. Martyr, M.A. Plint, Engine testing: theory and practice, Elsevier, 2011.

[6] S.S. Bhatti, S. Verma, S.K. Tyagi, Energy and exergy based performance evaluation of variable compression ratio spark ignition engine based on experimental work, Thermal Science and Engineering Progress, 9 (2019) 332-339.

[7] J. Fu, J. Liu, R. Feng, Y. Yang, L. Wang, Y. Wang, Energy and exergy analysis on gasoline engine based on mapping characteristics experiment, Applied Energy, 102 (2013) 622-630.

[8] M. Özkan, D.B. Özkan, O. Özener, H. Yılmaz, Experimental study on energy and exergy analyses of a diesel engine performed with multiple injection strategies: Effect of pre-injection timing, Applied Thermal Engineering, 53 (2013) 21-30.

[9] R. Stone, Introduction to internal combustion engines, (1999).

[10] R. Saidur, M. Rezaei, W.K. Muzammil, M.H. Hassan, S. Paria, M. Hasanuzzaman, Technologies to recover exhaust heat from internal combustion engines, Renewable and Sustainable Energy Reviews, 16 (2012) 5649-5659.

[11] Turbocharger, DOI: https://en.wikipedia.org/wiki/Turbocharger#cite_note-3, 05th Nov, 2017.

[12] C. Gray, A Review of Variable Engine Valve Timing, SAE Transactions, 97 (1988) 631-641.

[13] R.H. Thring, Homogeneous-charge compression-ignition (HCCI) engines, SAE Technical paper, 1989.

[14] H. Raheman, S.V. Ghadge, Performance of diesel engine with biodiesel at varying compression ratio and ignition timing, Fuel, 87 (2008) 2659-2666.

[15] A.M.K.P. Taylor, Science review of internal combustion engines, Energy Policy, 36 (2008) 4657-4667.
[16] J. Hartman, Turbocharging Performance Handbook, MotorBooks International.
[17] N. Baines, K.D. Wygant, A. Dris, The Analysis of Heat Transfer in Automotive Turbochargers, Journal of Engineering for Gas Turbines and Power, 132 (2010) 042301-042301-042308.
[18] K. NICE, How Turbochargers Work, DOI: https://auto.howstuffworks.com/turbo3.htm, 05th,Nov, 2017.
[19] H. Nguyen-Schäfer, Rotordynamics of Automotive Turbochargers, Springer, 2015.
[20] J.H. Tuttle, Controlling engine load by means of late intake-valve closing, SAE Transactions, (1980) 2429-2441.
[21] T. Dresner, P. Barkan, A Review and Classification of Variable Valve Timing Mechanisms, SAE Transactions, 98 (1989) 1275-1288.
[22] H. Hong, G.B. Parvate-Patil, B. Gordon, Review and analysis of variable valve timing strategies—eight ways to approach, Proceedings of the Institution of Mechanical Engineers, Part D: Journal of Automobile Engineering, 218 (2004) 1179-1200.
[23] G. Fontana, E. Galloni, Variable valve timing for fuel economy improvement in a small spark-ignition engine, Applied Energy, 86 (2009) 96-105.
[24] R. Fiorenza, M. Pirelli, E. Torella, P. Pallotti, P.E. Kapus, G. Kokalj, M. Lebenbauer, VVT+ port deactivation application on a small displacement SI 4 cylinder 16V engine: An effective way to reduce vehicle fuel consumption, SAE Technical Paper, 2003.
[25] F. Zhao, T.N. Asmus, D.N. Assanis, J.E. Dec, J.A. Eng, P.M. Najt, Homogeneous Charge Compression Ignition (HCCI) Engines, SAE International, 2003.
[26] T. Ando, Y. Isobe, D. Sunohara, Y. Daisho, J. Kusaka, Homogeneous charge compression ignition and combustion characteristics of natural gas mixtures: the visualization and analysis of combustion, JSAE Review, 24 (2003) 33-40.

[27] A. Dubreuil, F. Foucher, C. Mounaı¨m-Rousselle, G. Dayma, P. Dagaut, HCCI combustion: Effect of NO in EGR, Proceedings of the Combustion Institute, 31 (2007) 2879-2886.
[28] X.-C. Lü, W. Chen, Z. Huang, A fundamental study on the control of the HCCI combustion and emissions by fuel design concept combined with controllable EGR. Part 1. The basic characteristics of HCCI combustion, Fuel, 84 (2005) 1074-1083.
[29] X.-C. Lü, W. Chen, Z. Huang, A fundamental study on the control of the HCCI combustion and emissions by fuel design concept combined with controllable EGR. Part 2. Effect of operating conditions and EGR on HCCI combustion, Fuel, 84 (2005) 1084-1092.
[30] J. Zheng, J.A. Caton, Effects of operating parameters on nitrogen oxides emissions for a natural gas fueled homogeneous charged compression ignition engine (HCCI): Results from a thermodynamic model with detailed chemistry, Applied Energy, 92 (2012) 386-394.
[31] T. Shudo, T. Takahashi, Influence of reformed gas composition on HCCI combustion of onboard methanol-reformed gases, SAE Technical Paper, 2004.
[32] L. Starck, B. Lecointe, L. Forti, N. Jeuland, Impact of fuel characteristics on HCCI combustion: Performances and emissions, Fuel, 89 (2010) 3069-3077.
[33] T. Kenjiro, Variable compression ratio internal combustion engine, in: U.S. Patent (ed.), Vol. No. 2,145,017. , U.S. Patent, USA, 1939.
[34] M. Jancer, How Infiniti's Variable-Compression Engine Works, DOI: https://www.popularmechanics.com/cars/car-technology/a22143603/infiniti-variable-compression-engine/, 7th, Mar, 2019.
[35] M. Christensen, A. Hultqvist, B. Johansson, Demonstrating the Multi Fuel Capability of a Homogeneous Charge Compression Ignition Engine with Variable Compression Ratio, SAE Transactions, 108 (1999) 2099-2113.
[36] V. Arul Mozhi Selvan, R.B. Anand, M. Udayakumar, Combustion Characteristics of Diesohol Using Biodiesel as an Additive in a Direct Injection Compression Ignition Engine under Various Compression Ratios, Energy & Fuels, 23 (2009) 5413-5422.
[37] J.F. Saco, W.R. Williamson, Waste heat utilizer, in, Google Patents, 1946.

[38] M. Karvonen, R. Kapoor, A. Uusitalo, V. Ojanen, Technology competition in the internal combustion engine waste heat recovery: a patent landscape analysis, Journal of Cleaner Production, 112 (2016) 3735-3743.
[39] J. Jadhao, D. Thombare, Review on exhaust gas heat recovery for IC engine, International Journal of Engineering and Innovative Technology (IJEIT) Volume, 2 (2013).
[40] G. Shu, Y. Liang, H. Wei, H. Tian, J. Zhao, L. Liu, A review of waste heat recovery on two-stroke IC engine aboard ships, Renewable and Sustainable Energy Reviews, 19 (2013) 385-401.
[41] The Paris Agreement, DOI: https://unfccc.int/process-and-meetings/the-paris-agreement/the-paris-agreement, 10th, Feb, 2019.
[42] L. Cozzi, World energy Outlook 2018, INTERNATIONAL ENERGY AGENCY, 2018.
[43] Annual Energy Outlook 2018, U.S. Energy Information Administration, U.S. Department of Energy, 2018.
[44] Annual Energy Review, DOI: https://www.eia.gov/totalenergy/data/annual/, 10th, Feb, 2019.
[45] World Energy Model Documentation, International Energy Agency, 2017.
[46] L. Waters, ENERGY CONSUMPTION IN THE UK, Department for Business, Energy & Industrial Strategy, 2017.
[47] T. Wang, Y. Zhang, J. Zhang, G. Shu, Z. Peng, Analysis of recoverable exhaust energy from a light-duty gasoline engine, Applied Thermal Engineering, 53 (2013) 414-419.
[48] A. Rahman, F. Razzak, R. Afroz, A.K.M. Mohiuddin, M.N.A. Hawlader, Power generation from waste of IC engines, Renewable & Sustainable Energy Reviews, 51 (2015) 382-395.
[49] R.J. Stevens, S.J. Weinstein, K.S. Koppula, Theoretical limits of thermoelectric power generation from exhaust gases, Applied Energy, 133 (2014) 80-88.
[50] H. Aghaali, H.-E. Ångström, A review of turbocompounding as a waste heat recovery system for internal combustion engines, Renewable and Sustainable Energy Reviews, 49 (2015) 813-824.

[51] J. Ringler, M. Seifert, V. Guyotot, W. Hübner, Rankine Cycle for Waste Heat Recovery of IC Engines, in, SAE International, 2009.
[52] J. Yang, Develop Thermoelectric Technology for Automotive Waste Heat Recovery, GM Research & Development Center, 2009.
[53] F.J. Disalvo, Thermoelectric Cooling and Power Generation, Science, 285 (1999) 703-706.
[54] M. Hamid Elsheikh, D.A. Shnawah, M.F.M. Sabri, S.B.M. Said, M. Haji Hassan, M.B. Ali Bashir, M. Mohamad, A review on thermoelectric renewable energy: Principle parameters that affect their performance, Renewable and Sustainable Energy Reviews, 30 (2014) 337-355.
[55] X. Zhang, L.-D. Zhao, Thermoelectric materials: Energy conversion between heat and electricity, Journal of Materiomics, 1 (2015) 92-105.
[56] R. Stobart, M.A. Wijewardane, Z.J. Yang, Comprehensive analysis of thermoelectric generation systems for automotive applications, Applied Thermal Engineering, 112 (2017) 1433-1444.
[57] X. Liu, Y.D. Deng, S. Chen, W.S. Wang, Y. Xu, C.Q. Su, A case study on compatibility of automotive exhaust thermoelectric generation system, catalytic converter and muffler, Case Studies in Thermal Engineering, 2 (2014) 62-66.
[58] D. Champier, Thermoelectric generators: A review of applications, Energy Conversion and Management, 140 (2017) 167-181.
[59] J.G. Haidar, J.I. Ghojel, Waste heat recovery from the exhaust of low-power diesel engine using thermoelectric generators, in: ICT2001: Proceedings of the 20th International Conference on Thermoelectrics, IEEE, Institute of Electrical and Electronics Engineers, USA, 2001.
[60] S.K. Yee, S. LeBlanc, K.E. Goodson, C. Dames, $ per W metrics for thermoelectric power generation: beyond ZT, Energy & Environmental Science, 6 (2013) 2561-2571.
[61] S. LeBlanc, S.K. Yee, M.L. Scullin, C. Dames, K.E. Goodson, Material and manufacturing cost considerations for thermoelectrics, Renewable & Sustainable Energy Reviews, 32 (2014) 313-327.
[62] Z.T.G. Chen, A Comprehensive Review of Heat Transfer in Thermoelectric Materials and Devices, (2016).

[63] A. Mahmoudi, M. Fazli, M.R. Morad, A recent review of waste heat recovery by Organic Rankine Cycle, Applied Thermal Engineering, 143 (2018) 660-675.
[64] T. Wang, Y. Zhang, Z. Peng, G. Shu, A review of researches on thermal exhaust heat recovery with Rankine cycle, Renewable and Sustainable Energy Reviews, 15 (2011) 2862-2871.
[65] F. Zhou, S.N. Joshi, R. Rhote-Vaney, E.M. Dede, A review and future application of Rankine Cycle to passenger vehicles for waste heat recovery, Renewable and Sustainable Energy Reviews, 75 (2017) 1008-1021.
[66] A. Domingues, H. Santos, M. Costa, Analysis of vehicle exhaust waste heat recovery potential using a Rankine cycle, 49 (2013) 71-85.
[67] M.G. He, X.X. Zhang, K. Zeng, K. Gao, A combined thermodynamic cycle used for waste heat recovery of internal combustion engine, Energy, 36 (2011) 6821-6829.
[68] S. Lion, C.N. Michos, I. Vlaskos, C. Rouaud, R. Taccani, A review of waste heat recovery and Organic Rankine Cycles (ORC) in on-off highway vehicle Heavy Duty Diesel Engine applications, Renewable and Sustainable Energy Reviews, 79 (2017) 691-708.
[69] S. Amicabile, J.-I. Lee, D. Kum, A comprehensive design methodology of organic Rankine cycles for the waste heat recovery of automotive heavy-duty diesel engines, Applied Thermal Engineering, 87 (2015) 574-585.
[70] E.H. Wang, H.G. Zhang, Y. Zhao, B.Y. Fan, Y.T. Wu, Q.H. Mu, Performance analysis of a novel system combining a dual loop organic Rankine cycle (ORC) with a gasoline engine, Energy, 43 (2012) 385-395.
[71] A. Boretti, Recovery of exhaust and coolant heat with R245fa organic Rankine cycles in a hybrid passenger car with a naturally aspirated gasoline engine, Applied Thermal Engineering, 36 (2012) 73-77.
[72] F. Yang, X. Dong, H. Zhang, Z. Wang, K. Yang, J. Zhang, E. Wang, H. Liu, G. Zhao, Performance analysis of waste heat recovery with a dual loop organic Rankine cycle (ORC) system for diesel engine under various operating conditions, Energy Conversion and Management, 80 (2014) 243-255.

[73] J. Li, P. Li, G. Pei, J.Z. Alvi, J. Ji, Analysis of a novel solar electricity generation system using cascade Rankine cycle and steam screw expander, Applied Energy, 165 (2016) 627-638.
[74] N. Nazari, P. Heidarnejad, S. Porkhial, Multi-objective optimization of a combined steam-organic Rankine cycle based on exergy and exergo-economic analysis for waste heat recovery application, Energy Conversion and Management, 127 (2016) 366-379.
[75] G. Shu, G. Yu, H. Tian, H. Wei, X. Liang, Z. Huang, Multi-approach evaluations of a cascade-Organic Rankine Cycle (C-ORC) system driven by diesel engine waste heat: Part A – Thermodynamic evaluations, Energy Conversion and Management, 108 (2016) 579-595.
[76] Y.M. Kim, D.G. Shin, C.G. Kim, G.B. Cho, Single-loop organic Rankine cycles for engine waste heat recovery using both low- and high-temperature heat sources, Energy, 96 (2016) 482-494.
[77] T. Chen, W. Zhuge, Y. Zhang, L. Zhang, A novel cascade organic Rankine cycle (ORC) system for waste heat recovery of truck diesel engines, Energy Conversion and Management, 138 (2017) 210-223.
[78] A. Uusitalo, J. Honkatukia, T. Turunen-Saaresti, Evaluation of a small-scale waste heat recovery organic Rankine cycle, Applied Energy, 192 (2017) 146-158.
[79] Exhaust Gas Heat Recovery System, DOI: http://www.bosal.com/en/case-studies/exhaust-gas-heat-recovery-system, 23rd May, 2018.
[80] P. Diehl, F. Haubner, S. Klopstein, F. Koch, Exhaust Heat Recovery System for Modern Cars, in, SAE International, 2001.
[81] S. Uppuluri, A.M. Naiknaware, H.R. Khalane, Evaluation of Exhaust Heat Recovery System Effectiveness in Engine Friction Reduction and Fuel Economy Improvement, in: Symposium on International Automotive Technology 2017, Society of Automotive Engineers (SAE), Pune , India, 2017.
[82] S. Uppuluri, H. R Khalane, A. Naiknaware, Evaluation of Exhaust Heat Recovery System Effectiveness in Engine Friction Reduction and Fuel Economy Improvement for Indian Hatchback, in, SAE International, 2017.
[83] S. Rai, S. Arslan, B. Jawad, Exhaust Heat Recovery System Study in Internal Combustion Engines, in, SAE International, 2018.

[84] E. Barrieu, EHRS Impact on Engine Warm up and Fuel Economy, 2011.
[85] The Faurecia compact Exhaust Heat Recovery System celebrates world first on the new Hyundai Ioniq Hybrid, DOI: https://www.faurecia.com/en/newsroom/faurecia-compact-exhaust-heat-recovery-system-celebrates-world-first-new-hyundai-ioniq-hybrid, 23rd May, 2018.
[86] M. Karlsson, M. Åbom, M. Lalit, R. Glav, A Note on the Applicability of Thermo-Acoustic Engines for Automotive Waste Heat Recovery, in, SAE International, 2016.
[87] J. Zhou, M. Karlsson, M. Abom, Study of Thermoacoustic Engine for Automotive Exhaust Waste Heat Recovery, in, SAE International, 2019.
[88] D. Sahoo, A. Kotrba, T. Steiner, G. Swift, Waste Heat Recovery for Light-Duty Truck Application Using ThermoAcoustic Converter Technology, in, SAE International, 2017.
[89] N. Rott, Thermoacoustics, Advances in Applied Mechanics, Vol. 20, Elsevier, 1980, pp. 135-175.
[90] H. Kang, P. Cheng, Z. Yu, H. Zheng, A two-stage traveling-wave thermoacoustic electric generator with loudspeakers as alternators, Applied Energy, 137 (2015) 9-17.
[91] V. Zorgnotti, G. Penelet, G. Poignand, S. Garrett, Prediction of limit cycle amplitudes in thermoacoustic engines by means of impedance measurements, Journal of Applied Physics, 124 (2018) 154901.
[92] N.A. Zolpakar, N. Mohd-Ghazali, M. Hassan El-Fawal, Performance analysis of the standing wave thermoacoustic refrigerator: A review, Renewable and Sustainable Energy Reviews, 54 (2016) 626-634.
[93] T. Yazaki, A. Iwata, T. Maekawa, A. Tominaga, Traveling wave thermoacoustic engine in a looped tube, Physical Review Letters, 81 (1998) 3128.
[94] S. Backhaus, G.W. Swift, A thermoacoustic-Stirling heat engine: Detailed study, The Journal of the Acoustical Society of America, 107 (2000) 3148-3166.
[95] M. Tijani, S. Spoelstra, A high performance thermoacoustic engine, Journal of Applied Physics, 110 (2011) 093519.

[96] K. De Blok, Low operating temperature integral thermo acoustic devices for solar cooling and waste heat recovery, Journal of the Acoustical Society of America, 123 (2008) 3541-3541.
[97] A. Ruziewicz, A. Kruse, Z. Gnutek, Thermodynamic analysis of a thermoacoustic travelling wave engine, Journal of Mechanical and Energy Engineering, 2 (2018) 67-74.
[98] P.J. Price, Theory of Transport Effects in Semiconductors - Thermoelectricity, Physical Review, 104 (1956) 1223-1239.
[99] C. Herring, Theory of the Thermoelectric Power of Semiconductors, Physical Review, 96 (1954) 1163-1187.
[100] D. Enescu, Thermoelectric Energy Harvesting: Basic Principles and Applications, Green Energy Advances, IntechOpen, 2019.
[101] G. Neeli, D.K. Behara, M.K. Kumar, State of the Art Review on Thermoelectric Materials, International Journal of Science and Research (IJSR), 5 (2016) 1833 - 1844.
[102] J.-c. Zheng, Recent advances on thermoelectric materials, Frontiers of Physics in China, 3 (2008) 269-279.
[103] C. Chang, L.-D. Zhao, Anharmoncity and low thermal conductivity in thermoelectrics, Materials Today Physics, 4 (2018) 50-57.
[104] K.L. Peng, X. Lu, H. Zhan, S. Hui, X.D. Tang, G.W. Wang, J.Y. Dai, C. Uher, G.Y. Wang, X.Y. Zhou, Broad temperature plateau for high ZTs in heavily doped p-type SnSe single crystals, Energy & Environmental Science, 9 (2016) 454-460.
[105] A.J. Minnich, M.S. Dresselhaus, Z.F. Ren, G. Chen, Bulk nanostructured thermoelectric materials: current research and future prospects, Energy & Environmental Science, 2 (2009) 466-479.
[106] J. Li, J.H. Sui, Y.L. Pei, C. Barreteau, D. Berardan, N. Dragoe, W. Cai, J.Q. He, L.D. Zhao, A high thermoelectric figure of merit ZT > 1 in Ba heavily doped BiCuSeO oxyselenides, Energy & Environmental Science, 5 (2012) 8543-8547.
[107] Q. Zhang, B. Liao, Y. Lan, K. Lukas, W. Liu, K. Esfarjani, C. Opeil, D. Broido, G. Chen, Z. Ren, High thermoelectric performance by resonant dopant indium in nanostructured SnTe, Proc Natl Acad Sci U S A, 110 (2013) 13261-13266.

[108] J.-F. Li, W.-S. Liu, L.-D. Zhao, M. Zhou, High-performance nanostructured thermoelectric materials, Npg Asia Materials, 2 (2010) 152.
[109] Q. Zhang, Y. Sun, W. Xu, D. Zhu, Organic thermoelectric materials: emerging green energy materials converting heat to electricity directly and efficiently, Advanced Materials, 26 (2014) 6829-6851.
[110] X. Liu, Z. Wang, Printable Thermoelectric Materials and Applications, Frontiers in Materials, 6 (2019).
[111] M. Orrill, S. Leblanc, Printed thermoelectric materials and devices: Fabrication techniques, advantages, and challenges, Journal of Applied Polymer Science, 134 (2017).
[112] C. Gayner, K.K. Kar, Recent advances in thermoelectric materials, Progress in Materials Science, 83 (2016) 330-382.
[113] J. He, T.M. Tritt, Advances in thermoelectric materials research: Looking back and moving forward, Science, 357 (2017) eaak9997.
[114] L.D. Zhao, G. Tan, S. Hao, J. He, Y. Pei, H. Chi, H. Wang, S. Gong, H. Xu, V.P. Dravid, C. Uher, G.J. Snyder, C. Wolverton, M.G. Kanatzidis, Ultrahigh power factor and thermoelectric performance in hole-doped single-crystal SnSe, Science, 351 (2016) 141-144.
[115] K. Biswas, J. He, I.D. Blum, C.I. Wu, T.P. Hogan, D.N. Seidman, V.P. Dravid, M.G. Kanatzidis, High-performance bulk thermoelectrics with all-scale hierarchical architectures, Nature, 489 (2012) 414-418.
[116] O. Bubnova, X. Crispin, Towards polymer-based organic thermoelectric generators, Energy & Environmental Science, 5 (2012) 9345-9362.
[117] K. Koumoto, Y.F. Wang, R.Z. Zhang, A. Kosuga, R. Funahashi, Oxide 'Thermoelectric Materials: A Nanostructuring Approach, Annual Review of Materials Research, Vol 40, 40 (2010) 363-394.
[118] F. Kim, B. Kwon, Y. Eom, J.E. Lee, S. Park, S. Jo, S.H. Park, B.S. Kim, H.J. Im, M.H. Lee, T.S. Min, K.T. Kim, H.G. Chae, W.P. King, J.S. Son, 3D printing of shape-conformable thermoelectric materials using all-inorganic Bi2Te3-based inks, Nature Energy, 3 (2018) 301-309.

[119] Z. Cao, J.J. Shi, R.N. Torah, M.J. Tudor, S.P. Beeby, All dispenser printed flexible 3D structured thermoelectric generators, Journal of Physics: Conference Series, 660 (2015) 012096.
[120] A.I. Hochbaum, R. Chen, R.D. Delgado, W. Liang, E.C. Garnett, M. Najarian, A. Majumdar, P. Yang, Enhanced thermoelectric performance of rough silicon nanowires, Nature, 451 (2008) 163.
[121] J.P. Heremans, V. Jovovic, E.S. Toberer, A. Saramat, K. Kurosaki, A. Charoenphakdee, S. Yamanaka, G.J. Snyder, Enhancement of thermoelectric efficiency in PbTe by distortion of the electronic density of states, Science, 321 (2008) 554-557.
[122] J.R. Sootsman, D.Y. Chung, M.G. Kanatzidis, New and old concepts in thermoelectric materials, Angew Chem Int Ed Engl, 48 (2009) 8616-8639.
[123] M. Zebarjadi, B.L. Liao, K. Esfarjani, M. Dresselhaus, G. Chen, Enhancing the Thermoelectric Power Factor by Using Invisible Dopants, Advanced Materials, 25 (2013) 1577-1582.
[124] B. Poudel, Q. Hao, Y. Ma, Y. Lan, A. Minnich, B. Yu, X. Yan, D. Wang, A. Muto, D. Vashaee, X. Chen, J. Liu, M.S. Dresselhaus, G. Chen, Z. Ren, High-thermoelectric performance of nanostructured bismuth antimony telluride bulk alloys, Science, 320 (2008) 634-638.
[125] S. Yazdani, M.T. Pettes, Nanoscale self-assembly of thermoelectric materials: a review of chemistry-based approaches, Nanotechnology, 29 (2018) 432001.
[126] Q.H. Zhang, X. Ai, L.J. Wang, Y.X. Chang, W. Luo, W. Jiang, L.D. Chen, Improved Thermoelectric Performance of Silver Nanoparticles-Dispersed Bi2Te3 Composites Deriving from Hierarchical Two-Phased Heterostructure, Advanced Functional Materials, 25 (2015) 966-976.
[127] H. Alam, S. Ramakrishna, A review on the enhancement of figure of merit from bulk to nano-thermoelectric materials, Nano Energy, 2 (2013) 190-212.
[128] Y. Wang, S. Li, Y. Zhang, X. Yang, Y. Deng, C. Su, The influence of inner topology of exhaust heat exchanger and thermoelectric module distribution on the performance of automotive thermoelectric generator, Energy Conversion and Management, 126 (2016) 266-277.

[129] C.Q. Su, W.S. Wang, X. Liu, Y.D. Deng, Simulation and experimental study on thermal optimization of the heat exchanger for automotive exhaust-based thermoelectric generators, Case Studies in Thermal Engineering, 4 (2014) 85-91.
[130] Y.D. Deng, X. Liu, S. Chen, N.Q. Tong, Thermal Optimization of the Heat Exchanger in an Automotive Exhaust-Based Thermoelectric Generator, Journal of Electronic Materials, 42 (2013) 1634-1640.
[131] E. Hatzikraniotis, K.T. Zorbas, I. Samaras, T. Kyratsi, K.M. Paraskevopoulos, Efficiency Study of a Commercial Thermoelectric Power Generator (TEG) Under Thermal Cycling, Journal of Electronic Materials, 39 (2010) 2112-2116.
[132] N.D. Love, J.P. Szybist, C.S. Sluder, Effect of heat exchanger material and fouling on thermoelectric exhaust heat recovery, Applied Energy, 89 (2012) 322-328.
[133] K.R. Rao, Proceedings of the Seventh International Conference on Thermoelectric Energy Conversion, University of Texas at Arlington, 1988.
[134] K. Ikoma, M. Munekiyo, K. Furuya, M. Kobayashi, T. Izumi, K. Shinohara, Thermoelectric module and generator for gasoline engine vehicles, in: Seventeenth International Conference on Thermoelectrics. Proceedings ICT98 (Cat. No. 98TH8365), IEEE, 1998, pp. 464-467.
[135] A. Kushch, The Effects of an Exhaust Thermoelectric Generator of a GM Sierra Pickup Truck, Hi-Z Technology Inc., 2004.
[136] H. Schock, Thermoelectric Conversion of Waste Heat to Electricity in an IC Engine Powered Vehicle, Cummins, 2007.
[137] E.F. Thacher, B.T. Helenbrook, M.A. Karri, C.J. Richter, Testing of an automobile exhaust thermoelectric generator in a light truck, Proceedings of the Institution of Mechanical Engineers, Part D: Journal of Automobile Engineering, 221 (2007) 95-107.
[138] Fiat, Final Report Summary - HEATRECAR (Reduced energy consumption by massive thermoelectric waste heat recovery in light-duty trucks), 25th, May, 2018.
[139] S.-K. Kim, B.-C. Won, S.-H. Rhi, S.-H. Kim, J.-H. Yoo, J.-C. Jang, Thermoelectric Power Generation System for Future Hybrid Vehicles Using Hot Exhaust Gas, Journal of Electronic Materials, 40 (2011) 778-783.

[140] A. Eder, M. Linde, Efficient and Dynamic –The BMW Group Roadmap for the Application of Thermoelectric Generators, BMW Group, 2011.
[141] F. Stabler, Automotive Thermoelectric Generator (TEG) Controls, General Motors & Future Tech LLC, 2012.
[142] D. Crane, Thermoelectric Waste Heat Recovery Program for Passenger Vehicles, Gentherm LLC, 2013.
[143] N. Zienna, A MODEL TO EVALUATE THE POTENTIAL BENEFITS OF A THERMOELECTRIC GENERATOR IN REDUCING CO2 EMISSIONS, Jaguar Land Rover Limited, 2017.
[144] Y.L. Zhang, M. Cleary, X.W. Wang, N. Kempf, L. Schoensee, J. Yang, G. Joshi, L. Meda, High-temperature and high-power-density nanostructured thermoelectric generator for automotive waste heat recovery, Energy Conversion and Management, 105 (2015) 946-950.
[145] M. Kober, H. Friedrich, Thermoelectric Generators (TEG) with high power density for application in hybrid cars, (2016).
[146] X. Liu, Y.D. Deng, Z. Li, C.Q. Su, Performance analysis of a waste heat recovery thermoelectric generation system for automotive application, Energy Conversion and Management, 90 (2015) 121-127.
[147] T.Y. Kim, A.A. Negash, G. Cho, Waste heat recovery of a diesel engine using a thermoelectric generator equipped with customized thermoelectric modules, Energy Conversion and Management, 124 (2016) 280-286.
[148] C.-C. Weng, M.-J. Huang, A simulation study of automotive waste heat recovery using a thermoelectric power generator, International Journal of Thermal Sciences, 71 (2013) 302-309.
[149] J.W. LaGrandeur, Thermoelectric Waste Heat Recovery Program for Passenger Vehicles, 2012.
[150] M. Hatami, D.D. Ganji, M. Gorji-Bandpy, Numerical study of finned type heat exchangers for ICEs exhaust waste heat recovery, Case Studies in Thermal Engineering, 4 (2014) 53-64.
[151] Y.D. Deng, Y.L. Chen, S. Chen, W.D. Xianyu, C.Q. Su, Research on Integration of an Automotive Exhaust-Based Thermoelectric Generator and a

Three-Way Catalytic Converter, Journal of Electronic Materials, 44 (2015) 1524-1530.
[152] H. Yang, G. Shu, H. Tian, X. Ma, T. Chen, P. Liu, Optimization of thermoelectric generator (TEG) integrated with three-way catalytic converter (TWC) for harvesting engine's exhaust waste heat, Applied Thermal Engineering, 144 (2018) 628-638.
[153] W. He, S.X. Wang, C. Lu, X. Zhang, Y.Z. Li, Influence of different cooling methods on thermoelectric performance of an engine exhaust gas waste heat recovery system, Applied Energy, 162 (2016) 1251-1258.
[154] K.P. Venkitaraj, S. Suresh, A. Venugopal, Experimental study on the thermal performance of nano enhanced pentaerythritol in IC engine exhaust heat recovery application, Applied Thermal Engineering, 137 (2018) 461-474.
[155] M.K. Altstedde, F. Rinderknecht, H. Friedrich, Integrating phase-change materials into automotive thermoelectric generators, Journal of Electronic Materials, 43 (2014) 2134-2140.
[156] Z.B. Tang, Y.D. Deng, C.Q. Su, W.W. Shuai, C.J. Xie, A research on thermoelectric generator's electrical performance under temperature mismatch conditions for automotive waste heat recovery system, Case Studies in Thermal Engineering, 5 (2015) 143-150.
[157] A. Montecucco, J. Siviter, A.R. Knox, The effect of temperature mismatch on thermoelectric generators electrically connected in series and parallel, Applied Energy, 123 (2014) 47-54.
[158] H. Mamur, R. Ahiska, Application of a DC–DC boost converter with maximum power point tracking for low power thermoelectric generators, Energy Conversion and Management, 97 (2015) 265-272.
[159] S. Twaha, J. Zhu, B. Li, Y. Yan, K. Huang, Parameter analysis of thermoelectric generator/dc-dc converter system with maximum power point tracking, Energy for Sustainable Development, 41 (2017) 49-60.
[160] S. Twaha, J. Zhu, L. Maraaba, K. Huang, B. Li, Y.Y. Yan, Maximum Power Point Tracking Control of a Thermoelectric Generation System Using the Extremum Seeking Control Method, Energies, 10 (2017) 18.

[161] S. Twaha, J. Zhu, Y. Yan, B. Li, K. Huang, Performance analysis of thermoelectric generator using dc-dc converter with incremental conductance based maximum power point tracking, Energy for Sustainable Development, 37 (2017) 86-98.
[162] Fitriani, R. Ovik, B.D. Long, M.C. Barma, M. Riaz, M.F.M. Sabri, S.M. Said, R. Saidur, A review on nanostructures of high-temperature thermoelectric materials for waste heat recovery, Renewable & Sustainable Energy Reviews, 64 (2016) 635-659.
[163] Global EV Outlook 2018, DOI: https://www.iea.org/gevo2018/, 3rd, Mar, 2019.
[164] X. Zhang, K.T. Chau, C.C. Chan, Overview of Thermoelectric Generation for Hybrid Vehicles, Journal of Asian Electric Vehicles, 6 (2008) 1119-1124.
[165] C. Yu, K. Chau, C. Chan, Thermoelectric waste-heat energy recovery for hybrid electric vehicles, in: International Electric Vehicle Symposium, 2007.
[166] K. Smith, M. Thornton, Feasibility of thermoelectrics for waste heat recovery in hybrid vehicles, National Renewable Energy Lab.(NREL), Golden, CO (United States), 2007.
[167] R. Vijayagopal, A. Rousseau, Impact of TEGs on the Fuel Economy of Conventional and Hybrid Vehicles, in, SAE International, 2015.
[168] M. Mori, T. Yamagami, M. Sorazawa, T. Miyabe, S. Takahashi, T. Haraguchi, Simulation of Fuel Economy Effectiveness of Exhaust Heat Recovery System Using Thermoelectric Generator in a Series Hybrid, in, SAE International, 2011.
[169] Q.E. Hussain, D.R. Brigham, C.W. Maranville, Thermoelectric Exhaust Heat Recovery for Hybrid Vehicles, in, SAE International, 2009.
[170] Most used 3D printing technologies in 2017 and 2018, 2nd, April 2019.
[171] C. Chang, M. Wu, D. He, Y. Pei, C.-F. Wu, X. Wu, H. Yu, F. Zhu, K. Wang, Y. Chen, L. Huang, J.-F. Li, J. He, L.-D. Zhao, 3D charge and 2D phonon transports leading to high out-of-plane ZT in n-type SnSe crystals, Science, 360 (2018) 778.
[172] M.R. Burton, S. Mehraban, D. Beynon, J. McGettrick, T. Watson, N.P. Lavery, M.J. Carnie, 3D Printed SnSe Thermoelectric Generators with High Figure of Merit, Advanced Energy Materials, (2019) 1900201.

[173] Harvesting unused energy with flat thermoelectrics, DOI: https://www.fraunhofer.de/en/press/research-news/2013/march/harvesting-unused-energy-with-flat-thermoelectrics.html, 3rd, April, 2019.
[174] Heat Transfer Module User's Guide COMSOL 5.3, COMSOL.
[175] S. Kakaç, R.K. Shah, W. Aung, Handbook of single-phase convective heat transfer, (1987).
[176] T.L. Perelman, On conjugated problems of heat transfer, International Journal of Heat and Mass Transfer, 3 (1961) 293-303.
[177] W.-Q. Tao, Numerical heat transfer, in, Xi'an Jiaotong University Press, Xi'an, 2001.
[178] A. Bejan, Convection heat transfer, John wiley & sons, 2013.
[179] R. Karvinen, Use of Analytical Expressions of Convection in Conjugated Heat Transfer Problems, (2010) 639-651.
[180] A. Dorfman, Z. Renner, Conjugate Problems in Convective Heat Transfer: Review, Mathematical Problems in Engineering, 2009 (2009).
[181] A.S. Dorfman, Conjugate problems in convective heat transfer, CRC Press, 2009.
[182] F.P. Incropera, A.S. Lavine, T.L. Bergman, D.P. DeWitt, Fundamentals of heat and mass transfer, Wiley, 2007.
[183] M. Haim, H. Kalman, The effect of internal particle heat conduction on heat transfer analysis of turbulent gas–particle flow in a dilute state, Granular Matter, 10 (2008) 341-349.
[184] S.L. Bertoli, C.K. de Souza, J.C.S.C. Bastos, J. de Almeida, J. de Almeida, S. Licodiedoff, V.R. Wiggers, Lumped parameter analysis criteria for heat transfer in a co-current moving bed with adiabatic walls, Powder Technology, 317 (2017) 381-390.
[185] H. Jääskeläinen, Diesel Exhaust Gas, DOI: https://www.dieselnet.com/tech/diesel_exh.php, 16, Dec, 2016.
[186] D. Li, G.Q. Zhang, K. Pan, X. Ma, L. Liu, J. Cao, Numerical simulation on heat pipe for high power LED multi-chip module packaging, in: 2009 International Conference on Electronic Packaging Technology & High Density Packaging, 2009, pp. 393-397.

[187] M. Jaegle, Multiphysics simulation of thermoelectric systems-modeling of Peltier-cooling and thermoelectric generation, in: COMSOL Conference 2008 Hannover, 2008.
[188] Performance Calculator, DOI: https://hi-z.com/performance-calculator/, 15th, Jan, 2016.
[189] L.L. Baranowski, G.J. Snyder, E.S. Toberer, Effective thermal conductivity in thermoelectric materials, Journal of Applied Physics, 113 (2013) 204904.
[190] S. Zhou, B.G. Sammakia, B. White, P. Borgesen, Multiscale modeling of thermoelectric generators for the optimized conversion performance, International Journal of Heat and Mass Transfer, 62 (2013) 435-444.
[191] I.P. Kandylas, A.M. Stamatelos, Engine exhaust system design based on heat transfer computation, Energy Conversion and Management, 40 (1999) 1057-1072.
[192] S. Kumar, S.D. Heister, X. Xu, J.R. Salvador, G.P. Meisner, Thermoelectric Generators for Automotive Waste Heat Recovery Systems Part I: Numerical Modeling and Baseline Model Analysis, Journal of Electronic Materials, 42 (2013) 665-674.
[193] S. Kumar, S.D. Heister, X. Xu, J.R. Salvador, G.P. Meisner, Thermoelectric Generators for Automotive Waste Heat Recovery Systems Part II: Parametric Evaluation and Topological Studies, Journal of Electronic Materials, 42 (2013) 944-955.
[194] X. Liu, Y.D. Deng, K. Zhang, M. Xu, Y. Xu, C.Q. Su, Experiments and simulations on heat exchangers in thermoelectric generator for automotive application, 71 (2014) 364-370.
[195] H. Lu, T. Wu, S. Bai, K. Xu, Y. Huang, W. Gao, X. Yin, L. Chen, Experiment on thermal uniformity and pressure drop of exhaust heat exchanger for automotive thermoelectric generator, Energy, 54 (2013) 372-377.
[196] W. He, S. Wang, Y. Li, Y. Zhao, Structural size optimization on an exhaust exchanger based on the fluid heat transfer and flow resistance characteristics applied to an automotive thermoelectric generator, Energy Conversion and Management, 129 (2016) 240-249.
[197] K.A. Joudi, A.M. Witwit, Improvements of gravity assisted wickless heat pipes, 41 (2000) 2041-2061.

[198] R.T. Dobson, Theoretical and experimental modelling of an open oscillatory heat pipe including gravity, 43 (2004) 113-119.
[199] Y. Zhang, A. Faghri, Heat transfer enhancement in latent heat thermal energy storage system by using the internally finned tube, International Journal of Heat and Mass Transfer, 39 (1996) 3165-3173.
[200] G. Fabbri, Heat transfer optimization in internally finned tubes under laminar flow conditions, 41 (1998) 1243-1253.
[201] W.-K. Tien, R.-H. Yeh, J.-C. Hsiao, Numerical Analysis of Laminar Flow and Heat Transfer in Internally Finned Tubes, Heat Transfer Engineering, 33 (2012) 957-971.
[202] M. Nitsche, R.O. Gbadamosi, Chapter 12 - Finned Tube Heat Exchangers, Heat Exchanger Design Guide, Butterworth-Heinemann, Boston, 2016, pp. 247-264.
[203] W.M. Kays, Convective heat and mass transfer, Tata McGraw-Hill Education, 2012.
[204] R.J. Moffat, Describing the uncertainties in experimental results, Experimental Thermal and Fluid Science, 1 (1988) 3-17.
[205] R.K. Shah, D.P. Sekulic, Fundamentals of heat exchanger design, John Wiley & Sons, 2003.
[206] K. Thulukkanam, Heat exchanger design handbook, CRC press, 2013.
[207] A.P. Fraas, Heat exchanger design, John Wiley & Sons, 1989.
[208] Logarithmic mean temperature difference, DOI: https://en.wikipedia.org/wiki/Logarithmic_mean_temperature_difference, 13th, Feb, 2019.
[209] A. Cengel, HEHT TRANSFER, (2007).
[210] S.J.M. Cartaxo, F.A.N. Fernandes, Counterflow logarithmic mean temperature difference is actually the upper bound: A demonstration, Applied Thermal Engineering, 31 (2011) 1172-1175.
[211] M. Nitsche, R.O. Gbadamosi, Chapter 2 - Calculations of the Temperature Differences LMTD and CMTD, Heat Exchanger Design Guide, Butterworth-Heinemann, Boston, 2016, pp. 21-35.

[212] S. Manikandan, S.C. Kaushik, The influence of Thomson effect in the performance optimization of a two stage thermoelectric generator, Energy, 100 (2016) 227-237.
[213] M. Comamala, T. Pujol, I.R. Cozar, E. Massaguer, A. Massaguer, Power and Fuel Economy of a Radial Automotive Thermoelectric Generator: Experimental and Numerical Studies, Energies, 11 (2018).
[214] S. Lan, Z.J. Yang, R. Stobart, R. Chen, Prediction of the fuel economy potential for a skutterudite thermoelectric generator in light-duty vehicle applications, Applied Energy, 231 (2018) 68-79.
[215] A. Massaguer, E. Massaguer, M. Comamala, T. Pujol, J.R. Gonzalez, M.D. Cardenas, D. Carbonell, A.J. Bueno, A method to assess the fuel economy of automotive thermoelectric generators, Applied Energy, 222 (2018) 42-58.
[216] S.H. Yu, Q. Du, H. Diao, G.Q. Shu, K. Jiao, Effect of vehicle driving conditions on the performance of thermoelectric generator, Energy Conversion and Management, 96 (2015) 363-376.
[217] M. Nitsche, R.O. Gbadamosi, Chapter 3 - Calculations of the Heat Transfer Coefficients and Pressure Losses in Convective Heat Transfer, Heat Exchanger Design Guide, Butterworth-Heinemann, Boston, 2016, pp. 37-63.
[218] T. Elnady, S. Elsaadany, M. Abom, Flow and Pressure Drop Calculation Using Two-Ports, Journal of Vibration and Acoustics-Transactions of the Asme, 133 (2011).
[219] M. Comamala, I.R. Cozar, A. Massaguer, E. Massaguer, T. Pujol, Effects of Design Parameters on Fuel Economy and Output Power in an Automotive Thermoelectric Generator, Energies, 11 (2018).
[220] X.L. Li, C.J. Xie, S.H. Quan, L. Huang, W. Fang, Energy management strategy of thermoelectric generation for localized air conditioners in commercial vehicles based on 48 V electrical system, Applied Energy, 231 (2018) 887-900.
[221] D.M. Rowe, J. Smith, G. Thomas, G. Min, Weight Penalty Incurred in Thermoelectric Recovery of Automobile Exhaust Heat, Journal of Electronic Materials, 40 (2011) 784.

[222] M.L.M. Tasuni, Z.A. Latiff, H. Nasution, M.R.M. Perang, H.M. Jamil, M.N. Misseri, Performance of a Water Pump in an Automotive Engine Cooling System, Jurnal Teknologi, 78 (2016) 47-53.
[223] The Mathematics of Pumping Water, The Royal Academy of Engineering, DOI: https://www.raeng.org.uk/publications/other/17-pumping-water, 2, 2019.
[224] V. Filipan, Z. Virag, A. Bergant, Mathematical modelling of a hydraulic ram pump system, Strojniski Vestnik-Journal of Mechanical Engineering, 49 (2003) 137-149.
[225] S. Lan, Z.J. Yang, R. Chen, R. Stobart, A dynamic model for thermoelectric generator applied to vehicle waste heat recovery, Applied Energy, 210 (2018) 327-338.
[226] I.S. Suh, H. Cho, M. Lee, Feasibility study on thermoelectric device to energy storage system of an electric vehicle, Energy, 76 (2014) 436-444.
[227] A. Elefsiniotis, T. Becker, U. Schmid, Thermoelectric Energy Harvesting Using Phase Change Materials (PCMs) in High Temperature Environments in Aircraft, 43 (2014) 1809-1814.
[228] S.-E. Jo, M.-S. Kim, M.-K. Kim, Y.-J. Kim, Power generation of a thermoelectric generator with phase change materials, 22 (2013) 115008.
[229] E. Yin, Q. Li, D. Li, Y. Xuan, Experimental investigation on effects of thermal resistances on a photovoltaic-thermoelectric system integrated with phase change materials, Energy, 169 (2019) 172-185.
[230] H. Ibrahim, A. Ilinca, J. Perron, Energy storage systems—Characteristics and comparisons, Renewable and Sustainable Energy Reviews, 12 (2008) 1221-1250.
[231] T.M.I. Mahlia, T.J. Saktisahdan, A. Jannifar, M.H. Hasan, H.S.C. Matseelar, A review of available methods and development on energy storage; technology update, Renewable and Sustainable Energy Reviews, 33 (2014) 532-545.
[232] R. Amirante, E. Cassone, E. Distaso, P. Tamburrano, Overview on recent developments in energy storage: Mechanical, electrochemical and hydrogen technologies, Energy Conversion and Management, 132 (2017) 372-387.
[233] S.M. Mousavi G, F. Faraji, A. Majazi, K. Al-Haddad, A comprehensive review of Flywheel Energy Storage System technology, Renewable and Sustainable Energy Reviews, 67 (2017) 477-490.

[234] A.A.K. Arani, H. Karami, G.B. Gharehpetian, M.S.A. Hejazi, Review of Flywheel Energy Storage Systems structures and applications in power systems and microgrids, Renewable and Sustainable Energy Reviews, 69 (2017) 9-18.
[235] B. Zalba, J.M. Marín, L.F. Cabeza, H. Mehling, Review on thermal energy storage with phase change: materials, heat transfer analysis and applications, Applied Thermal Engineering, 23 (2003) 251-283.
[236] A. Sharma, V.V. Tyagi, C.R. Chen, D. Buddhi, Review on thermal energy storage with phase change materials and applications, Renewable and Sustainable Energy Reviews, 13 (2009) 318-345.
[237] F. Agyenim, N. Hewitt, P. Eames, M. Smyth, A review of materials, heat transfer and phase change problem formulation for latent heat thermal energy storage systems (LHTESS), Renewable and Sustainable Energy Reviews, 14 (2010) 615-628.
[238] A.M. Khudhair, M.M. Farid, A review on energy conservation in building applications with thermal storage by latent heat using phase change materials, Energy Conversion and Management, 45 (2004) 263-275.
[239] H. Chen, T.N. Cong, W. Yang, C. Tan, Y. Li, Y. Ding, Progress in electrical energy storage system: A critical review, Progress in Natural Science, 19 (2009) 291-312.
[240] K.C. Divya, J. Østergaard, Battery energy storage technology for power systems—An overview, Electric Power Systems Research, 79 (2009) 511-520.
[241] X. Luo, J. Wang, M. Dooner, J. Clarke, Overview of current development in electrical energy storage technologies and the application potential in power system operation, Applied Energy, 137 (2015) 511-536.
[242] A.K. Rohit, K.P. Devi, S. Rangnekar, An overview of energy storage and its importance in Indian renewable energy sector: Part I – Technologies and Comparison, Journal of Energy Storage, 13 (2017) 10-23.
[243] A.K. Rohit, S. Rangnekar, An overview of energy storage and its importance in Indian renewable energy sector: Part II – energy storage applications, benefits and market potential, Journal of Energy Storage, 13 (2017) 447-456.
[244] M.S. Guney, Y. Tepe, Classification and assessment of energy storage systems, Renewable and Sustainable Energy Reviews, 75 (2017) 1187-1197.

[245] M. Aneke, M. Wang, Energy storage technologies and real life applications – A state of the art review, Applied Energy, 179 (2016) 350-377.
[246] A.B. Gallo, J.R. Simões-Moreira, H.K.M. Costa, M.M. Santos, E. Moutinho dos Santos, Energy storage in the energy transition context: A technology review, Renewable and Sustainable Energy Reviews, 65 (2016) 800-822.
[247] S. Ould Amrouche, D. Rekioua, T. Rekioua, S. Bacha, Overview of energy storage in renewable energy systems, International Journal of Hydrogen Energy, 41 (2016) 20914-20927.
[248] L.F. Cabeza, A. Castell, C. Barreneche, A. de Gracia, A.I. Fernández, Materials used as PCM in thermal energy storage in buildings: A review, Renewable and Sustainable Energy Reviews, 15 (2011) 1675-1695.
[249] S. Ayyappan, K. Mayilsamy, V.V. Sreenarayanan, Performance improvement studies in a solar greenhouse drier using sensible heat storage materials, Heat and Mass Transfer, 52 (2016) 459-467.
[250] K. Du, J. Calautit, Z. Wang, Y. Wu, H. Liu, A review of the applications of phase change materials in cooling, heating and power generation in different temperature ranges, Applied Energy, 220 (2018) 242-273.
[251] W. Su, J. Darkwa, G. Kokogiannakis, Review of solid–liquid phase change materials and their encapsulation technologies, Renewable and Sustainable Energy Reviews, 48 (2015) 373-391.
[252] H. Ge, H. Li, S. Mei, J. Liu, Low melting point liquid metal as a new class of phase change material: An emerging frontier in energy area, Renewable and Sustainable Energy Reviews, 21 (2013) 331-346.
[253] Y. Galazutdinova, M. Grágeda, L.F. Cabeza, S. Ushak, Novel inorganic binary mixture for low-temperature heat storage applications, International Journal of Energy Research, 41 (2017) 2356-2364.
[254] H. Garg, S. Mullick, V.K. Bhargava, Solar thermal energy storage, Springer Science & Business Media, 2012.
[255] F. Agyenim, P. Eames, M. Smyth, A comparison of heat transfer enhancement in a medium temperature thermal energy storage heat exchanger using fins, Solar Energy, 83 (2009) 1509-1520.

[256] Y. Lin, Y. Jia, G. Alva, G. Fang, Review on thermal conductivity enhancement, thermal properties and applications of phase change materials in thermal energy storage, Renewable and Sustainable Energy Reviews, 82 (2018) 2730-2742.

[257] R. Velraj, R.V. Seeniraj, B. Hafner, C. Faber, K. Schwarzer, HEAT TRANSFER ENHANCEMENT IN A LATENT HEAT STORAGE SYSTEM1Paper presented at the ISES Solar World Congress, Taejon, South Korea, 24–29 August 1997.1, Solar Energy, 65 (1999) 171-180.

[258] T.-U. Rehman, H.M. Ali, A. Saieed, W. Pao, M. Ali, Copper foam/PCMs based heat sinks: An experimental study for electronic cooling systems, International Journal of Heat and Mass Transfer, 127 (2018) 381-393.

[259] S. Mat, A.A. Al-Abidi, K. Sopian, M.Y. Sulaiman, A.T. Mohammad, Enhance heat transfer for PCM melting in triplex tube with internal–external fins, 74 (2013) 223-236.

[260] U. Stritih, An experimental study of enhanced heat transfer in rectangular PCM thermal storage, 47 (2004) 2841-2847.

[261] Y.B. Tao, Y.-L. He, A review of phase change material and performance enhancement method for latent heat storage system, Renewable and Sustainable Energy Reviews, 93 (2018) 245-259.

[262] R. Akhilesh, A. Narasimhan, C. Balaji, Method to improve geometry for heat transfer enhancement in PCM composite heat sinks, International Journal of Heat and Mass Transfer, 48 (2005) 2759-2770.

[263] Thermoelectric Generator Modules, DOI: https://www.europeanthermodynamics.com/products/thermoelectric-modules/seebeck-generator, 12th, Aug, 2018.

[264] K.P. Venkitaraj, S. Suresh, Experimental Study on Thermal and Chemical Stability of Pentaerythritol Blended with Low Melting Alloy as Possible PCM for Latent Heat Storage, Experimental Thermal and Fluid Science, (2017).

[265] V. K P, S. S, P. B, A. Venugopal, S. C Nair, Pentaerythritol with alumina nano additives for thermal energy storage applications, Journal of Energy Storage, 13 (2017) 359-377.

[266] X. Wang, E. Lu, W. Lin, T. Liu, Z. Shi, R. Tang, C. Wang, Heat storage performance of the binary systems neopentyl glycol/pentaerythritol and neopentyl glycol/trihydroxy methyl-aminomethane as solid–solid phase change materials, Energy Conversion and Management, 41 (2000) 129-134.
[267] L. Nkhonjera, M. Kuboth, A. König-Haagen, G. John, C. King'Ondu, D. Brüggemann, T. Bello-Ochende, Experimental Investigation of a Finned Pentaerythritol-based Heat Storage Unit for Solar Cooking at 150-200℃, 93 (2016) 160-167.
[268] P. Hu, P.-P. Zhao, Y. Jin, Z.-S. Chen, Experimental study on solid–solid phase change properties of pentaerythritol (PE)/nano-AlN composite for thermal storage, Solar Energy, 102 (2014) 91-97.
[269] Pentaerythritol, DOI: https://en.wikipedia.org/wiki/Pentaerythritol, 10th, Nov, 2017.
[270] B.D. Shaw, Uncertainty Analysis of Experimental Data with R, Chapman and Hall/CRC, 2017.
[271] B.M. Ayyub, G.J. Klir, Uncertainty modeling and analysis in engineering and the sciences, Chapman and Hall/CRC, 2006.
[272] D. Yan, Modeling and Application of a Thermoelectric Module, in, 2011.

Appendix 1

The original script from MATLAB of calculating one-dimensional TEM power generation, which is referred to David Yan's thesis [272], is shown as below, the explanations is follow the code behind the "%".

```
close all
clear all
%Geometric parameters input and length of stepx
top_height=300*10^-6;                %input the height of top-connector   unit: m
bottom_height=300*10^-6;             %input the height of bottom-connector
unit: m
middle_height=1500*10^-6;            %input the height of TE          unit: m
A=1400*10^-6*300*10^-6;              %input the area of TE            unit: m^2
stepx=100*10^-6;                     %input the length of step        unit: m
%mesh description (convert the geometric size into grids)
a=round(top_height/stepx);c=round(middle_height/stepx);d=round(bottom_height
/stepx);
m=a+c+d+2;
%physics of Aluminium
k1=237;                              %thermal conductivity    unit: W/mk
Ce1=1/(2.7*10^-8);                   %electrical conductivity unit: A/Vm
%Set the boundary conditions
```

```
I=0;                                %input the current           unit: A
j0=I/A;                             %input the current density unit: A/m^2
Vamb=0;                             %input the boundary electric potential unit:
V
Thigh=150+273.15;                   %input the high boundary temperature
unit: K
Tlow=30+273.15;                     %input the high boundary temperature unit:
K
%Set the initial value of iterative
tol = 10^-6;                        %the criterion of convergence
T=zeros(m,1);                       %establish the temperature distribution
Tinitial=(Thigh+Tlow)/2;
T(1:m,1)=Tinitial;                  %Set the temperature initial value
jx=zeros(m,1);                      %establish the current density distribution
V=zeros(m,1);                       %establish the temperature distribution
V(1:m,1)=-5*10^-16*(Tinitial-273.15)^4+4*10^-13*(Tinitial-273.15)^3-3*10^-
9*(Tinitial-273.15)^2+7*10^-7*(Tinitial-273.15)+0.000164;
S=S1XDfun(T,m,a,c);                 % Seebeck coefficient   unit: V/k
Ce=Ec1XDfun(T,m,a,c);               % Electric conductivity unit: A/Vm
k=K1XDfun(T,m,a,c);                 % thermal conductivity unit: W/mk
TM=TM1XDfun(T,m,a,c);               % Thomson coefficient unit: V/K


for p = 1:1000000                   % Loop through iterations
  Told=T;
  Vold=V;
```

```
 %%%%%%%%%%%%%%%%%%%%%%%%%%%%%%%% calculation of T start
  for i=1:m
     if i==1
         T(i)=(T(i+1)+2*(Thigh))/3;
     elseif i>1 && i<a
         T(i)=(T(i+1)+T(i-1))/2;
     elseif  i==a
         T(i)=(2*T(i+1)+T(i-1))/3;
     elseif i==a+1
         T(i)=(k1*T(i-1)+k(i+1)*T(i+1)+S(i+1)^2*Ce(i+1)*T(i+1)^2-
Ce(i+1)*T(i+1)*S(i+1)*(V(i+1)-V(i)))/(k1+k(i+1)+S(i+1)^2*Ce(i+1)*T(i+1));
     %%%%%%%%%%%%%%%%%%%%%%% TE section
     elseif i==a+2
         jx(i)=-(Ce(i)*(V(i+1)-V(i))/stepx-Ce(i)*S(i)*(T(i+1)-T(i))/stepx);
         T(i)=((k(i+1)+k(i))*T(i+1)/2+2*k(i)*T(i-
1)+stepx*TM(i)*jx(i)*(0.5*(T(i)+T(i+1))-T(i-
1))+jx(i)^2*stepx^2/Ce(i))/((k(i+1)+k(i))/2+2*k(i));
     elseif i>a+2 && i<a+c+1
         jx(i)=-0.5*(Ce(i)*(V(i+1)-V(i-1))/stepx-Ce(i)*S(i)*(T(i+1)-T(i-1))/stepx);
         T(i)=((k(i+1)+k(i))*T(i+1)/2+(k(i-1)+k(i))*T(i-
1)/2+stepx*TM(i)*jx(i)*(T(i+1)-T(i-
1))/2+jx(i)^2*stepx^2/Ce(i))/((k(i+1)+k(i))/2+(k(i)+k(i-1))/2);
     elseif i==a+c+1
         jx(i)=-(Ce(i)*(V(i)-V(i-1))/stepx-Ce(i)*S(i)*(T(i)-T(i-1))/stepx);
         T(i)=(2*k(i)*T(i+1)+(k(i-1)+k(i))*T(i-1)/2+stepx*TM(i)*jx(i)*(T(i+1)-
0.5*(T(i)+T(i-1)))+jx(i)^2*stepx^2/Ce(i))/(2*k(i)+(k(i)+k(i-1))/2);
```

```
    %%%%%%%%%%%%%%%%%%%%%%%% TE section
    elseif i==a+c+2
        T(i)=(k1*T(i+1)+k(i-1)*T(i-1)+S(i-1)^2*T(i-1)^2*Ce(i-1)+Ce(i-1)*S(i-1)*T(i-1)*(V(i)-V(i-1)))/(k1+k(i-1)+S(i-1)^2*T(i-1)*Ce(i-1));
    elseif i==a+c+3
        T(i)=(T(i+1)+2*T(i-1))/3;
    elseif i>a+c+3 && i<m
        T(i)=(T(i+1)+T(i-1))/2;
    elseif i==m
        T(i)=(T(i-1)+2*(Tlow))/3;
    end
  end
 %%%%%%%%%%%%%%%%%%%%%%%%%%%%%%%% calculation of T end
 Ce=Ec1XDfun(T,m,a,c);          %Update the thermoelectric coefficients
 k=K1XDfun(T,m,a,c);
 TM=TM1XDfun(T,m,a,c);
 S=S1XDfun(T,m,a,c);
 %%%%%%%%%%%%%%%%%%%%%%%%%%%%%%%% calculation of V start
 for i=1:m
    if i==1
        V(i)=V(i+1)+j0*stepx/Ce1;
    elseif i>1 && i<a
        V(i)=(V(i+1)+V(i-1))/2;
    elseif  i==a
```

```
        V(i)=(2*V(i+1)+V(i-1))/3;
    elseif i==a+1
        V(i)=(Ce(i+1)*V(i+1)+Ce1*V(i-1)-S(i+1)*Ce(i+1)*(T(i+1)-
T(i)))/(Ce(i+1)+Ce1);
  %%%%%%%%%%%%%%%%%%%%%%% TE section
    elseif i==a+2
        Cee=0.5*(Ce(i)+Ce(i+1));
        Se=0.5*(S(i)+S(i+1));
        V(i)=(Cee*V(i+1)-Se*Cee*(T(i+1)-T(i))-j0*stepx)/(Cee);
    elseif i>a+2 && i<a+c+1
        Cee=0.5*(Ce(i)+Ce(i+1));
        Cew=0.5*(Ce(i)+Ce(i-1));
        Se=0.5*(S(i)+S(i+1));
        Sw=0.5*(S(i)+S(i+1));
        V(i)=(Cee*V(i+1)-Cee*Se*(T(i+1)-T(i))+Cew*V(i-1)+Cew*Sw*(T(i)-
T(i-1)))/(Cee+Cew);
    elseif i==a+c+1
        Cew=0.5*(Ce(i)+Ce(i-1));
        Sw=0.5*(S(i)+S(i-1));
        V(i)=(2*Ce(i)*Vamb-2*Ce(i)*S(i)*(T(i+1)-T(i))+Cew*V(i-
1)+Cew*Sw*(T(i)-T(i-1)))/(2*Ce(i)+Cew);
  %%%%%%%%%%%%%%%%%%%%%%% TE section
    elseif i==a+c+2
        V(i)=(Ce1*V(i+1)+Ce(i-1)*S(i-1)*(T(i)-T(i-1))+Ce(i-1)*V(i-1))/(Ce(i-
1)+Ce1);
    elseif i==a+c+3
```

```
            V(i)=(V(i+1)+2*V(i-1))/3;
        elseif i>a+c+3 && i<m
            V(i)=(V(i+1)+V(i-1))/2;
        elseif i==m
            V(i)=(V(i-1)+2*Vamb)/3;
        end
    end
    %%%%%%%%%%%%%%%%%% calculation of V end
    diff1 = max(max(abs((T - Told)./T)));     % Max difference between iterations
    diff2 = max(max(abs((V - Vold)./V)));     % Max difference between iterations
    fprintf('IterT = %8.0f - Dif. = %10.6f deg. C\n', p, diff1);
    fprintf('IterV = %8.0f - Dif. = %10.6f deg. C\n', p, diff2);
  if (diff1 < tol) && (diff2 < tol)% Exit iteration loop because of convergence
        break
    end
  end
```

The “Ec1XDfun.m”, “K1XDfun.m”, “S1XDfun.m” and “TM1XDfun.m” are called by the main code, and they are the functions of important coefficients for the TE materials. The functions below show the Lagrange polynomial approximation from different references.

```
function [Ce]=Ec1XDfun(T,m,a,c) %the function of the Electric conductivity of the TE Materials

Ce=zeros(m,1);
for i=a+2:a+c+1
Ce(i)=1/(8.826*10^-6*(1+5.88*10^-3*(T(i)-300)+8.93*10^-6*(T(i)-300)^2));
 end
end

function [k]= K1XDfun(T,m,a,c) %the function of the thermal conductivity of the TE Materials
k=zeros(m,1);
for i=a+2:a+c+1
k(i)=100*(-8*10^-13*(T(i)-273.15)^4+3*10^-10*(T(i)-273.15)^3+6*10^-08*(T(i)-273.15)^2-3*10^-05*(T(i)-273.15)+0.0122);
end
 end

function [S]= S1XDfun(T,m,a,c) %the function of the Seebeck coefficient of the TE Materials
```

```
S=zeros(m,1);
for i=a+2:a+c+1
S(i)=2.207*10^-4*(1+1.55*10^-3*(T(i)-300)-3.15*10^-6*(T(i)-300)^2);
end
end

function [TM]=TM1XDfun(T,m,a,c) %the function of the Thomson coefficient of the TE Materials
TM=zeros(m,1);
for i=a+2:a+c+1
TM(i)=4*(-1*10^-15*(T(i)-273.15)^4)-3*(10^-12*(T(i)-273.15)^3)+2*(10^-9*(T(i)-273.15)^2)-3*10^-7*(T(i)-273.15);
end
end
```

Appendix 2

The COMSOL Multiphysics simulation results of temperature and velocity field is presented in this part. The temperature and velocity field under engine speed of 3000 rpm and various exhaust temperature is selected as a representative for all the simulation results.

From these figures, it is can be seen that there are an obvious accumulation and reflux of the exhaust gas at the outlet of each heat exchanger, due to the reduction in cross-section at the outlet of the heat exchanger. Furthermore, accumulation and reflux of the exhaust gas will enhance the heat transfer for the heat pipes located in this area and force the hot-side temperature of the TEMs rise. This also gives evidence of the curves displayed in Chapter Five. In addition, by comparing Figure 0-1, Figure 0-2, Figure 0-3 and Figure 0-5, the gas flow between the heat pipes has been improved after the insertion of the angled fins. By comparing Figure 0-4 and Figure 0-5, the airflow between the heat pipes becomes weaker in the heat exchanger with different heat pipe lengths, but the temperature distribution becomes harmonious. Therefore, it is better to combine the heat exchanger with different heat pipe length and angled fins.

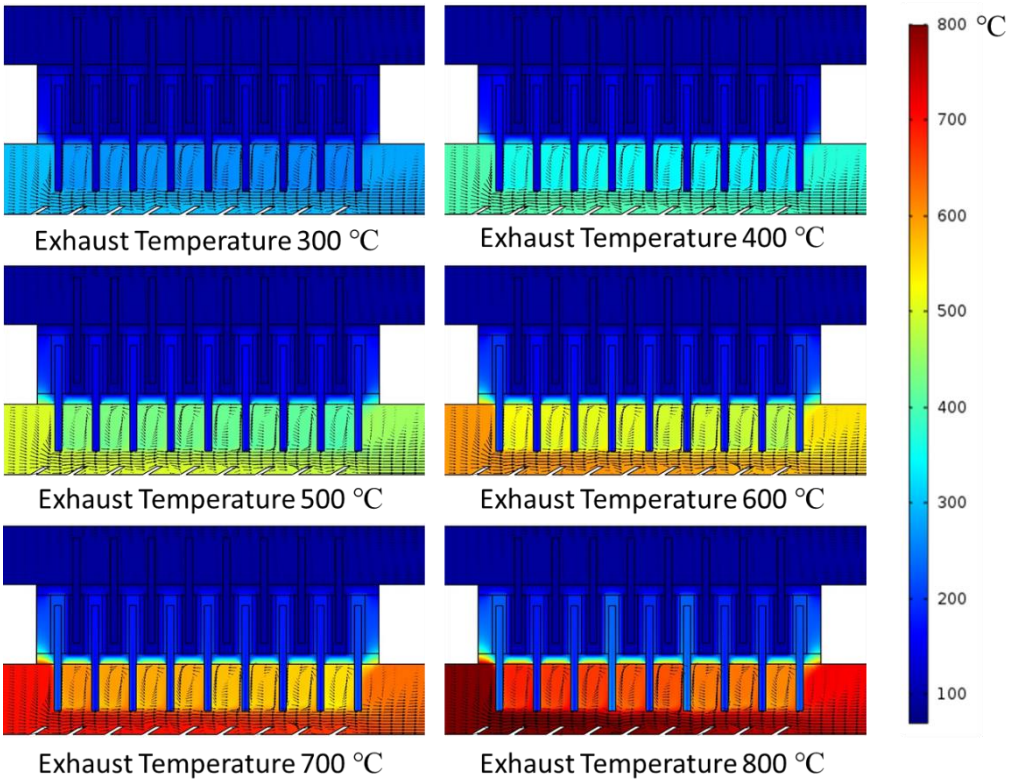


Figure 0-1 Temperature and velocity field of heat exchanger with 30° fins

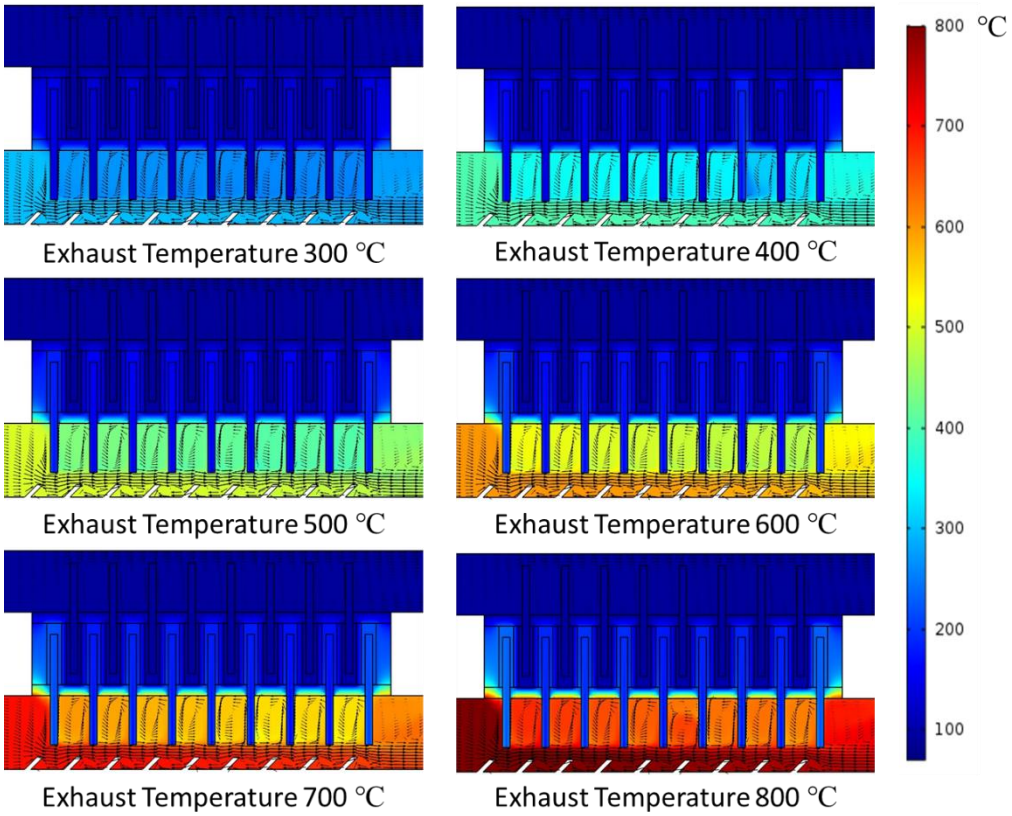


Figure 0-2 Temperature and velocity field of heat exchanger with 45° fins

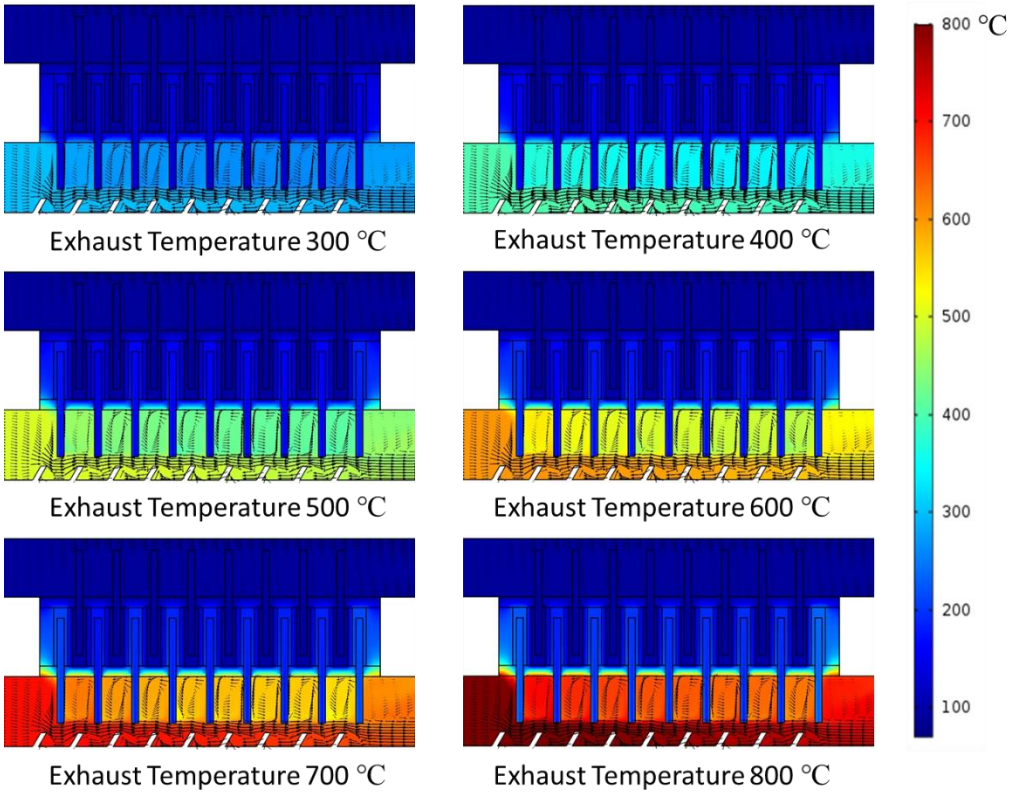


Figure 0-3 Temperature and velocity field of heat exchanger with 60° fins

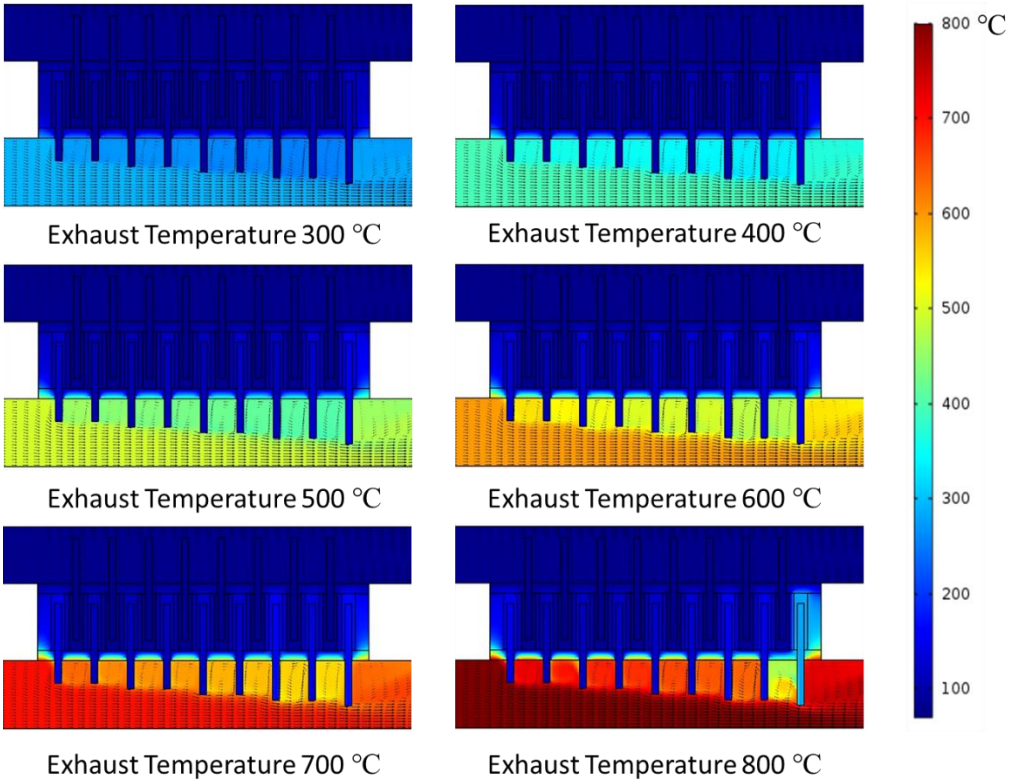


Figure 0-4 Temperature and velocity field of heat exchanger with different heat pipe length

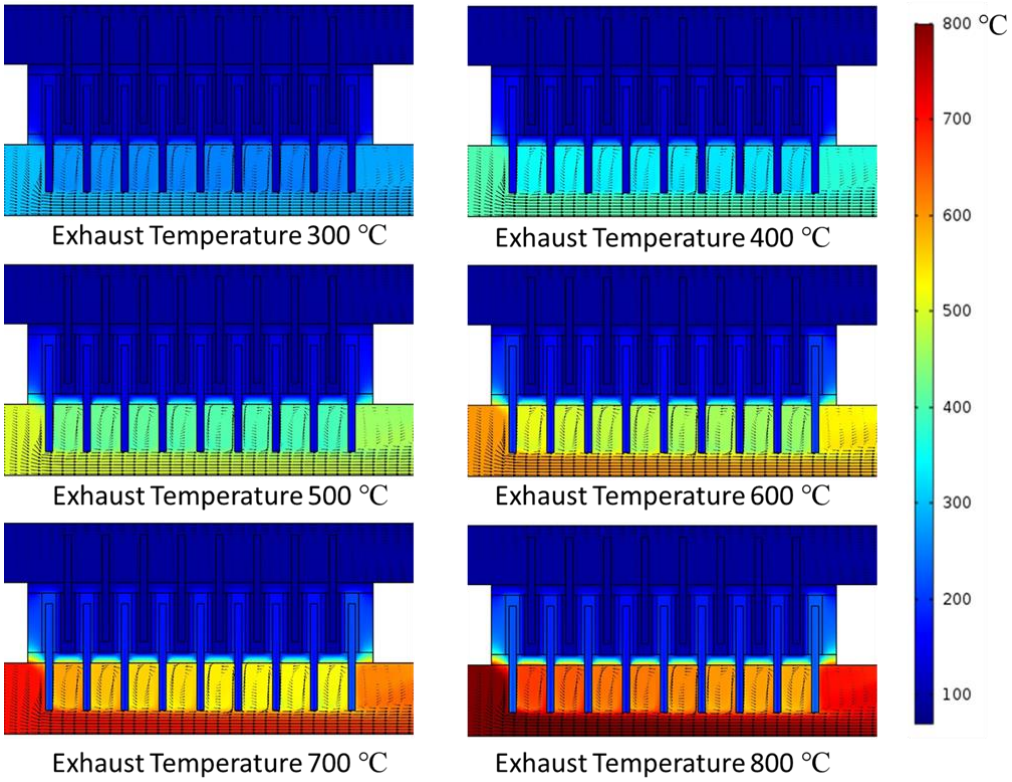


Figure 0-5 Temperature and velocity field of heat exchanger without fin